Soft X-ray Spectroscopic Study of Electronic and Magnetic Properties of Magnetic Topological Insulators

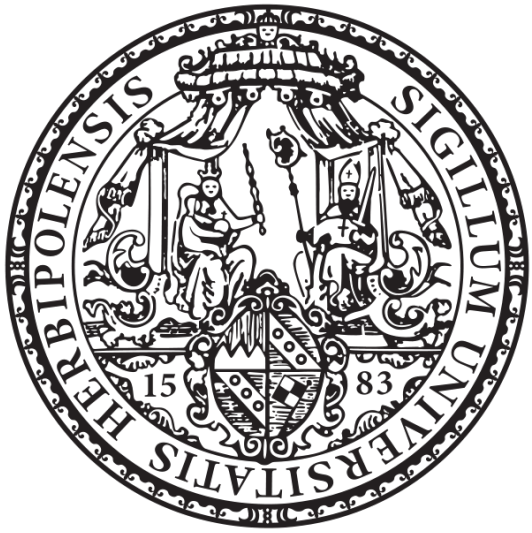

Dissertation zur Erlangung des
naturwissenschaftlichen Doktorgrades
der Julius-Maximilians-Universität Würzburg

vorgelegt von
Abdul-Vakhab Tcakaev
aus Grosny

Würzburg 2022

Eingereicht am:

bei der Fakultät für Physik und Astronomie

1. Gutachter: Prof. Dr. Vladimir Hinkov

2. Gutachter: Prof. Dr. Hartmut Buhmann

3. Gutachter:

der Dissertation

Vorsitzende(r):

1. Prüfer: Prof. Dr. Vladimir Hinkov

2. Prüfer: Prof. Dr. Hartmut Buhmann

3. Prüfer: Prof. Dr. Giorgio Sangiovanni

im Promotionskolloquium

Tag des Promotionskolloquiums:

Doktorurkunde ausgehändigt am:

"Read in the Name of your Lord Who created –
created humans from a clinging clot.
Read! And your Lord is the Most Generous,
Who taught by the pen –
***taught humanity what they knew not**."*

Quran 96:1-5

Dedicated to my Parents

Abstract

After the discovery of three-dimensional topological insulators (TIs), such as tetradymite chalcogenides Bi_2Se_3, Bi_2Te_3 and Sb_2Te_3 – a new class of quantum materials characterized by their unique surface electronic properties – the solid state community got focused on topological states that are driven by strong electronic correlations and magnetism. An important material class is the magnetic TI (MTI) exhibiting the quantum anomalous Hall (QAH) effect, i.e. a dissipationless quantized edge-state transport in the absence of external magnetic field, originating from the interplay between ferromagnetism and a topologically non-trivial band structure. The unprecedented opportunities offered by these new exotic materials open a new avenue for the development of low-dissipation electronics, spintronics, and quantum computation. However, the major concern with QAH effect is its extremely low onset temperature, limiting its practical application. To resolve this problem, a comprehensive understanding of the microscopic origin of the underlying ferromagnetism is necessary.

V- and Cr-doped $(Bi,Sb)_2Te_3$ are the two prototypical systems that have been widely studied as realizations of the QAH state. Finding microscopic differences between the strongly correlated V and Cr impurities would help finding a relevant model of ferromagnetic coupling and eventually provide better control of the QAH effect in these systems. Therefore, this thesis first focuses on the V- and Cr-doped $(Bi,Sb)_2Te_3$ systems, to better understand these differences. Exploiting the unique capabilities of x-ray absorption spectroscopy and magnetic circular dichroism (XAS/XMCD), combined with advanced modeling based on multiplet ligand-field theory (MLFT), we provide a detailed microscopic insight into the local electronic and magnetic properties of these systems and determine microscopic parameters crucial for the comparison with theoretical models, which include the d-shell filling, spin and orbital magnetic moments. We find a strongly covalent ground state, dominated by the superposition of one and two Te-ligand-hole configurations, with a negligible contribution from a purely ionic 3+ configuration. Our findings indicate the importance of the Te $5p$ states for the ferromagnetism in $(Bi, Sb)_2Te_3$ and favor magnetic coupling mechanisms involving pd-exchange. Using state-of-the-art density functional theory (DFT) calculations in combination with XMCD and resonant photoelectron spectroscopy (resPES), we reveal the important role of the $3d$ impurity states in mediating magnetic exchange coupling. Our calculations illustrate that the kind and strength of the exchange coupling varies with the impurity $3d$-shell occupation. We find

a weakening of ferromagnetic properties upon the increase of doping concentration, as well as with the substitution of Bi at the Sb site. Finally, we qualitatively describe the origin of the induced magnetic moments at the Te and Sb sites in the host lattice and discuss their role in mediating a robust ferromagnetism based on a *pd*-exchange interaction scenario. Our findings reveal important clues to designing higher T_C MTIs.

Rare-earth ions typically exhibit larger magnetic moments than transition-metal ions and thus promise the opening of a wider exchange gap in the Dirac surface states of TIs, which is favorable for the realization of the high-temperature QAH effect. Therefore, we have further focused on Eu-doped Bi_2Te_3 and scrutinized whether the conditions for formation of a substantial gap in this system are present by combining spectroscopic and bulk characterization methods with theoretical calculations. For all studied Eu doping concentrations, our atomic multiplet analysis of the $M_{4,5}$ x-ray absorption and magnetic circular dichroism spectra reveals a Eu^{2+} valence, unlike most other rare earth elements, and confirms a large magnetic moment. At temperatures below 10 K, bulk magnetometry indicates the onset of antiferromagnetic ordering. This is in good agreement with DFT results, which predict AFM interactions between the Eu impurities due to the direct overlap of the impurity wave functions. Our results support the notion of antiferromagnetism coexisting with topological surface states in rare-earth doped Bi_2Te_3 and corroborate the potential of such doping to result in an antiferromagnetic TI with exotic quantum properties.

The doping with impurities introduces disorder detrimental for the QAH effect, which may be avoided in stoichiometric, well-ordered magnetic compounds. In the last part of the thesis we have investigated the recently discovered intrinsic magnetic TI (IMTI) $MnBi_6Te_{10}$, where we have uncovered robust ferromagnetism with $T_C \approx 12$ K and connected its origin to the Mn/Bi intermixing. Our measurements reveal a magnetically intact surface with a large moment, and with FM properties similar to the bulk, which makes $MnBi_6Te_{10}$ a promising candidate for the QAH effect at elevated temperatures. Moreover, using an advanced ab initio MLFT approach we have determined the ground-state properties of Mn and revealed a predominant contribution of the d^5 configuration to the ground state, resulting in a *d*-shell electron occupation $n_d = 5.31$ and a large magnetic moment, in excellent agreement with our DFT calculations and the bulk magnetometry data. Our results together with first principle calculations based on the DFT-GGA+U, performed by our collaborators, suggest that carefully engineered intermixing plays a crucial role in achieving a robust long-range FM order and therefore could be the key for achieving enhanced QAH effect properties.

We expect our findings to aid better understanding of MTIs, which is essential to help increasing the temperature of the QAH effect, thus facilitating the realization of low-power electronics in the future.

Zusammenfassung

Nach der Entdeckung von dreidimensionalen topologischen Isolatoren (TIs), einer neuen Klasse von Quantenmaterialien, die sich durch ihre einzigartigen elektronischen Oberflächeneigenschaften auszeichnen – und zu denen beispielsweise die Tetradymit-Dichalkogenide Bi_2Se_3, Bi_2Te_3 und Sb_2Te_3 gehören –, gerieten zunehmend topologische Zustände, deren Eigenschaften von starken elektronische Korrelationen und Magnetismus bestimmt werden, in den Fokus aktueller Festkörperforschung. Eine wichtige Materialklasse bilden die magnetischen TI (MTI), die einen quantenanomalen Hall-Effekt (QAH) aufweisen, d.h. eine dissipationsfreie, quantisierte Randzustandsleitfähigkeit in Abwesenheit eines externen Magnetfeldes, die aus dem Zusammenspiel von Ferromagnetismus und einer topologisch nicht-trivialen Bandstruktur resultiert. Die beispiellosen Möglichkeiten, die solche neuen, exotischen Materialien bieten, eröffnen einen neuen Weg für die Entwicklung von Elektronik mit geringer Verlustleistung, sowie von Spintronik und von Quantencomputern. Das Hauptproblem des QAH-Effekts ist jedoch die extrem niedrige Temperatur, bei der er auftritt, was seine praktische Anwendung einschränkt. Um dieses Problem zu lösen, ist ein umfassendes Verständnis des mikroskopischen Ursprungs des zugrunde liegenden Ferromagnetismus erforderlich.

V- und Cr-dotiertes $(Bi,Sb)_2Te_3$ sind die beiden prototypischen Systeme, die als Realisierungen des QAH-Zustands umfassend untersucht wurden. Die Suche nach mikroskopischen Unterschieden zwischen den stark korrelierten V- und Cr-Dotieratomen würde helfen, ein relevantes Modell für die ferromagnetische Kopplung zu finden und schließlich eine bessere Kontrolle des QAH-Effekts in diesen Systemen zu ermöglichen. Daher konzentriert sich diese Arbeit zunächst auf die V- und Cr-dotierten $(Bi,Sb)_2Te_3$-Systeme, um diese Unterschiede besser zu verstehen. Unter Ausnutzung der einzigartigen Möglichkeiten der Röntgenabsorptionsspektroskopie und des magnetischen Zirkulardichroismus (XAS/XMCD), kombiniert mit fortschrittlicher Modellierung auf der Grundlage der Multiplett-Liganden-Feld-Theorie (MLFT), geben wir einen detaillierten mikroskopischen Einblick in die lokalen elektronischen und magnetischen Eigenschaften dieser Systeme und bestimmen mikroskopische Parameter, die für den Vergleich mit theoretischen Modellen entscheidend sind. Wir finden einen stark kovalenten Grundzustand,

der von der Überlagerung von Ein- und Zwei-Te-Liganden-Loch-Konfigurationen dominiert wird, mit einem vernachlässigbaren Beitrag einer rein ionischen 3+ Konfiguration. Unsere Ergebnisse weisen auf die Bedeutung der Te 5*p*-Zustände für den Ferromagnetismus in (Bi, Sb)$_2$Te$_3$ hin und deuten auf magnetische Kopplungsmechanismen mit *pd*-Austausch hin. Unter Verwendung modernster Dichtefunktionaltheorie (DFT)-Rechnungen in Kombination mit XMCD und resonanter Photoelektronenspektroskopie (resPES) demonstrieren wir die wichtige Rolle der 3*d*-Dotieratomzustände bei der Vermittlung der magnetischen Austauschkopplung. Unsere Berechnungen zeigen, dass die Art und Stärke der Austauschkopplung mit der 3*d*-Schalenbesetzung der Dotieratome variiert. Wir stellen eine Abschwächung der ferromagnetischen Eigenschaften bei Erhöhung der Dotierungskonzentration fest, ebenso wie bei Substitution von Bi an der Sb-Stelle. Schließlich beschreiben wir qualitativ den Ursprung der induzierten magnetischen Momente an den Te- und Sb-Stellen im Wirtsgitter und diskutieren ihre Rolle bei der Vermittlung eines robusten Ferromagnetismus auf der Grundlage des *pd*-Austauschwechselwirkungsszenarios. Unsere Ergebnisse liefern wichtige Anhaltspunkte für die Entwicklung von MTIs mit höherem T_C.

Seltenerdionen weisen typischerweise größere magnetische Momente auf als Übergangsmetall-Ionen und legen daher die Öffnung einer größeren Austauschlücke in den Dirac-Oberflächenzuständen von TIs nahe, was für den Hochtemperatur-QAH-Effekt günstig ist. Daher haben wir uns weiter auf Eu-dotiertes Bi_2Te_3 konzentriert und untersucht, ob die Bedingungen für die Bildung einer substantiellen Lücke in diesem System gegeben sind, indem wir spektroskopische und Bulk-Charakterisierungsmethoden mit theoretischen Berechnungen kombiniert haben. Für alle untersuchten Eu-Dotierungskonzentrationen zeigt unsere atomare Multiplettanalyse der $M_{4,5}$-Röntgenabsorptions- und der magnetischen Zirkulardichroismus-Spektren eine Eu^{2+}-Valenz, im Gegensatz zu den meisten anderen Seltenen Erden, und bestätigt ein großes magnetisches Moment. Bei Temperaturen unter 10 K zeigt die Magnetometrie das Einsetzen einer antiferromagnetischen Ordnung an. Dies steht in guter Übereinstimmung mit DFT-Ergebnissen, die AFM-Wechselwirkungen zwischen den Eu-Dotieratomen aufgrund des direkten Überlapps der Wellenfunktionen der Dotieratome vorhersagen. Unsere Ergebnisse unterstützen die Annahme von Antiferromagnetismus, der mit topologischen Oberflächenzuständen in mit Seltenerdatomen dotiertem Bi_2Te_3 koexistiert, und bestätigen das Potenzial einer solchen Dotierung, einen antiferromagnetischen TI mit exotischen Quanteneigenschaften zu erzeugen.

Dotierung führt zu einer für den QAH-Effekt nachteiligen Unordnung, die in stöchiometrischen, gut geordneten magnetischen Verbindungen vermieden werden kann. Im letzten Teil der Arbeit haben wir den kürzlich entdeckten, intrinsischen magnetischen TI (IMTI) $MnBi_6Te_{10}$ untersucht, in dem wir robusten Ferromagnetismus mit $T_C \approx$ 12 K beobachtet und seinen Ursprung mit Mn/Bi-Antilagendefekte (Substitution von

Mn auf Bi-Plätzen und umgekehrt) in Verbindung gebracht haben. Unsere Messungen zeigen eine magnetisch intakte Oberfläche mit einem großen Moment und mit FM-Eigenschaften, die denen im Inneren des Materials ähnlich sind, was $MnBi_6Te_{10}$ zu einem vielversprechenden Kandidaten für den QAH-Effekt bei erhöhten Temperaturen macht. Darüber hinaus haben wir mit Hilfe eines fortgeschrittenen ab initio MLFT-Ansatzes die Grundzustandseigenschaften von Mn bestimmt und einen vorherrschenden Beitrag der d^5-Konfiguration zum Grundzustand festgestellt, was zu einer d-Schalen-Elektronenbesetzung $n_d = 5.31$ und einem großen magnetischen Moment führt, in hervorragender Übereinstimmung mit unseren DFT-Berechnungen und den Daten der Magnetometrie. Unsere Ergebnisse, kombiniert mit den auf DFT-GGA+U basierenden First-Principle-Berechnungen, die von Kollegen durchgeführt wurden, deuten darauf hin, dass sorgfältig herbeigeführte Antilagendefekte eine entscheidende Rolle bei der Erzielung einer robusten langreichweitigen FM-Ordnung spielen und daher der Schlüssel zur Erzielung verbesserter QAH-Eigenschaften sein könnten.

Wir erwarten, dass unsere Ergebnisse zu einem besseren Verständnis von MTIs beitragen werden, was wiederum die Erhöhung der Temperatur des QAH-Effekts und damit die Realisierung von Low-Power-Elektronik in der Zukunft erleichtern wird.

Contents

List of Figures

List of Tables

Chapter 1

Introduction

The success of modern information and communication era is deeply rooted in the ever-evolving semiconductor technology. After the development of the first semiconductor transistor in the late 1940's, the subsequent research and improvements in technology led to the fact that semiconductors-based devices, like smart phones, computers, solar cells, LEDs and laser diodes to name just a few, became an indispensable part of our everyday life.

However, for the first time in more than 50 years, the semiconductor industry is on the verge of entering uncharted territory and the progress is about to slow down [3]. The reason for this inevitable slow-down is that the demand for smaller-sized and more power efficient devices led the semiconductor technology to reach its fundamental limits [4]. Obviously, the conventional approach of improving the integrated circuits by simply making transistors ever smaller so they can be placed at higher densities on chips has a limit. The shrinking of the transistors affects electrical properties, e.g. it exacerbates the off-state current leakage [5]. Moreover, overheating is an inevitable result when more and more transistors are packed on tiny chips. Therefore, it is necessary to abandon the traditional approach of transistor scaling and develop new classes of materials, with qualitatively new physical characteristics compared to traditional semiconductor compounds, for the use in electronic applications.

One of these new classes of materials are topological insulators (TIs) [6, 7], for the theoretical groundwork of which the 2016 Nobel Prize in Physics was awarded. These are the materials that have insulating properties in the bulk yet feature conductive surface states or edge states at the boundary. These surface states originate from the topological property of the bulk electronic structure and protected by time-reversal symmetry (TRS). Furthermore, in such topological insulators, the symmetry protection of the surface states makes them robust against disorder. Therefore, topological insulators can be highly relevant for commercial applications, as they offer a great opportunity for high performance devices with low dissipation.

Additionally, TIs offer new interesting quantum phenomena deriving from their peculiar properties. An important example is the quantum anomalous Hall (QAH) effect originating from the interplay between ferromagnetism and topological properties of

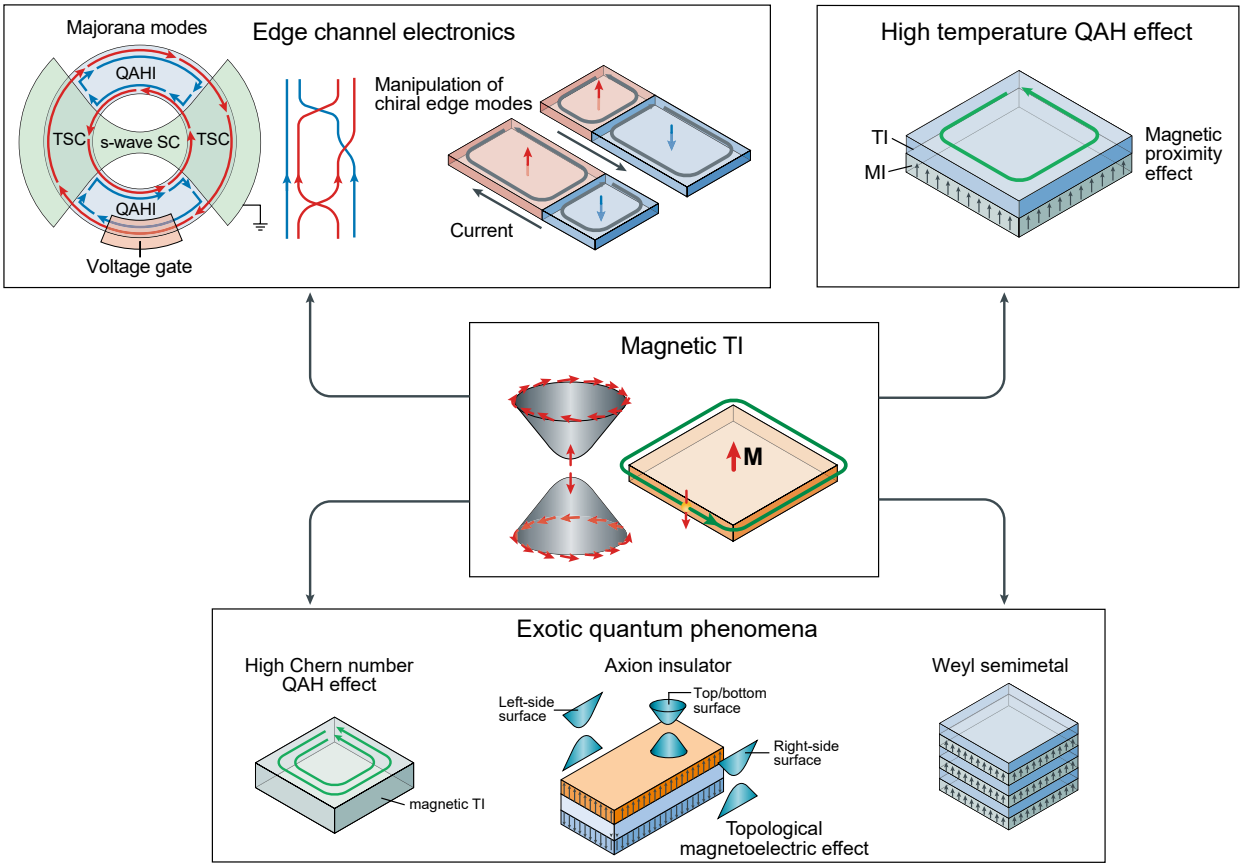

Figure 1.1: Future perspectives and potential applications of magnetic topological insulators (MTIs). Magnetic proximity effects in heterostructures based on magnetic insulators (MI) and TIs may yield the QAH effect at high temperatures. The stacking of MIs and TIs, or of trivial insulators and MTIs, may result in the realization of Weyl semimetals through fine-tuning of the film thickness. An axion insulator state can be realized in a QAH effect thin film when the magnetization directions on the two surfaces (top and bottom) are opposite, yielding quantized topological magnetoelectric effects. In MTIs the QAH effect with high Chern number, i.e with multiple chiral edge channels, may be obtained by appropriate material choices and fine-tuning spin–orbit coupling, ferromagnetic exchange energy, and film thickness [1]. It is proposed that the proximity of the QAH insulator (QAHI) to a *s*-wave superconductor (SC) in an elaborate device design results in the formation of a topological SC (TSC), accompanied by the appearance of chiral Majorana edge modes, which are important for topological quantum computation. Finally, the manipulation of magnetic domain walls (local reversal of the magnetization direction) by electrical or optical means will enable fast control of chiral edge modes. Adapted from Ref. [2].

electronic band structures. Introduction of ferromagnetism into TIs, e.g. by magnetic doping with transition metals, breaks the TRS and suppresses one of the spin-polarized edge channels, resulting in a single chiral edge mode which propagates with virtually no dissipation either clockwise or counterclockwise around the boundary of the material, depending on the direction of magnetization. The experimental fingerprint of QAH effect is a Hall conductance quantized to ne^2/h at zero magnetic field. Here n is the so-called Chern number, which depends on the topological properties of the band structure, as will

be discussed in the following chapter. The two prototype materials that have been widely studied as realizations of the QAH state are the magnetically doped TIs Cr:$(Bi,Sb)_2Te_3$ and V:$(Bi,Sb)_2Te_3$. The realization of such magnetic TIs (MTIs) featuring pure edge channel transport even in the absence of external magnetic fields, in contrast to the quantum Hall effect, was a milestone in the development of topological insulators.

Since the discovery of the quantum Hall effect, the QAH effect remains one of the few topological quantum effects unambiguously observed in experiments [8, 9]. It opens a new avenue for the development of resistance metrology [10], topological quantum computation [11] and spintronics [2]. Indeed, the chiral dissipationless transport, pursued by spintronics, is a key signature of the QAH effect, which can be used for elimination of Joule heat in densely packed integrated circuits [12]. As the only source of electrical resistance in QAH devices is the contact resistances, it was proposed to use that QAH devices to construct chiral interconnects, which are more efficient than an ordinary metal wires [13]. Moreover, spin polarized current carried by the chiral edge states [14] enables the potential applications of QAH systems in spintronics. The idea behind spintronics is to exploit electron spins instead of the charge as the basic carriers for the device functionality [15]. For example, MTIs might enable an efficient current-induced magnetization switching, which is highly desirable for building new storage devices and logical devices based on spintronics [2, 16]. The QAH effect can also be used to realize other exotic quantum phenomena, such as topological superconductivity [17, 18] and axion electrodynamics [19–22] (see Fig. 1.1). Topological superconductors (TSC) are essential for the realization of chiral Majorana edge modes, which are now considered as a main route to realize topological quantum computing [2, 16]. In turn, axion insulators, which can be realized in QAH effect systems when the magnetization directions on the two surfaces are opposite, exhibit a unique coupling between their electromagnetic properties, known as the topological magnetoelectric effect, when the application of a magnetic field induces an electric polarization or, conversely, an electric field induces a magnetization [2, 4]. Clearly, MTIs exhibit rich physics and emergent phenomena and have great potential for future applications in low-dissipation electronics and quantum computations.

Nevertheless, despite the above attractive prospects, the major concern with the QAH effect is the extremely low temperature, at which the effect sets in. For example, in the prototypical V-doped $(Bi,Sb)_2Te_3$ QAH system, robust quantization characteristics are observed only at $T = 25$ mK, which is several orders of magnitude lower than the T_C of the system [8]. The further increase of the observation temperature up to 300 mK is achieved by magnetic codoping of $(Bi,Sb)_2Te_3$ TI with V and Cr [23], while spatially modulated magnetic doping results in the observation of the fully quantized QAH effect at 0.5 K [24]. Hence, the major task ahead is to further raise the temperature at which the QAH effect can be observed. Increasing the temperature at least to a few kelvins would already allow one to expand the number of the available experimental techniques, which could

further advance our understanding of QAH effect and other related phenomena, with the potential application of dissipationless conduction channels in electronic devices.

To resolve the problem of the low temperature required for the QAH effect in magnetically doped TIs, a comprehensive understanding of the exact mechanism of the QAH effect and, in particular, the microscopic origin of the underlying ferromagnetism and the electronic states inducing the magnetic coupling is necessary. This is one of the primary goals of the current thesis. Despite the recent progress in this direction, the microscopic nature of the magnetic order in these systems remains controversial and highly debated. The electronic structure of the magnetic ion 3*d* states near the Fermi level, hybridization between the valence or conduction states of the host material and the 3*d* states of the doped magnetic ions, as well as the impurity band in the band gap may play an important role in the mechanisms of intrinsic ferromagnetism. Indeed, comparative theoretical studies of different dopants show that the exact configuration of the magnetic impurity 3*d* states is important to understand the magnetic coupling [25–30], which requires its experimental determination. This can be accomplished by means of experimental methods used in the thesis, such as element-specific x-ray absorption spectroscopy (XAS), x-ray magnetic circular dichroism (XMCD) and resonant photoelectron spectroscopy (resPES), together with multiplet ligand-field theory (MLFT) calculations. XAS is a powerful tool to investigate the electronic structure of materials, with a high sensitivity to the site symmetry and the crystal field, the spin–orbit interaction, the spin configuration and the valence state, among others. In turn, XMCD offers a very efficient way to determine unambiguously and element-selectively the magnetic properties of the system. And finally, MLFT calculations allow one to determine in full detail the local magnetic and electronic structure, including the 3*d*-shell occupation, spin and orbital moments.

The discovery of the QAH effect in 3*d*-transition-metal-doped TIs further stimulated a material research for new QAH systems. Among the first was the idea of doping the strong TIs with rare earth elements, such as Gd, Eu, Sm, Ho, and Dy, in order to benefit from their typically larger magnetic moments compared to 3*d* transition metals, which could open a wider exchange gap in the Dirac surface states preferential for a more stable QAH effect. The present work also contributes in this direction: In Chapter 6 we study one such system, namely Eu-doped Bi_2Te_3 thin films, by means of various spectroscopic techniques, such as XAS/XMCD and resPES/ARPES, in combination with bulk magnetometry and theoretical methods, like density functional theory (DFT) and atomic multiplet calculations.

Another possibility to increase the temperature of the QAH effect is to use intrinsic magnetic topological insulators (IMTIs). Since IMTIs are stoichiometric, well-ordered magnetic compounds, they offer a uniform and large magnetic exchange gap as a result of homogeneous surface magnetic ordering. Recently, $MnBi_2Te_4$ (MBT) was theoretically

identified as the first candidate for IMTI [31, 32], and was subsequently widely scrutinized, both experimentally and theoretically [22, 33–41]. It was proposed that, due to its layered antiferromagnetic nature, MBT can be switched between a QAH state and an axion insulator state, depending on the number of constituent septuple-layers [22, 32]. Indeed, the realization of both QAH and axion insulator states was recently reported for few-septuple-layer thin flakes of $MnBi_2Te_4$ [41, 42]. Despite this significant experimental progress, an external magnetic field is still required to enhance the QAH effect and achieve exact quantization in Hall resistance. The observation of these phenomena in MBT has prompted further research of the higher-n members of the $(MnBi_2Te_4)(Bi_2Te_3)_n$ family, such as $MnBi_4Te_7$ and $MnBi_6Te_{10}$. $MnBi_6Te_{10}$ might be a good candidate for the realization of a high-precision QAH effect under zero magnetic field, since increasing n weakens the interlayer AFM coupling and FM properties develop, promising a further substantial increase of the onset temperature of the QAH effect. Therefore, the investigation of electronic and magnetic properties of $MnBi_6Te_{10}$ using bulk-sensitive superconducting quantum interference device (SQUID) magnetometry and surface-sensitive XMCD, in combination with theoretical approaches, is another goal of the current work.

Outline of the Thesis

This thesis can be divided into two parts. In the first part (Chapter 2 and 3) we present the essential background of the physics of topological insulators (TI), with the emphasis on magnetic TIs, and discuss the experimental and theoretical methods used in the research work. The second part, Chapters 4 to 7, presents original results on the electronic and magnetic properties of different magnetic TIs, such as prototypical QAH systems V- and Cr-doped $(Bi,Sb)_2Te_3$, rare-earth doped Bi_2Te_3, and the recently discovered intrinsic magnetic TI $MnBi_6Te_{10}$, which is a promising candidate for the QAH effect at elevated temperatures. In the following, an outline of the individual chapters is given.

Chapter 2 comprises a brief introduction to the field of TIs and discusses the basic concepts of MTIs and their experimental realization. It starts with a discussion of TIs in the 2D case, with the purpose of facilitating the description of 3D TIs. Later, an overview of the QAH effect in different MTIs, such as transition metal and rare earth doped TIs, as well as IMTIs, is given. The different mechanisms of ferromagnetism proposed in doped TIs are also summarized.

Chapter 3 presents a detailed description of the different experimental and theoretical methods relevant for this work. In addition to a general introduction to the core-level spectroscopy, the processes of x-ray absorption and XMCD, which are the main experimental techniques employed in this thesis, are discussed. The corresponding experimental aspects of XAS and XMCD are also briefly reviewed. The last part of the chapter

deals with different approaches to the analysis of the measured spectra, such as sum rules analysis and configuration-interaction cluster calculations.

In Chapter 4, a detailed microscopic insight into the electronic and magnetic properties of the V-and Cr-doped $(Bi,Sb)_2Te_3$ is provided to better understand the difference between the two dopants and the origin of the more robust realization of the ideal QAH state in V-doped systems as compared to Cr-doped systems. The line shapes of V and Cr $L_{2,3}$ XAS and XMCD spectra are comprehensively modeled using MLFT calculations and their correlated many-particle ground state is determined.

Chapter 5 explains the exchange coupling mechanisms underlying the onset of ferromagnetism in V-and Cr-doped $(Bi,Sb)_2Te_3$ thin films. The fundamental link between the local impurity electronic structure and magnetic coupling is established in a joint experimental and theoretical approach. The electronic and magnetic fingerprints of the 3*d* states of Cr and V impurities are systematically probed as a function of impurity concentration by means of XMCD and resPES. The effect of Bi/Sb substitution in the host on the magnetic properties is also studied. Moreover, the origin of the induced magnetic moments at the otherwise non-magnetic Te and Sb atoms in the host lattice, as well as their role in mediating a robust ferromagnetism, is explained based on the Zener-type *pd*-exchange interaction scenario.

Chapter 6 provides a deep look into the magnetic properties of the Eu-doped Bi_2Te_3 films by XMCD and SQUID, as well as the electronic structure of the material by resPES and ARPES. A comprehensive investigation of a series of high structural quality samples with three different Eu concentrations is conducted. The line shape of Eu $M_{4,5}$ XAS and XMCD spectra are modeled with atomic multiplet calculations, which allows one to determine the valence state and magnetic moment of the dopants. These results are compared to the results of a sum rules analysis. The bulk properties of the samples are investigated by means of SQUID magnetometry. Furthermore, the electronic properties are characterized by combination of resPES and ARPES. Finally, the DFT model established based on photoemission measurements, explains the magnetic properties observed with SQUID magnetometry.

In Chapter 7 one member of the recently discovered IMTIs, namely $MnBi_6Te_{10}$, is investigated. It provides insight into the surface and bulk properties of this new topological material by means of XMCD and SQUID measurements. The effect of Mn substoichiometry and Mn/Bi site intermixing on the magnetic ground state of the system is addressed by sample characterization methods and extensive DFT calculations. Important microscopic physical parameters, including the Mn 3*d*-shell occupation, and the spin and orbital magnetic moments are determined by analysis of spectroscopic data using sum rules and *ab initio* MLFT calculations.

Finally, the last part summarizes the results of the present work and gives a short outlook to further investigations. All chapters are organized in such a way that they are

self-contained and can be read independently of each other.

Chapter 2

Magnetic Topological Insulators - Theoretical Concepts and Prototypical Examples

In this chapter we briefly introduce the reader to the field of topological insulators (TIs) — a conceptually new quantum phase of matter — and discuss the basic concepts of magnetic topological insulators (MTIs) and their experimental realization, together with the discovery of a novel quantum effect – the quantum anomalous Hall (QAH) effect. This chapter is not meant as a comprehensive discourse of TIs or even MTIs. Instead we only focus on the important aspects relevant to the scope of this work and the research projects that will be discussed later. There are a number of excellent reviews on TIs [6, 7, 43], as well as MTIs [1, 2, 12, 44], where a comprehensive description of the field can be found.

2.1 Topological states of matter

Distinguishing between the different phases of matter is one of the greatest achievements of condensed matter physics in the last century. Often, distinctive phases of matter can be classified by the principle of spontaneous symmetry breaking according to the Landau–Ginzburg theory [6, 7, 45]. For instance, (i) in the crystalline solids ions are arranged periodically, thereby breaking the continuous symmetry of space under rotations and translations, (ii) in typical magnets some of the rotational symmetry of spin space is broken, together with the time-reversal symmetry, (iii) a superconductor breaks gauge symmetry [43]. Nevertheless, it turns out that there are still some phase transitions that cannot be explained by a broken symmetry. In the 1980s, this approach of classification by symmetry breaking was challenged by the notion of topological order. It is possible for two very similar phases with the same symmetries to be different from one another.

The concept of topological order was first introduced in condensed matter physics with the discovery of the integer quantum Hall effect (QHE) in 1980 and the subsequent theoretical efforts to explain it [46–48]. It was experimentally observed that electrons

confined to two dimensions (2D) and subjected to a sufficiently strong magnetic field at low temperature exhibit one dimensional conduction channels at the edges of the sample, as schematically shown in Fig. 2.1 (a), while the bulk of the sample is insulating. These unidirectional (or "chiral") edge channels are non-dissipative and characterized by a quantized Hall conductivity $\sigma_{xy} = ne^2/h$, where the integer n corresponds to the number of edge channels, as well as to the occupancy of the Landau levels. Theoretical works explaining the experimental results [47, 48] revealed that the precise quantization of σ_{xy} is due to the fact that n can be understood as a topological invariant called the Chern number, which does not depend on the details of the underlying material.

In one of the branches of mathematics known as topology, topological invariance is used to classify different geometrical objects into broad classes. For example, according to the Gauss–Bonnet theorem, the 2D surfaces can be topologically classified by their genus, which counts the number of holes present in them, regardless of their specific shapes. So in this sense, a sphere is topologically equivalent to an ellipsoid, while a doughnut is equivalent to a coffee cup because they both have only one hole. In an analogous manner, the energy bands of the 2D electron system can be topologically characterized by the Chern number, which is defined as the surface integral of the Berry curvature over the whole Brillouin zone divided by 2π [49]. The Chern number is odd under time reversal and therefore is nonzero only in a material with broken time-reversal symmetry (TRS) [1], for example, by an external magnetic field or spontaneous magnetization. In the case of QHE, the total Chern number is nonzero, while for the vacuum, which can be considered as a trivial insulator, the Chern number is 0. Therefore, the QHE system is topologically distinct from the trivial insulator, and owing to a phenomenon known as bulk-boundary correspondence, this results in the appearance of a gapless state at the interface between these two different topological phases, which forms $|n|$ chiral edge channels, see Fig. 2.1 (a).

2.2 2D topological insulators and quantum spin Hall effect

The integer QHE is restricted to high-mobility 2D systems with applied magnetic field, i.e. with broken time-reversal symmetry (TRS). The natural question to ask is whether a QHE can exist without an external magnetic field, or, in other words, is there a similar quantum version of the anomalous Hall effect, i.e. a "quantum anomalous Hall effect". In fact, attempts to answer this question led to the discovery of topological insulators (TIs), which we will discuss below.

In 1988 Haldane proposed a model demonstrating the theoretical possibility of realizing a QHE without an external magnetic field and the formation of Landau levels [50]. This toy tight-binding model employs a graphene-like honeycomb lattice with the TRS broken by a hypothetical periodic magnetic field with zero net magnetic flux in the unit

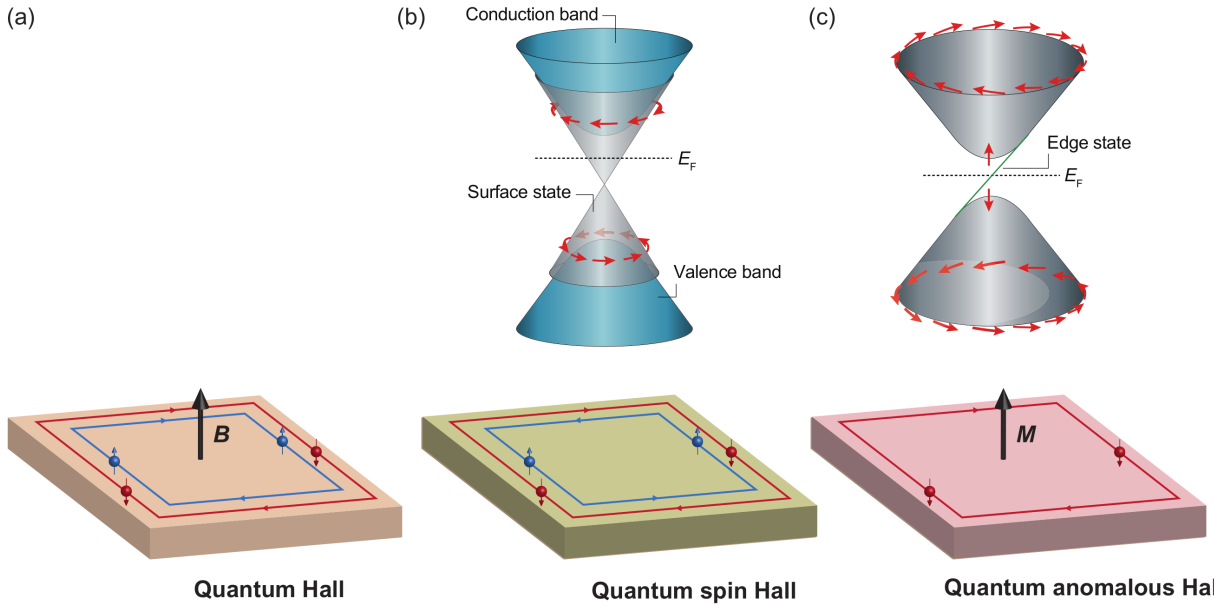

Figure 2.1: Schematics of the (a) chiral edge states of the QHE, (b) helical edge states of the QSHE, and (c) chiral edge states of the QAH effect. Horizontal arrows indicate the directions of electron propagation, and vertical arrows indicate spin direction. Top panel in (b) depicts the massless Dirac-like dispersion of the surface state with spin–momentum locking in a topological insulator and in (c) the gapped Dirac-like dispersion of the surface state in a magnetic topological insulator (adopted from Ref.[2]). The red arrows show the spin polarization.

cell of a periodic 2D system. As there is no net magnetic field, the quantized Hall conductance originates from the band structure of electrons in the lattice and not from the discrete Landau levels in a strong magnetic field. Pristine graphene is a semimetal possessing an interesting band structure: It has a double-cone-shaped electronic band structure forming a Dirac cone, with no DOS and band gap at the cone apex, the Dirac point. So near this point the electronic dispersion resembles the linear dispersion of massless relativistic particles described by the Dirac equation [6]. The broken TRS opens a gap at the Dirac point, rendering the system a Chern insulator, i.e. a system with energy bands that are characterized by a non-zero Chern number.

Although the aforementioned Haldane model highlighted the theoretical possibility of a material topologically equivalent to a QHE system in the absence of external magnetic field, namely a QAH effect system, the experimental evidence for such a system remained elusive for another two decades, until the discovery of TIs. TIs were theoretically predicted by extending the formalism for 2D topological phases with broken TRS to 2D or 3D systems with preserved TRS. Indeed, in 2005 Kane and Mele generalized the Haldane model and introduced strong spin–orbit coupling to replace the periodic magnetic flux [51, 52]. The introduction of a spin–orbit interaction term leads to a gap opening in the otherwise gapless Dirac cone of graphene, which happens without any magnetic field, and turns it not into a trivial insulator, but into a topological one. As a result, one

observes helical edge states that comprise a pair of counter-propagating chiral states with spin-momentum locking, wherein electrons that transport in opposite directions carry opposite spins, as schematically illustrated in Fig. 2.1 (b). This feature comes from time-reversal symmetry, which forbids electron backscattering, i.e. the edge states are robust against impurities or disorders as long as time-reversal symmetry is preserved. When the bulk state is insulating, the transport signal is provided mainly by the helical edge states and gives rise to the so-called quantum spin Hall effect (QSHE) [53]. This effect can be considered as a combination of two copies of a QAH effect system shown in Fig. 2.1 (c), with mutually opposite magnetizations. It was experimentally realized in HgTe/CdTe quantum wells by König *et al.* [54] soon after the theoretical proposal [55].

The QSHE system is regarded as a 2D topological insulator. As the TRS in such a system is preserved and, hence, the Chern number is zero, Kane and Mele proposed classifying such time-reversal invariant systems by another type of topological invariant known as the $\mathbb{Z}_2$ invariant [52]. This invariant can take only two values, 0 or 1, depending on the parity of the number of intersections between the edge states and the Fermi level [6, 53]. Thus, an insulator with $\mathbb{Z}_2 = 0$ is considered as topologically trivial, in which the edge states intersect with the Fermi level an even number of times, while an insulator with $\mathbb{Z}_2 = 1$ is identified as a TI in which the edge states intersect with the Fermi level an odd number of times and always exist in the bulk gap [6, 52, 53].

2.3 3D topological insulators

The prediction of the QSHE and 2D TIs was followed by a generalization of them to 3D materials [56–58] that are categorized by four $\mathbb{Z}_2$ topological invariants as weak and strong 3D TIs, depending on their robustness against disorder. The strong 3D TIs host gapless 2D surface states at each of their surfaces. Hence, if E_F lies within the bulk band gap, the 3D TI shows metallic conduction at the surfaces, but is insulating in the bulk. These topological surface states (TSS) of 3D TI exhibit a Dirac-cone-shaped band structure with linear band dispersion and a helical spin texture wherein the spin is locked to the momentum, which means that the spin rotates with $\mathbf{k}$ around the Fermi surface, as shown in top panel of Fig. 2.1 (b). This spin texture also has implications for the robustness of the surface states against disorder: electrons in the 2D surface state cannot be localized since backscattering by 180° is forbidden, as long as TRS is preserved, otherwise a spin flip would be required.

$Bi_{1-x}Sb_x$ was the first candidate for 3D TI predicted by Fu and Kane [59] and experimentally verified soon after the prediction using angle-resolved photoemission spectroscopy (APRES) [60]. The reported band structure of $Bi_{1-x}Sb_x$ fitted the theoretical predictions postulating that in a material with strong spin–orbit interactions a band inversion

could be induced. This inversion of bands with different parities signals a quantum phase transition between the trivial insulator and the TI.

Later, it was proposed that the chalcogenide compounds Bi_2Te_3, Bi_2Se_3 and Sb_2Te_3 are also 3D TIs with comparably large band gaps and single Dirac cone surface states [61]. All these compounds are layered materials composed by the stacking of quintuple layers (QLs), consisting of five atomic layer of e.g. Te-Bi-Te-Bi-Te, along the z direction, see Fig. 4.1. The coupling between two atomic layers within a quintuple layer is strong, while that between quintuple layers is much weaker and of the van der Waals type. The crystals are therefore very easy to cleave and made into a ultrathin flake. The inversion symmetry of the crystals is given by the inversion center at the Te/Se site in the middle of the quintuple layer. Similar to HgTe, these compounds are topologically non-trivial due to the inversion between Bi (Sb) and Te (Se) p_z orbitals with opposite parity at the Γ point, which is driven by the strong spin–orbit coupling of Bi and Te [61]. Surface-sensitive probes, such as APRES and scanning tunneling spectroscopy (STM), have indeed experimentally confirmed the existence of the TSS with a single Dirac cone and spin-momentum locking for these materials [6, 7, 62, 63]. These second generation 3D TIs are by far the most popular and widely studied TI materials owing to their relatively large bulk gaps ($\sim$ 0.3 eV in Bi_2Se_3), simple surface band structure and the fact, that these materials are easily synthesized as they have long been used for thermoelectric applications [64–66]. On the other hand, they generally suffer from a large number of structural defects [67, 68], which prevents unambiguous access to the surface states in transport and ARPES experiments.

2.4 Magnetic Topological insulators and QAH effect

In the previous section we discussed that the discovery of the integer QHE has raised many intriguing questions. We mentioned that the Haldane model opened up the idea of the existence of the QAH effect theoretically, which was nevertheless not realized in real systems experimentally. The discovery of 3D TIs greatly expands the scope of topological states of matter and facilitates the experimental exploration of various topological quantum effects, including the QAH effect.

As was already mentioned, the QSHE in 2D TIs is deeply related to the QAH effect: It can be considered as a combination of two copies of a QAH effect system with opposite magnetization vectors, i.e. opposite spins, as illustrated in Fig. 2.1. Intuitively, we can consider the electrons with one spin component in QSHE system as already in the QAH state, with the only problem that due to the TRS two electrons with opposite spin components result in zero net Hall conductance [12]. Hence, if one could remove the QAH effect resulting from electrons of one spin component, the electrons with opposite spin component would give rise to a chiral edge state carrying a quantized Hall conductance of e^2/h, as shown in Fig. 2.1 (c). In practice, this can be done by introducing ferromagnetism

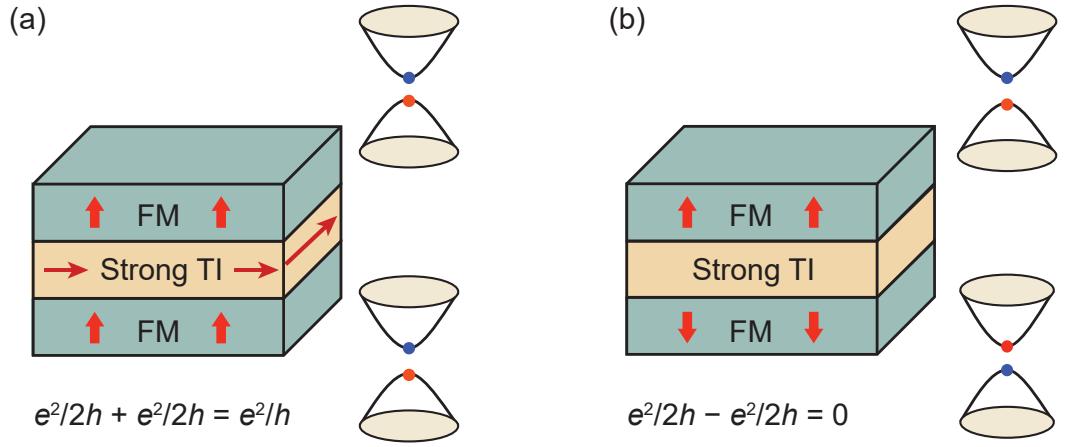

Figure 2.2: Schematic illustration of the Hall conductance in a ferromagnet/TI heterostructure. (a) When the magnetization at the top and bottom surfaces are parallel and the Fermi level is located in the mass gap induced by the magnetic exchange interaction, there are chiral edge states which are responsible for the quantized Hall conductance in TI films. The edge electrons conduct electricity without dissipation in one direction along the sample boundary. Gapped Dirac cones have distinct topological characters due to their opposite normal directions. (b) When the magnetizations are opposite, the Hall conductance from the top and bottom surfaces cancel each other. Adapted from Ref. [12].

in a TI, which will break TRS and suppress one of the spin channels in the QSH edge state. This approach was first proposed in a HgTe/CdTe 2D TI doped with Mn impurities [69]. However, Mn ions are paramagnetic rather than ferromagnetic in this material and a small external magnetic field is still required to realize the QAH effect. Similarly, introducing ferromagnetism in a 3D TI film can also lead to the QAH effect. To understand the basic mechanism of the QAH effect in a 3D magnetic TI (MTI), in the following we briefly discuss the impact of induced magnetization on the TSS.

The 2D surface state of the 3D TI with a single Dirac cone and preserved TRS is described by the low-energy effective Hamiltonian [2]

$$\mathcal{H}_{\text{surface}} = v_{\text{F}}(-k_y\sigma_x + k_x\sigma_y), \tag{2.1}$$

where v_{F} is the Fermi velocity and σ_x and σ_y are the Pauli matrices. Here we consider the z direction perpendicular to the sample surface. This Hamiltonian implies the spin-momentum locking of the massless Dirac electrons, see Fig. 2.1 (b). The introduction of an out-of-plane spontaneous magnetization into the surface of a 3D TI leads to important modifications of the surface electronic structure, as described by the effective Hamiltonian

$$\mathcal{H}_{\text{surface}} = v_{\text{F}}(-k_y\sigma_x + k_x\sigma_y) + m\sigma_z, \tag{2.2}$$

where the mass term $m\sigma_z$ breaks the TRS, which results in the opening of a mass gap in the Dirac cone, see Fig. 2.1 (c). The Hall conductance, which is half-integer in this

particular case (as we consider only one surface, e.g. the top surface), is given by

$$\sigma_{xy} = \frac{m_z}{|m_z|}\frac{e^2}{2h}, \tag{2.3}$$

where $m_z/|m_z|$ is the Chern number and its sign is that of the mass term, which depends on the magnetization direction. For our purposes, we consider an MTI thin film for which there are two surfaces, the top and bottom one. We may introduce magnetization to gap 2D TSS at both surfaces: The gapped Dirac cones are topologically distinct due to the opposite direction of the surface normals. [1, 12]. When E_F is located within the mass gap and the magnetizations at the top and bottom surfaces are parallel, we find both surface states contribute to the Hall conductance with the same sign, resulting in the quantized total Hall conductance $\sigma_{xy} = \pm e^2/h$, and zero longitudinal conductance σ_{xx} without applied magnetic field, which implies the emergence of a QAH effect, one of the hallmarks of MTIs. Accordingly, the QAH effect gives rise to chiral edge states trapped at the side surfaces of the film [1, 44], the direction of which depends on the sign of the Chern number and hence on the magnetization direction. For clarity, in Fig. 2.2 (a) we show the Hall conductance in the case of a ferromagnet/TI heterostructure. However, when the magnetizations at the top and bottom surfaces are opposite, the Hall conductances for two surface states cancel each other, as illustrated in Fig. 2.2 (b). Hence, the uniform magnetization in 3D TI thin films can lead to the QAH effect.

In a thin film of MTI, one cannot neglect the coupling between top and bottom surface states, as we did it in Eq. 2.2. If the film becomes thin enough that the wave functions of top and bottom TSS have significant overlap, a hybridization gap opens at the surface states [1, 70]. Its size increases with decreasing thickness. Nevertheless, the QAH effect can still be observed as long as the hybridization gap is smaller than the magnetic exchange gap [71], which is induced by an interaction between the electrons in TSS and the spontaneous magnetization, as described by the mass term in Eq. 2.2. Otherwise, the film becomes a topological trivial insulator.

2.4.1 QAH effect in $3d$ transition-metal-doped TIs

Despite the simple picture, the experimental realization of the QAH effect in MTIs is complicated by several simultaneous requirements to a candidate system. First, the Dirac point of the parent TI should be well within its bulk band gap and the chemical potential has to be tuned to the Dirac point. Second, the introduced magnetic subsystem should lead to a substantial long-range ferromagnetic order that can survive in the insulating regime, with the easy axis perpendicular to the surface to open a large exchange gap at the Dirac point. Third, the MTI film should have well-controlled thickness: It should be as thin as possible to localize the dissipative conduction electrons from bulk bands and

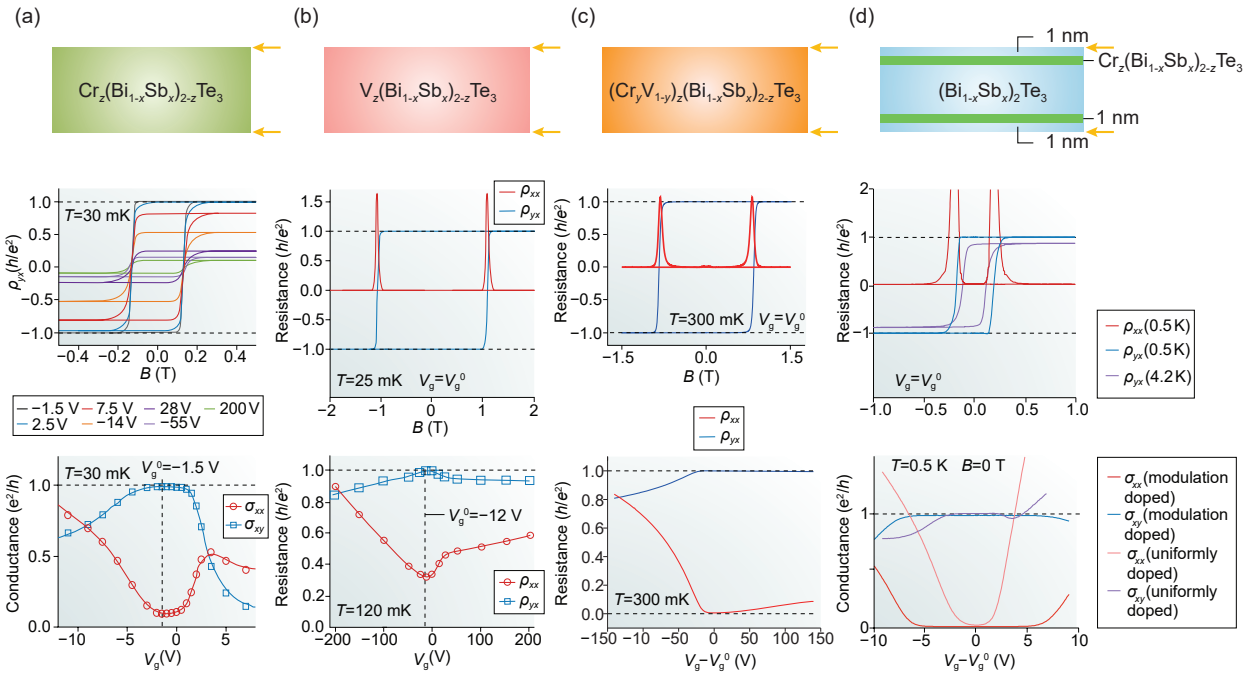

Figure 2.3: Schematic illustration of the Hall conductance in ferromagnet/TI heterostructure. (a) The first experimental observation of the QAH effect in Cr-doped $(Bi,Sb)_2Te_3$ thin film at 30 mK. Yellow arrows indicate the locations of the surface states at the top and bottom of the film. The middle panel shows the magnetic field dependence of the Hall resistance ρ_{yx} for various gate voltages (V_g). The V_g dependences of the Hall σ_{xy} and longitudinal σ_{xx} conductance are shown in the bottom panel. (b) QAH effect in a V-doped $(Bi,Sb)_2Te_3$ thin film at 25 mK. Middle panel: Magnetic field dependence of the Hall ρ_{yx} and longitudinal ρ_{xx} resistance. Bottom panel: Dependence of ρ_{yx} and ρ_{xx} on V_g at $T = 120$ mK. (c) Similar measurements for a Cr- and V-codoped system. The temperature of the QAH effect is significantly increased such that full quantization is achieved at 300 mK, and zero-field Hall resistance of 0.97 h/e^2 is observed at 1.5 K. (d) Schematic of the modulation-doped penta-layer heterostructure in which two heavily Cr-doped $(Bi,Sb)_2Te_3$ 1 nm layers sandwich a nonmagnetic $(Bi,Sb)_2Te_3$ layer and are enclosed by two other nonmagnetic 1 nm layers. Middle panel: Magnetic field dependence of ρ_{yx} at 0.5 K and 4.2 K and of ρ_{xx} at 0.5 K. Bottom panel: Dependence of σ_{xy} and σ_{xx} on V_g for the uniformly doped and modulation-doped film at $T = 0.5$ K. Adapted from Ref. [2] and Ref. [23].

surface states, but thick enough to assure that the hybridization gap is smaller than the magnetic exchange gap. Finally, the E_F has to be fine-tuned into the magnetic gap in the TSS [1, 71, 72].

Magnetic doping with various $3d$ transition metals (TM) is a common approach to introduce stable long-range ferromagnetic order in 3D TIs. This approach owes its success to the knowledge accumulated from studies of diluted magnetic semiconductors. In the theoretical prediction of the QAH effect in the Bi_2Te_3 family of TIs, two TM ions, namely Cr and Fe, were proposed for magnetic doping [71]. It turns out that the magnetic property of this family of materials strongly depends on both parent compounds and magnetic dopants, as we will also see in Chapter 4 and 5 of the current work. Clear long-range ferromagnetic order has been observed in Cr- and V-doped Sb_2Te_3 [73–80] and Mn-doped

Bi_2Te_3 [81, 82], whereas spin glassy behavior was observed in Fe-doped Bi_2Te_2 [83]. For Fe-doping in Sb_2Te_3 and Bi_2Se_3, the compounds remained paramagnetic [84, 85]. Of all the single-ion dopants tried so far, V and Cr possess the most robust long-range ferromagnetic (FM) order with out-of-plane anisotropy.

In line with these findings, the first experimental observation of the QAH effect was made in Cr-doped $(Bi,Sb)_2Te_3$ thin films with 5 QLs grown by molecular beam epitaxy (MBE) on a $SrTiO_3$ substrate [9]. As shown in Fig. 2.3 (a), at zero magnetic field and a temperature lowered to 30 mK, the gate-tuned Hall conductance σ_{xy} almost reaches the quantized value of e^2/h ($\sigma_{xy} = 0.987e^2/h$), accompanied by significant drop in longitudinal conductance to $\sigma_{xx} = 0.096e^2/h$. As for the magnetic field dependence of the resistance measured at different gate voltages (V_g), as shown in the middle panel of Fig. 2.3 (a), the Hall resistance ρ_{yx} switches between $+h/e^2$ and $-h/e^2$, accompanying the magnetization reversal resulting from the application of low positive and negative magnetic fields. Under a strong magnetic field of up to $\sim$ 10 T, the longitudinal resistance ρ_{xx} vanishes (as well as the corresponding $\sigma_{xx} = \rho_{xx}/(\rho_{yx}^2 + \rho_{xx}^2)$), while ρ_{yx} remains at the quantized value h/e^2. All these observations demonstrate the realization of the QAH effect in this system, which rapidly disappears with increasing temperature [9].

Nevertheless, the perfect quantization of the Hall conductance in a Cr-doped sample requires very low temperature of $\sim$ 30 mK and a magnetic field of several tesla. In the past years, great efforts have been made to improve the MTI materials and raise the temperature at which the QAH effect can be observed. Increasing the temperature to at least a few kelvins would already allow the investigation of this effect with more experimental techniques, which could further advance our understanding of it and lead to the application of dissipationless conduction channels in future electronic devices.

Two years after the first observation of the QAH effect, the effect was also demonstrated for V-doped $(Bi,Sb)_2Te_3$ thin films [8], which have more robust magnetic properties compared to the Cr-doped system, with about twice as large Curie temperature (T_C) at the same doping level and a larger coercive field of $\sim$ 1 T at 25 mK. This system displays better quantization characteristics, with the zero-field ρ_{xx} down to $0.00013 \pm 0.00007h/e^2$ and a Hall conductance reaching $0.9998 \pm 0.0006e^2/h$ at 25 mK, see Fig. 2.3 (b). Unfortunately, enhanced ferromagnetic properties achieved in V-doped films has little influence on the onset temperature of the QAH effect: Temperature lower than $\sim$ 100 mK, which is several orders of magnitude lower than T_C, is still required to reach full quantization of Hall conductance. The QAH effect in other candidate materials, such as $(Bi,Sb)_2Te_3$ or Bi_2Se_3 doped with other $3d$ transition metals [71, 86], although identified theoretically, has not yet been experimentally realized.

To further improve the observation temperature of the QAH effect, unconventional approaches, such as magnetic codoping of $(Bi,Sb)_2Te_3$ TI with V and Cr, have been utilized [23]. In an optimized sample, full quantization is achieved at 300 mK, see Fig. 2.3 (c), and

a zero-field Hall resistance of $0.97h/e^2$ is observed at 1.5 K, which is a result of improved ferromagnetic order and electronic structure by magnetic codoping. This indicates that the QAH effect may be further enhanced by combining different magnetic elements. Furthermore, spatially modulated magnetic doping significantly increases the temperature of the QAH effect in Cr-doped $(Bi,Sb)_2Te_3$ up to 0.5 K, due to the improved crystalline quality and the homogeneity of the ferromagnetism [24]. The effect was observed in a penta-layer heterostructure with total thickness of 8 nm, in which two Cr:$(Bi,Sb)_2Te_3$ layers with a high Cr concentration sandwich a nonmagnetic $(Bi,Sb)_2Te_3$ layer and are enclosed by two other nonmagnetic layers, as shown in Fig. 2.3 (d). Magnetic layers induce a large exchange coupling to the TSS at the top and bottom $(Bi,Sb)_2Te_3$ layers. Hence, the gapped surface states are located only at the top and bottom surfaces of the heterostructure, as in uniformly doped samples, which eventually enhances the QAH effect.

It is worth mentioning another approach to introduce ferromagnetism in a TI for a potentially higher-temperature realization of the QAH effect—magnetic proximity. If a 3D TI film is sandwiched between two ferromagnetic insulator (FMI) layers, which are perpendicularly magnetized in the same direction, as shown in Fig. 2.2 (a), one may be able to observe the QAH effect [1, 87] since FMI layers can gap the Dirac surface states of the top and bottom surfaces. Such an FMI/TI/FMI heterostructure is likely to exhibit the QAH effect at high temperature due to the high T_C of some FMI materials reaching values above room temperature. The proximity-induced ferromagnetism has been demonstrated in heterostructures with FMI such as EuS, $Cr_2Ge_2Te_6$, $Y_3Fe_5O_{12}$ and $Tm_3Fe_5O_{12}$ [88–94]. However, the observed anomalous Hall resistivity was far from the quantized value [2]. The reason is probably the weak bonding between TI and FMI layers, and consequently, the weak exchange coupling resulting in a small magnetization gap. As the surface states of TIs usually derive from s and p orbitals, the $3d$ or $4f$ states of FMIs should strongly hybridize with them in order to induce a large exchange gap [1]. Hence, a suitable choice of the FMI yielding strong hybridization with the s and p orbitals of Bi, Sb and Te is the right direction towards the high-temperature realization of the QAH effect [1, 2]. Moreover, it was reported that the TSS may relocate into the subsurface region of the TI upon formation of the FMI/TI interface, which significantly reduces the magnetic proximity effect [95, 96]. The solution to that is the insertion of FMI layers in the subsurface regions of a TI film, for example, as shown in Fig. 2.3 (d).

2.4.2 Origins of magnetism in doped TIs

To resolve the problem of the low temperature required for the QAH effect, a comprehensive understanding of the microscopic origin of the ferromagnetism and the electronic states inducing the FM coupling in magnetically doped TIs is necessary, which is one of the goals of the current thesis. In particular, establishing microscopic differences between

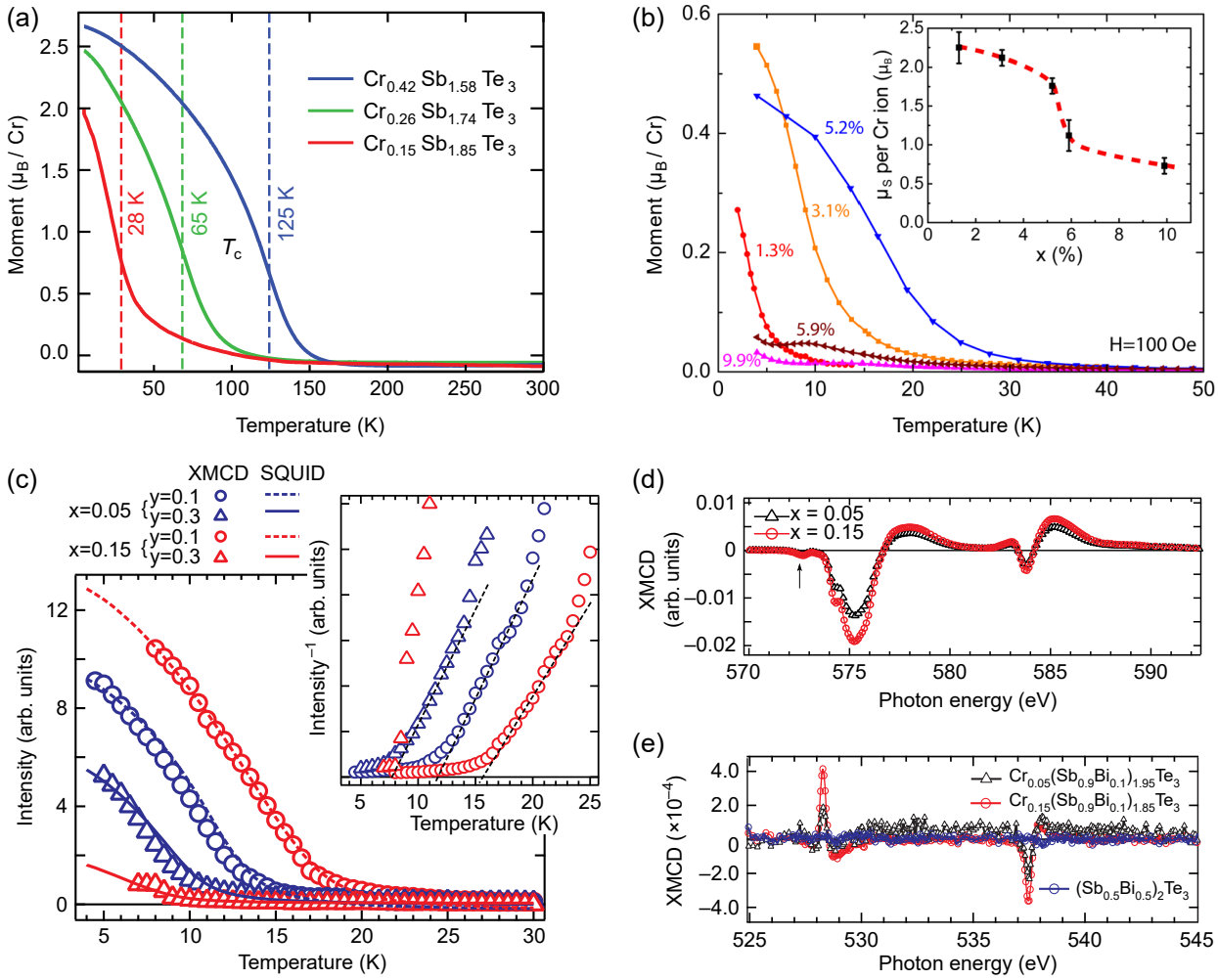

Figure 2.4: (a) Temperature dependence of the magnetization $M(T)$ of Sb_2Te3 thin films with varying Cr concentration measured whilst cooling in a 20 mT applied out-of-plane field. The observed transition temperatures are marked by dashed lines. Taken from Ref. [97]. (b) Magnetic moment per Cr ion as a function of temperature estimated from SQUID measurements with an applied field of 100 Oe in Cr-doped Bi_2Se_3 thin films. The inset shows the magnetic saturation moment per Cr ion as a function of Cr concentration x. The dashed curve is a guide to the eye. Taken from Ref. [98]. (c) XMCD intensities (symbols) and SQUID magnetization data (lines) obtained for different Cr doping concentrations x and different Sb to Bi ratios in counter-doped $Cr_x(Sb_{1-y}Bi_y)_{2-x}Te_3$ crystals. From the plot of the inverse intensity in the panel on the right, the transition temperature is estimated, which shows that T_C increases with x, whereas an increase in Bi/Sb ratio strongly reduces it. (d) XMCD spectra of $Cr_x(Sb_{1-y}Bi_y)_{2-x}Te_3$ crystals at the Cr L_{23} edges in a magnetic field of 0.1 T at 5 K, which reveals the increase of Cr magnetic moment with higher Cr concentration. The arrow indicates a small intensity at the energy of the Te M_5 edge. (e) XMCD spectra of the same system measured at the Sb $M_{4,5}$ edges, compared with Cr-free sample $(Sb_{0.5}Bi_{0.5})_2Te_3$. The XMCD signal is due to an induced spin polarization in the Sb p-states, indicating significant pd hybridization between the host $5p$ states and the dopant $3d$ states. Panels (c-e) are taken from Ref. [80].

the strongly correlated V and Cr impurities in $(Bi,Sb)_2Te_3$ using an element selective local probe sensitive to the magnetic ground-state properties, such as XMCD, would help with

evaluating the relevance of the various proposed models of FM coupling [27, 28, 71, 73, 74] and eventually provide better control of the QAH effect, as it is discussed in Chapter 4 and 5.

Magnetically doped TIs are actually diluted magnetic semiconductors (DMS) in the low carrier density regime, which are characterized by complicated magnetic properties and strong disorder [1]. Interplay among chiral edge states, magnetic structure and disorders plays a key role in understanding the QAH effect. As was already mentioned, for the emergence of the QAH effect and other properties of MTIs, the formation of a magnetic exchange gap in the TSS is essential. The gap is induced by an interaction between the electrons in the TSS and the spontaneous magnetization, and described by the mass term $m\sigma_z \equiv -Jn_S\langle S_z\rangle\sigma_z$ in Eq. 2.3, where J is the exchange coupling between the z component σ_z of the spin of the Dirac electrons and the localized spin $\mathbf{S}$, and n_S is the areal density of localized spins, which have an average z component $\langle S_z\rangle$. Hence, the size of the gap is governed by the coupling strength as well as by the effective spin density.

Several mechanisms have been considered in the literature as a possible origin for ferromagnetism in MTIs, such as the carrier-mediated Ruderman-Kittel-Kasuya-Yosida (RKKY) mechanism, double and superexchange mechanisms, and the local valence-electron-mediated Bloembergen-Rowland, or Van Vleck, mechanism. The requirement of an insulating FM state rules out coupling mechanisms based on free carriers, such as RKKY-like long-range coupling in many FM DMSs [99, 100]. Hence, in a pioneering work predicting the QAH effect in magnetically doped TIs, it was hypothesized that a Van Vleck mechanism may be responsible for the FM coupling between the dopants [71]: Strong spin–orbit coupling and the topologically non-trivial band ordering in these materials may lead to a rather large van Vleck susceptibility that is proportional to the nonzero matrix element of the spin operator between valence and conduction bands, i.e. $\chi_e \propto \langle nk|\, S_z\, |mk\rangle \langle mk|\, S_z\, |nk\rangle$, where $|mk\rangle$ and $|nk\rangle$ are the Bloch wave functions in the conduction and valence bands [44]. Magnetic impurities in MTI can be ferromagnetically coupled by the large van Vleck susceptibility even in the insulating regime, when the E_F of the material lies in the bulk gap. Although some experimental support for this scenario has been reported [44, 73, 101], more recent *ab initio* calculations find that the strength of the exchange interactions in V- and Cr-doped $(Bi,Sb)_2Te_3$ is, in fact, largely independent of SOC [27, 28], indicating that the Van Vleck mechanism is insufficient to explain the complex ferromagnetic state in these systems. Crucially, a doping concentration-dependent T_C shown in Fig.2.4 for various Cr-doped TIs, investigated by superconducting quantum interference device (SQUID) magnetometry (for the method description see Section 3.6 in Chapter 3), XMCD (see Section 3.1.2 in Chapter 3), and polarized neutron reflectometry (PNR), is incompatible with the notion of magnetic order dominated by van Vleck mechanism [80, 97, 98, 102, 103].

Moreover, alternative mechanisms based on the Zener-type *pd*-exchange interaction were brought into focus, including double and superexchange [29, 78, 104], see Fig. 2.4 (d,e). For example, the first-principles calculations by Vergniory *et al*. [29] have shown that the long-range magnetic interaction is mainly mediated out of plane by the double exchange mechanism via chalcogen atoms and in-plane by the indirect exchange coupling via free carriers, i.e. RKKY, similar to traditional DMSs [105–107]. In this context, spin-polarized first-principles calculations predict a reduced exchange interaction with increasing *d*-shell electron occupation n_d [29], which seems to agree with the observation of a more robust FM order with a higher T_C in the case of V doping as compared to Cr [8].

Comparative theoretical studies of different dopants show that the exact configuration of the TM impurity 3*d* states [25–30] is essential for the magnetic coupling and requires its experimental determination, which can be accomplished by means of experimental methods used in the thesis, such as XMCD and resonant photoelectron spectroscopy (resPES), together with multiplet ligand-field theory (MLFT) calculations. For instance, in V-doped TIs, impurity bands caused by the V 3*d* states are found near the E_F and Dirac point of the system [29, 30, 104, 108]. These states appear to stabilize the magnetic ordering. So far, however, a comprehensive understanding of how this behavior is related to the local impurity electronic structure is still absent.

As for the aforementioned *d*-shell electron occupation n_d (and the electron configuration in general), often it is inferred from the nominal valence of the dopant in a simplified ionic picture [8, 76, 109]. But even in comparatively more ionic oxides this picture is of limited use since the effects of charge transfer—and the electronic correlations in the *d*-shell—cannot be neglected [110, 111]. Earlier x-ray absorption spectroscopy (XAS) and XMCD studies already indicated the covalent character of Cr doping in $(Bi,Sb)_2(Se,Te)_3$ [112, 113], yet within a pared down atomic multiplet model considering only one ligand hole.

Thus, despite the broad interest in MTIs after the experimental observation of the QAH effect in both Cr- doped and V-doped systems, the microscopic origin of the ferromagnetism remains to be clarified with further theoretical and experimental investigations, which is one of the central goals of the current thesis.

2.4.3 Rare Earth Doping of TIs

Recently, many reports have been published dealing with samples, in which rare earth ions (RE) instead of TM were used as dopants in order to benefit from their large, localized magnetic moments [114–118], which might result in a larger exchange gap in the TSS since its size is directly dependent on the size of the magnetic moment [86, 102, 114]. The large magnetic moment of the RE elements, originating from the unpaired 4*f* electrons

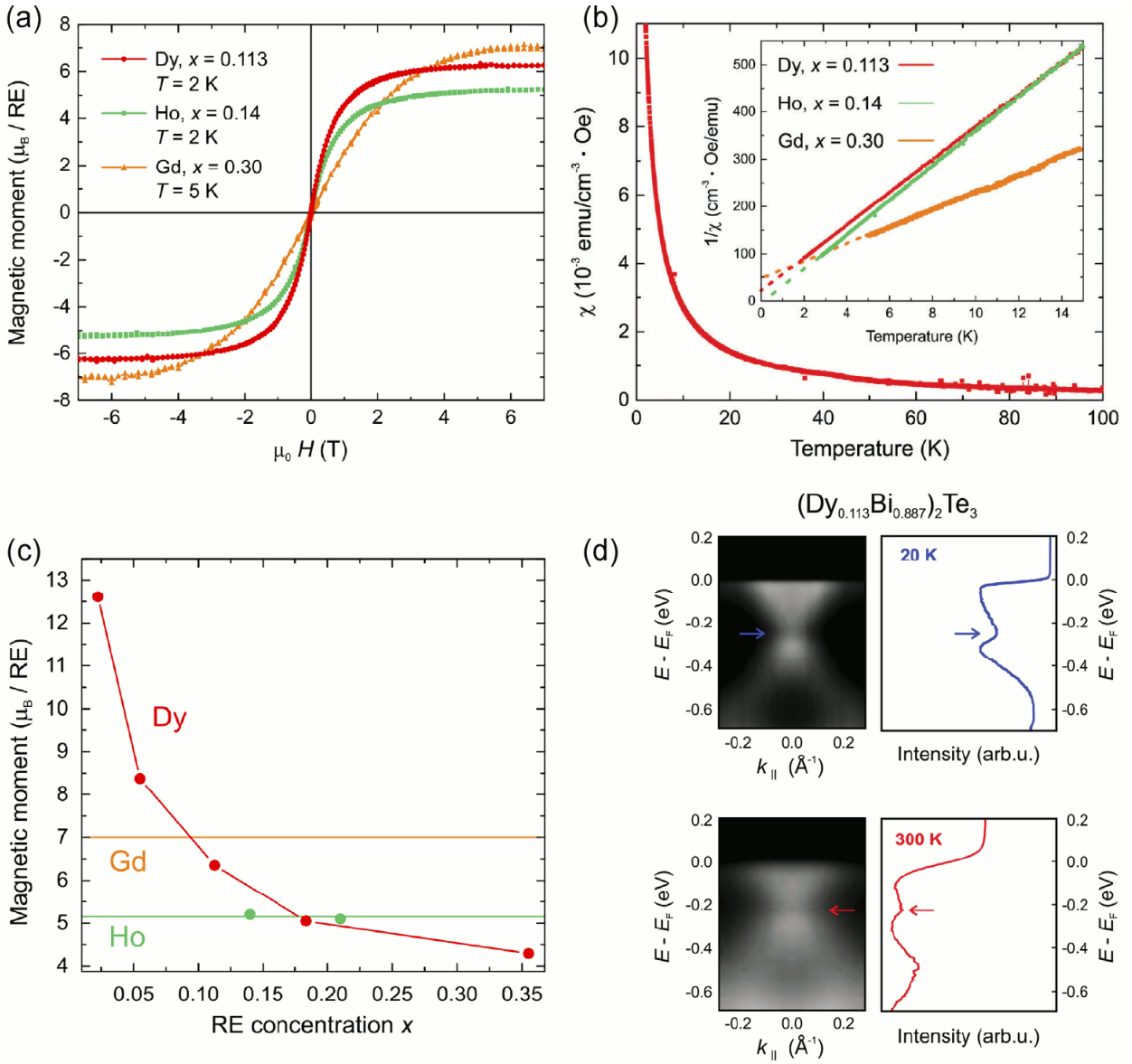

Figure 2.5: (a) SQUID measurements of $M(H)$ loops for selected Dy and Ho doped films at 2 K, and a Gd doped film at 5 K. The field was applied in-plane. All three loops show qualitatively the same behavior, no remanent magnetization and no loop opening, indicative of the absence of ferromagnetic long-range ordering. (b) Temperature dependence of the magnetization. The plot shows the zero-field-cooled magnetic susceptibility χ for a Dy doped film with a doping concentration of $x = 0.113$ as a function of the temperature. The inset shows a comparison of the inverse magnetic susceptibility for the three selected Dy, Ho, and Gd doped films at low temperatures from 2 to 15 K. The straight lines represent linear Curie-Weiss fits to the experimental data, all yielding small negative Weiss temperatures. (c) Comparison of the magnetic moment per RE ion as function of RE concentration at base temperature. For the Dy doped films, a surprising concentration dependence of the effective magnetic moment was found, while Gd and Ho moments show no concentration dependence. (d) ARPES spectra of Dy-doped Bi_2Te_3 sample with $x = 0.113$. The measurements were carried out at base temperature (20 K) and room temperature (300 K) as shown in the top and bottom panel, respectively. The spectra show a $\sim$ 85 meV wide gap, which persists up to room temperature. All panels are taken from Ref. [114].

[119], would also allow for a decrease in the doping concentration for the same gap size, thereby preserving crystal quality by reducing the number of defects and leading to a more stable QAH effect at a higher temperature. The highest effective magnetic moment of $12.6\mu_B$ was observed at 2 K for $(Dy_xBi_{1-x})_2Te_3$ with $x = 0.023$ [120]. However, the magnetic moment of the Dy ions was found to be strongly concentration dependent, in contrast to Gd and Ho dopants in Bi_2Te_3 thin films, possessing an effective magnetic moment of $\sim 7\mu_B$ (close to the maximum free ion value) and of $\sim 5.15\mu_B$ (half of the theoretical maximum moment), respectively [114], as shown in Fig. 2.5 (c). Despite these large magnetic moments, most investigations found no long-range FM order down to 2 K, see Fig. 2.5 (a) and (b), and thus no gap opening in the TSS [117, 121, 122]. Only in the case of Dy-doping above a critical doping concentration a sizable gap has been reported in angle-resolved photoemission spectroscopy (ARPES), which appears to persist up to room temperature [115], as seen in Fig. 2.5 (d). This gap is observed despite the absence of long-range magnetic order, and could originate from short-range FM fluctuations caused by inhomogeneous doping and aggregation of magnetic dopants into superparamagnetic clusters [116], as in the case of Cr-doped Bi_2Se_3 [123]. First principle calculations using density functional theory (DFT) suggest that Eu and Sm ions can introduce stable long-range ferromagnetic order in Bi_2Se_3 [124]. This, however, was experimentally confirmed only for Sm ions [125].

Using antiferro- rather than ferromagnetism has also been studied as an avenue to gapped surface states in layered van der Waals compounds. Recently, the realization of such an antiferromagnetic (AFM) topological insulator in $MnBi_2Te_4$ has been reported [31, 40]. It is well known that RE chalcogenides such as EuTe can exhibit AFM order [126, 127]. Therefore, it appears promising to take advantage of the larger RE moments to enhance the effect on the TSS in Bi_2Te_3, just like in the case of FM order.

Whereas $MnBi_2Te_4$ is a stoichiometric compound and the AFM order there is intrinsic, here we rather rely on RE doping of Bi_2Te_3 to induce antiferromagnetism, not least to circumvent RE solubility issues. The general feasibility of this approach has been demonstrated for $Ce_zBi_{2-z}Te_3$ [128], $Sm_zBi_{2-z}Te_3$ [129] and $Gd_zBi_{2-z}Te_3$ [130]. As determined by magnetometry [128–130], the onset of AFM interactions is achieved even at low RE concentrations (in case of Sm $z = 0.025$ already suffices). However, x-ray absorption spectroscopy (XAS) and x-ray magnetic circular dichroism (XMCD) investigations addressing the character of the magnetic moments and the impact on the TSS are scarce [131] and limited to temperatures nearly an order of magnitude above the AFM onset temperature, which calls for further investigations.

In Chapter 6 we provide a comprehensive investigation of the surface and bulk magnetic (by means of XMCD and SQUID) and electronic (by means of resPES and ARPES) properties of one of such systems, namely Bi_2Te_3 thin films doped with Eu ions.

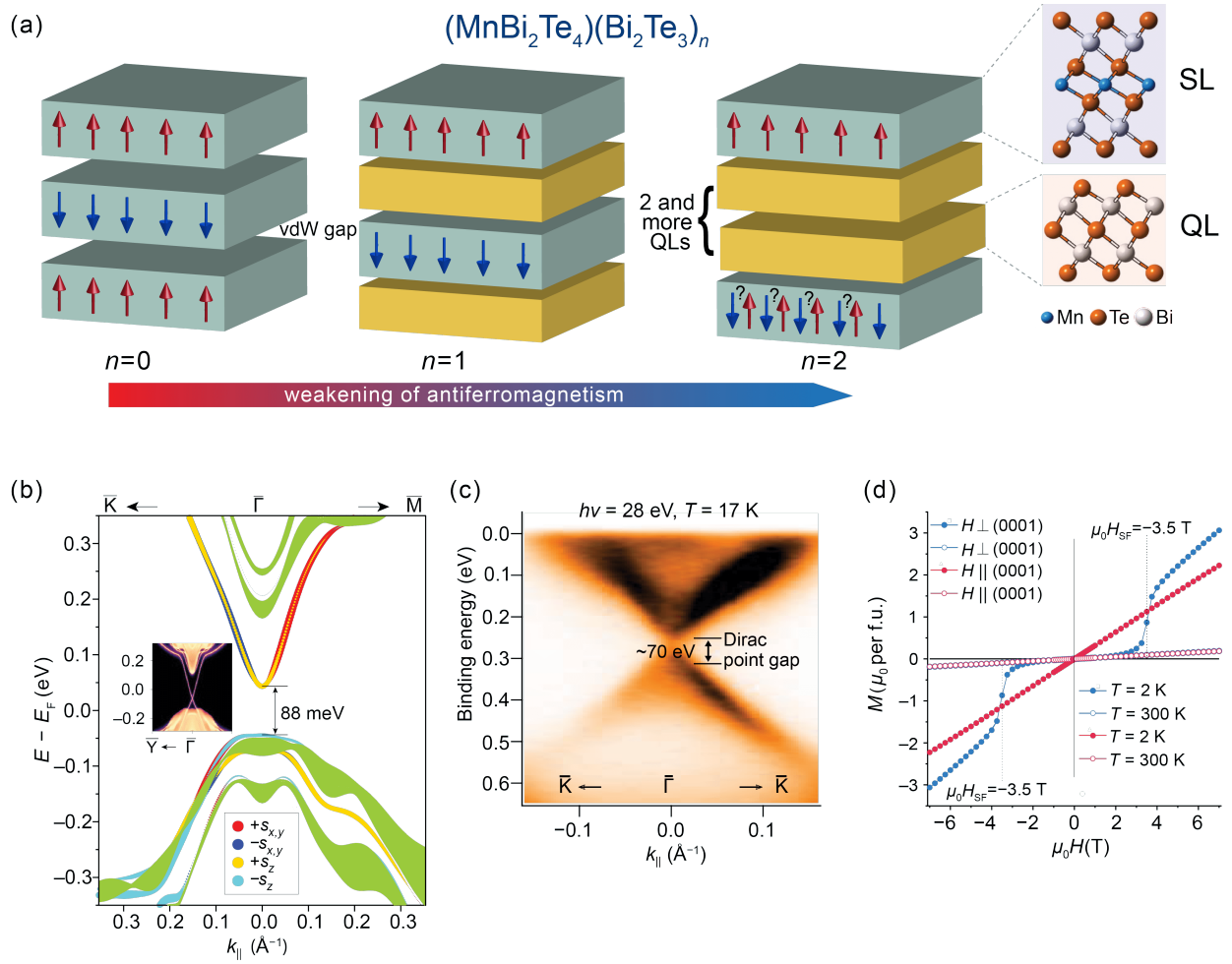

Figure 2.6: (a) Different members of the family of layered van der Waals materials $(MnBi_2Te_4)(Bi_2Te_3)_n$, in which the SLs are separated by a stack of n quintuple layers (QLs) of non-magnetic Bi_2Te_3. The number of QLs n defines the magnetic configuration of the system, such that increasing n weakens the interlayer AFM coupling and eventually leads to the FM configuration. (b) Spin-resolved electronic structure of the $MnBi_2Te_4(0001)$ surface illustrating 88-meV-wide band gap. The size of the coloured circles that comprise the data reflects the value and sign of the Cartesian projections of the spin-vector **s**. The green areas correspond to the bulk band structure projected onto the surface Brillouin zone. The inset shows the tight-binding calculated electronic band structure of the S-preserving (1011) surface. The regions with a continuous spectrum correspond to the 3D bulk states projected onto the 2D Brillouin zone. (c) Dispersion of $MnBi_2Te_4(0001)$ measured using ARPES at 17 K with a photon energy of 28 eV. Two almost linearly dispersing bands form a Dirac-cone-like structure with strongly reduced intensity at the crossing point. The energy distribution curves (not shown) reveal an energy gap of about 70 meV at the $\bar{\Gamma}$ point that separates the upper and lower parts of the cone. (d) Field-dependent magnetization curves for the two directions, measured at 2 K (blue) and 300 K (red) indicating a 3D AFM order below $T_N \sim 24$ K with a spin-flop transition at $\mu_0 H_{SF} \sim 3.5$ T, which is in line with an out-of-plane easy axis of the magnetization. Panels (b-d) are taken from Ref. [31].

2.4.4 Intrinsic magnetic topological insulators

In the previous sections we have considered doping on the TIs as a common approach to introduce ferromagnetism, which is one of the prerequisites for observation of novel quantum effects, such as the QAH effect [1, 8, 9, 44, 69] and the topological magnetoelectric effect [19–22]. Since the discovery of the QHE, the QAH effect remains one of the few topological quantum effects unambiguously observed in experiments [8, 9]. Requiring no external magnetic field and high carrier mobility, as well as being relatively simple and clear in its physics, the QAH effect is promising for applications in the field of spintronics. Despite the remarkable progress in the growth of magnetically doped TIs and complex heterostructures with them, hitherto the QAH effect has only been demonstrated in the (sub-)kelvin range [8, 9, 132]. The most plausible reason for the suppression of the observation temperature is the inhomogeneous ferromagnetism, which is inevitably introduced by the randomly distributed magnetic dopants. Inhomogeneous ferromagnetism in a QAH system implies disorder in the magnetic exchange gap, to be specific, the sample contains regions with small magnetic gap size, as well as many regions without FM ordering even below the nominal T_C. Chiral QAH edge states passing through such regions would be strongly scattered into bulk or surface states [133]. Eventually, dissipation to chiral edge states occurs, which deteriorates the QAH effect and results in the overall transport properties of the MTI deviating from precise quantization. Effects of magnetic disorder can be suppressed only at very low temperature or under a strong magnetic field, which explains why the QAH effect in doped TIs require such low temperature. The evidence for inhomogeneous ferromagnetism in magnetically doped $(Bi,Sb)_2Te_3$ films was found using STM, nano-SQUID, and transport measurements [134–137]. For example, the spatial distribution of the exchange gap in a single crystal of $Cr_{0.08}(Bi_{0.1}Sb_{0.9})_{1.92}Te_3$ with $T_C = 18$ K was characterized at $T = 4.5$ K by STM [134]. The conductance spectra acquired at different positions on the surface indicate that the gap size ranges between 9 meV and 48 meV. Hence, although the QAH effect is quite robust against lattice disorder, it can be greatly influenced by magnetic disorder and the improvement in the spatial uniformity of the ferromagnetism plays a vital role in the realization of a large gap in the surface state.

The aforementioned issue with inhomogeneous ferromagnetism can be solved with a new and efficient means of incorporating magnetisms into TIs, i.e., using intrinsic magnetic topological insulators (IMTI) – stoichiometric, well-ordered magnetic compounds, which offer uniform and large magnetic exchange gaps as a result of homogeneous surface magnetic ordering. Recently, $MnBi_2Te_4$ (MBT) was theoretically identified as the first candidate for IMTI, and was subsequently widely scrutinized, both experimentally and theoretically. It consists of Te-Bi-Te-Mn-Te-Bi-Te septuple layers (SLs), which can be viewed as intercalating a MnTe bilayer into a Bi_2Te_3 QL, as seen in Fig. 2.6 (a). Within the

SLs, the Mn atoms carrying the magnetic moment are arranged periodically and couple ferromagnetically with an out-of-plane easy axis (along the c-axis). The SLs are separated by a van der Waals gap, and Mn moments in neighboring SLs couple antiferromagnetically, resulting in A-type antiferromagnetism below a Néel temperature of $T_N \sim 24$ K, see Fig. 2.6 (d). The magnetic properties are provided mainly by the 3*d* states of Mn, while the topologically nontrivial properties are dominated by the *p* states of Bi and Te.

In fact, MBT has already been investigated in the early years for finding a potential candidate for achieving the QAH effect at higher temperatures [138, 139]. However, it was first considered as a trivial magnetic insulator [16, 140]. Later, *ab initio* calculations of the band structure of MBT based on the A-type AFM ground state showed a single band inversion at the Γ point exhibited when introducing spin–orbital coupling, indicating that MBT is a topologically nontrivial rather than a trivial insulator [22, 31, 32]. It was shown, that such 3D AFM TIs can also be classified with a $\mathbb{Z}_2$ invariant on the basis of combined time-reversal Θ and the primitive lattice translation $T_{1/2}$ symmetry, i.e. $S = \Theta T_{1/2}$ symmetry [141]. $\mathbb{Z}_2 = 1$ was found for MBT, confirming its topologically nontrivial nature [31]. First principle calculations showed a 88-meV-wide band gap at the (0001) surface of the MBT, where the *S* symmetry is broken and the out-of-plane magnetization of the near-surface ferromagnetic layer opens a Dirac point gap [31], see Fig. 2.6 (b). This gap is larger than the ones in the previously discussed magnetically doped TIs, and it favors the realization of a high-temperature QAH effect. In contrast, the *S*-preserving surface is gapless, as expected for a TI, see the inset of Fig. 2.6 (b). The band gap in the TSS of about 70 meV at the Γ point was experimentally observed in ARPES measurements [31], as shown in Fig. 2.6 (c). However, the increase of the temperature above T_N does not lead to the Dirac point gap closing at MBT (0001) [31], so the energy gap might not originate from the magnetic order. On the contrary, some high-resolution ARPES experiments have reported the top and bottom surfaces as having a gapless surface state [142–145] with only a small evolution with temperature, which is obviously inconsistent with the theoretical predictions for the surface gap opened by the out-of-plane magnetic moments. It was argued, that the observation of gapless surface states can be explained by spatially dependent magnetic moments on the surface [142]: the AFM coupling between the surface layer and the underlying layer may be weaker than the AFM coupling of the bulk state, which leads to fluctuation of the magnetic moment on the surface, forming a series of magnetic moment domains with the same or opposite directions, where the opposite magnetic moments induce gapped surface states with gaps of opposite sign. Hence, gapless edge states crossing the energy gap appear between the domains [53], resulting in the observation of the gapless surface state in the ARPES experiment. Further more spatially resolved spectroscopy measurements, such as scanning tunneling spectroscopy and point-contact technology, are required to verify the aforementioned hypothesis.

Furthermore, it was reported that the topological nature of MBT can be manipulated

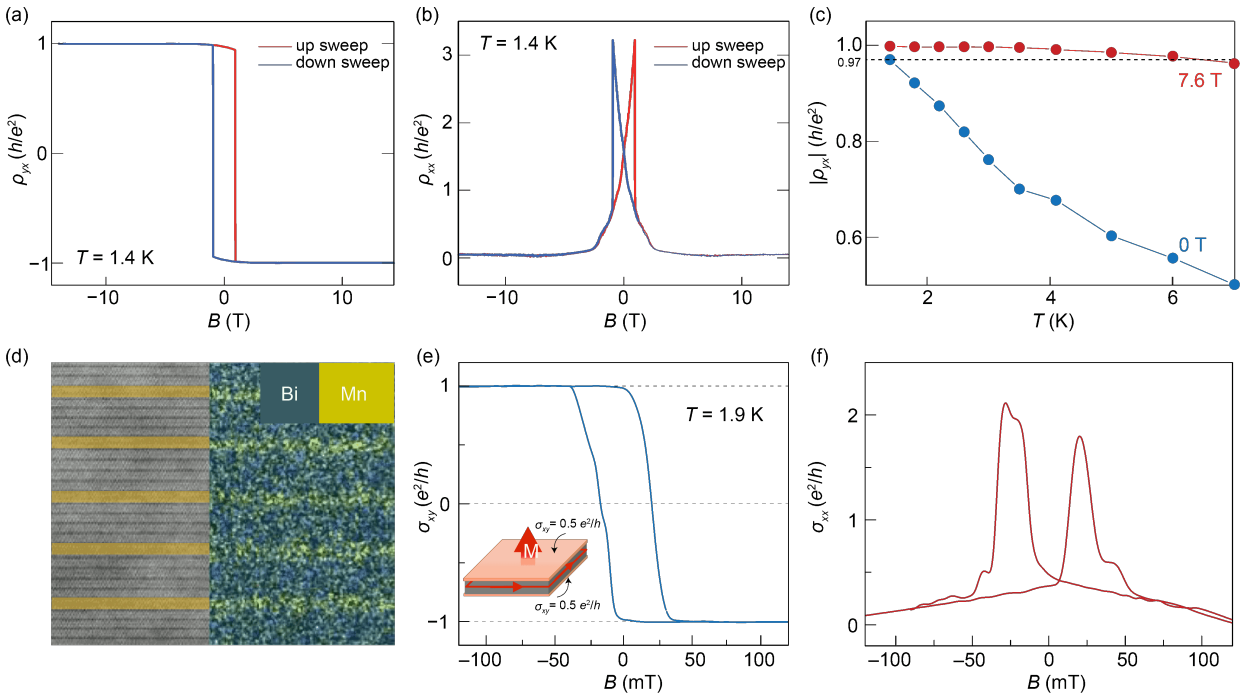

Figure 2.7: (a) ρ_{yx} and (b) ρ_{xx} as a function of magnetic field, measured at 1.4 K in a five-SL $MnBi_2Te_4$ flake. Up and down sweeps of the magnetic field are shown in red and blue, respectively. A nearly quantized Hall resistance $\rho_{yx} = 0.97h/e^2$ is observed at zero magnetic field, and ρ_{xx} reaches $0.061h/e^2$. (c) $|\rho_{yx}|$ as a function of temperature obtained under external magnetic fields of 7.6 T (red) and 0 T (blue). Assuming the quantization criterion of $\rho_{yx} = 0.97h/e^2$, a quantization temperature of 6.5 K was obtained under an external magnetic field of 7.6 T. (d) Periodic sequence of Bi_2Te_3 QLs and $MnBi_2Te_4$ SLs in a magnetic superlattice $MnBi_2Te_4/Bi_2Te_3$. (e) A nearly square zero-field quantized σ_{xy} hysteresis loop measured at 1.9 K. The inset illustrates the out-of-plane magnetization, with 1D chiral channels on the edges of a 3D TI. Both surfaces contribute to the Hall conductance $\sigma_{xy} - 0.5e^2/h$ with the same sign, resulting in a total $\sigma_{xy} = \pm e^2/h$, as discussed in Section 2.4. (f) The corresponding longitudinal conductance σ_{xx}. Panels (a-c) are adopted from Ref. [42] and panels (d-f) are adopted from Ref. [146].

by tuning the magnetism and the thickness of this material. For example, the single SL of MBT is a topologically trivial (quasi-) 2D ferromagnet [37]. Based on the A-type AFM structure, even-layer MBT is a topologically nontrivial fully compensated antiferromagnet. The upper and lower surfaces contribute half quantum Hall conductance with opposite signs, giving zero net Hall conductance. This configuration is known as axion insulator state and it exhibits the topological magnetoelectric effect [22]. On the other hand, odd-layer MBT with three or more layers is an uncompensated antiferromagnet exhibiting net magnetization and nonzero Chern number. It has been suggested that MBT thin films with such a magnetic configuration can exhibit a high-temperature QAH effect. Indeed, the QAH effect was recently reported for five-SL thin flakes of MBT with a nearly quantized Hall resistance of $\rho_{yx} = 0.97h/e^2$ and a longitudinal resistance of $\rho_{xx} = 0.061h/e^2$ at 1.4 K under zero magnetic field, see Fig. 2.7 (a) and (b). A better plateau of $0.998h/e^2$ was obtained upon increasing the out-of-plane magnetic field to 2.5

T. A higher external magnetic field of 7.6 T, which drives the system from an AFM to a FM regime, appears to further enhance the robustness of the QAH effect, increasing its onset temperature to 6.5 K, as shown in Fig. 2.7 (c). Later, a QAH effect with considerably higher onset temperature was reported in seven-SL thin flakes of MBT [147]. A well-quantized Hall plateau of $\rho_{yx} = 0.98h/e^2$ at 1.9 K was observed by applying a small gate voltage $V_g = 6.5$ V, along with a nearly vanishing resistance of $\rho_{xx} = 0.012h/e^2$. Nevertheless, a strong out-of-plane magnetic field is still required to reach a fully polarized magnetic state of the sample and obtain a nearly quantized Hall resistance. Most recently, a nearly quantized Hall conductance was observed at zero-field and 1.9 K in a 300 nm $MnBi_2Te_4/Bi_2Te_3$ superlattice consisting of SLs roughly separated by four QLs [146], see Fig. 2.7 (d). The superlattice exhibits FM properties with $T_C \sim 13$ K. A nearly square zero-field quantized σ_{xy} hysteresis loop and the corresponding change in σ_{xy} are shown in Fig. 2.7 (e) and (f).

Generally speaking, MBT is a member of the larger family of layered van der Waals materials $(MnBi_2Te_4)(Bi_2Te_3)_n$ ($n = 0, ..., 4$) [148], in which the SLs are separated by a stack of n quintuple layers (QLs) of non-magnetic Bi_2Te_3 [148–151], as shown in Fig. 2.6 (a). Increasing n weakens the interlayer AFM coupling and FM properties develop, promising a further substantial increase of the QAH effect onset temperature. Hence, the magnetic properties of this family of IMTIs are highly tunable by the number n of Bi_2Te_3 layers. Whereas in $MnBi_4Te_7$ ($n = 1$) AFM order is still established at a low temperature of about 13 K [149], further increasing n beyond 2 or 3 seems to decouple the SLs [150, 151], eventually leading to non-interacting (quasi-) 2D ferromagnetic layers. Obviously, for the QAH effect, it is desirable to realize an IMTI with a zero-field FM state. However, the exact n at which the transition from AFM to FM state occurs is disputed. Most studies report a complex metamagnetic behavior in $MnBi_4Te_7$ and $MnBi_6Te_{10}$ [149, 151–155] and a clear FM state only for $n \geq 3$ [151, 153, 156].

A comprehensive study of $MnBi_4Te_7$ combining crystal growth, magnetic bulk characterization, photoemission, electron and x-ray spectroscopy with density functional theory calculations revealed two main phase transitions—one at 13 K (paramagnetic to AFM) and the other one at 5 K (AFM to FM-like), with both ordered phases exhibiting a strong out-of-plane anisotropy [149], in line with the recent report which evidenced the anisotropy-controlled transition from an A-type collinear antiferromagnet to a fully saturated metamagnetic state in weakly coupled magnetic multilayers of $(MnBi_2Te_4)(Bi_2Te_3)_n$ [152]. Whereas all experimental reports appear to be compatible with FM ordering within the SLs and with out-of-plane oriented moments, different interlayer ordering can be stabilized as a function of temperature and magnetic field [37, 148, 149, 153]. This rich magnetic phase diagram indicates the presence of competing magnetic orders in $(MnBi_2Te_4)(Bi_2Te_3)_n$, which, in combination with the topological surface states, may provide a versatile platform for tunability between different topological regimes.

In particular, it was established by single-crystal x-ray diffraction (XRD) that $(MnBi_2Te_4)(Bi_2Te_3)_n$, $n = 0, ..., 2$ features inherent magnetic defects [33, 149, 157], namely statistical Mn/Bi intermixing and Mn vacancies in the cationic atomic positions. It was soon recognized that this antisite disorder has strong impact on the magnetic properties [158, 159]. For example, based on scanning tunneling microscopy (STM), XRD, and theoretical calculations (DFT) it was suggested that intermixing of Mn and Sb is decisive to render a related compound $MnSb_2Te_4$ both ferromagnetic with $T_C \approx 45$–50 K and topologically non-trivial [160]. Also, for the $(MnBi_2Te_4)(Bi_2Te_3)_n$ family vastly ranging values for the antisite intermixing and vacancy concentrations caused by different synthesis conditions are concomitant with a variation of magnetic properties [153–155, 161, 162]. In Chapter 7 we address this issue and show that carefully engineered intermixing plays a crucial role in accomplishing robust FM order and therefore could be the key towards enhanced QAH effect properties.

Chapter 3

Experimental and theoretical methods

In this chapter the experimental and theoretical methods most relevant to this thesis are introduced. We will shortly describe the core level spectroscopy methods employed to characterize the electronic and magnetic properties of our samples, including x-ray absorption spectroscopy (XAS), x-ray magnetic circular and linear dichroism (XMCD/XMLD) and x-ray photoemission spectroscopy (PES). Further we will discuss the experimental aspects of XAS and XMCD measurements and the data acquisition and evaluation procedure. Next we will introduce the magneto-optical sum rules and describe the multiplet ligand-field theory (MLFT) calculation within the cluster model, used to interpret the XAS and XMCD line shapes and determine the ground state electronic and magnetic properties of magnetic topological insulators (MTIs). Finally, the superconducting quantum interference device (SQUID) magnetometry employed to characterize bulk magnetic properties of our samples will be addressed.

3.1 Core level spectroscopy

The term core-level x-ray spectroscopy refers to a group of spectroscopic methods that investigate the properties of a system by exciting the core electrons of its component atoms with high-energy x-ray photons produced by modern synchrotron sources (see Section 3.2.1). If the photon energy is high enough to excite these electrons into unbound states they can be detected as photoelectrons in photoemission spectroscopy (PES). However, if the photon energy matches the energy difference between the core and a shallower energy level, the excitation can occur between these two states, resulting in a variety of absorption spectra and their derivatives, such as magnetic circular and linear dichroism. The created core holes (the absence of core electrons, see Fig. 3.1 (b)) are unstable and interact with other core and valence states, which eventually causes its decay after certain lifetime ($\sim 10^{-15}$ seconds) with the system dissipating the absorbed energy via emission of photons or nonradiative Auger decay. Measuring the energy and momentum of the emitted particles allows one to deduce various properties of the system's ground or excited state.

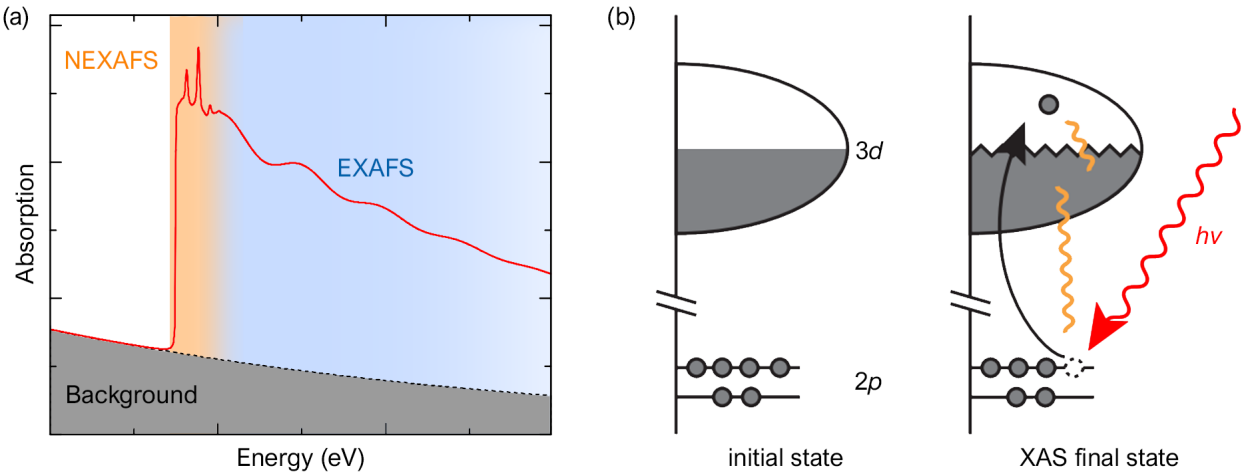

Figure 3.1: (a) A representative XAS spectrum with the three main regions labeled. (b) Schematic representation of core level spectroscopy at the $L_{2,3}$ edges. The initial state includes a fully occupied $2p$ shell and a partially filled $3d$ valence shell. An incoming photon of certain energy and polarization excites a core electron into a valence shell leaving behind a core hole. This is the final state for XAS. The system is left in a highly energetic state after the absorption of a photon. The core hole is unstable and interacts with other core and valence states.

In this sections we will focus the discussion on those spectroscopy techniques, which are the most relevant for this thesis, namely XAS, XMCD and PES.

3.1.1 X-ray Absorption Spectroscopy

The measurement of the absorption of the x-rays as a function of the incoming beam energy is called X-ray Absorption Spectroscopy (XAS). XAS is a very powerful type of spectroscopy, which provides information about the ground-state properties of the system. It is element specific and can likewise be applied to solid-state samples, molecular complexes, gases and liquids [163]. It can be used to study surfaces, interfaces, buried layers, and impurities at low concentrations, such as those studied in this thesis. By choosing the right excitation energies, element-specific quantities can be determined, such as the number of electrons (or holes) in specific shells, and in the case of magnetic ions the atomic spin- and orbital magnetic moments. Moreover, solid state properties influencing the local atomic environment can be analyzed, such as crystal fields, the orbital symmetry and the magneto-crystalline anisotropy.

In 1913 Julius Hedwig and Maurice de Broglie working independently reported the observation of an x-ray absorption spectrum [164, 165]. The first application of synchrotron radiation using soft x-rays for an absorption measurement started in 1954. However, XAS spectroscopy became increasingly popular starting from the 1980s with the advent of synchrotron radiation sources providing an intense, continuous spectrum of polarized light, as discussed in section 3.2.1.

Numerous processes may take place when a photon is absorbed by a material, depending on how the photon energy relates to the edge. In order to demonstrate some of these processes, in Fig. 3.1 (a) we show a fictitious absorption edge representing a typical x-ray absorption spectrum. There are three regions in the spectrum, which can be distinguished. Below the edge of interest, when the photon energy $h\nu$ is lower than the binding energy E_B of the core level, the corresponding electron cannot be excited and the absorption governed by what are typically called background processes. This pre-edge region might contain contributions from the excitation of less energetic core levels, i.e. the tails of the lower energy absorption edges. When the photon energy is equal or slightly above (up to approximately 50 eV) the E_B the absorption leads to excitation of core electrons into the empty states. This region is often called the Near Edge X-ray Absorption Fine Structure (NEXAFS) or X-ray Absorption Near Edge Structure (XANES) [166]. The spectrum here reflects the electronic structure and depending on the edge and material studied it may be dominated by multiplet effects (like in the case of the $L_{2,3}$ edges of $3d$ transition metals, see Subsection 3.1.1) or it can be a *close representative* of the unoccupied density of states (DOS), like in the case of the K edge of oxygen [167]. NEXAFS is strongly sensitive to the local bonding of the absorbing atom. It yields an element-specific information about the unoccupied states and owing to its polarization dependence can be used to investigate the local electronic and magnetic properties of the absorbing atom [166]. The XAS data presented in this thesis is measured in the NEXAFS region.

Further, for higher energies above the edge, the core electron gets sufficient energy to reach unbound continuum states, which leads to a general decay of the absorption. This is the extended region (up to several hundred eV above the absorption edge) which is referred to as Extended X-ray Absorption Fine Structure (EXAFS) [168]. While the pre-edge region is essentially structureless, the are oscillation-like structures appearing in the extended region, which result from the scattering of the excited electron at neighboring atoms. Therefore, EXAFS spectrum allows for extraction of the local structure around the absorber. Indeed, it is widely used to determine the distances, coordination number, and species of the neighbors of the absorbing atom by analyzing these oscillatory interference patterns.

Light-matter interaction

Let us first consider the absorption process sketched in Fig. 3.1 (b). When electromagnetic radiation (x-ray) with photon energy $E = h\nu$ penetrates the matter under investigation, its intensity $I_0(E)$ decays with penetration depth t due to the interaction between the photons and the absorbing material according to the Beer-Lambert law [169, 170]

$$I(E,t) = I_0(E)e^{-\mu(E)t}. \tag{3.1}$$

Here $I(E,t)$ is the detected intensity and $\mu(E)$, which is inversely proportional to the x-ray penetration length λ_x, is the linear x-ray absorption coefficient (attenuation coefficient). In general, $\mu(E)$ depends on the photon energy $E = h\nu$ and it is a material-specific quantity. For a certain material composed of one element, it can be written as

$$\mu(E) = \rho_a \sigma_{abs}(E) = \left(\frac{\rho_m N_\mathrm{A}}{A} \right) \sigma_{abs}(E), \tag{3.2}$$

where ρ_a is the atomic number density [atoms/volume], ρ_m is the atomic mass density [mass/volume], $N_\mathrm{A} = 6.02214 \cdot 10^{23}$ is Avogadro's number, A is the atomic mass number and $\sigma_{abs}(E)$ is the atomic absorption cross-section [169, 170]. Because of this proportionality between $\mu(E)$ and the atomic absorption cross-section $\sigma_{abs}(E)$ of a single atom, the XAS intensities refer to the absorption cross section of corresponding elements.

In a quantum mechanical treatment, the absorption process can be described in terms of transition probabilities T_{if} between an initial state $|i\rangle$ and a final state $|f\rangle$, which are both many-body states. In the simplest picture, a photon with energy $E = h\nu$ is absorbed by an electron in a core shell of energy E_i and it is excited from its initial state $|i\rangle$ to a final state $|f\rangle$ with energy $E_f = E_i + E$ and the DOS of the final state $\rho_{DOS}(E_f)$, as illustrated in Fig. 3.1 (b). In this one-electron picture we simply focus only on what happens to the exited electron [169] and ignore what happens to all other remaining electrons in the atom during the excitation process. The x-ray absorption cross-sections is calculated by consideration of the time-dependent perturbation of the matter by the electromagnetic field of the incoming x-rays. Using first-order perturbation theory, the transition probability per unit time T_{if} between initial and final state is given by Fermi's Golden Rule [171, 172]:

$$T_{if} = \frac{2\pi}{\hbar} \left| \langle f | \, \mathcal{H}_{int} \, | i \rangle \right|^2 \delta(E_f - E_i - h\nu), \tag{3.3}$$

where $\mathcal{H}_{int}$ is the electron-photon interaction Hamiltonian and the delta function assures energy conservation. The absorption cross-section $\sigma_{abs}(E)$ is obtained from the T_{if} by normalization to the incident photon flux Φ_0. Summing over all transitions that can be reached with the certain energy $E = h\nu$ of the incident photons, we get the total atomic absorption cross-section

$$\sigma_{abs}^{tot}(E) = \sum_{E_f - E_i \leq E} \frac{T_{if}}{\Phi_0}. \tag{3.4}$$

Now it is obvious that the variation of the photon energy can be used to select which transitions contribute to the XAS signal.

The electron-photon interaction Hamiltonian $\mathcal{H}_{int}$ which enters the transition matrix

elements $M_{if} = \langle f | \mathcal{H}_{int} | i \rangle$ in Eq. 3.3 describes the interaction of an external photon electromagnetic field (expressed by the vector potential $\mathbf{A}(\mathbf{r}, t)$) with the material. In a semi-classical description, this interaction is introduced as perturbation by the canonical replacement of the momentum operator $\mathbf{p} \rightarrow \mathbf{p} - e\mathbf{A}(\mathbf{r}, t)$ in the unperturbed Hamiltonian $\mathcal{H}_0 = \frac{\mathbf{p}^2}{2m} + V(\mathbf{r})$, where we considered that electron is subject to an external potential $V(\mathbf{r})$, which can be the potential of a nucleus for instance. In can be shown, that in dipole approximation, which assumes that the size of the absorbing atomic shell is small relative to the incident x-ray wavelength, i.e. $|r| \ll 1/|\mathbf{k}| = \lambda/2\pi$, $\mathcal{H}_{int}$ simplifies to

$$\mathcal{H}_{int} = -\frac{e}{m}\mathbf{A} \cdot \mathbf{p} = -\frac{e\hbar}{im}\boldsymbol{\epsilon} A_0 e^{-i\omega t} \cdot \nabla, \tag{3.5}$$

where $\mathbf{A}(\mathbf{r}, t)$ is expressed in terms of electromagnetic plane wave with the amplitude A_0, the wave vector $\mathbf{k}$, frequency ω and polarization vector $\boldsymbol{\epsilon}$. As in this thesis we are mainly probing the $L_{2,3}$ absorption edges of $3d$ transition metals using photon energies up to 1000 eV, it is useful to investigate how far the dipole approximation is justified in this energy range. $E = 1000$ eV corresponds to a wavelength $\lambda \geq 1.2$ nm. The extension of the absorbing atomic shell can be roughly estimated from the Bohr model via $|\mathbf{r}| \approx 2a_0/Z$, where a_0 is the Bohr radius and Z is the atomic number. For example, in case of transitions from the $2p$ core shell of V ($Z = 23$) the radius can be estimated as $|\mathbf{r}| \approx 0.05$ Å. So we have $|\mathbf{r}| \approx 0.05$ Å$\ll \lambda/(2\pi) \approx 2$ Å, from which it follows that the dipole approximation is valid in the used energy range.

Having applied the dipole approximation, we can evaluate the first-order matrix element $M_{if} = \langle f | \mathcal{H}_{int} | i \rangle$ in Eq. 3.3, which describes the x-ray absorption process[1]:

$$\begin{aligned} M_{if} = \langle f | \mathcal{H}_{int} | i \rangle \propto \langle f | \boldsymbol{\epsilon} \cdot \mathbf{p} | i \rangle = \frac{m}{i\hbar} \langle f | [\boldsymbol{\epsilon} \cdot \mathbf{r}, \mathcal{H}_0] | i \rangle \\ = i\frac{m}{\hbar}(E_f - E_i) \langle f | \boldsymbol{\epsilon} \cdot \mathbf{r} | i \rangle = im\omega \langle f | \boldsymbol{\epsilon} \cdot \mathbf{r} | i \rangle . \end{aligned} \tag{3.6}$$

Here we employed the commutator relation $\mathbf{p} = \frac{m}{i\hbar}[\mathbf{r}, \mathcal{H}_0]$ [167], assuming that the final and initial states are eigenfunctions of the unperturbed Hamiltonian $\mathcal{H}_0$. Later we made use of the relation $E_f - E_i = \hbar\omega$. Hence, M_{if} represents a spatial integral over the product of two wave functions and the polarization-dependent dipole operator $\mathcal{O} = \boldsymbol{\epsilon} \cdot \mathbf{r}$.

Thus, within the dipole approximation the x-ray absorption cross-section can be written as

[1] Note that the initial state $|i\rangle$ is a product of electronic and incident photon state, and the final state $|f\rangle$ is purely electronic. It can be shown, that by quantizing the electromagnetic field, one can separate the electronic and photon parts, evaluate the photon part, and obtain the matrix elements in terms of transitions between two electronic states [169]. From now on we change conventions and describe purely electronic states by $|i\rangle$ and $|f\rangle$ with energies E_i and E_f , respectively.

$$\sigma_{abs} = 4\pi^2 \alpha \hbar\omega \left| \langle f | \boldsymbol{\epsilon} \cdot \mathbf{r} | i \rangle \right|^2 \delta(E_f - E_i - \hbar\omega), \tag{3.7}$$

where $\alpha \approx 1/137$ is the fine structure constant [169]. As in this thesis we are generally only concerned with spectral shapes, rather than absolute cross-sections, we can rewrite the equation above as an approximate proportionality relation. Finally, recalling that the measured XAS intensity is proportional to the absorption cross-section and consequently also to the transition probability, we have for the XAS intensity

$$I_{\mathrm{XAS}}(\hbar\omega, \boldsymbol{\epsilon}) \propto \sum_f \left| \langle f | \boldsymbol{\epsilon} \cdot \mathbf{r} | i \rangle \right|^2 \delta(E_f - E_i - \hbar\omega), \tag{3.8}$$

where we sum over intensities associated with different possible final states.

Matrix elements and selection rules

As one can see from the Eq. 3.8, the intensity of the XAS spectrum is proportional to the square of the matrix element $M_{if} \propto \langle f | \boldsymbol{\epsilon} \cdot \mathbf{r} | i \rangle$, where the transition operator $\mathcal{O} = \boldsymbol{\epsilon} \cdot \mathbf{r}$ is written within the dipole approximation, with $|i\rangle$ and $|f\rangle$ being the initial and final eigenstates of the unperturbed Hamiltonian $\mathcal{H}_0$. Now it makes sense to have a closer look at this matrix element and investigate the conditions at which it is not vanishing. Since the many-particle states $|i\rangle$ and $|f\rangle$ are expected to have some resemblance to those of a free atom, one generally uses a one-particle basis $\{\psi_{nlm_lm_s}\}$ composed from atomic-like spin orbitals $\psi_{nlm_lm_s}(r, \theta, \phi) = R_{nl}(r) Y_l^{m_l}(\theta, \phi) \chi_{m_s}$, which are naturally separated into radial, angular and spin parts. Here the index $m_s = \pm 1/2$ switches between two spinors for spin-up and spin-down directions.

First, we notice that the transition matrix element clearly depends on the polarization $\boldsymbol{\epsilon}$ of the incoming x-rays. Therefore, the absorption process is substantially influenced by the details of light polarization. We are particularly interested in linear and circular polarized light. In case of linearly polarized x-rays, for the three extreme cases, where the electric vector $\mathbf{E}$ is aligned along x-, y-, and z-axis in the coordinate system of the sample, the corresponding polarization vectors can be defined as $\boldsymbol{\epsilon}_x = \mathbf{e}_x$, $\boldsymbol{\epsilon}_y = \mathbf{e}_y$ and $\boldsymbol{\epsilon}_z = \mathbf{e}_z$, where $\mathbf{e}_x$, $\mathbf{e}_y$ and $\mathbf{e}_z$ are Cartesian basis vectors. For the right- and left-circularly polarized x-rays with wave vector $\mathbf{k} \parallel \mathbf{e}_z$[1] the polarization vectors can be expressed as $\boldsymbol{\epsilon}^{+1} = \boldsymbol{\epsilon}^R = -(\boldsymbol{\epsilon}_x + i\boldsymbol{\epsilon}_y)/\sqrt{2}$ and $\boldsymbol{\epsilon}^{-1} = \boldsymbol{\epsilon}^L = (\boldsymbol{\epsilon}_x - i\boldsymbol{\epsilon}_y)/\sqrt{2}$, where we have used the handedness convention of Stöhr [169]. The position vector operator $\mathbf{r}$ can be expressed in spherical basis as $r_q = rC_q^{(1)}$, where for the brevity of notation we used the Racah's spherical tensor operators defined as

[1] z-axis is the quantization axis along which the magnetic field is applied in a typical XMCD experiment.

$$C_q^{(k)} = \sqrt{\frac{4\pi}{2k+1}} Y_{l=k}^{m_l=q}(\theta,\phi), \tag{3.9}$$

with $q = 0, \pm 1$ for linearly and circularly polarized light, respectively. Hence, the general expression for transition operator reads as $\boldsymbol{\epsilon}\cdot\mathbf{r} = r\sum_q \epsilon^q C_q^{(1)}$. It can be shown that, for example, in the case of circularly polarized light the corresponding transition operator reads as $\boldsymbol{\epsilon}^{\pm 1}\cdot\mathbf{r} = \mp(x \pm iy)/\sqrt{2} = rC_{\pm 1}^{(1)}$ and for linearly polarized light $\boldsymbol{\epsilon}^0\cdot\mathbf{r} = z = rC_0^{(1)}$.

Let's first assume that the system consists of a single electron and $|i\rangle$ and $|f\rangle$ are some two one-electron states from the one-particle basis $\{\psi_{nlm_lm_s}\}$, i.e. $|i\rangle = |nlm_lm_s\rangle$ and $|f\rangle = |n'l'm_l'm_s'\rangle$. In this basic case the transition matrix element becomes

$$M_{if} \propto \langle n'l'm_l'm_s'|\boldsymbol{\epsilon}\cdot\mathbf{r}|nlm_lm_s\rangle = \delta_{m_sm_s'}\langle R_{n'l'}|r|R_{nl}\rangle\langle Y_{l'}^{m_l'}|\sum_q \epsilon^q C_q^{(1)}|Y_l^{m_l}\rangle =$$

$$\delta_{m_sm_s'}\langle n'l'|r|nl\rangle\sum_q \epsilon^q\sqrt{(2l'+1)(2l+1)}\begin{pmatrix} l' & 1 & l \\ 0 & 0 & 0\end{pmatrix}\begin{pmatrix} l' & 1 & l \\ -m_l' & q & m_l\end{pmatrix}, \tag{3.10}$$

where the last integral over three spherical harmonics we have expressed via the product of two Wigner's $3j$ symbols [173, 174]. By requiring non-vanishing of each of the $3j$ symbols we immediately obtain the two dipole selection rules complementing the spin conservation:

$$\Delta m_s = m_s' - m_s = 0, \qquad \Delta l = l' - l = \pm 1, \qquad \Delta m_l = m_l' - m_l = q = 0, \pm 1. \tag{3.11}$$

Now we can easily see that the magnetic quantum number is changed according to the polarization of the incoming x-rays, such that for light linearly polarized along z-axis ($q = 0$) the magnetic quantum number in the final state must be the same as in the initial, while for the circularly polarized light ($q = \pm 1$) this number must be either higher or lower by 1, depending on the helicity. This gives the polarization dependence of the XAS, which can lead to the observation of dichroism effects, i.e. difference in two absorption spectra obtained for different light polarizations, which we discuss in Subsection 3.1.2 in more details.

For spin–orbit coupled state, when the eigenstates should be described by the (j, m_j) quantum numbers instead of (l, m_l, m_s), the dipole selection rules can be deduced as $\Delta j = 0, \pm 1$ (but not $j = 0 \to j = 0$ transitions) and $\Delta m_j = q$. However, for extended final states (the Bloch-like wave functions in density functional methods), when j is not a good quantum number, these rules do not necessarily hold [174].

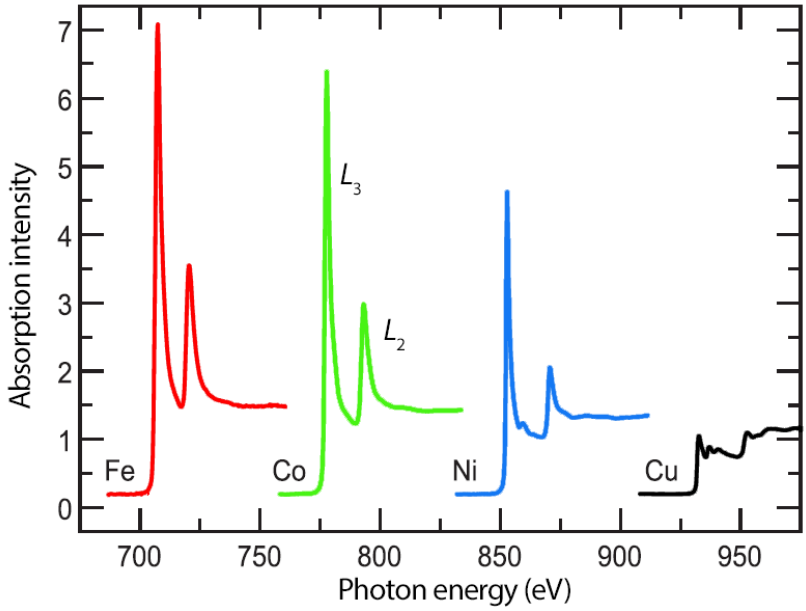

Figure 3.2: $L_{2,3}$ edge x-ray absorption spectra for the pure metals Fe, Co, Ni, and Cu plotted on an absolute cross section scale. Adopted from Ref. [169]

XAS at $L_{2,3}$ edges of $3d$ transition metals

The excitation of the $2p$ core electrons to the unoccupied $3d$ states is historically called the $L_{2,3}$ edge. These excitations are governed by dipole selection rules (see Eq. 3.11) and found in the $\sim 350 - 1000$ eV energy range in case of $3d$ transition metals. The dipole selection rules also allow for $2p \rightarrow 4s$ excitations, though their contribution to the spectra is insignificant and excitations to $3d$ states dominate the spectra.

In Fig. 3.2 as an example, we show $2p$ XAS spectra for several $3d$ transition metals. What one can immediately notice, is that different elements have their absorption edge at different energies, with heavy elements having it at higher energies. The reason is that binding energy of the core electron increases with number of protons in the nucleus, hence also more energy is needed to excite the core electron into the $3d$ shell. Another observation one can make is that the edge intensity decreases along the series. This is due to the higher filling of the $3d$ states with increasing the atomic number Z. Since the intensity of isotropic XAS spectrum is directly proportional to the number of the empty $3d$ states, i.e. the number of $3d$ holes [169], which is known as charge sum rule. This is intuitive, since the intensity should increase with more empty final states available for the transition from the initial state. Furthermore, the spectral shape also depends on the $3d$ electron count [111].

There are also some common features that all $2p$ core level XAS spectra in Fig. 3.2 share. For every spectrum we can notice two sets of peaks (manifolds), for instance, one around 780 eV and another around 795 eV in case of Co. These two manifolds, split in energy due to the $2p$ spin–orbit coupling, are referred to as L_3 and L_2 edge. One can also

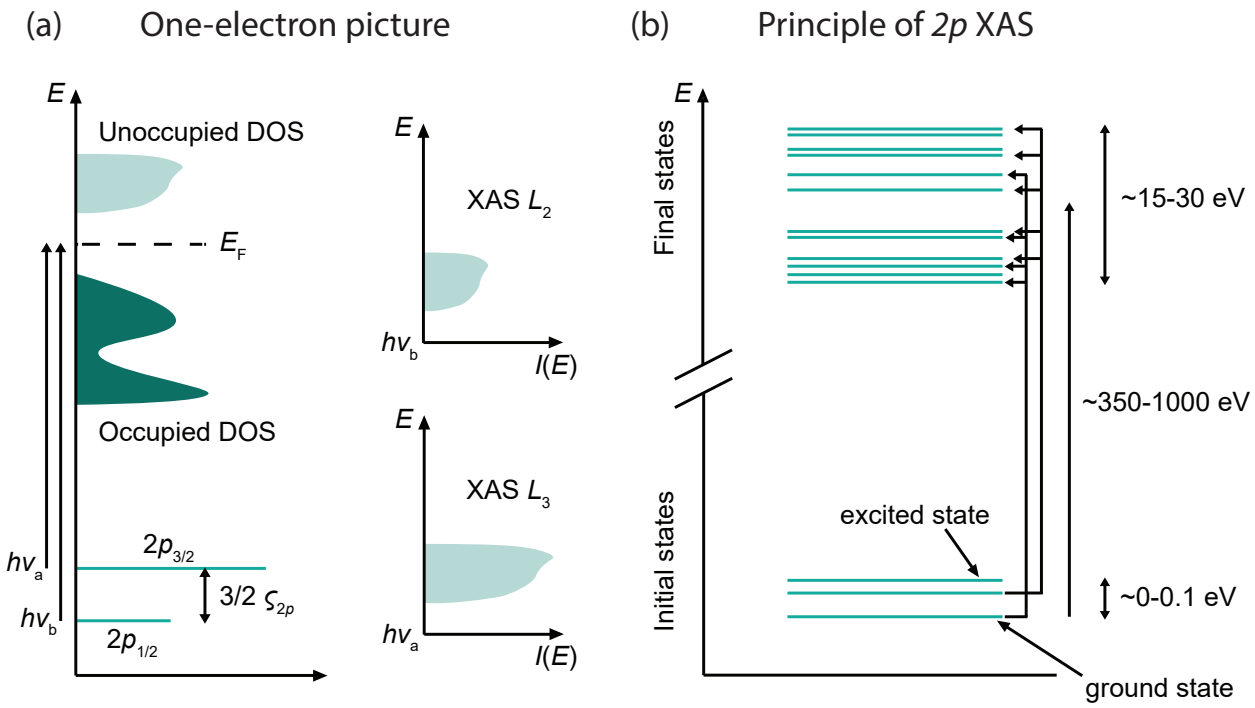

Figure 3.3: (a) Interpretation of $L_{2,3}$ edge spectrum within a one-electron picture. The spectral shape represents the unoccupied DOS. (b) The basic idea of $2p$ XAS. There is a ground state, which can be degenerate, and important low excited states. Much higher in energy, there are many final states. Dipole selection rules determine which of these states can be reached. For each of the initial state there the set of final states that can be reached is different. Inspired by Ref. [177]

notice that the splitting between L_3 and L_2 edge increases along the series. This is because the $2p$ spin–orbit interaction gets stronger for later transition metal atoms since it relates directly to the nuclear charge and inversely to the orbital radii [173]. This spin–orbit splitting is quite important when interpreting spectral shapes, as well as applying sum rules (see Section 3.4). For the late TMs the L_3 and L_2 edges are well separated, so there is not much mixing between the two, while for the early TMs the edges are very close to each other, which results in XAS intensity of the two edges being affected by coherent mixing between them [175]. Finally, one more common feature for all spectra in Fig. 3.2 is that the intensity at the beginning of the spectra is smaller than at the end. This is called the continuum edge-jump, which is due to excitations into delocalized conduction band states [176].

In order to understand the features present in $L_{2,3}$ edge XAS, let us first consider what one should expect within the one-electron picture (or independent electron approximation). As mentioned before, in one-electron picture, which is often used to describe the x-ray absorption process, one simply focuses on only what happens to the exited electrons and neglects the influence of the remaining electrons, assuming that they do not participate in the process. Fig. 3.3 (a) shows the DOS of an arbitrary insulator. The Fermi level lies in $3d$ valence shell where states below E_F are occupied and those above E_F are

empty. Fig. 3.3 (a) also shows the $2p$ core levels at lower energies as two delta functions, since they are highly localized, resulting in flat bands and delta functions as DOS [177]. These two delta function are split by $2p$ spin–orbit coupling. In the initial $2p$ core state, electron has an angular momentum $l = 1$ and spin $s = 1/2$, which results in total angular momentum $j = 1/2$ and $j = 3/2$. So the spin–orbit coupling produces two energy states, $2p_{3/2}$ and $2p_{1/2}$. Since there are twice as many states with $j = 3/2$ as there are states with $j = 1/2$, the $2p_{3/2}$ delta function is shown twice as large as $2p_{1/2}$. The separation between $2p_{3/2}$ and $2p_{1/2}$ states is given by $3/2\zeta_{2p}$, where ζ_{2p} is $2p$ spin–orbit coupling constant. The electronic excitation from $2p_{3/2}$ is called the L_3 edge, while the excitation from $2p_{1/2}$ is called the L_2 edge. On the right side of Fig. 3.3 (a) the XAS spectrum expected within the one-electron picture is shown. The spectrum represents a convolution of the occupied $2p$ core DOS and unoccupied $3d$ valence DOS. Since $2p$ core DOS is represented by two delta functions, XAS spectrum consists of two unoccupied $3d$ DOS shifted by $3/2\zeta_{2p}$. Because there are 4 states with $j = 3/2$ and only two with $j = 1/2$, the intensity at the L_3 edge is twice that at L_2. Hence, within the one-electron picture the line shapes of L_3 and L_2 edges are equal (here we do not consider spin–orbit coupling in the $3d$ shell). However if we look at spectra in Fig. 3.2 or any other XAS spectrum in this thesis, we notice that L_2 and L_3 edge are typically very different, indicating that the one-electron picture is not sufficient. Moreover, it is misleading, since it considers the spin-orbit splitting of the $2p$ core shell in the initial state, although it is clear that in the initial state, the $2p$ shell is fully filled with 6 electrons and therefore there is no observable effect of spin–orbit interaction [169, 177, 178].

The reason why $L_{2,3}$ XAS spectra can not be fully described within one-electron pictures is that this picture ignores interactions between electrons, i.e. electron-electron correlations, including the correlations between the $3d$ electrons and especially between created $2p$ core hole and the $3d$ electrons/holes in the final state of the $2p$ XAS process [177, 179, 180]. The correlation effects in atomic physics are often referred to as "multiplet effects" [173, 179]. Multiplet effects, combined with the $3d$ spin–orbit coupling, completely modify the L_3 and L_2 edges from their one-electron interpretation [179]. As a result, L_2 and L_3 edges are very different from each other. Furthermore, if multiplet effects are of the same order of magnitude as the $2p$ spin–orbit coupling, they can result in significant mixing of the L_3 and L_2 edges and deviation of their intensity ration from the regular 2:1 [180]. This, in turn, also complicates the application of sum rule analysis (see Section 3.4).

Therefore, for the proper description of the XAS process, one should argue in a "configuration picture", where the whole atomic arrangement of electrons/holes before and after the excitation process is taken into account. In a configuration picture, an atom is excited from a ground or initial state configuration to an excited or final state configuration. For the $L_{2,3}$ edge XAS, the initial state has $2p^6 3d^n$ electron configuration and the

final state has $2p^5 3d^{n+1}$, and the transitions between the configurations are described by $M \propto \langle 2p^6 3d^n | \, P^q_\alpha \, | 2p^5 3d^{n+1} \rangle$.

The final state thus has a $2p^5 3d^{n+1}$ configuration. The $2p$ core hole can be in six different states split by $2p$ spin–orbit coupling into two groups of four states with $j = 3/2$ and two states with $j = 1/2$. If we consider the final state of V^{3+} ion with $2p^5 3d^3$ configuration, there are also 7 holes in the $3d$ shell which one needs to take into account. These 7 holes can be in 10 different $3d$ orbitals. In total there are $\frac{6 \cdot 10!}{2 \cdot 3!} = 1814400$ different final states: 6 for the $2p$ hole, 10 for the first $3d$ hole, 9 for the second $3d$ hole, 8 for the third $3d$ hole and so on divided by 2 because electrons are equivalent. These states present in the $2p^5 3d^3$ configuration are spread out over a wide energy range due to multiplet effects, such as the electron-electron repulsion between different $3d$ and $2p$ orbitals. In general, the multiplet structure depends on the configuration of the element in question, since Slater integrals which determine the strength of the electron-electron Coulomb and exchange interactions, as well as crystal fields and spin–orbit coupling constants differ from element to element. Nevertheless, not all of these multiplets are present in the spectrum, which is obvious when looking at the multiplet calculations shown, for example, in Fig. 4.7. Indeed there are much fewer delta-peaks present in the calculated spectra and the experimental spectrum also consists of distinct peaks with clear structure. The reason is the dipole selection rules shown in Eq. 3.11, that restrict the number of accessible final states.

To conclude, the basic principle of $2p$ XAS can be briefly summarized as illustrated in Fig. 3.3 (b). The are different states belonging to the initial $2p^6 3d^n$ configuration, including ground state (the state with lowest energy) and excited states above it, and there are many states belonging to the final $2p^5 3d^{n+1}$ configuration. Only a few of these final states can be reached in the $2p \rightarrow 3d$ XAS process due to the dipole selection rules. Hence, XAS is sensitive to the ground state electronic structure [181], and even the ground state spin configuration [182]. Indeed, small changes in the initial state, for example some shifts in energy of the states caused by applied magnetic or exchange field, can result in significant changes in the absorption spectrum, since a different set of final states can be reached for each initial state [177]. Therefore $2p$ XAS is very sensitive to small changes in the ground state.

3.1.2 X-ray magnetic circular dichroism

A difference in absorption of left- and right-circularly polarized x-rays is called circular dichroism. This effect occurs when the inversion or the time-reversal symmetry of the material is broken. In the former case, the effect is called x-ray natural circular dichroism and in the latter case it is known as x-ray magnetic circular dichroism (XMCD). Here, we

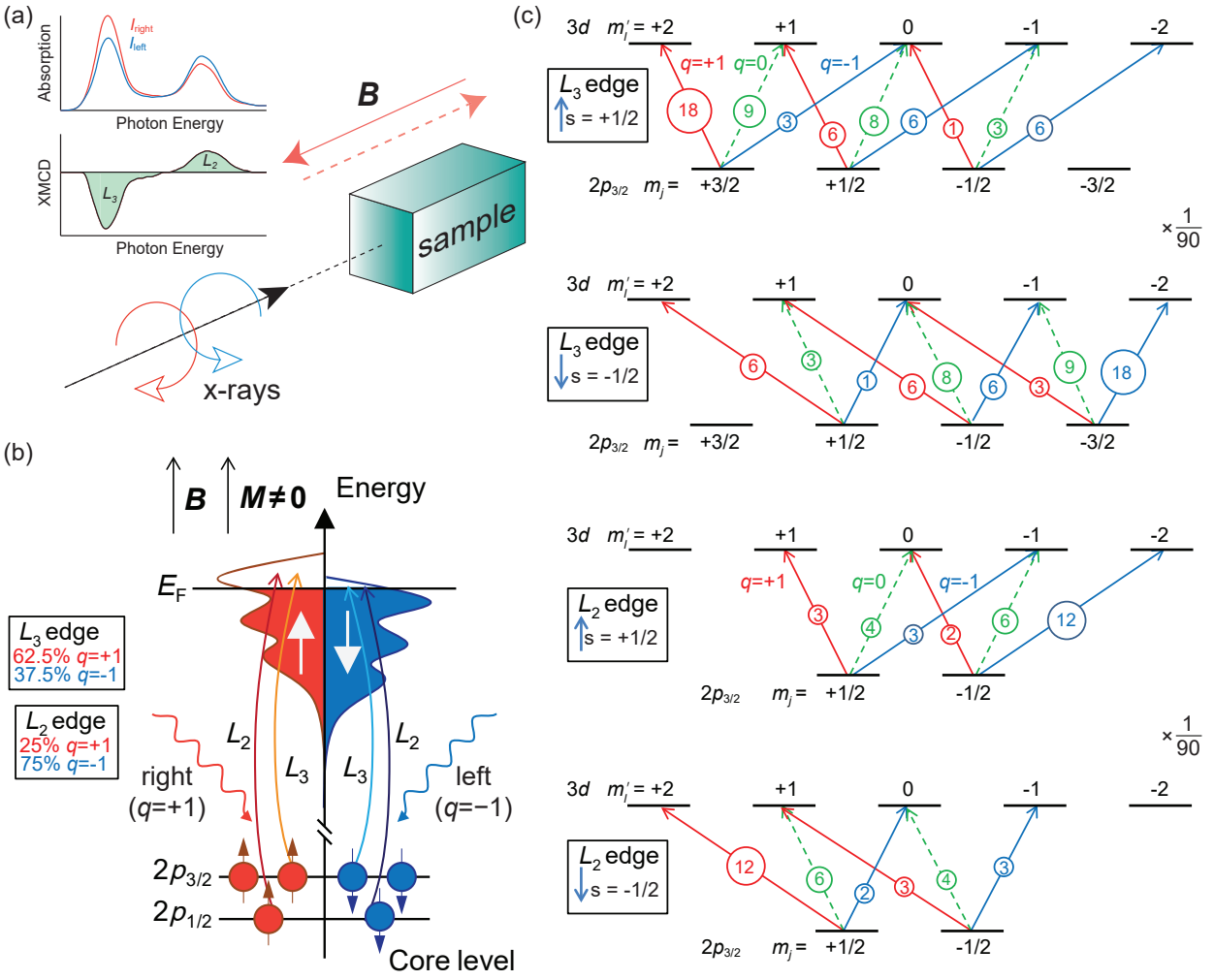

Figure 3.4: (a) Experimental setup for XMCD measurements. (b) Schematic representation of the two-step model of XMCD at the $L_{2,3}$ edges for $3d$ transition metals. (c) One-electron electric-dipole transition probabilities $2p \rightarrow 3d$ for spin-up at the L_3 and L_2 edges with left-circular ($q = -1$), linear (z, $q = 0$), and right-circular ($q = +1$) light polarization, indicated by blue, green dashed, and red arrows, respectively. Adapted from Ref. [111].

will focus on discussion of only XMCD, as it is one of the main spectroscopic method employed in this thesis.

As we already mentioned, XMCD originates from the time-reversal symmetry breaking, for example in a material with spontaneous magnetization like a ferromagnet or in a paramagnetic system with applied external magnetic field, see Fig. 3.4 (a). XMCD is a parity even and time odd effect, which means that it reverses also when the magnetization is inversed. This fact is of great practical importance, as we will see later. XMCD has been theoretically predicted in 1975 by Erskine and Stern for the $M_{2,3}$ edges of Nickel by expanding consideration from the magneto-optical effects to the x-ray region [183] and was first observed in 1987 by Schütz *et al.* at the K edge of Fe [184]. Indeed, XMCD resembles the magneto-optical effects in the visible light region, such as the Faraday effect, with the difference that XMCD arises from the excitation of a core electron instead of a

valence electron [111].

In practice, the XMCD spectrum is obtained as the difference between the two XAS spectra with the incident x-rays helicity vector parallel and antiparallel to the magnetization direction of a material, i.e. difference between XAS spectra measured with left- ($q = -1$) and right- ($q = +1$) circularly polarized light, see Fig. 3.4 (a). The line shape of the XMCD spectrum reflects the magnetic ground-state properties of the system under investigation. Its analysis by means of magnetic sum rules (see Section 3.4) or MLFT calculations (see Section 3.5) yields valuable quantitative information on element- and orbital specific magnetic moments. Therefore, XMCD is a powerful tool to investigate the magnetic properties of materials, such as magnetic topological insulators studied in this work.

The two-step model

In the simple one-electron picture, the basic idea of the XMCD effect can be explained by a two-step model first introduced by Störn [185]. The first step describes the excitation of a spin polarized electron from a core shell by circularly polarized x-rays, while in the second step the excited electron has to find its place in the partially filled valence shell, which essentially acts as a "spin detector" for this electron [111, 169, 178, 186]. In the following, we discuss these two steps in more detail.

Let us consider the $2p \rightarrow 3d$ XAS process in a magnetic material with the quantization axis defined along the magnetization **M** or the external magnetic field **B** direction, as illustrated in the Fig. 3.4 (b). We consider the magnetization direction fixed along the propagation direction of the incoming x-rays, say along the z-axis of our coordinate system (or c-axis of the sample). The first question to address is how a spin polarized electron is created in the first step of the two-step model. The $2p$ core state is split into the $2p_{3/2}$ (L_3 edge) and $2p_{1/2}$ (L_2 edge) levels, which have opposite spin–orbit coupling ($l + s$ and $l - s$). Right- (helicity $q = +1$) or left- ($q = -1$) circularly polarized photons transfer their angular momentum $q\hbar$ to the excited $2p$ electron. The photon's angular momentum can be (partially) transferred to the spin angular momentum of the electron through the $2p$ spin–orbit coupling (Fano effect [187]) resulting in spin polarized electrons. Due to opposite spin–orbit coupling of the $2p_{3/2}$ and $2p_{1/2}$, the spin polarization will be opposite at the L_3 and L_2 edge. As depicted in Fig. 3.4 (b), from the $2p_{3/2}$ level x-rays with right circular polarization excite 62.5% spin-up electrons and 37.5% spin-down electrons, while the $2p_{1/2}$ level gives 25% spin-up and 75% spin-down electrons. Left-circularly polarized x-rays do the opposite at both edges. The core shell can therefore be viewed as an atom-specific, localized "source" of spin-polarized electrons.

The above preferences in spin polarization of the electron for the left- and right-circularly polarized x-rays do not automatically lead to XMCD. The XMCD appears if

there is an imbalance for the spin-up and spin-down electrons (or equivalently holes) in the $3d$ valence shell, which is the case of the magnetized sample. In Fig. 3.4 (b) for clarity we visualized this imbalance using the Stoner band picture, where $3d$ DOS is exchange split at the Fermi level with an unequal number of available spin-up and spin-down holes. Note that the minority electron (majority hole) spin direction is the same as that of the sample magnetization **M**. Instead, one can also use atomic model with $3d$ states split by Zeeman term, depending on the system under investigation. Thus, in the second step of the model the exited spin-polarized electrons have to find a place in the partially filled $3d$ valence shell, and this exchange-split valence shell can be seen as a sensitive "spin detector" for the spins of excited electrons. The quantization axis of the "spin detector" is given by the magnetization direction which for maximum XMCD should be aligned parallel to the propagation direction of x-rays ($\mathbf{M} \parallel \mathbf{k}$), since the XMCD magnitude depends on the cosine of the angle between the two axes. Similarly, if there is spin–orbit coupling in the valence shell, it can act as an "orbital momentum detector" when there is an imbalance of states with different magnetic quantum numbers m_l', since according to dipole selection rules (see Eq. 3.11), only transitions with $\Delta m_l = \pm 1$ are allowed for circularly polarized x-rays.

Since for the case presented in Fig. 3.4 (b) the occupancy of spin–down states is larger than that of the spin-up states and the spin is conserved ($\Delta m_s = 0$ selection rule), the electrons excited from $2p_{3/2}$ ($2p_{1/2}$) with right-circularly polarized x-rays probe mostly the spin-up (spin-down) DOS above the Fermi level. Hence, the absorption of right-circularly polarized x-rays is enhanced at the L_3 edge and reduced at the L_2 edge with respect to the exchange-split $3d$ states. The opposite is valid for left-circularly polarized light. This difference in the absorption $I_{\mathrm{XMCD}}(E) = I_{\mathrm{left}}(E) - I_{\mathrm{right}}(E)$ defines the XMCD.

One-electron transition probabilities

For a more accurate and quantitative description of the XMCD effect we now use the atomic one-electron model and calculate the individual transition intensities $2p_{j=1/2,3/2} \rightarrow 3d$ invoking the dipole selection rules as given in Eq. 3.11 as well as the Fermi's golden rule for XAS given in Eq. 3.8 with substitution of the matrix element in the form given by Eq. 3.10. Most elegantly this can be done using Wigner's $3j$ symbols [173]. Since the dipole operator does not act on spin (i.e. $\Delta m_s = 0$), the matrix element can be written with regard to only l and m_l. According to the dipole selection rules for circularly polarized x-rays the transitions occur from $2p$ states $|l, m_l\rangle$ into the $3d$ states $\left|l' = l+1, m_l' = m_l \pm 1\right\rangle$. Hence, using the Wigner's $3j$ symbols and considering only the angular part (see Eq. 3.10), the relevant expression for the possible transition matrix elements are given by

$$\left\langle l', m_l' \right| C^{(1)}_{\pm 1} \left| l, m_l \right\rangle = -\sqrt{\frac{(l \pm m_l + 2)(l \pm m_l + 1)}{2(2l+3)(2l+1)}}. \tag{3.12}$$

Next we have to include the spin–orbit coupling of the core level. We need to couple the orbital and spin components of the core level to the total angular momentum components m_j of the spin–orbit split levels $j = l \pm s$. This can be done using the Clebsch-Gordan coefficients

$$\left|j, m_j\right\rangle = \sum_{m_l, m_s} C_{j,m_j|l,m_l,s,m_s} \left|l, m_l, s, m_s\right\rangle \tag{3.13}$$

Clebsch-Gordan coefficients can also be described in terms of Wigner's $3j$ symbols [111]. In order to get the relative intensity contribution, every transition matrix element from a $|l, m_l\rangle$ state must be weighted by its Clebsch-Gordan coefficient and then squared (according to Eq. 3.8 or Eq. 3.3)

$$I^{\pm 1}_{l,m_l} \propto |C_{j,m_j|l,m_l,s,m_s} \left\langle l', m'_l\right| C^{(1)}_{\pm 1} \left|l, m_l\right\rangle|^2. \tag{3.14}$$

Using the Wigner's $3j$ symbols this expression can be conveniently written in the following form [111]

$$\sum_{m_l, m_j} (2j+1) \begin{pmatrix} l' & 1 & l \\ -m'_l & q & m_l \end{pmatrix}^2 \begin{pmatrix} l & s & j \\ m_l & m_s & -m_j \end{pmatrix}^2, \tag{3.15}$$

where the first $3j$-symbol gives the probability $|l, m_l\rangle \rightarrow \left|l', m'_l\right\rangle$ and is nonzero for $m_l = m'_l - q$. The second $3j$-symbol gives the core spin–orbit coupling and is nonzero for $m_j = m_l + m_s$ [111]. For clarity, in Eq. 3.15 we assume that the $3d$ states are diagonal in $\left|l', m'_l\right\rangle$, without cross terms, calculation of which is required when the m'_l levels are mixed by crystal field interaction [111].

Fig. 3.4 (c) shows all possible $2p \rightarrow 3d$ transitions, where the transition probabilities for linear z-polarized ($q = 0$), left-circularly ($q = -1$) and right-circularly ($q = +1$) polarized x-rays are given by the displayed integer multiplied by $1/90$. For example, according to Eq. 3.15 the dipole transition from the core $2p$ level $\left|l = 1, m_l = -1, m_j = -3/2\right\rangle$ to the lowest $3d$ level $\left|l' = 2, m'_l = -2, m'_s = -1/2\right\rangle$ with left-circularly polarized light has nonzero transition probability $1/5$. By summing over m'_l we obtain the spin polarization due to the core spin–orbit interaction (i.e., Fano effect), which was used in the first step of the two-step model in Fig. 3.4 (b). For example, for spin up electrons excited from the L_3 edge, $I^- : I^0 : I^+ = 3 : 4 : 5$, and from the L_2 edge, $I^- : I^0 : I^+ = 3 : 2 : 1$. Within the configuration picture we will be dealing with entangled wave functions in intermediate coupling, with a complexity that demands numerical calculations [111].

Finally, using Eq. 3.12 one can show that for XMCD measurements a change in the photon helicity relative to the fixed magnetization direction is equivalent to a change of magnetization direction relative to the fixed photon helicity. This observation has a practical importance, because the change of polarization requires a change in the optical path

of the x-rays through the monochromator, which can result in energy shifts complicating the analysis of experimental data. We will discuss the analysis of XAS and XMCD data in more detail in Section 3.3.

3.1.3 X-ray Photoemission Spectroscopy

Since in Chapter 6 we discuss the electronic and band structure of Eu-doped Bi_2Te_3 topological insulator studied with photoemission—in particular with angle-resolved photoemission (ARPES)—it could be both essential and helpful for the general reader to make a brief introduction to the method. In this section, the most relevant basic principles of photoemission are introduced with focus on the applications within this thesis and based on several reviews and textbooks to which the interested reader is referred for further details [188–191].

Photoelectron spectroscopy (PES), also known as photoemission spectroscopy, is one of the most powerful and widely used analytical techniques in solid state physics, allowing insight into the electronic structure of materials. Its basic principle relies on the measurement of the kinetic energy of electrons which are emitted from a material via the photoelectric effect, i.e., the emission of electrons upon irradiation of a solid with light, which was discovered by Hertz in 1887 [192]. The microscopic mechanism of this effect was later explained by Einstein in 1905 [193], when he introduced the concept of a quantum of light — the photon. Beginning in the 1950's, Siegbahn established x-ray photoemission spectroscopy as a routine experimental technique by developing instruments and methods to analyze the binding energies of electrons in a material [194]. In the 1970's angle-resolved photoemission spectroscopy (ARPES) using ultraviolet light was developed to study the band dispersions of valence states in crystalline solids by measuring the photoelectron intensity as function of energy and angle [190]. To date, the design and development of novel photoelectron spectroscopy techniques is ongoing and comprises hard x-ray PES, spin-resolved PES, two-photon absorption, time-resolved PES and many other applications.

Instrumentation and basic principle

Photoemission is a photon-in electron-out process. This process can be described with the one-step model: The incoming photon excites an electron from its initial state (a core level or a valence Bloch state), into a final state. For the simplicity, the photoemission process is often divided into three independent and sequential steps within the so-called three-step model: (i) excitation of the photoelectron inside the solid, (ii) propagation of the photoelectron to the sample surface, (iii) escape of the photoelectron into the vacuum. Assuming this model, the probability to measure a photoelectron with kinetic energy E_{kin} using photons with energy $h\nu$ is proportional to the product of the probabilities of the

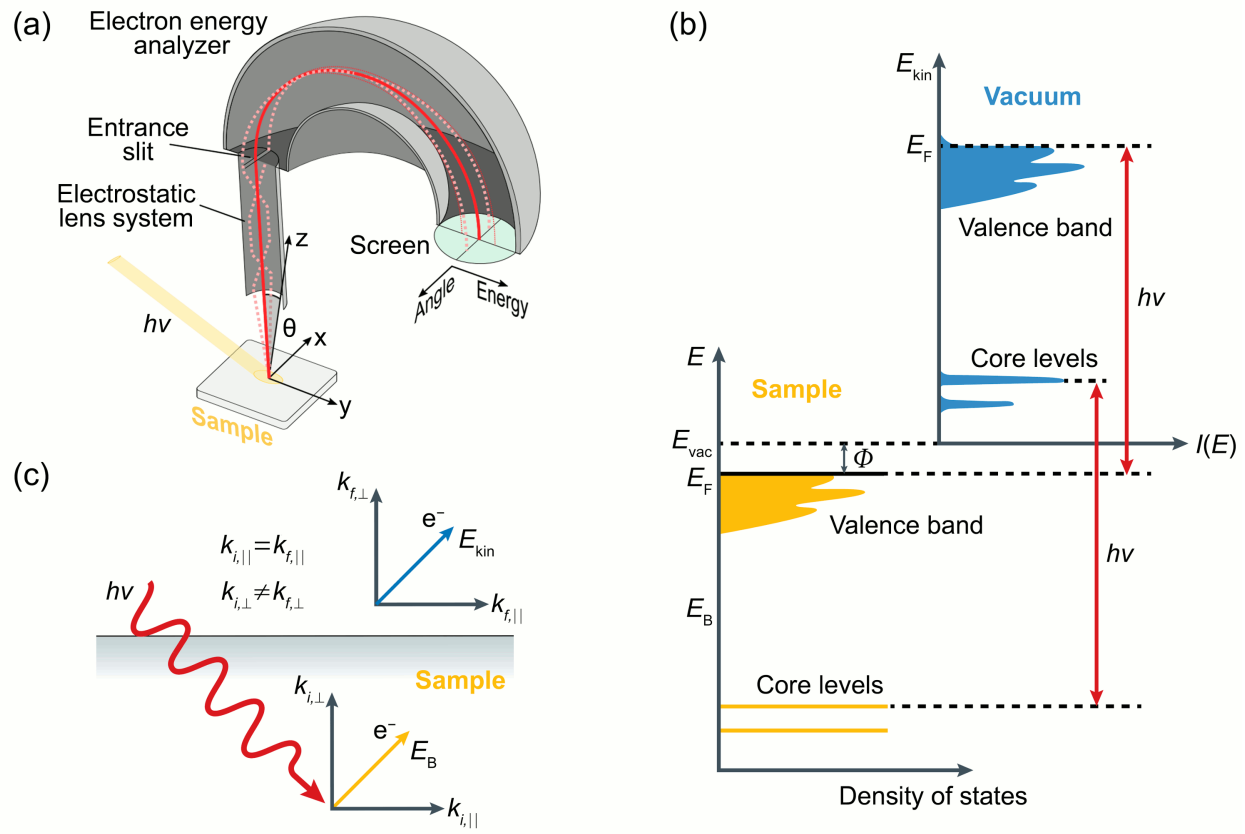

Figure 3.5: (a) Schematic diagram of ARPES experiment. A flux of photon with energy $h\nu$ shines on the sample. The outgoing photoelectron with kinetic energy E_{kin} escaping at the polar and azimuthal angles θ and ϕ are detected by the electron analyzer. (b) Correspondence between the electronic structure of a sample and the recorded photoemission spectra. (c) Schematic representation of the momentum conservation of electrons. In the photoemission process, the momentum parallel to the surface is conserved ($k_{i,\parallel} = k_{f,\parallel}$). By contrast, the momentum in the direction perpendicular to the surface is not conserved, $k_{i,\perp} \neq k_{f,\perp}$ (adopted from Ref. [191]).

three sequential steps. The most basic principles of PES can be understood even without going into the details of each step [188], just by evoking simple arguments of energy and momentum conservation. A typical photoemission setup is sketched in Fig 3.5 (a). A sample is placed under ultrahigh vacuum next to an electron analyser. A monochromatized photon beam impinges on the sample and excites electrons. At high enough photon energy the ejected electrons can escape the sample. These emitted electrons, known as photoelectrons, are then detected by a hemispherical analyzer. PES measures the resulting photocurrent as a function of the kinetic energy and the emission angle. The energy and momentum of the electrons inside the sample are directly connected to those of the photoelectrons by the conservation of energy and momentum parallel to the sample surface. As sketched in the energy diagram depicted in Fig 3.5 (b) the kinetic energy E_{kin} of the photoelectron in vacuum is connected to the binding energy E_{B} of the electrons in the

solid and the energy $h\nu$ of the incident photons by

$$E_{\text{kin}} = h\nu - E_{\text{B}} - \Phi, \tag{3.16}$$

where Φ denotes the work function, which is a measure of the potential barrier at the surface preventing the valence electrons from escaping, E_{kin} is the kinetic energy of a photoelectron and $h\nu$ is the photon energy. Fig 3.5 (b) also illustrates how the electronic structure of the solid translates into the experimentally measured spectra in the independent electron approximation. In the spectra the core-level electrons appear as broadened peaks centered around the respective binding energies. The broadening usually can be described by a Voigt profile, i.e., a convolution of a Lorentzian resolution (caused by the finite lifetime of the core hole) and a Gaussian (the instrumental) resolution. In reality, more complex line shapes result from interactions between the core hole and the remaining electrons. From the shape and the intensity of the core level lines one can study the elemental composition as well as the chemical structure of the sample.

The valence electrons form bands and appear in spectra as broad features near the Fermi level, which essentially reflect the density of states (in the independent electron approximation). Probing the electron emission angle dependence in valence band photoemission, the angle (momentum)-resolved electronic band structure $E(\mathbf{k})$ can be investigated, which is the main principle of angle-resolved photoemission spectroscopy (ARPES). For that, PES spectra are measured for a series of emission angles θ, which can be realized by tilting the sample surface with respect to the analyzer, see Fig 3.5 (a). Such measurements rely on the fact the photoelectron momentum is conserved in the measurement process, as sketched in Fig 3.5 (c). The photoelectron momentum in vacuum is determined from the kinetic energy E_{kin} of the photoelectron

$$|\mathbf{p}| = \hbar|\mathbf{k}_f| = \sqrt{2mE_{\text{kin}}}. \tag{3.17}$$

It can be separated into a component oriented parallel to the sample surface $p_{\parallel} = \hbar k_{f,\parallel}$ and a component perpendicular to the sample surface $p_{\perp} = \hbar k_{f,\perp}$

$$\hbar k_{f,\parallel} = \sqrt{2mE_{\text{kin}}}\sin\theta \quad \text{and} \quad \hbar k_{f,\perp} = \sqrt{2mE_{\text{kin}}}\cos\theta, \tag{3.18}$$

where m is the free electron mass and θ is the electron emission angle with respect to the sample surface normal. Within the solid the excited photoelectron has the quasimomentum (or crystal momentum) $\mathbf{p}_i = \hbar\mathbf{k}_i$. Then, exploiting the quasimomentum conservation in a periodic crystal lattice, one can write

$$\mathbf{k}_f = \mathbf{k}_i + \mathbf{G} + \mathbf{k}_{ph}, \tag{3.19}$$

where **G** is a reciprocal lattice vector and $\mathbf{k}_{ph}$ is the incident photon momentum, which can be neglected at low photon energies since it is much smaller than the size of the Brillouin zone. As the symmetry of the crystal lattice is broken perpendicular to the surface, quasimomentum conservation holds for the electron momentum parallel to the surface and does not apply for the momentum component oriented perpendicular

$$k_{f,\parallel} = \frac{1}{\hbar}\sqrt{2mE_{\text{kin}}}\sin\theta = k_{i,\parallel} + G_{\parallel} + k_{ph,\parallel}. \tag{3.20}$$

In order to determine $k_{i,\perp}$, which is not conserved ($k_{i,\perp} \neq k_{f,\perp}$), one can model the surface as a potential step of size V_0 which the electron has to overcome [190]. Employing a free electron approximation for the photoelectron final states, $k_{i,\perp}$ is given by

$$k_{i,\perp} = \frac{1}{\hbar}\sqrt{2m(E_{\text{kin}}\cos^2\theta + V_0)}. \tag{3.21}$$

V_0, often referred to as inner potential, is typically treated as an empirical parameter which is adapted to the experimental spectra. Note that for angle-integrated measurements or in the case of one- or two-dimensional systems the determination of $k_{i,\perp}$ becomes irrelevant. Using Eq. 3.16, Eq. 3.20 and Eq. 3.21, the energy-momentum relations of electronic excitations can be inferred from the angle- or momentum-resolved energy distribution curves of a PES experiment. Therefore, photon-energy-dependent ARPES measurements are an effective way to probe the electronic structure in the 3D Brillouin zone. This capability is crucial for studying topological materials [191].

Probing Depth

An important parameter of ARPES is the incident photon energy. In the past years, the energy range of photons has greatly expanded due to the development of laser and synchrotron light sources. At present, the incident light used varies from vacuum ultraviolet (VUV) to soft and even hard x-rays. Among these, the most commonly used is VUV light. The universal curve of the inelastic mean free path (IMFP) of a photoelectron as a function of its kinetic energy [195] in Fig. 3.6 (a) shows that for incident photon energies above 20 eV in the VUV region, the IMFP is short (< 0.6 nm), which means that ARPES is an extremely surface-sensitive technique, and a ARPES signal is mostly representative of only the topmost surface layer of a sample. On the one hand, this surface sensitivity is an advantage when the aim is to probe surface states, such as those in topological insulators and Weyl semimetals. However, it requires ARPES experiments to be performed on atomically clean and well-ordered flat surfaces. To obtain a clean surface and to avoid surface contamination, samples are usually cleaved *in situ* and measured in ultrahigh vacuum (UHV) chambers, but even then, a freshly cleaved surface has a finite measurement lifetime. To obtain more bulk sensitive spectra the universal curve suggests either

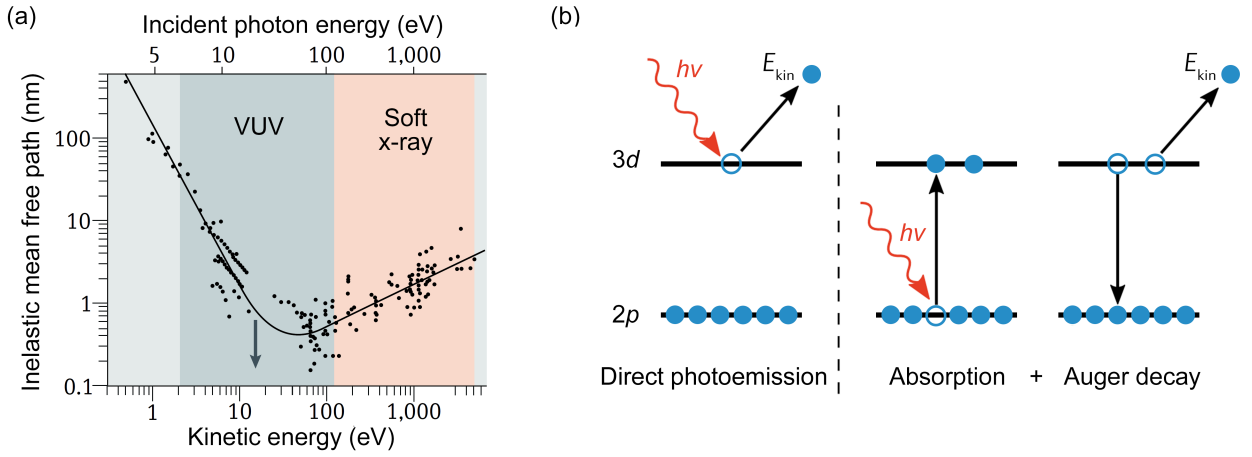

Figure 3.6: (a) The universal curve of the inelastic mean free path of photoelectrons as a function of kinetic energy (bottom axis) and incident photon energy (top axis; calculated on the assumption that materials have a typical work function of 4 eV and electrons are located at the Fermi level). Coloured regions correspond to the typical photon energy ranges of VUV and soft x-ray light (adopted from Ref. [191]). (b) Photoexcitation channels in resonant photoemission measurements at the $L_{2,3}$ absorption edge. The left panel shows direct photoemission from the $3d$ states. The right panel shows the two step process of absorption followed by an Auger decay. Note that for both processes the final state is identical.

to decrease or increase the energy of photoelectrons. The former can be achieved by using laser light excitation, however, the universality of IMFP for low energies is still under debate and a strong impact of the final state dispersion in this energy range complicates this approach. Another option is to employed the hard x-ray regime to increase the PES probing depth.

Resonant Photoemission Spectroscopy

Now, after we have discussed the basic aspets of PES, in particular ARPES, it is time to briefly introduce another special technique called resonant PES (ResPES), which we also employed in Chapters 5 and 6. ResPES allows for a selective enhancement of the photoemission signal from specific orbitals by tuning the photon energy to an appropriate absorption threshold, for example $2p \rightarrow 3d$ x-ray absorption threshold, i.e. $L_{2,3}$ edges. These kind of measurements are possible due to the availability of light sources with tunable photon energies over a wide spectral range at synchrotron radiation facilities discussed in section 3.2.1.

In the ResPES, additionally to the direct photoemission process, when the $3d$ electrons are excited by the photon beam and escape the solid as photoelectrons (see Fig. 3.6 (b)), another Auger-like channel: $2p$ core electron might be excited to a $3d$ level, the excited state may subsequently decay to the ground state by direct recombination which is accompanied by the emission of an Auger electron. It should be noted that the final states

of both channels are identical and the escaping electrons also have the same kinetic energy

$$\begin{aligned} 2p^6 3d^n &\rightarrow 2p^6 3d^{n-1} + e^- \qquad \text{(direct PES)}, \\ 2p^6 3d^n \rightarrow 2p^5 3d^{n+1} &\rightarrow 2p^6 3d^{n-1} + e^- \qquad \text{(Auger decay)}, \end{aligned}$$

where e^- denotes the ejected photoelectron. The probability amplitudes of both channels interfere quantum-mechanically (constructively or destructively) and depending on the exact photon energy can give rise to an enhanced $3d$ spectral weight. If the photon energy is increased above the absorption threshold, the coherence in the intermediate state $2p^5 3d^{n+1}$ is lost and the final states of the two channels differ. Thereby, the Auger decay becomes incoherent and does no longer interfere with the direct PES channel [196]. In general, the resonant photoemission intensity in second-order perturbation theory is given by the following expression

$$w = 2\pi \sum_f \left| \langle f | \mathcal{H}_R | i \rangle + \sum_m \frac{\langle f | \mathcal{H}_A | m \rangle \langle m | \mathcal{H}_R | i \rangle}{E_i - E_m + i\Gamma_m/2} \right|^2 \delta(E_f - E_i), \tag{3.22}$$

where $|i\rangle$, $|f\rangle$ and $|m\rangle$ are the initial, the final and the intermediate state, Γ_m is the life-time width of the core-exited state. H_R and H_A denote the radiative (photoabsorption) and Coulomb (Auger) contributions to the interaction, respectively. The first term in Eq. 3.22 represents the direct photoemission process, whereas the second term accounts for the Auger decay channel [197]. Evaluating the squared sum yields a mixed term between the two channels inducing the interference. It can be seen that the resonant behavior arises when the denominator of the second term tends to zero, which occurs when $E_i = h\nu + E_g$ (E_g is the energy of ground state) is equal to the E_m, in other words when the energy of the incident photon is equal to the difference in the energy between the intermediate and ground states, $h\nu = E_m - E_g$.

How effectively the resonant enhancement indeed works can be judged, for example, from the comparison of angle-integrated on- and off-resonance spectra of V $L_{2,3}$ in Fig. 5.11. Thus, one can analyze the partial density of states employing ResPES and selecting appropriate absorption edges.

3.2 Experimental aspects of XAS and XMCD measurements

Now, after we have discussed the theoretical aspects of x-ray absorption spectroscopy (XAS) and x-ray magnetic circular dichroism (XMCD), it is time to briefly review the experimental requirements for measuring XAS and XMCD spectra. Conceptually, x-ray absorption spectroscopy is a photon-in photon-out process and it can be described in three steps: (i) irradiation of a sample with photons, (ii) interaction of photons with matter, and

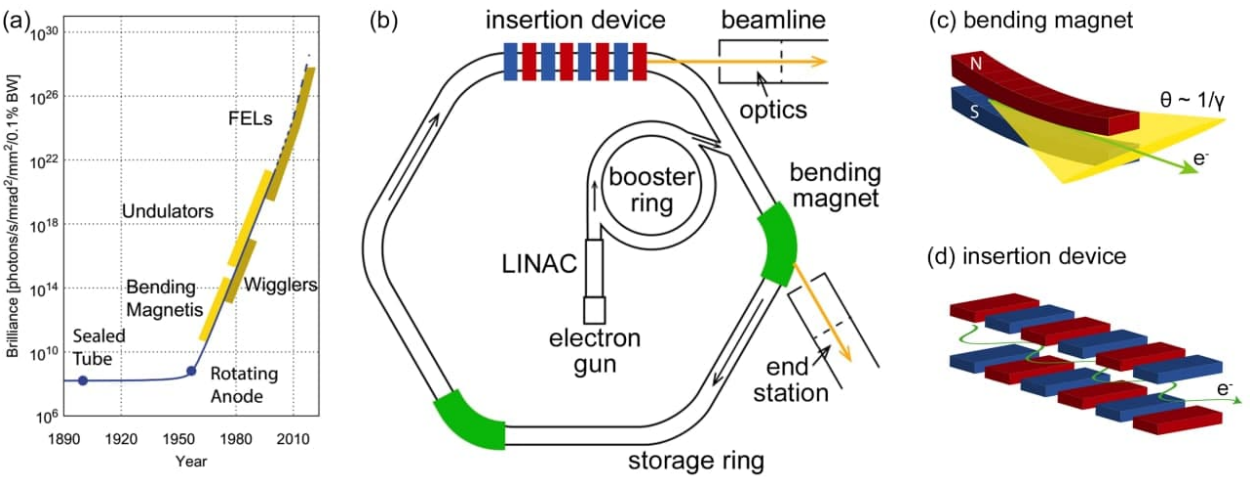

Figure 3.7: (a) The historical development of the brilliance of the available x-ray sources (adopted from Ref. [198]). (b) Schematic setup of a synchrotron radiation source with a listing of the main components: electron gun, linear accelareator (LINAC), booster ring, storage ring with bending magnets and other insertion devices, and the beamline including the optics and the experimental hutch. Electron trajectory and emission profile for (c) a bending magnet and (d) an insertion device (adopted from Ref. [199]).

finally (iii) collection of the emitted photons and analysis of their properties. The basic setup for these three steps is relatively simple and requires just three main components, namely a photon source, a sample, and a detector. Nevertheless, in the real experiment performing the aforementioned steps is a highly non-trivial task, and the listed setup components in reality constitute very complex devices, which have been in constant developments during the past decades.

The present section is meant to provide a brief description of the appropriate light source required for XAS and XMCD experiments, namely a synchrotron radiation source. After that we will give a more detailed description of the XMCD beamlines used for the investigations presented in this thesis: BOREAS beamline at the ALBA synchrotron radiation facility (Barcelona, Spain), UE46 PGM-1 beamline at BESSY II (Berlin, Germany) and I10 beamline at Diamond (Didcot, UK). Finally, we will discuss the common detection modes for XAS, namely transmission, electron yield and fluorescence yield modes.

3.2.1 Synchrotron radiation

The measurement of x-ray absorption spectra requires a source of high-intensity x-ray beams with tunable photon energy. In the case of $L_{2,3}$ edges of transition metals and $M_{4,5}$ edges of rare-earth elements the required spectrum ranges from about 400 to 1500 eV. Additionally, x-ray magnetic circular dichroism experiments require circularly polarized light with a high degree of polarization. These can only be achieved by the use of a synchrotron light source and is not feasible using a standard laboratory x-ray tube sources.

Several aspects of an x-ray source determine the quality of the x-ray beam it produces and these aspects can be combined into a single quantity, so called brilliance [170, 174]. The term "brilliance" collectively describes the spatial and spectral distribution of the photon flux and it is often used to compare different x-ray sources. Fig. 3.7 (a) shows such comparison of various x-ray sources, including laboratory sources (sealed tube, rotating anode) and the devices employed at synchrotrons (bending magnet, wigglers and undulators). Typically, the maximum brilliance from third generation undulators is about 10 orders of magnitude higher than from a rotating anode.

The fundamental parts of a typical modern synchrotron radiation source are sketched in Fig. 3.7 (b). To achieve the necessary high energies, the electrons must be accelerated in steps. First, electrons emitted from an electron gun are pre-accelerated in a linear accelerator (LINAC) to about 100 MeV. Then they are inserted in a booster ring, where they are further accelerated until they reach a kinetic energy typically of a few GeVs. Next, the relativistic electrons are injected periodically into a storage ring, which consists of arced and straight sections, as seen in Fig 3.7 (b). In the storage ring the huge numbers of electrons are accelerated using radio-frequency cavities and are kept in a stable orbit using various dipole and quadrupole magnets. Synchrotron radiation is emitted when a relativistic electron beam is deflected in arrays of dipole bending magnets (see Fig 3.7 (c)) placed at the arcs. These deflected relativistic electrons emit highly collimated light with an angular spread $\theta \sim 1/\gamma$ around the motion direction (tangential to their orbit in the storage ring), where Lorentz factor $\gamma = \mathcal{E}_e/mc^2$ is the electron energy in units of the rest mass energy, which is typically around 10^{-4}, or ~ 0.1 mrad.

In the modern (third-generation) synchrotrons there are periodic assemblies of magnets, called insertion devices (see Fig 3.7 (d)), that are placed in the straight sections of the storage ring. The insertion devices consist of arrays of dipole magnets that produce magnetic fields with alternating directions and force the electrons to follow an oscillatory path. Common insertion devices can be classified into two classes: a wiggler and an undulator. A wiggler can be considered as a series of bending magnets as the electron gets deflected similarly at each turn. In such a way, the intensity of generated radiation relative to a bending magnet is enhanced by a factor of $2N$, where N is the number of electron oscillation periods. In an undulator the electrons follow a less modulated path, such that the radiation from each oscillation period can overlap and constructively interfere, boosting the intensity further by a factor of N^2. Moreover, the use of undulators allows for excellent polarization tunability of the emitted x-rays by changing the lateral shift of different magnetic rails placed next to each other, such that shift of 0° gives linear polarization and 90° gives circular polarization. In order to tune the energy of emitted x-rays to the range of interest in an experiment, for example V or Cr $L_{2,3}$ edges, the amplitude of the electrons oscillation is modified by changing the gap between the magnetic dipole arrays [170, 198, 200].

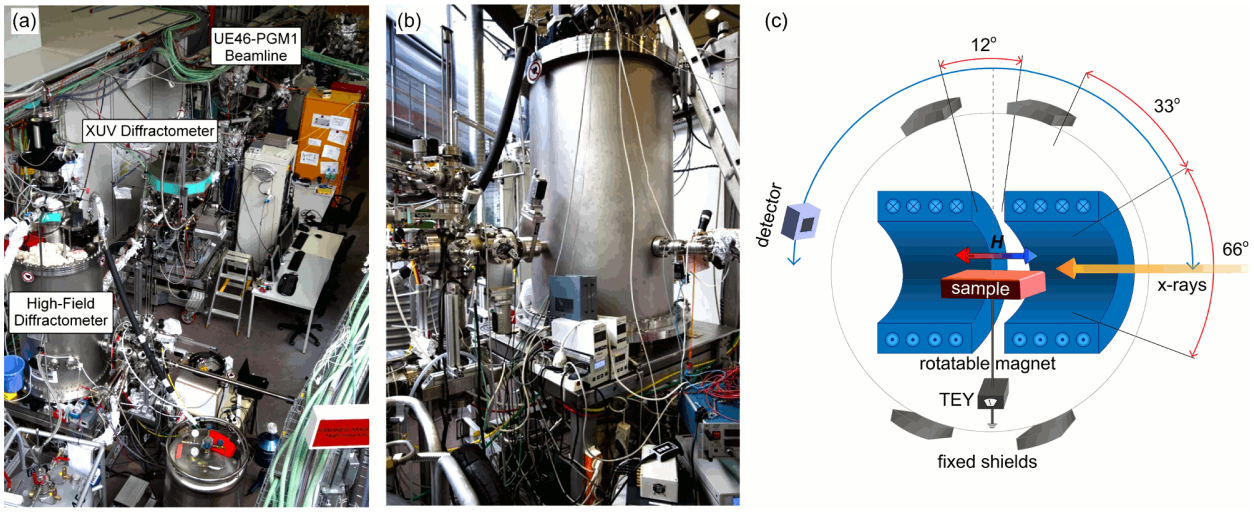

Figure 3.8: (a) Overview of beamline UE46 PGM-1 with the two endstations. (b) View of the High-Field Diffractometer and (c) experimental geometry of the UHV-chamber.

The radiation generated by the bending magnets or insertion devices further transported by specially designed front ends and beamlines to the experimental hatch in the experimental hall, where one conducts experiments. These beamlines have very different properties depending on the scientific questions to be studied. However, in most cases the front end of a beamline consists of several optical components for collimating and focusing the x-ray, including mirrors and a monochromator. Monochromator selects the desired wavelength of x-rays from the polychromatic beam. In the case of hard x-rays, the monochromator is based on crystal optics. The incoming beam is diffracted on a crystal and the wavelength of the diffracted beam is given by Bragg's law $n\lambda = 2d\sin(\theta)$. The energy of the x-ray beam can be varied by changing the angle θ between the beam propagation and the crystal surface. In the case of soft x-rays the wavelengths are much larger and crystals with large d-spacing are required. Therefore, for the soft x-rays artificial gratings are used instead of crystals [174].

Although various beamlines and experimental setups may share some similarities in their design and key components, they usually differ substantially in technical details depending on the scientific questions to be studied. In the present work, we mainly performed XAS and XMCD experiments on the diluted magnetic compounds in the soft x-ray region. Therefore, in the following subsection, as an example, we give a brief introduction to a design of the beamlines and end stations designed for such experiments.

3.2.2 Bessy UE46 PGM-1 beamline

Some of the XAS and XMCD measurements presented in this thesis (Chapters 5 and 7) were performed at the High-field Diffractometer of UE46 PGM-1 beamline (see Fig. 3.8) at BESSY II synchrotron facility located in Berlin, Germany. The beamline is equipped

with a plane grating monochromator with 1200 mm^{-1} grid and an APPLE2-type elliptical undulator with a tunable polarization. The combination delivers a resolving power $R = E/\Delta E$ of about 10^4 at photon energies ranging from 120 to 2000 eV.

The high-field diffractometer, used in this work, is one of the two stationary end stations available at the beamline (see Fig. 3.8 (a,b)). It is designed for XAS/XMCD and resonant soft x-ray scattering experiments in magnetic fields up to 7 Tesla at temperatures down to 4 K. The unique feature of the diffractometer is a superconducting magnet that can be rotated in vacuum independently from the sample, see Fig. 3.8 (c), which makes it perfectly suited for XMCD and XMLD experiments in various geometries [201].

The three-stage load lock system enables a fast and convenient transfer of the samples into a sample holder, directly attached to the cold finger of a liquid He flow cryostat, which provides temperatures down to 4 K. The end station operates under UHV conditions with typical base pressure in the load lock better then $2 \cdot 10^{-9}$ mbar and the pressure in the measurement chamber down to $5 \cdot 10^{-11}$ mbar. The last stage of the load-lock system can also be used as a preparation chamber for sample cleaving, annealing, or for a connection of a mobile vacuum suitcase.

The spectra are typically measured in total electron yield (TEY) mode, using the sample drain current normalized by the incoming photon intensity. The continuous-mode scans allow for absorption spectra with a very high signal-to-noise ratios ($\sim 10^4$) to be recorded just under 10 minutes or even less, depending on the absorption edge of interest. The XMCD spectra are then obtained by properly subtracting absorption data measured with left and right circular polarization.

3.2.3 ALBA BOREAS beamline

BOREAS (Beamline fOr REsonant Absorption and Scattering experiments) is a soft x-ray beamline dedicated to the study of the magnetic properties of materials by means of the techniques based on the dichroism in the absorption (XMCD and XMLD) or on the resonant scattering of x-rays. Like a Bessy UE46 PGM-1 beamline, it consists of two end stations.

BOREAS is based on a grating monochromator and covers a very extended photon energy range, from 80 eV to above 4000 eV, with high flux (10^{12} photons/s within 150–1000 eV range) and resolving power ($E/\Delta E > 10000$ for 80–1500 eV), together with full control of the x-ray beam polarization [204]. The degree of circular polarization is above 99.6% at all energies up to 1050 eV, which fully covers V, Cr and Mn $L_{2,3}$ absorption edges studied in this thesis. An x-ray absorption spectrum can be acquired routinely in 2–3 min with high accuracy and reproducibility (typically 100–200 eV wide with energy step smaller that 0.05 eV). The beam size at sample can be adjusted from about 100×100 um to 1×1 mm owing to vertical and horizontal refocusing mirror system.

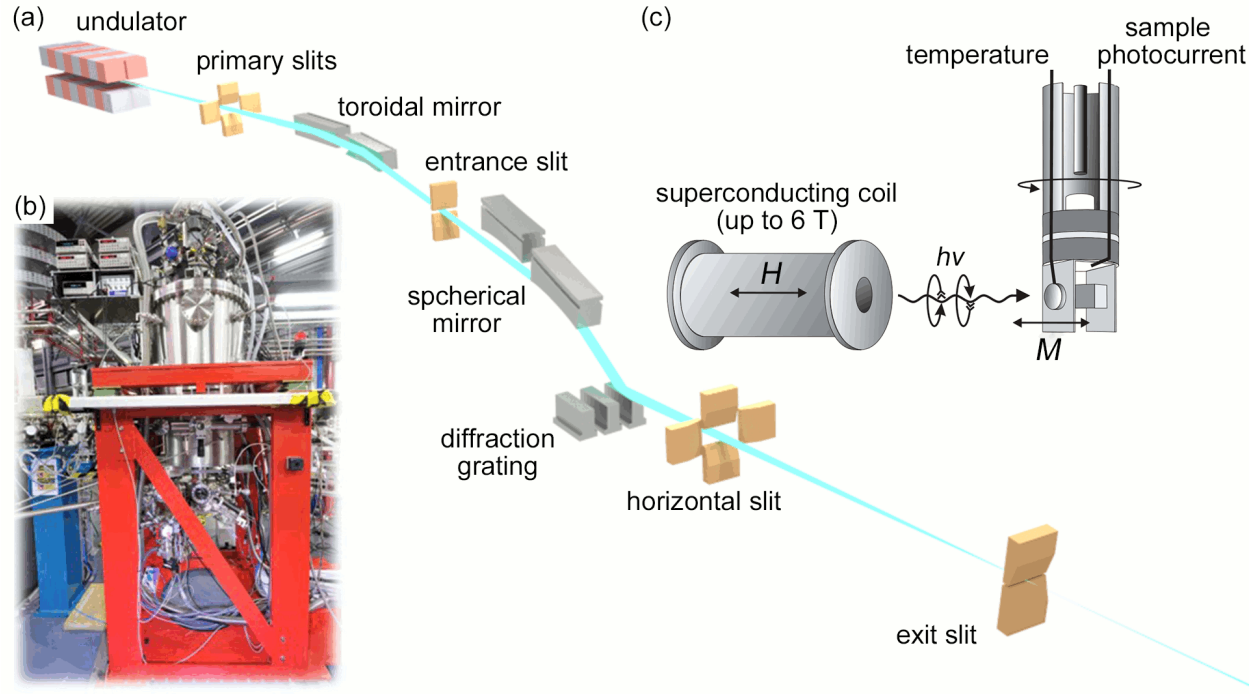

Figure 3.9: (a) Layout of the BOREAS beamline at the ALBA synchrotron light source facility. The blue line shows the beampath from the undulator via the optical components of the sample stage. (b) Photograph of the HECTOR end station. The layout and the photograph is adopted from Ref. [202]. (c) Experimental setup of the HECTOR UHV-chamber (adopted from Ref. [203]).

The optical layout of BOREAS is shown in Fig. 3.9 (a). It includes a white-beam section with a plane and toroidal mirror, a monochromator section with two spherical mirrors, three plane gratings, and an entrance and an exit slit.

The measurements presented in Chapters 4, 5 and 7 were conducted at the HECTOR (High fiEld veCTOR magnet) endstation shown in Fig. 3.9 (b). The end station operates under UHV conditions with a base pressure better than 10^{-10} mbar. The samples are mounted on a sample holder attached to the cold finger of a variable temperature cryostat (2–350 K). The sample insert is electrically insulated in order to perform drain current measurements, see Fig. 3.9 (c). The magnet consists of a set of three orthogonal superconducting split-coils allowing maximum fields of up to 6 T in the horizontal plane along the beam direction and 2 T in the horizontal and vertical plane perpendicular to the x-ray beam.

3.2.4 Diamond I10 BLADE beamline

The data presented in Chapter 6 was measured at the High Field Magnet end station at I10 BLADE (Beamline for Advanced Dichroism Experiments) beamline of Diamond Light Source [205]. BLADE delivers asoft x-ray beam in the energy range from 400 to 2000 eV.

Two APPLE II undulators produce photons with linear or circular polarisation. A high energy resolution $E/\Delta E > 7000$ is achieved using a plane grating monochromator.

The High Field Magnet end station operates under UHV conditions and equipped with a superconducting split-pair coil with a uni-axial magnetic field of 14 T along the incident beam direction. The sample can be cooled by variable temperature inserts down to 3 K.

3.2.5 Detection methods

In order to utilize the features of XAS, it is necessary to measure the photon energy-dependent absorption coefficient $\mu(E)$. There are various possibilities of doing so (see Fig 3.10) and depending on the measurement conditions and especially on the samples themselves, some of them may be more suitable than others.

According to the Eq. 3.1, the most obvious and direct way to determine $\mu(E)$ is to measure the transmitted x-rays intensity and relate it to the intensity of the incoming light for varying energies. This measurement mode is referred to as *transmission mode* and it is schematically sketched in Fig. 3.10 (a). The major advantage of transmission mode is that only it allows to measure the absolute absorption cross sections (see Eq. 3.7). Moreover transmission experiments are not exclusively sensitive to the surface only, but probe the entire sample, and there can be no effects due to yield variation [174, 206]. XAS experiments in transmission mode are standard for hard x-rays [174]. However, this measurement mode imposes serious technological challenges for most materials in the soft x-ray regime because of the stronger absorption of soft x-rays by matter [206], i.e. due to the short penetration length $\lambda_x = 1/\mu$ of soft x-rays of the order of $\sim$ 100 nm, which requires very thin samples. Moreover, the samples for transmission measurements need to be spatially homogeneous to avoid non-linear effects [206]. Usually no one works with free standing samples thinner than $\sim$ 1 micron. The thin films investigated here are thinner than 100 nm, but they are deposited on thick substrates, making the measurements in transmission mode not possible.

Alternatively, the absorption coefficient $\mu(E)$ can be determined using yield techniques, which take advantage of what occurs after an x-ray is absorbed, i.e. of secondary effects. When the core electron is excited by an absorbed x-ray photon into a valence shell leaving behind a core hole, the system is left in a highly exited state. The created core hole is unstable and it decays after certain lifetime (of the order of $\sim 10^{-15}$ s). The two dominant decay processes involve the emission of either a photon (radiative process) or an Auger electron (nonradiative process) which leave the atom in addition to direct photoelectron produced by continuum absorption. These two decay processes are competitive and strongly depend on the core-hole shell and the atomic number Z [208]. The detection of the emitted photons and electrons as a measure of the absorption coefficient is called

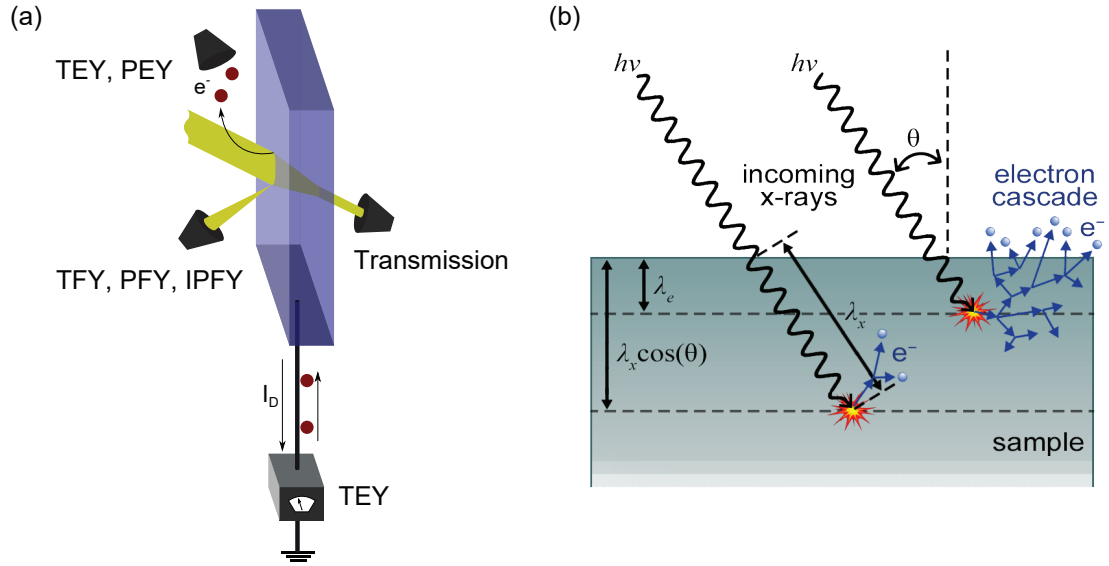

Figure 3.10: (a) Common detection modes for XAS that are described in the text. With the transmission detection one measures $\mu(E)$ by relating the intensity of photons that pass through the sample to the intensity of the incoming photons. In the electron yield modes (TEY and PEY) primary Auger or secondary electrons are detected. In the fluorescence yield modes (TFY, PFY and IPFY) emitted photons are detected. Adopted from Ref. [207]. (b) Qualitative description of the TEY detection mode. The length scales involved in the TEY detection are illustrated: electron escape (or sampling) depth λ_e, x-ray *penetration length* $\lambda_x(E) = 1/\mu(E)$ (also called the x-ray attenuation length) and x-ray *penetration depth* $\lambda_x \cos\theta$, where θ is the x-ray incidence angle from the surface normal.

the fluorescence yield (FY) and electron yield mode. In the present thesis we employed both detection modes. Therefore, we discuss them in more details.

Electron yield

In general, any process which is a true measure of the number of created in the absorption process core holes can be used for quantification of x-ray absorption spectroscopy, as the x-ray absorption cross section of an atom is proportional to the number of core holes [169, 209]. In the Auger decay process, the core hole created during the absorption is filled by an electron from a higher shell which is accompanied by the emission of a third (Auger) electron, see Fig. 3.10 (b). The energy of the emitted Auger electron is independent of the energy of the incoming photon. It will have a kinetic energy dependent on which levels are involved in the decay process [208]. Therefore, the number of emitted Auger electrons is proportional to the number of created core holes and simply by detecting these Auger electrons as the incident x-ray energy is scanned one can obtain an XAS spectrum. From the universal curve shown in Fig. 3.6 (a) one can find that, for instance, 500 eV Auger electron has the mean free path of $\sim 10-20$ Å, which is much shorter than the x-ray penetration length (λ_x in Fig. 3.10 (b)) into the sample. So the Auger electrons deliver information from the topmost $\sim$ 10 – 20 Å, which makes the electron yield a

very surface sensitive method. Note that Auger electrons can be directly detected as they are emitted from the sample surface (after overcoming the work function), by using a channeltron electron multiplier [111]. In this way, when emitted electrons of a particular kinetic energy are selected, detection method is called partial electron yield (PEY) or, alternatively, Auger electron yield (AEY).

Additionally, the scattering of the primary Auger electron in the sample produces secondary electrons resulting in a cascading electron avalanche, as depicted in Fig. 3.10 (b). When all electrons, including primary photoelectrons, Auger and secondary electrons escaping from the sample surface are collected regardless of their energy, the detection method is known as total electron yield (TEY). Often TEY is conveniently obtained by measuring the electric current draining from the sample to the electrical ground by means of a picoammeter, as sketched in Fig. 3.10 (a). Primary electrons contribute the least to the TEY signal, which is dominated by secondary electrons. Hence, the TEY method takes advantage of the avalanche of low kinetic energy secondary electrons produced through inelastic electron-electron scattering from the primary high-energy Auger electrons. The emission of electrons may be facilitated by an electric field, for example, by applying a negative voltage on the sample with respect to ground. The strong secondary electron emission and the easiness of their detection renders TEY as the preferred and most widely used detection method in the soft x-ray range. Since the creation, migration, and escape of secondary electrons are highly material-dependent, the probing depth[1] and related surface sensitivity of TEY is certainly also material-dependent. It is typically estimated taking the AEY probing depth as the lower boundary and $\sim$ 10 nm as the upper boundary. For example, in case of Ni L_3 edge (853 eV) in Tb/Ni(110) the mean probing depth of 25 Å was estimated [210], while for the same edge in Dy/Ni(110) it was found to be 60 Å [211]. For O K edge in Ta_2O_5 the mean probing depth was estimated around 19 Å [210].

As we have already mentioned above, it is common and more convenient to measure the sample drain current instead of collecting the elections emitted from the sample. This is the method that we used for our measurements. To determine the absorption coefficient from the drain current, the relation between these two quantities must be known. This relationship depends on the various length scales of the sample, as well as on measurement geometries. The two important length scales are the x-ray penetration depth $\lambda_x \cos\theta$ and the electron escape (or sampling) depth λ_e, as illustrated in Fig. 3.10 (b). It has been quantitatively demonstrated that TEY is linearly proportional to the $\mu(E)$ if the electron escape depth is much smaller that the x-ray penetration depth, i.e when $\lambda_e \ll \lambda_x \cos\theta$, where $\lambda_x = 1/\mu$ is the x-ray penetration length [166, 169, 212]. This length depends strongly on the photon energy. For Fe $L_{2,3}$ resonant edges it ranges between $\sim$ 6000 Å in the

[1] Assuming that the contribution from layers below the sample surface decays exponentially toward the bulk, one typically defines the probing depth as the average length from which the fraction $1-(1/e) \approx 2/3$ of the total signal originates [169].

pre-edge and 800 Å in post-edge region [169]. If $\lambda_e \gg \lambda_x \cos\theta$, all incident photons will be converted into photoelectrons and TEY will be proportional only to the incident photon intensity I_0 and not to the $\mu(E)$, resulting in the completely saturated signal. When λ_e is comparable to $\lambda_x \cos\theta$, the intensities of the largest absorption peaks are reduces compared to the rest of the spectrum. This is known in literature as the saturation effect [111, 169, 209]. Note that as the x-ray incident angle θ increases, approaching more grazing incidence, the x-ray penetration depth $\lambda_x \cos\theta$ is reduced, resulting in larger saturation effect at grazing angles as compared to normal incidence.

Fluorescence yield

Besides the Auger decay, the fluorescent decay of the core hole can be also used to determine the x-ray absorption coefficient. In the fluorescent decay process, a core hole is filled by the valence or shallow core electron with emission of a photon whose energy corresponds to the energy difference of the levels. Detection of such photons as a measure of $\mu(E)$ is then called fluorescence yield (FY). As with electron yield, FY may be measured in total or partial modes. If all emitted photons are detected, the method is called total fluorescence yield (TFY), whereas if only photons of certain energy are detected, it is called partial fluorescence yield (PFY). FY is usually measured with a photodiode placed close to the sample, as illustrated in Fig. 3.10 (a). PFY measurements requiring an energy-selective detector to register photons only within a certain energy range.

The amount of fluorescent decay increases with energy and a comparison with the Auger decay shows that the latter is dominant for all core levels below 1 keV [174]. In $3d$ metals, the probability for a $2p$ hole to decay via Auger process is more than 99% [111, 213], whereas the K edges show strong fluorescence. Since inelastic interaction of photons with matter can be neglected, the mean free path of the photon created in the fluorescent decay is of the same order of magnitude as that of the incoming x-ray. For metals in the soft x-ray range, it is typically of the order of $\sim$ 100 nm, leading to probing depths larger than for electron yields. That is why TFY detection is regarded as a bulk-sensitive method.

However, FY is very susceptible to certain types of distortions, which make it a nonlinear function of the absorption coefficient. One of such distortions is due to the saturation effects, which commonly occur for the systems with high concentration of the absorbing elements or when the specific edge absorption is very strong compared to the background absorption (see Fig. 3.1). In such case, the x-ray penetration length is less than or of the order of the escape depth. Since FY has larger escape depth, it is more prone to saturation than TEY. As a result, the highest peaks in the FY spectra appear suppressed with respect to the lower peaks, making the data mostly unusable. As for diluted systems,

FY detection is in general found to be a good measure of the x-ray absorption coefficient [208, 213].

Another issue of FY is so-called self-absorption [213], which occurs when emitted photons are reabsorbed by sample on their way to the detector. This leads to a reduction of the recorded signal. When the fluorescent decay of a core hole takes place at the energy which is strongly reabsorbed, the FY spectral shape will be distorted in a rather complicated manner with the distortion varying at different parts of the XAS spectrum. This kind of distortions are less understood than saturation and are very difficult to correct for.

Finally, it has been shown that FY spectra differ from the "true XAS spectra" not only due to saturation effects and self-absorption, but also due to the inherently built-in distortions of the fluorescence decay process [213, 214]. The reason behind these distortions is a large variation in the fluorescence decay depending on the symmetry of the final state in the absorption process, since fluorescence decay is governed by electric-dipole transitions, which are strongly state dependent [111]. Hence, the fluorescence decay strongly varies over the spectrum, which in case of $2p$ XAS results in the L_2 edge having stronger fluorescence than the L_3 edge [174, 213].

Apparently, saturation and self-absorption effects together with the intrinsic distortions make the FY rather unsuitable for the quantitative analysis using the sum rules [111, 214], which are discussed in Section 3.4.

Recently, a new method to measure the absorption coefficient, which is also bulk sensitive but free of saturation or self-absorption effects, has been introduced [215, 216]. This method, called inverse partial fluorescence yield (IPFY), also measures fluorescence photons, but here the non-resonant x-ray emission from a different element with a lower energy edge than the absorption edge under investigation, is detected. So, essentially, one uses secondary atoms as a set of x-ray transmission detectors dispersed throughout the sample. The inverse of this signal is shown to be proportional to the absorption cross-section and free of self-absorption or saturation effects [215]. However, this method is not always applicable, since it requires an available lower energy edge, that is sufficiently apart from the absorption edge of interest.

3.3 XMCD data acquisition and evaluation

As we showed in Section 3.1.2 the XMCD spectrum is obtained by the substraction of the two XAS spectra measured with different circular polarization of x-rays, i.e. $I_{\mathrm{XMCD}} = I_{\mathrm{left}} - I_{\mathrm{right}}$. In general, the intensity of the XAS spectra depends on the photon flux at the beamline, the absorption cross section of the relevant element and the fraction of this element in the sample volume that is probed with the given detection method (see Section 3.2.5). At the same time, the size of the XMCD signal relative to the intensity

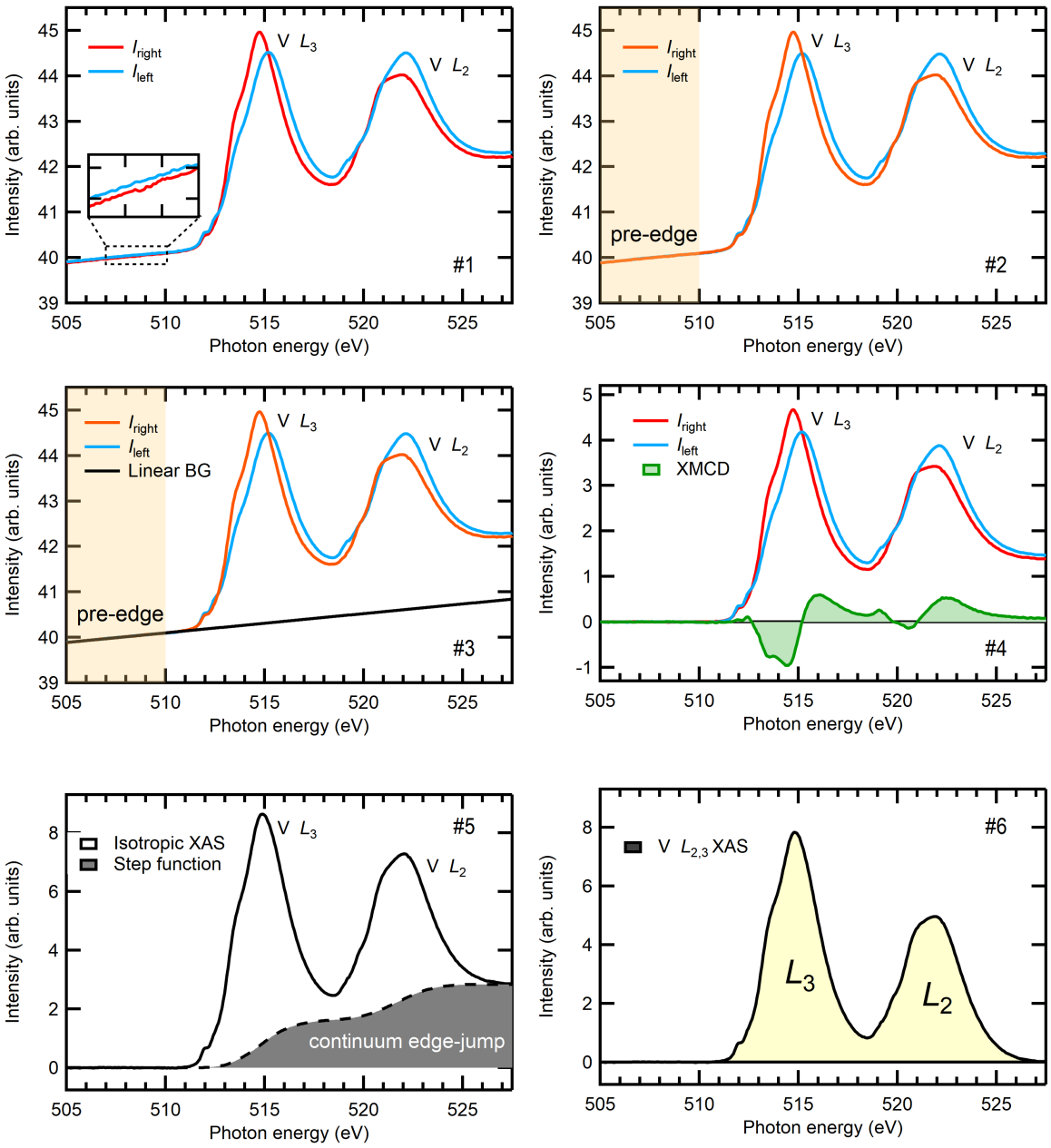

Figure 3.11: Illustration of the XAS and XMCD data evaluation. The case of V-doped $(Bi,Sb)_2Te_3$ magnetic topological insulator is shown as an example. The data is acquired at remanence and low temperature $T \sim 5$ K. The evaluation procedure is discussed in the main text.

of the isotropic XAS spectrum depends on the magnitude of sample magnetization, the degree of circular photon polarization and the angle θ between the photon propagation direction and the sample magnetization direction, see Fig. 3.10 (b). The photon flux and the degree of circular polarization was not the issue at the beamlines used to measure XAS/XMCD in the present work. Also the cross sections of the elements probed here were high enough. Furthermore, the investigated magnetic topological insulators have high magnetization and were mostly measured at normal incidence geometry. Therefore, neither the signal-to-noise ration of XAS spectra, nor the intensity of the XMCD signal

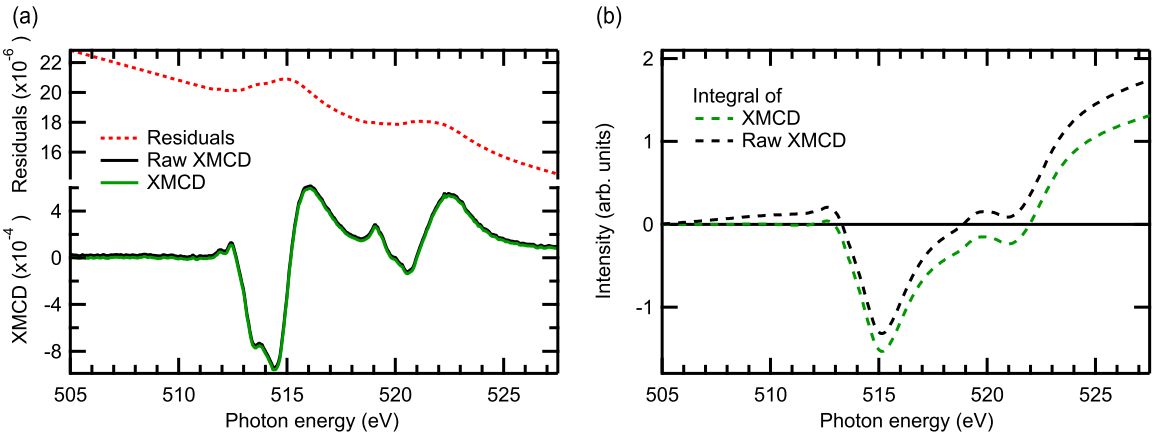

Figure 3.12: (a) Comparison of the XMCD spectra before (black curve) and after corrections (green curve). (b) Comparison of the integral of XMCD spectra before corrections with the integral of raw XMCD signal.

was of serious concern in the current work.

Generally speaking, the experimental conditions at which the data is acquired, such as the magnitude of applied magnetic field, temperature of the sample, as well as the angle of incidence, which can be varied at the experimental end station, are essential. Many important conclusions about the physical properties of the sample can be drawn by analyzing the XMCD data measured in dependence of these conditions. Therefore, in the current work we widely employed them.

After the acquisition of the experimental XAS/XMCD data, it is important to correctly analyze and present it for the further sum rule analysis and MLFT simulations. The relative alignment of the two XAS spectra, I_{left} and I_{right}, considerably affects their difference, I_{XMCD}. A misalignment of the spectra can result in spurious spectral features. The relevant for us source of misalignment is the relative shifts in energy and intensity, as well as a scaling between to spectra. If the spectra are shifted in energy relative to each other, a derivative-like difference is obtained, which can be confused with a real XMCD signal. This is especially important for weakly magnetized samples with small XMCD signals and/or for measurements at high temperatures close to the critical one. The energy shift may occur due to a bad reproducibility of the monochromator position during the subsequent measurements or/and due to the thermal drifts altering the characteristics of the beamline. If there is a relative shift in the intensities of the two spectra, it can result in a constant difference signal that is superimposed on the true XMCD. Another source of the offset in the intensities is a contamination of the sample surface, that might contribute to the XAS signal as a constant continuum background. Contamination can produce a time-dependent change of the background intensity. The acquisition of XAS spectra consecutively in quartets (I_{left}, I_{right}, I_{right}, I_{left}) or even octets can help to average out potential time-dependent changes. Therefore, we recorded the spectra in that manner.

In the following, we illustrate in Fig. 3.11 the analysis of XAS spectra using as an

example the absorption at V $L_{2,3}$ edges of the magnetically doped topological insulator V:$(Bi,Sb)_2Te_3$ discussed in Chapters 4 and 5. Data for other systems were analyzed in a similar manner. The spectra of V were recorded at remanence ($B \sim 0.02$ T) and low temperature ($\sim$ 5 K) in TEY mode, under normal incidence conditions. Therefore, no TEY saturation effect corrections were required (see Section 3.2.5). The normal incidence also assures a maximum XMCD signal, as the easy axis of the system is along the *c*-axis (normal to the film surface). The objective of this detailed description of the evaluation procedure is, on the one hand, to ensure the transparency of the data shown in the following chapters, and to emphasize the care that must be taken to obtain reliable results, on the other.

(i) First of all, the absorption spectra measured in TEY mode are always normalized to the incoming photon flux I_0, which usually shows an energy and time dependence. I_0 is usually measured by the absorption of a gold mesh reference placed in front of the sample. In this way one accounts for synchrotron- or energy-dependent variations of the photon flux. Panel #1 in Fig. 3.11 shows XAS spectra for left- (blue curve) and right-circularly (red curve) polarized x-rays after the normalization to I_0.

(ii) Next, the offset between two spectra along the y-axis, indicated in the inset of panel #1, is corrected. The effect of such an offset can be seen in Fig. 3.12, where it results in a slight intensity shift of the raw XMCD spectrum (black curve). Offset correction is critical to the application of the sum rules, especially the orbital sum rule, in which the XMCD spectrum is integrated. If the XMCD spectrum is shifted, then this introduces an additional slope into the integrated XMCD spectrum, as shown in Fig. 3.12 (b). The offset corrections cannot be performed by just subtracting the shift in the y-axis, one has to find the multiplicative relation between the two spectra. In the following, be briefly show the correction procedure.

The measured XMCD signal is given by $I_{\mathrm{XMCD}} = k^- I_{\mathrm{left}} - k^+ I_{\mathrm{right}}$, where k^- and k^+ are the constants defining the proportionality of the TEY signal and the absorption signal. On the other hand, the polarization-averaged absorption spectrum is given by the $I_{\mathrm{XAS}} = (I_{\mathrm{left}} + I_{\mathrm{right}})/2$ and the true XMCD is $\mathrm{XMCD} = I_{\mathrm{left}} - I_{\mathrm{right}}$. Hence, one can isolate the $I_{\mathrm{left}} = I_{\mathrm{XAS}} + \mathrm{XMCD}/2$ and the $I_{\mathrm{right}} = I_{\mathrm{XAS}} - \mathrm{XMCD}/2$. Finally, one can write $I_{\mathrm{XMCD}} = (k^- - k^+) I_{\mathrm{XAS}} + \frac{k^- + k^+}{2}\mathrm{XMCD}$. If the constants k^- and k^+ are equal, then there will be no offset observed in the measured XMCD signal. However, if they are different, then the fraction of I_{XAS} will be added to the measurements. This can be clearly seen in Fig. 3.12 (a), where the residuals (red curve) between raw and corrected XMCD signal resemble the XAS spectrum. Thus, the correction of the XMCD signal is given by the following expression $\mathrm{XMCD} = I_{\mathrm{XMCD}}(E) + c I_{\mathrm{XAS}}(E)$. Since XMCD only occurs at resonant energies, the correction factor c is evaluated such that $\int_{pre-edge} (I_{\mathrm{XMCD}}(E) + c I_{\mathrm{XAS}}(E))\, dE$ in a defined pre-edge region (sometimes pre- and post-edge regions) becomes minimized. The pre-edge region is denoted by an orange background color in panel #2 of Fig. 3.11.

(iii) The next step is the subtraction of the linear background by fitting the spectra in pre-edge region with a linear function, as seen in panel #3 of Fig. 3.11. In this way, one obtains a pair of absorption spectra I_{left} and I_{right} together with the corresponding XMCD spectrum, as illustrated in panel #4. The resulting XMCD spectrum (green curve) is ready to be used in the sum rule analysis.

(iv) For the application of the sum rules one also needs total XAS spectrum, i.e. $I_{\text{left}} + I_{\text{right}}$. It is necessary to separate the resonant absorption intensity due to the dipole transition we are interested in, $2p \rightarrow 3d$, from transitions into higher unoccupied states or into the continuum, appearing in the XAS spectrum as the continuum edge-jump, see panel #5 of the Fig. 3.11. In the case of the $3d$ transition metals, the latter can be described by an *ad hoc* two step-like function. The simulation of the continuum edge-jump remains, however, rather arbitrary and approximative, which can result in systematic errors in the estimated spin and orbital magnetic moments. As a two-step-like function one can use the theoretical off-resonant absorption spectrum provided by Chantler [217], scaled to match with the measured XAS spectrum at pre- and post-edge regions. Alternatively, one can use a Shirley background [218]. After correcting for the continuum edge-jump, the total XAS spectrum shown in panel #6 can be further used in sum rule analysis or in comparison with the theoretical spectra simulated by MLFT cluster calculations. The general idea of the sum rules is discussed in Section 3.4, and the specific details of the application of the sum rules are given in the corresponding experimental sections of the thesis. An example for the application of the sum rules is given in Fig. 5.10 for the case V $L_{2,3}$ of doped MTI and in Fig. 7.13 for Mn $L_{2,3}$ of intrinsic MTI. One can also normalize the XMCD spectrum in panel #4 to the total XAS spectrum in panel #6 in order to obtain the sample magnetization information on a per atom basis. Moreover, these two spectra can be used for the XMCD asymmetry analysis discussed in Chapter 7.

Finally, in Fig. 3.12 (a) we show the XMCD spectum before (black curve) and after (green curve) the corrections, together with the difference between the two (red curve). Although one might think that the difference between them is insignificant and could be neglected, Fig. 3.12 (b) illustrates the considerable change in the integrals of the spectra, which can introduce significant error in the magnetic moments estimated by the sum rule, especially the orbital moment.

3.4 Magneto-optical sum rules

Previously we have qualitatively discussed the basic principles of the XMCD. However, the considerations made so far can be developed further to acquire quantitative information from XMCD and XAS spectra, such as the ground-state expectation values $\langle L_z \rangle$ and $\langle S_z \rangle$ and, thus, the respective magnetic moments μ of the valence shell. In Section 3.5 we will discuss one of such approaches based on the comparison of calculated within

multiplet ligand-field theory (MLFT) XAS and XMCD spectra with the measured spectra. We will show how based on such comparison one can deduce information about operator values of the ground-state of the system under consideration. This actually implies that all interactions that influence the ground-state and the spectrum are incorporated correctly, which is far from trivial. Often it becomes quite hard to get a good fit to the experimental spectra within the MLFT calculation: It becomes even harder when the system has a symmetry lower than octahedral (O_h) and therefore more parameters to model the crystal field (and covalency) should be considered in calculations. Fortunately, besides the MLFT calculations there is another method to derive information from XAS and XMCD spectra. B. T. Thole, P. Carra *et al.*. [219, 220] have derived sum rules that relate the integrated XAS and XMCD spectral weights of a specific shell to expectation values of some operators of the ground state. These relations are very powerful since they are simple and ready to use.

The first magnetic sum rule, derived by Thole *et al.* in 1992 [219], relates the integrated signal of the XMCD to the ground state expectation value of the orbital magnetic moment, $\langle L_z \rangle$. In 1993 Carra *et al.* [220] derived a second sum rule for XMCD, spin sum rule, which relates the branching ratio of the XMCD to the expectation value of the spin magnetic moment, $\langle S_z \rangle$, and the magnetic dipole term, $\langle T_z \rangle$, in the ground state. Experimentally, the sum rules have been first confirmed by Chen *et al.* [221] for the transition metals iron and cobalt.

The derivation of the sum rules relies on several approximations and their application is only possible under certain assumptions, which we will discussed later in this section. In the following we discuss spin and orbital sum rules in more details.

3.4.1 Spin and orbital sum rule

The original sum rules have been derived within a localized picture, i. e. single ions in a crystal field with a partially field valence shell [219, 220, 222]. Later they have been rederived within a one-electron approximation [223]. It has been shown that the sum-rules are an intrinsic property of the dipole operator. They do not depend on the assumptions made on the local symmetry and they are independent of the framework in which one is working, namely, many-electron theory or one-electron theory [177, 224]. While the theoretical derivation of the magnetic sum rules in a general way is sophisticated and is thus not reproduced here, their application and the resulting formulas are rather simple. In its form for general edges as developed by Thole and Carra the orbital sum rule is

$$\frac{\int_{j^+ + j^-} dE(I^+ - I^-)}{\int_{j^+ + j^-} dE(I^+ + I^- + I^0)} = \frac{1}{2} \frac{l(l+1) + 2 - c(c+1)}{l(l+1)(4l + 2 - n)} \langle L_z \rangle, \tag{3.23}$$

and the spin sum rule is

$$\frac{\int_{j^+} dE(I^+ - I^-) - [(c+1)/c]\int_{j^-} dE(I^+ - I^-)}{\int_{j^+ + j^-} dE(I^+ + I^- + I^0)} = \frac{l(l+1) - 2 - c(c+1)}{3c(4l+2-n)}\langle S_z\rangle + \frac{l(l+1)(l(l+1) + 2c(c+1) + 4) - 3(c-1)^2(c+2)^2}{6lc(l+1)(4l+2-n)}\langle T_z\rangle, \quad (3.24)$$

where c is the orbital quantum number of the initial state and l the one of the final state, $\langle S_z\rangle$, $\langle L_z\rangle$, $\langle T_z\rangle$ are the expectation values of the spin operator, orbital operator, and the magnetic dipole operator, respectively. $\langle T_z\rangle$ corresponds to the asphericity of the charge density of the l valence shell and cannot be separated from $\langle S_z\rangle$. Later on, we will show how one can estimate $\langle T_z\rangle$. The number of unoccupied final states in the valence shell which contains n electrons is given by $n_h = (4l + 2 - n)$. The two spin–orbit split edges are denoted by j^+ and j^-. The $I^\pm$ are normalized cross-sections for left/right polarized photons propagating perpendicular to the magnetization axis, and I^0 for linear polarization parallel to the magnetization. In experimental spectra, we usually measure the left and right polarized spectra only, therefore we use the $I^+ + I^- + I^0 \approx 3/2(I^+ + I^-)$ approximation. Note that $I^\pm$ are normalized such that $I^\pm_{j^\pm}(E) = \frac{1}{4\pi^2\alpha\hbar\omega}\sigma^\pm_{j^\pm}(E)$, see Eq. 3.7.

For different absorption edges, the sum rules exhibit different numerical factors, whereas the general structure of the equations is always the same. The orbital sum rule states that the integral of the XMCD spectrum over both spin–orbit-splitted absorption cross sections $j^\pm$ is proportional to the orbital magnetic moment $m_{\text{orb}} = -\langle L_z\rangle$. The spin sum rule yields that the spin moment $m_{\text{spin}} = -2\langle S_z\rangle$ is obtained from the difference of the integrated signals of two separated, spin–orbit-splitted absorption cross sections. The sum rules yield the magnetic moment per atom. In the present thesis results of the application of the sum rules to experimental data are given in units of Bohr magnetons μ_B.

Eqs. 3.23 and 3.24 become more accessible when considered for specific edges. The magnetic properties of $3d$ transition metals, such as V, Cr and Mn, investigated in the thesis are probed at the $L_{2,3}$ absorption edges ($2p \rightarrow 3d$ transition). Using $c = 1$ and $l = 2$ for $L_{2,3}$ edges the sum rules become readily

$$\langle L_z\rangle = 2n_h \frac{\int_{L_3+L_2} dE(I^+ - I^-)}{\int_{L_3+L_2} dE(I^+ + I^- + I^0)},$$

$$2\langle S_z\rangle + 7\langle T_z\rangle = 3n_h \frac{\int_{L_3} dE(I^+ - I^-) - 2\int_{L_2} dE(I^+ - I^-)}{\int_{L_3+L_2} dE(I^+ + I^- + I^0)}. \quad (3.25)$$

For the sum rule analysis, Chen *et al.* [221] introduced the alternative notation

$$p = \int_{L_3} dE(I^+ - I^-), \quad q = \int_{L_3+L_2} dE(I^+ - I^-), \quad r = \int_{L_3+L_2} dE(I^+ + I^-), \tag{3.26}$$

which together with the assumption $I^+ + I^- + I^0 = 3/2(I^+ + I^-)$ rewrites the sum rules as

$$m_{\text{orb}} = -\langle L_z \rangle = -\frac{4}{3}\frac{q}{r} n_h, \quad m_{\text{spin}} = -2\langle S_z \rangle = -\frac{6p - 4q}{r} n_h C + 7\langle T_z \rangle. \tag{3.27}$$

Here we also introduced a correction factor C, which will be discussed later.

As one can notice, in order to apply sum rule analysis, the value of n_h is required. Sometimes, the ambiguity in the definition of the number of $3d$ holes might introduce uncertainty in the estimated m_{spin} and m_{orb}. Therefore, Wu *et al.* [225] proposed to use the ratio of the orbital and spin sum rules

$$\frac{\langle L_z \rangle}{2\langle S_z \rangle + 7\langle T_z \rangle} = \frac{2}{3} \frac{\int_{j^+ + j^-} dE(I^+ - I^-)}{\int_{j^+} dE(I^+ - I^-) - 2\int_{j^-} dE(I^+ - I^-)} \tag{3.28}$$

or

$$\frac{m_{\text{orb}}}{m_{\text{spin}} - 7\langle T_z \rangle} = \frac{1}{(9/2)(p/q) - 3}. \tag{3.29}$$

In this way the orbital to spin magnetic moment ratio is expressed as a function of only the branching ratio, p/q, of the XMCD signal. In this ratio, uncertainties of the number of holes n_h and the degree of circular polarization (assumption that $I^+ + I^- + I^0 \approx 3/2(I^+ + I^-)$) cancel out.

As for the $M_{4,5}$ edges ($3d \rightarrow 4f$ transition) of rare earth elements, like Eu studied in Chapter 6, $c = 2$ and $l = 3$ and the sum rules read

$$\begin{aligned} \langle L_z \rangle &= 3n_h \frac{\int_{M_5+M_4} dE(I^+ - I^-)}{\int_{M_5+M_4} dE(I^+ + I^- + I^0)}, \\ \frac{2}{3}\langle S_z \rangle + \frac{1}{2}\langle T_z \rangle &= n_h \frac{\int_{M_5} dE(I^+ - I^-) - \frac{3}{2}\int_{M_4} dE(I^+ - I^-)}{\int_{M_5+M_4} dE(I^+ + I^- + I^0)} \end{aligned} \tag{3.30}$$

or

$$m_{\text{orb}} = -\langle L_z \rangle = -\frac{2q}{r} n_h, \quad m_{\text{spin}} = -2\langle S_z \rangle = \frac{5p - 3q}{r} n_h C + 6\langle T_z \rangle. \tag{3.31}$$

The practical illustration of the sum rules application for $L_{2,3}$ edges of $3d$ transition metals can be seen in Fig. 5.10, while for the $M_{4,5}$ edges of rare earth element it can be seen in Fig. 6.3.

3.4.2 Limitations of the sum rules

Deriving the sum rules Thole and Carra made several assumptions, which need to be well understood if one wishes to apply the sum rules carefully [226, 227]. The most important assumptions (especially for $L_{2,3}$ and $M_{4,5}$ edges) are discussed in the following.

(i) First of all, dipole-allowed transitions $c \rightarrow l = c - 1$ have been neglected. For $3d$ transition metal compounds, for example, this would be $2p \rightarrow 4s$ transitions. A mixture of the two transition channels will hinder the application of the sum rules. Unfortunately, in the x-ray absorption spectra the contributions from the two channels cannot be separated. However, comparing the radial matrix elements for $2p \rightarrow 3d$ and $2p \rightarrow 4s$ transitions, one finds $\frac{||\langle 4s|r|2p\rangle||^2}{||\langle 3d|r|2p\rangle||} \approx 1/50$ ratio, which means that transitions into d-like final states are dominant and account for 98% of the absorption process at the $L_{2,3}$ edges [226, 228]. This allows for applying the sum rules considering entirely $2p \rightarrow 3d$ transitions.

(ii) A second approximation concerns the fact that the sum rules are derived based on the assumption that transitions occur between a pure $c^{4c+2}l^n$ initial configuration and a pure $c^{4c+1}l^{n+1}$ final configuration, which are $2p^6 3d^n$ and $2p^5 3d^{n+1}$ for the case of $L_{2,3}$ edges. However, the initial and final states in principle can not be described by pure configurations, and configuration interactions should be considered. It has been argued by Thole *et al.* that configuration interactions, at least in case of Gd and Ni, should not change the conclusion concerning the sum rules significantly [229].

(iii) Next simplifying assumption by theory is that energy dependence of the wave functions has been neglected. In particular, it is assumed that the radial matrix elements are constant over the absorption edge, which is not exactly true. Indeed, the radial matrix element is energy- and spin-dependent and needs to be considered when using the sum rules [230]. Wu *et al.* showed that the radial matrix integrals at the Ni $L_{2,3}$ in the metal vary linearly with photon energy from the bottom to the top of the d band by 30% due to a change in spin–orbit interaction [225]. Since this change is proportional to the $\langle L_z \rangle$, the effect on the orbital sum rule is not dramatic. However, the effect on the spin sum rule can be larger [225, 226]. Such effects are usually absent in the strongly localized f shell of the rare earths, which have narrow band widths.

(iv) So far we have been only dealing with electric dipole transitions. Higher-order transitions, such as electric quadrupole transitions, usually have very small contributions to the cross-sections and can be safely neglected. However, for magnetic dichroism, the electric quadrupole terms can be large, like in the case for the $3d$ transition metals K edges or the $L_{2,3}$ edges of rare earth elements. Therefore, before applying electric dipole sum rules one needs to make sure that the quadrupolar transitions are well identified and well separated in energy from the electric dipole transitions. There are other sum rules for electric quadrupole transitions [222].

(v) Finally, there is another important assumption relevant to the elements studied in

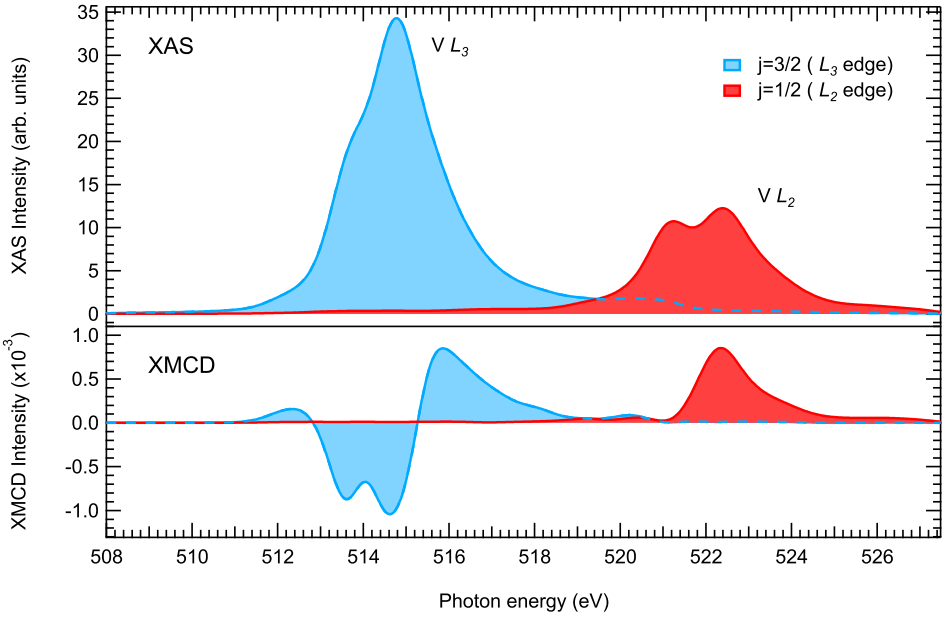

Figure 3.13: Example of V XAS/XMCD $L_{2,3}$ partial excitations from the $2p_{j=1/2}$ and $2p_{j=3/2}$ orbitals illustrating considerable overlap of the two manifolds (jj mixing).

this thesis: It is assumed, that the two spin–orbit split edges j^+ and j^- (for example $L_{2,3}$ edges) do not interfere. Thus, the spin sum rule is strictly valid only if the core angular momentum j is a good quantum number. Although this might sound reasonable, there are a large class of systems whereby j of the core-hole is not a good quantum number. There is a strong interaction between the core hole and the valence electrons. This interaction mixes states with different j of the core hole, and the effect is referred to as jj mixing. For the rare earth elements in less than half-filled $4f$ shells, the deviation from the spin sum rule was shown to increase from $\sim$ 60% in case of Ce^{3+} to $\sim$ 230% for Sm^{3+}, while in a half-filled (like Eu^{2+} discussed in Chapter 6) and more than half-filled $4f$ shells it is less than $\sim$ 10% [231]. Nevertheless, the spin sum rule holds reasonably well if the core spin–orbit splitting is much larger than the core-valence interaction, which is the case for Fe, Co, and Ni $L_{2,3}$ edges ($\sim$ 10% deviation of the spin moment value [221, 232]). However, this is not the case for the early $3d$ TM elements, such as V, Cr and Mn, where strong core hole and the valence electrons interaction redistributes the $L_{2,3}$ transition channels and leads to considerable disagreement of the spin magnetic moment value obtained from the application of spin sum rule. This effect has been encountered and analyzed for V, Cr and Mn $L_{2,3}$ edges in the preset thesis.

To estimate how strong the jj mixing can be, in Fig. 3.13 we show, as an example, decomposed excitations from the $j = 1/2$ and $j = 3/2$ sub-shells of the $2p$ orbitals of V ion. One can notice essential overlap between the two manifolds, often leading to the error in sum rule analysis. It should be noticed, that these two contributions do not just overlay and add up to the total spectrum, but rather interact and lead to slightly modified

Table 3.1: Spin sum rule correction factor C and the expectation values of the magnetic dipole operator $\langle T_z \rangle$ estimated from cluster-model-based theoretical spectra.

	$V^{3+}\ 2p^6 3d^2$	$Cr^{3+}\ 2p^6 3d^3$	$Mn^{2+} 2p^6 3d^5$	$Eu^{2+}\ 3d^{10} 4f^7$
C	1.2	1.7	1.4	1.06
$\langle T_z \rangle$	$0.08\hbar$	$0.5 \cdot 10^{-3}\hbar$	$0.2 \cdot 10^{-3}\hbar$	$-0.004\hbar$

multiplet structure.

In order to take into account the jj mixing between $2p_{3/2}$ and $2p_{1/2}$ manifolds (as well as $3d_{5/2}$ and $3d_{3/2}$) we followed the approach of Refs. [233, 234] and introduced the correction factor C as shown in Eqs. 3.27 and 3.31. We formally applied the spin sum rule to our cluster-model-based theoretical spectra and derived the values of C by comparison with the spin momenta directly calculated for the ground state of the same model. The correction factors C for the relevant elements are shown in Table 3.1.

3.4.3 Evaluation of the magnetic dipole term

The calculation of the spin magnetic moment by means of the spin sum rule shown in Eq. 3.24 requires the expectation value of the magnetic dipole operator $\langle T_z \rangle$. $\langle T_z \rangle$ corresponds to the asphericity of the charge density of the l valence shell ($3d$ for transition metals and $4f$ for lanthanides). The expectation value of magnetic dipole term provides detailed information on the anisotropy of the electron spin-density distribution distorted by the spin-orbit interaction or the crystal-field effect [235].

Many authors often neglect this term for $3d$ electrons, arguing that it results only in a small correction. However this is true only under certain circumstances. In $3d$ transition metal systems with cubic symmetry and a weak $3d$ spin–orbit coupling (compared to the crystal-field and the exchange splitting) the magnetic dipole term is usually much smaller than the spin moment and can be neglected [235]. Nonetheless, this is certainly not the case in $4f$ and $5f$ metals [236], where its contribution can be larger than that of $\langle S_z \rangle$ [237]. Its contribution also increases considerably with lowering the symmetry or reducing the dimensionality of the system [235].

In the limit of small $3d$ spin–orbit interaction the magnetic dipole term can be written as $\langle T_z \rangle = \langle S_z \rangle \langle Q_{zz} \rangle$, where $\mathbf{Q}$ is an electric quadrupole operator with a vanishing trace ($Q_{xx} + Q_{yy} + Q_{zz} = 0$) [238]. Therefore, for the systems with non-cubic symmetry the contribution of the $\langle T_z \rangle$ to the spin sum rule can be eliminated by averaging over XMCD measurements in three orthogonal directions. Alternatively, one can perform "magic angle" measurement, when the magnetic field is applied at angle (54.73 deg) with the surface normal where the $\mathbf{Q}$ contribution vanishes.

In general, the magnetic dipole operator is given as

$$\mathbf{T} = \sum_i \mathbf{S}_i - 3\mathbf{r}_i(\mathbf{r}_i \cdot \mathbf{S}_i), \tag{3.32}$$

where i runs over all electrons, $\mathbf{S}_i$ and $\mathbf{r}_i$ are the spin angular momentum and radius vector of the ith electron [177]. One only needs the value of T_z. We write it in spherical harmonics:

$$T_z = \sum_i (1 - 3\hat{z}^2)S_z^i - 3\hat{z}\hat{x}S_x^i - 3\hat{z}\hat{y}S_y^i = \sum_i -2C_0^{(2)}S_z^i - \frac{1}{2}\sqrt{6}(-C_1^{(2)}S_i^- + C_{-1}^{(2)}S_i^+), \tag{3.33}$$

where $C_q^{(k)}$ are defined in Eq. 3.9, $S_x = \frac{1}{2}(S^+ + S^-)$, $S_y = \frac{i}{2}(-S^+ + S^-)$.

Knowing the ground state of the system from our MLFT calculations we can readily estimate the expectation value of the magnetic dipole term $\langle T_z \rangle$. Our estimations of $\langle T_z \rangle$ done for V ion show that it's contribution to the m_{spin} is small but not negligible, while for Cr and in the particular case of Mn^{2+} (d^5) and Eu^{2+} (f^7) with the half-filled valence shells, its contribution to the m_{spin} is indeed negligible, see Table 3.1.

3.4.4 Summary

Despite many theoretical limitations the sum rules are powerful tools to extract direct quantitative information from XAS/XMCD spectra. When applied carefully, properly accounting for the theoretical and experimental complications, the sum rules can provide very useful information, such as the orbit and spin contributions to the total magnetic moment. This information is obtained in non-destructive and element-specific way, with the sensitivity to buried interfaces and sub-monolayer coverages. In general, sum rules are applicable to all magnetic materials, such as 3d, 4d and 5d transition metals, lanthanides and actinides [111].

Since XMCD intensity scales with the magnetization, whereas the isotropic XAS intensity remains constant, there is an alternative method to obtain the quantitative information on the magnetic moments based on the asymmetry of the experimental XMCD. This method is discussed in more details in Chapter 7.

3.5 Multiplet ligand-field theory calculations

Now that we have described in detail the experimental techniques utilized in the current work to obtain extensive information about the materials of interest, it is time to discuss how to extract this information from the measured spectra. One way, obviously, is to compare the measured spectra with those of another well understood material found in the literature, which sometimes allows one to understand some electronic and magnetic

properties of the system under investigation. However, often there is no suitable reference system available for such a comparison and therefore a theoretical interpretation of the spectra is necessary. Here we discuss one of such theoretical approaches used to analyze XAS and XMCD spectra of the magnetic topological insulators studied in the current work.

The properties of a quantum many-body system are governed by a microscopic Hamiltonian. Even modern computer facilities cannot handle Hamiltonians including all possible interactions between pairs of particles constituting solid. To circumvent this issue, we have to develop meaningful approximations, which capture key features of the system under investigation and give valuable insight into its properties. As an example, $L_{2,3}$ edge transition metal spectra, in contrast to ligand K edge spectra, are dominated by local effects and usually very well described using small local clusters limited to merely a single cation surrounded by its nearest-neighbor ligands. Therefore, in the current work this kind of cluster model was employed in order to interpret our XAS and XMCD results on magnetic topological insulator. For that purpose, we considered the basic building block, TM-Te_6 octahedra, consisting of the central transition metal cation surrounded by six tellurium ligands, as illustrated in Fig. 4.1 (a) for V-doped $(Bi,Sb)_2Te_3$ MTI. Moreover, we consider only those orbitals of the cluster, which are relevant for the interpretation of core-level spectra, such as $3d$ and $2p$ orbitals of the TM cation to capture the resonant transitions and the ligand orbitals, which comprise in our cases the $5p$ orbitals of the Te anion.

The fundamental principle of such cluster model calculations can be found in the multiplet ligand-field theory (MLFT), which was originally developed in quantum chemistry to describe the electronic structure of TM and rare-earth compounds [239]. The reasons why these calculations, which are not *ab initio* and consider only the local symmetry of an ion, lead to such an excellent agreement with experiment [240–242] are that within the MLFT calculations the initial and final states of the XAS process are both taken into account and electron correlations, spin–orbit coupling, crystal field and charge transfer effects are included. This means that detailed information concerning the initial state (ground state) can be obtained once the experimental spectrum has been reproduced. Thereby, MLFT cluster calculations are an essential tool, which allows the extraction of important microscopic parameters relevant to describe the electronic and magnetic structure and corresponding physics of magnetic topological insulators.

3.5.1 Model Hamiltonian

The model Hamiltonian of the TM-Te_6 cluster, which includes the relevant for us interactions, can be written as

$$\mathcal{H} = \mathcal{H}_{\text{Coul}} + \mathcal{H}_{\text{CF}} + \mathcal{H}_{\text{SO}} + \mathcal{H}_{\text{p-d hopping}}, \tag{3.34}$$

where the four terms represent the electron-electron interactions, the crystal-field potential, the electron spin-orbit interaction, and interaction of the TM ion with surrounding ligands. In the given form, $\mathcal{H}$ can be solved using exact diaganization, which is for example implemented in programs such as Quanty [243–245]. In the following we discuss each term of the model Hamiltonian in more details.

Coulomb interactions

The many-body Hamiltonian in Eq. 3.34 comprises a one-particle and a two-particle part. The two-particle part includes only one term–the electron-electron interactions, i.e Coulomb interactions, which we will consider first. The inclusion of Coulomb interactions substantially changes the spectrum of the eigenstates, which in turn leads to a more complex set of transitions as observed in XAS spectrum (splitting of the multiplets, see Section 3.1.1). The electron-electron Coulomb interaction term $\mathcal{H}_{\text{Coul}}$ in second quantization is gives by

$$\mathcal{H}_{\text{Coul}} = \frac{1}{2} \sum_{ii'jj'} U_{ii'jj'} c_i^\dagger c_{i'}^\dagger c_j c_{j'}, \tag{3.35}$$

with the Coulomb interaction coefficients

$$U_{ii'jj'} = \delta_{\sigma_i\sigma_j}\delta_{\sigma_{i'}\sigma_{j'}} \sum_{k=0}^{\infty} R^k_{ii'jj'} \times \sum_{q=-k}^{q=k} (-1)^q \delta_{q,m_j-m_i}\delta_{q,m_{i'}-m_{j'}} \left\langle l_i m_i \right| C^{(k)}_{-q} \left| l_j m_j \right\rangle \left\langle l_{i'} m_{i'} \right| C^{(k)}_{q} \left| l_{j'} m_{j'} \right\rangle, \tag{3.36}$$

where the angular part is given directly by the Wigner-Eckart theorem and the radial parts are expressed by so-called Slater integrals

$$R^k_{ii'jj'} = e^2 \int_0^\infty \int_0^\infty \frac{r^k_<}{r^{k+1}_>} R_{n_i l_i}(r) R_{n_{i'} l_{i'}}(r') R_{n_j l_j}(r) R_{n_{j'} l_{j'}}(r') r^2 r'^2 dr dr' \tag{3.37}$$

with $r_< = \min(r, r')$ and $r_> = \max(r, r')$, which can be further separated into so-called direct Slater integrals $F^k(ii') = R^k_{ii'ii'}$ for the direct contribution of the Coulomb interaction and exchange Slater integrals $G^k_{ij} = R^k_{ijji}$ for the exchange part of the Coulomb interaction. More details on Slater integrals are given by Cowan [173] and Ballhausen [239]. In our model, we fully account for the $3d-3d$ and $2p-3d$ electron-electron interactions. For example, the $3d-3d$ contribution ($l = 2$) has the following form:

$$U^{dd}_{ii'jj'} = \sum_{k=0}^{l} a_k(i,i',j,j') F^{(2k)}_{dd}, \tag{3.38}$$

where all a_k are known coefficients specific to the set of the d orbitals so that U_{dd} is fully determined by the three Slater integrals F^0_{dd}, F^2_{dd}, and F^4_{dd}

$$U_{dd} = F^0_{dd} - 2/63(F^2_{dd} + F^4_{dd}). \tag{3.39}$$

In a similar way, the $2p-3d$ part depends on three other parameters, controlling direct (F^2_{pd}) and exchange (G^1_{pd}, G^3_{pd}) Coulomb interactions between $3d$ and $2p$ orbitals

$$U_{pd} = F^0_{pd} - 1/15G^1_{pd} - 3/70G^3_{pd}. \tag{3.40}$$

The Slater integrals themselves are usually calculated, considering certain approximations. For an isolated atom, their values can be calculated within the Hartree–Fock approximation with the use of Cowan's code [173] and, if necessary, later refined by fitting to experimental data. For a solid, they can be calculated in a similar fashion by using the localized Wannier orbitals as the basis functions [245]. The values for F^2_{dd}, F^4_{dd}, F^2_{pd}, G^1_{pd}, and G^3_{pd} for $3d$ and $4d$ transition metals are tabulated in Ref. [177]. We also list them for our considered ions in corresponding experimental parts. It is noteworthy that the F^0 integral usually cannot be determined reliably due to the screening by the conduction electrons [246]. Since the F^0 results in a rigid shift of the absorption spectrum as a whole, which is fitted in our calculations anyway, this theoretical challenge does not entail any practical consequence for our considerations.

We should note that when comparing to experiments, these calculated F^k and G^k values are subject to different renormalizations due to the screening effects in solids. Empirically, a scaling factor $\beta \sim 0.8$ is enough to reproduce experimental spectra for transition metal compounds [240, 247]. However, if covalency is not treated appropriately in the model, one typically needs to reduce the Slater integrals further. This can be understood semi-classically in terms of the so-called nephelauxetic effect: Due to interaction with the ligands, the transition metal orbitals are getting more delocalized, such that their electrons are further apart from each other, and their mutual repulsion is reduced [174].

Spin–orbit coupling

Next we consider the spin–orbit interaction which also enters our model Hamiltonian. Most generally, within the central field approximation, spin–orbit interaction is given by

$$\mathcal{H}_{\mathrm{SO}} = \zeta \sum_i \mathbf{l}_i \cdot \mathbf{s}_i, \tag{3.41}$$

where the sum runs over all electrons i. Spin–orbit coupling is nonzero only for partially filled shells, which in our case is the $3d$ and the $2p$ shell in the final state configuration ($2p^5d^{n+1}$). Hence, the spin–orbit interaction reduces to two constants ζ_{2p} and ζ_{3d}, determining the strength of the spin–orbit coupling in the $2p$ and $3d$ shells, respectively

$$\mathcal{H}_{\mathrm{SO}} = \zeta_{2p}\mathbf{L}_{2p} \cdot \mathbf{S}_{2p} + \zeta_{3d}\mathbf{L}_{3d} \cdot \mathbf{S}_{3d}. \tag{3.42}$$

The spin–orbit coupling lifts the degeneracy between states with different quantum number J^2. A more detailed insight into the spin–orbit coupling can be found elsewhere [173, 239]. The values for ζ_{3d} and ζ_{2p} are constants that have been calculated for all transition metal ions within the Hartree–Fock approximation [177]. Those relevant for us are also listed in the corresponding experimental parts.

Crystal field splitting

Next we want to discuss the effect of the surrounding ligands on the central TM ion. Looking at the middle panel of Fig. 3.14, one can see the typical six-fold octahedral coordination of the TM ion by Te ligands. The simple approach is to model these ligands as point charges. Then the $3d$ electrons of interest are only subject to an electrostatic potential which leads to a splitting of the energy levels of the central TM ion. This treatment of ligands is known as the crystal field model [180], which was applied to the analysis of $L_{2,3}$ edge XAS spectra in the 1980s [182, 247].

Fig. 3.14 illustrates the effect of the crystal field of different symmetries on the $3d$ orbitals. Within a one-electron picture, we see that all five $3d$ orbitals are initially degenerate. However, when the central ion is subjected to a crystal field of octahedral symmetry O_h, the $3d$ orbitals split in energy into two groups. The two $3d$ orbitals (d_{z^2} and $d_{x^2-y^2}$ denoted as e_g orbitals), which have the angular lobes pointing towards the ligands, are more strongly affected by the crystal field, while the other three orbitals (d_{xz}, d_{xy}, d_{yz} denoted as t_{2g} orbitals) are directed between the ligands and are less affected by crystal field. This means the e_g orbitals have higher energy ($E_{e_g} = 6Dq$) than the t_{2g} orbitals ($E_{t_{2g}} = -4Dq$), resulting in the energy splitting between them known as the crystal field splitting. In the highly symmetric O_h case the crystal field is fully described just by one parameter $10Dq$, which is often determined by fitting to experimental data. If the symmetry is reduced, the TM $3d$ levels will split further. For example, in the case of trigonal symmetry C_{3v}, one of the t_{2g} orbitals from the O_h case splits off to a_{1g} orbital. The rest mix together to form two e_g groups. In order to describe such crystal field splitting one needs already three parameters, $10Dq$, $D\sigma$, and $D\tau$ [239]. A more comprehensive description of crystal field model, including the crystal field parameters and specific expressions for the energies of the one-electron states in case of various crystal field symmetries, can be found elsewhere [177, 239].

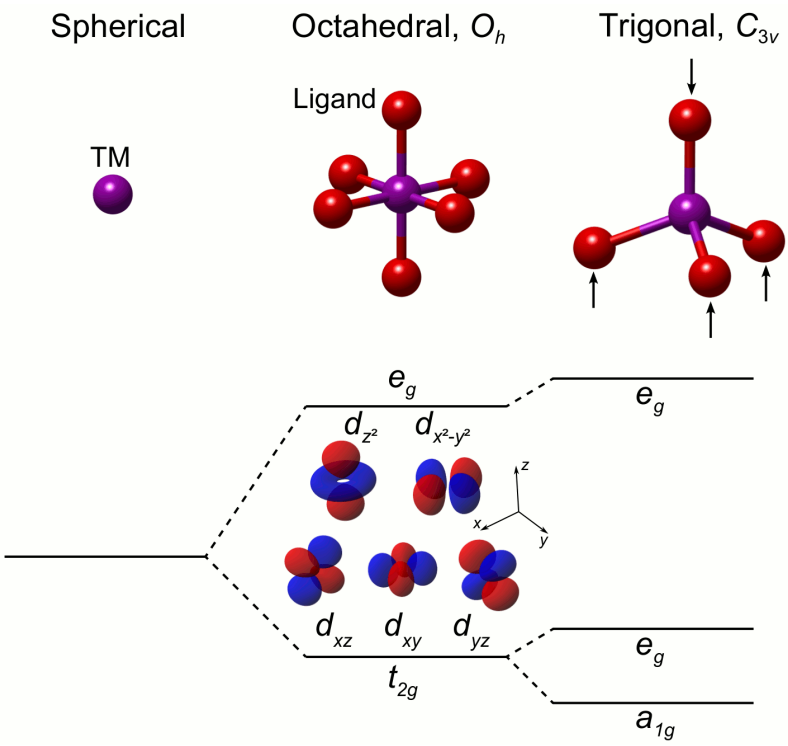

Figure 3.14: Crystal field symmetries relevant for this work. The specific arrangements of neighboring ligand atoms lead to the energetic splitting of the TM 3*d* orbitals into different groups. The angular wavefunctions of different 3*d* orbitals are also shown.

In the case of the relevant for the current work O_h symmetry, the crystal field term in Hamiltonian can be written as

$$\mathcal{H}_{\mathrm{CF}} = \sum_m \epsilon_m c_m^\dagger c_m \tag{3.43}$$

with

$$\epsilon_m = \begin{cases} +\frac{3}{5}(10Dq) & \text{for } e_g, \\ -\frac{2}{5}(10Dq) & \text{for } t_{2g}. \end{cases} \tag{3.44}$$

Covalency

The last term in the model Hamiltonian to consider, i.e. $\mathcal{H}_{\text{p-d hopping}}$, describes the covalency effects, which arises from the hopping of electrons between the ligand and the transition metal. Within our cluster model this is the term which mixes different ligand to metal charge-transfer configurations (specific arrangements of the electrons within the cluster). The strength of the mixing depends on the hopping integrals and the energy difference between the transition metal 3*d* orbitals E_d and the ligand orbitals E_L. In the following we discuss this term in more details.

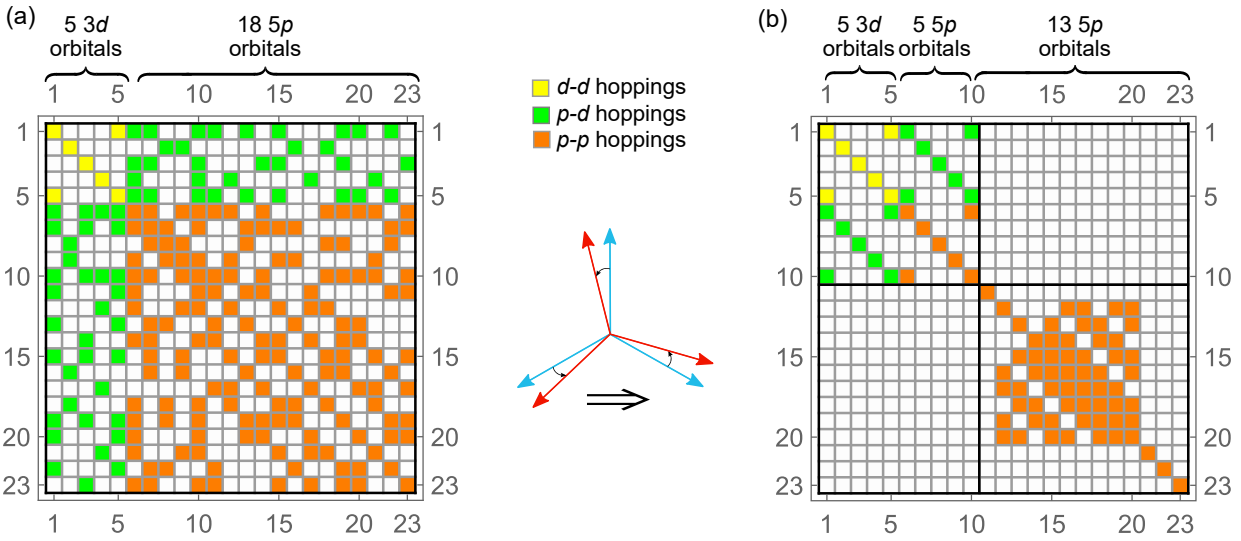

Figure 3.15: (a) The tight-binding Hamiltonian resulting from on-site energies and hopping terms. (b) The tight-binding Hamiltonian after basis transformation. The upper left 10×10 matrix decouples from the rest of the system. Ligand $5p$ and $3d$ orbitals as well as hopping between them show O_h symmetry.

Previously we considered a simple crystal field model, where the ligand atoms were approximated by point charges. This model is quite suitable for some relatively ionic systems [174]. However, for the proper description of covalent systems, this model needs to be improved. The natural way of improving it is to include not only the electrostatic effects of the ligands, but also covalency effects, which arise from the hopping of electrons between the ligand and the TM site. For that, we have to extend our basis (consisting of $2p$ and $3d$ orbitals of the TM) to include some of the ligand orbitals. In our cluster model shown in Fig. 3.14 it is sufficient to include only Te $5p$ orbitals.

The electron hopping between the ligands and the central transition metal in the cluster model is treated within a tight-binding approach. The Tm-Te_6 cluster we are considering contains five $3d$ orbitals and $6 \times 3 = 18$ Te $5p$ orbitals resulting in a 23×23 tight-binding Hamiltonian, as illustrated in Fig. 3.15 (a). The hopping, or equivalently the overlap, between two atomic orbitals at different sites can be expressed in the Slater–Koster parameters. For our cluster model with O_h symmetry only two covalent hopping integrals (Slater–Koster parameters) $pd\sigma$ and $pd\pi$ between the TM $3d$ and ligand $5p$ orbitals are needed. Additionally, there will be hopping between pairs of ligand $5p$ orbitals similarly parametrized by the overlaps $pp\sigma$ and $pp\pi$. These hopping parameters define the off-diagonal elements of the tight-binding Hamiltonian. The diagonal terms of the Hamiltonian are given by the on-site energies of every orbital. Fortunately, we can significantly simplify the 23×23 tight-binding Hamiltonian by a unitary basis transformation, which blockdiagonalizes the Hamiltonian. Ligand orbitals then consist of linear combinations of atomic orbitals with the same symmetry as the TM ion. The Hamiltonian

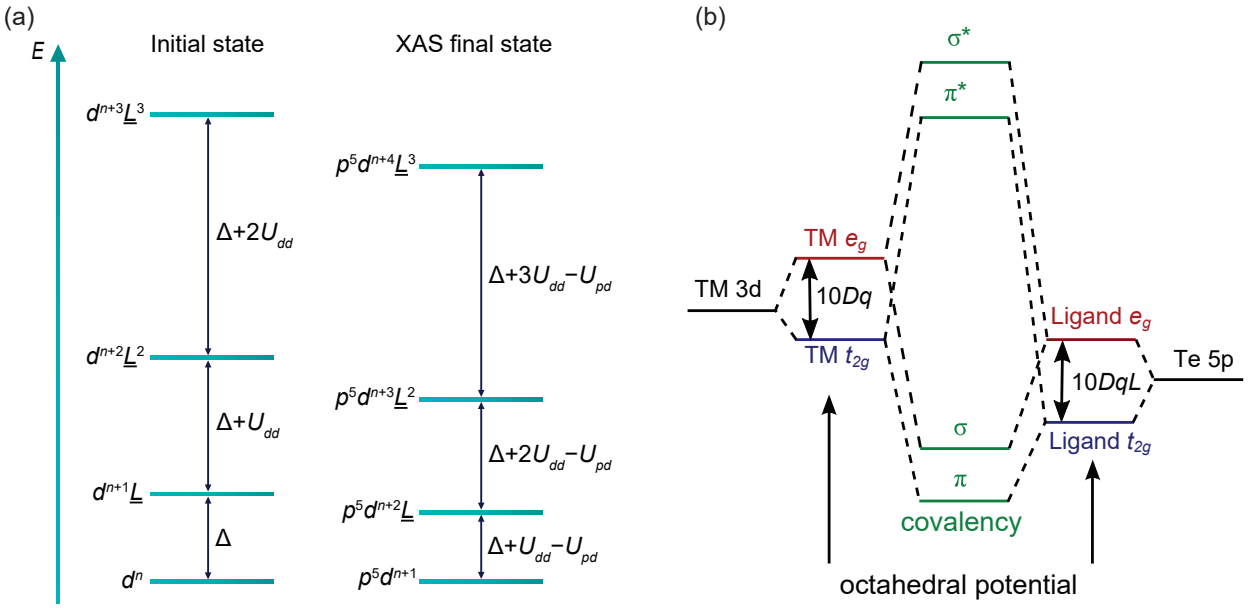

Figure 3.16: (a) Schematic diagram showing the on-site energies of the various configurations for the initial state and XAS final state when the hybridization (V_{e_g}) is zero. (b) Definition of $10Dq$ and $10DqL$ in MLFT. TM $3d$ and Te $5p$ atomic orbitals (black) split under the influence of an octahedral potential O_h in orbitals with e_g (red) and t_{2g} (blue). Due to hopping, bonding (σ, π) and antibonding (σ^*, π^*) energy levels appear (green).

after such transformation is illustrated in Fig. 3.15 (b). One can notice, that the upper left 10×10 matrix block decouples from the rest of the system, which means that we can diagonalize it separately and don't have to consider the entire 23×23 matrix. Hence, we limit our model to only five Te $5p$ orbitals, which interact with the TM ion, whereas the other 13 ligand orbitals have no overlap with the TM $3d$ orbitals. As we fixed the five $3d$ orbitals during the basis transformation, we see that the d block (yellow squares) still has O_h symmetry with crystal field splitting parametrized by $10Dq$. One can also notice, that the ligand block (orange squares), has the same structure as the d block. Moreover, the hoppings between ligands and $3d$ orbitals (green squares) also have the same structure. Therefore, similar to $10Dq$ parametrizing the splitting of $3d$ orbitals, for ligand orbitals we shall call this parameter $10DqL = 2T_{pp} = 2(pp\sigma - pp\pi)$ [245], see Fig. 3.16 (b). In the following, we will consider the positively defined $V_{e_g} = -\sqrt{3}pd\sigma$ and $V_{t_{2g}} = 2pd\pi$ to describe the hopping terms between the $5p$ orbitals at the ligand sites and the TM $3d$ orbitals of e_g and t_{2g} symmetry, respectively. The reduction of the Hamiltonian by unitary basis transformation is crucial for efficient MLFT calculations since it leads to a crucial gain of computational convenience [245].

We can improve our TM-Te_6 cluster model to better account for covalency effects by adding more configurations. Besides the nominal ion configuration $2p^63d^n$ we consider additional ligand to metal charge-transfer configurations $2p^6d^{n+k}\underline{L}^k$ and mix them

together using the hopping integrals discussed above. This is knows as configuration-interaction scheme. Here, $\underline{L}^k$ denotes k holes in the Te $5p$ orbitals, which means that k electrons have moved from the ligand orbitals to the TM $3d$ orbitals. For the V- and Cr-doped MTI systems studied in this thesis, it was sufficient to consider three additional charge-transfer configurations $d^{n+1}\underline{L}$, $d^{n+2}\underline{L}^2$ and $d^{n+3}\underline{L}^3$, see Fig. 3.16 (a), while for the intrinsic MTI system studied in Chapter 7 already two charge-transfer configurations were enough. Hence, with our basis set the ground state wavefunction can be written as the linear combination of the different configurations:

$$|\Psi_{\mathrm{GS}}\rangle = |\Psi_n\rangle + |\Psi_{n+1}\rangle + ... + |\Psi_{n+k}\rangle\,, \tag{3.45}$$

where $|\Psi_{n+k}\rangle = c_k \left|d^{n+k}\underline{L}^k\right\rangle$ and $\langle\Psi_{n+k}|\Psi_{n+k}\rangle = c_k^2$ gives the weight of each configuration. In the same manner, the XAS final state is described by a linear combination of p^5d^{n+1}, $p^5d^{n+2}\underline{L}$, $p^5d^{n+3}\underline{L}^2$ and $p^5d^{n+4}\underline{L}^3$.

The configuration-interaction scheme is shown in Fig. 3.16 (a) for the initial state and XAS final state on the system. Here we use the energy definitions introduced by Zaanen *et al.* [248] to calculate the on-site energies of the TM ion and the ligands. First, looking at the initial state configurations, one can notice that the ionic configuration is lowest in energy, and the first charge-transfer configuration $3d^{n+1}\underline{L}$ is higher in energy by an amount equal to the parameter Δ[1]. Δ is called the charge-transfer energy, which is defined as the energy required to transfer an electron from the ligands to the TM ion, i.e. $\Delta = E(d^{n+1}\underline{L}) - E(d^n)$. The next configuration $3d^{n+2}\underline{L}^2$ is another unit of Δ above the second configuration because it involves another charge-transfer process, but also has a unit of Coulomb repulsion energy U_{dd} due to the interaction between the two extra $3d$ electrons present in this case. Similar explanations apply for the next configuration, as well as for final states of the XAS. Each time a charge-transfer process happens, we add a unit of Δ, and for every extra pair of electron-electron interactions, we add a value of on-site Coulomb repulsion U_{dd}. One can notice another parameter U_{pd} for the final state, which describes the Coulomb interaction between the $2p$ core hole created in the XAS process and $3d$ electrons.

As we have already mentioned the amount of configurations mixing, i.e the weights of different charge-transfer configurations, depends not only on the covalent hopping integrals, but also on the on-site energies of the shells. The on-site energies E^i_{3d}, E^i_L of the $3d$ and ligand shell in the initial state are given by

[1] This does not always have to be the case. Some covalent materials can exhibit negative charge transfer energies, as those studied in Chapter 4.

$$E^i_{3d} = \frac{10\Delta - n_{3d}(19 + n_{3d})U_{dd}/2}{10 + n_{3d}},$$
$$E^i_L = n_{3d}\frac{(1 + n_{3d})U_{dd}/2 - \Delta}{10 + n_{3d}}. \quad (3.46)$$

For the final state

$$E^f_{3d} = \frac{10\Delta - n_{3d}(31 + n_{3d})U_{dd}/2 - 90U_{pd}}{16 + n_{3d}},$$
$$E^f_{2p} = \frac{10\Delta - (1 + n_{3d})(n_{3d}U_{dd}/2 - (10 + n_{3d})U_{pd})}{16 + n_{3d}},$$
$$E^f_L = \frac{(1 + n_{3d})(n_{3d}U_{dd}/2 + 6U_{pd}) - (6 + n_{3d})\Delta}{16 + n_{3d}}. \quad (3.47)$$

Hence, the on-site energies in all three shells of our model are controlled by charge-transfer parameter Δ and the Coulomb parameters U_{dd}, U_{pd}. Therefore, in order to reproduce the experimental spectrum one has to find the proper values for these parameters, as well as for covalent hopping integrals V_{e_g} and $V_{t_{2g}}$. Adopting published results [249–252], we fix U_{dd}/U_{pd} to 0.83 and $pd\sigma/pd\pi$ to -2.0, which also allows us to reduce the number of parameters and speed up fitting of the experimental spectra.

Magnetic interactions

Since we want to interpret the XMCD spectra measured on magnetic samples with and without applied external magnetic field, we have to include the corresponding magnetic interaction terms in our model Hamiltonian. In our local cluster model the magnetization of the sample is treated in the context of mean-field theory by introducing an exchange field term acting on the spin

$$\mathcal{H}_{ex} = J\mathbf{S}_z \quad (3.48)$$

with the spin operator $\mathbf{S}_z$ and the Heisenberg exchange J which one can estimate as $J \sim k_B T_C$, using the critical temperature, such as Curie or Néel temperature, obtained from experiment. This term in our calculations, as long as it is relatively small, does not change the line shape of the XAS spectra, but it changes the magnitude of the XMCD spectrum. In our cluster calculations the local magnetic moments are assumed fully saturated, i.e. we obtain the maximum XMCD strength.

In the model the external magnetic field is accounted for by the Zeeman term in the Hamiltonian $\mathcal{H}_{\text{Zeeman}} = \mu_B B_z(g_l\mathbf{L}_z + g_s\mathbf{S}_z)$, where B_z in the magnetic field applied along

the z- axis (c-axis of our samples). This term hardly changes the spectral shape in the magnetic field range ($\lesssim 6$ T) available at the beamlines.

3.5.2 Calculation of the spectrum

After constructing a proper model Hamiltonian for the initial and the final state of our system, we diagonalize the Hamiltonian in the many–electron configuration interaction basis, which gives us all the eigenfunctions and eigenvalues of the system. The XAS spectrum then can be calculated using the Fermi's golden rule for XAS given in Eq. 3.8, i.e. by evaluating the matrix element between the initial state and all final states invoking the dipole selection rules in Eq. 3.11. This way we will obtain the spectrum as a set of delta-peaks (see Fig. 4.7), which after proper broadening can be compared with an experimental spectrum. Traditionally $2p$ XAS spectra are broadened with a Lorentzian function in order to capture the lifetime of the excited state, plus a Gaussian function to describe the experimental broadening. The experimental broadening is constant, with a typical value of $0.2 - 0.4$ eV full-width half-maximum (FWHM), while the lifetime broadening is considered energy-dependent.

A close look at Fig. 3.3 reveals that often one can have excited states very close in energy to the ground state. If the energies of these states are within a few $k_{\mathrm{B}}T$ from the ground state, then they will be populated due to thermal excitations according to Boltzmann statistics. Therefore, it is often very important to take this detail into account. To do so, we simply need to carry out calculations for each relevant initial state, weighting the overall intensity by the Boltzmann factor. Thus, for temperature dependent XAS, we have

$$I_{\mathrm{XAS}}(\hbar\omega, \boldsymbol{\epsilon}, T) = \sum_i \frac{1}{Z} \exp\left(-\frac{E_i - E_g}{k_{\mathrm{B}}T}\right) I^i_{\mathrm{XAS}}(\hbar\omega, \boldsymbol{\epsilon}), \tag{3.49}$$

where $Z = \sum_i \exp\left(-\frac{E_i - E_g}{k_{\mathrm{B}}T}\right)$ is the partition function, E_g is the ground state energy, and all other symbols are defined as before.

Diagonalization of a many-particle Hamiltonian is not an easy task to solve by hand. Even in the case of one ionic configuration, the initial state configuration consists of $\binom{10}{n} = \frac{10!}{(n-10)!n!}$ individual states (45 in the case of $2p^6 3d^2$ of V^{3+}), and the final state configuration $2p^5 3d^3$ consists of $\binom{6}{5}\binom{10}{n+1}$ states (720 for $2p^5 3d^3$ of V^{3+}). By allowing for additional charge-transfer configurations, even more individual states are included. Fortunately, computer algorithms do the work for us. To perform the actual calculation we used the Quanty software package developed by Prof. M. W. Haverkort [243–245],

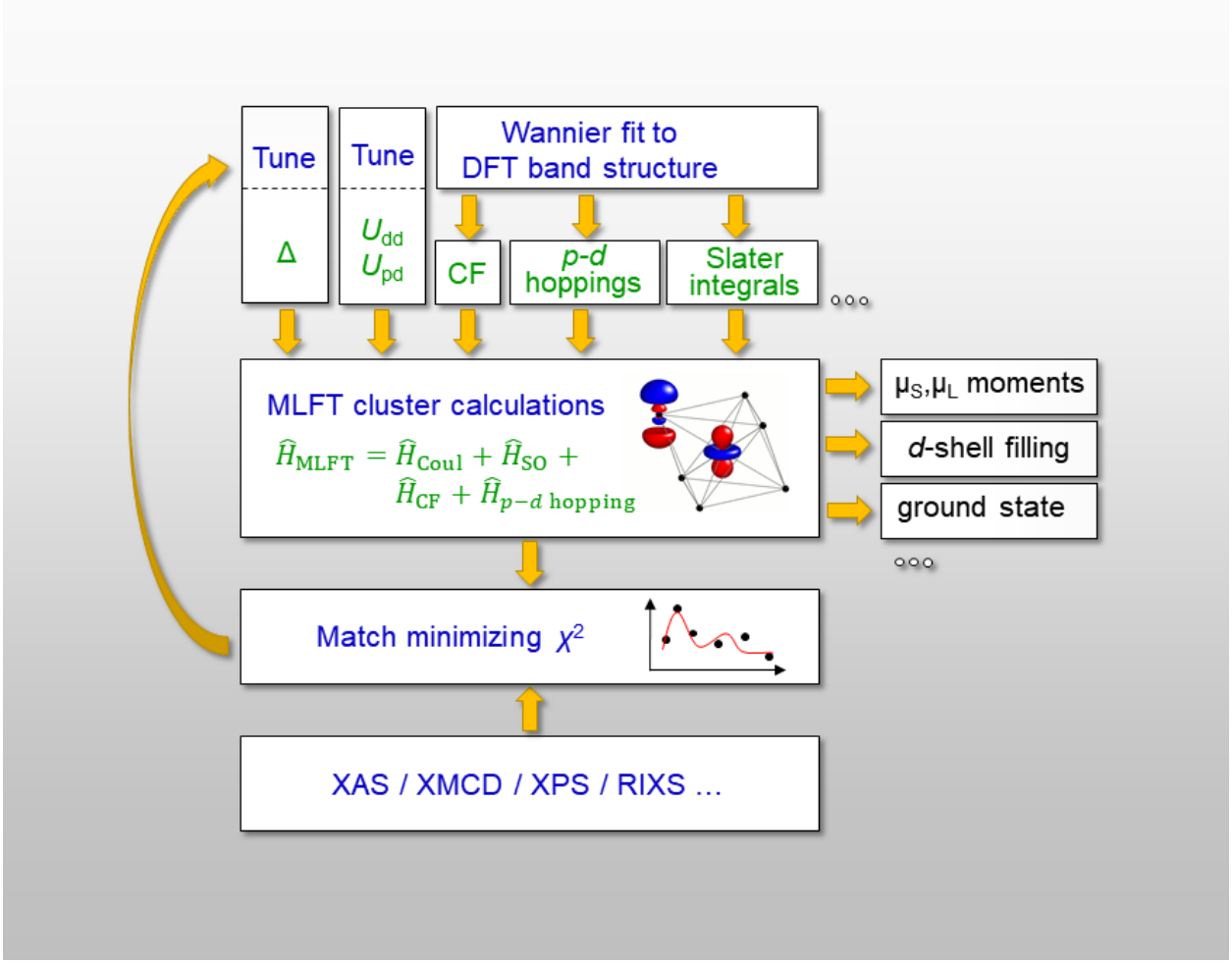

Figure 3.17: Flowchart of the *ab initio* MLFT calculations.

which offers a convenient and flexible way to program this quantum mechanical problem in second quantization. Quanty uses Lanczos iterative algorithm [253] for diagonalization of the Hamiltonian and calculation of the spectrum. It is important to realize that the spectra produced in Quanty are calculated with respect to a basis formed by the angular parts of the many-electron wavefunctions, i.e. the radial functions are not accounted for.

3.5.3 *Ab initio* MLFT

MLFT calculations discussed above are performed by fitting the input parameters to the experimental data. Among these parameters are the scaling parameter β for the Hartree–Fock values of the Slater integrals, the charge-transfer Δ, the Coulomb interaction energies U_{dd} and U_{pd}, covalent hopping integrals $V_{t_{2g}}$ and V_{e_g}, and the crystal-field splitting parameter $10Dq$. Despite being a great help for understanding and interpreting experimental results, this approach is, however, not completely satisfactory and, over the years,

numerous theoretical methods have therefore been developed to obtain MLFT parameters ab initio. In Chapter 7 we will show one such *ab initio* method, which allows one to notably reduce the number of the input fit parameters, such as the Slater integrals, crystal-field and covalent hopping parameters. Then the only remaining fit parameters in our model are Δ, U_{dd} and U_{pd}. The theoretical aspects of the approach are comprehensively explained elsewhere [245, 254]. We start the *ab initio* MLFT calculations with conventional density function theory (DFT) calculations in local-density approximation (LDA) for the the proper experimental crystal structure using the FPLO package [255]. Therefrom we compute a set of Wannier functions which we use to obtain the one body terms (such as CF and hybridization parameters) needed to set up the local MLFT cluster calculation. Many-body effects beyond LDA are subsequently treated on the MLFT level using Quanty. Schematically this approach is illustrated in Fig 3.17. More details in the particular case of the intrinsic MTI $MnBi_6Te_{10}$ are discussed in Chapter 7.

3.5.4 MLFT fit to experiment

The most straightforward way to fit the MLFT parameters to experimental data can be realized by minimizing the quadratic deviation between the experimental spectrum $S(\omega)$ and the modeled spectrum $M(\omega) = R(\omega) + Bg(\omega)$, consisting from the resonant $R(\omega)$ and background $Bg(\omega)$ parts:

$$\chi(p_1,...,p_k) = \int_{E_1}^{E2} \left(S(\omega) - R(\omega, p_1,...,p_k) - Bg(\omega)\right)^2 d\omega = \\ \|S(\omega) - R(\omega, p_1,...,p_k) - Bg(\omega)\|_2 , \quad (3.50)$$

where $p_1,...,p_k$ represent the remaining parameters that are to be optimized by matching the theory to experiment. The resonance part $R(\omega)$ in our fits is obtained directly from the MLFT calculation by convolving raw MLFT spectra with a Lorentzian and Gaussian to account for the effects of finite life-time and experimental resolution.

Whereas $R(\omega)$ is produced in a physical and a well controlled manner, an estimate of a similar quality for $Bg(\omega)$ may be difficult to achieve. Besides modeling the continuum step $Bg(\omega)$ with $\arctan(x)$, in some cases, an empirical Shirley-like background

$$Bg(\omega) = \int_{E_1}^{\omega} \alpha(\omega) R(\omega') d\omega' \approx \alpha \int_{E_1}^{\omega} R(\omega') d\omega' \quad (3.51)$$

can be used as an adequate approximation. There are, though, no good reasons for assuming the scaling parameter α to be a universal energy-independent constant, same for

all resonant edges. Moreover, there are known systems, where the resonant peaks appear at energies notably lower than that of the continuum step, which clearly invalidates the general applicability of Eq. 3.51 and further complicates the correct modeling of $Bg(\omega)$.

It is, however, clear that errors in $Bg(\omega)$ cannot be simply ignored. If an estimate for the $Bg(\omega)$ were not correct, then $S(\omega) - Bg(\omega)$ would contain artifacts, which in the best case could result in a poorly looking fit. In a worse case, they may falsify the resulting fit parameters, since $R(\omega)$ would be accounting for what it is not responsible for.

Fortunately, the information about the resonant structure of the ion that we want to capture with our MLFT calculation is mostly contained in the "wiggly" spectral features, the features to which contribution of the smooth $Bg(\omega)$ is mostly negligible. Therefore a better fitting algorithm, instead of minimizing χ as defined in Eq. 3.50, should put an extra weight to these "wiggly" features and tone down, or even completely ignore, the smooth ones, thus evading the problems with correct background modeling.

In practice, we achieve this by expanding $S(\omega)$, $R(\omega)$ and $Bg(\omega)$ in a Fourier series and summing the Fourier components up to a particular $n = m$ to from what we will call a "low frequency" part, while leaving the rest of the series in a "high frequency" part. For example for $S(\omega)$ we would write

$$S(\omega) = \sum_{n=0}^{s} mS_n(\omega) \; + \sum_{n=m+1}^{+\infty} S_n(\omega) = S^{\mathrm{LF}}(\omega) + S^{\mathrm{HF}}(\omega). \tag{3.52}$$

Here and in the following we use the sine-cosine form with odd n indexing the cosine and even n the sine components:

$$S_n(\omega) = \begin{cases} s_n \cos\left(\frac{2\pi}{E_2 - E_1}\frac{n}{2}\omega\right), & n = 0, 2, 4, \ldots \\ \\ s_n \sin\left(\frac{2\pi}{E_2 - E_1}\frac{n-1}{2}\omega\right), & n = 1, 3, 5, \ldots \end{cases} \tag{3.53}$$

Since the Fourier components of different n are orthogonal to each other this allows for a similar splitting of the merit function into a *low* and *high* frequency parts (which in its essence is based on the Parseval's theorem):

$$\begin{aligned} \chi(p_1, \ldots, p_k) = \left\| \sum_{n=0}^{+\infty} S_n(\omega) - R_n(\omega, p_1, \ldots, p_k) - Bg_n(\omega) \right\|_2 = \\ \sum_{n=0}^{+\infty} \left\| S_n(\omega) - R_n(\omega, p_1, \ldots, p_k) - Bg_n(\omega) \right\|_2 \stackrel{\mathrm{def}}{=} \sum_{n=0}^{+\infty} \chi_n = \\ \sum_{n=0}^{m} \chi_n(\omega) + \sum_{n=m+1}^{+\infty} \chi_n(\omega) = \chi^{\mathrm{LF}}(\omega) + \chi^{\mathrm{HF}}(\omega). \end{aligned} \tag{3.54}$$

In a conventional fit one would weigh all the Fourier contributions χ_n to the total merit function equally. Since $Bg(\omega)$ unlike $R(\omega)$ is a smooth function, for a sufficiently large $n > m$ the contribution of $Bg_n(\omega)$ to χ_n becomes negligible, regardless of how good or bad the model for $Bg(\omega)$ is. Therefore, considering only these high frequency components we can mitigate possible deficiencies in the modeled $Bg(\omega)$.

Owing to this self-correcting property of the fitting algorithm we used the simple $\arctan(x)$ for background $Bg(\omega)$ with the optimal cutoff value of m set at $(E_2 - E_1)/W$, where $W \sim 1$ eV parameterizes the sharpest features allowed in the true background. The corrected approximation for $Bg(\omega)$ was then obtained by assuming a perfect fitness for the low frequency components, i.e. $\chi_n = 0$ for $n \leq m$ and hence

$$Bg^{\text{opt}}(\omega) \approx B^{\text{LF}}(\omega) = \sum_{n=0}^{m} B_n(\omega) = \sum_{n=0}^{m} S_n(\omega) - R_n(\omega). \tag{3.55}$$

3.6 Superconducting quantum interference devices

Since the goal of doping topological insulators with various transition metal and rare-earth elements is to induce long-range magnetic order and open a surface band gap relevant for the QAH effect, detailed investigation of the magnetic properties of MTIs is important. Previously we have discussed the XMCD method, which allows for element-specific investigation of magnetic properties. Often XMCD measurements are performed in TEY detection mode, which is surface sensitive with probing depth typically in the 1-5 nm range for the $L_{2,3}$ edges [174, 208]. However, there are other techniques, which allow for studying bulk magnetic properties, such as superconducting quantum interference device (SQUID) magnetometry. In contrast to XMCD, SQUID magnetometry is a bulk-averaging method and not element-specific. This section gives a brief overview of the SQUID magnetometry method, which we employed in Chapters 6 and 7 of the current thesis to study bulk magnetic properties of MTIs. For a more detailed look one should consult the literature on this topic [256–258].

Magnetometry in general refers to measuring the magnetization or the magnetic moment of a sample. Since both are vectorial quantities, magnetometry often measures only one component of the magnetization vector. In many cases, magnetometry is performed in an applied magnetic field and mostly the projection of magnetization onto the field direction is measured.

The SQUID magnetometer is a commercially available lab-based device, which allows a fully automated measurement of sample magnetization as a function of magnetic field and/or temperature [256]. A SQUID magnetometer uses the Josephson effect to measure extremely small variations in magnetic flux created by mechanically moving the sample through a superconducting pick-up coil which is converted to a voltage. Typically, a

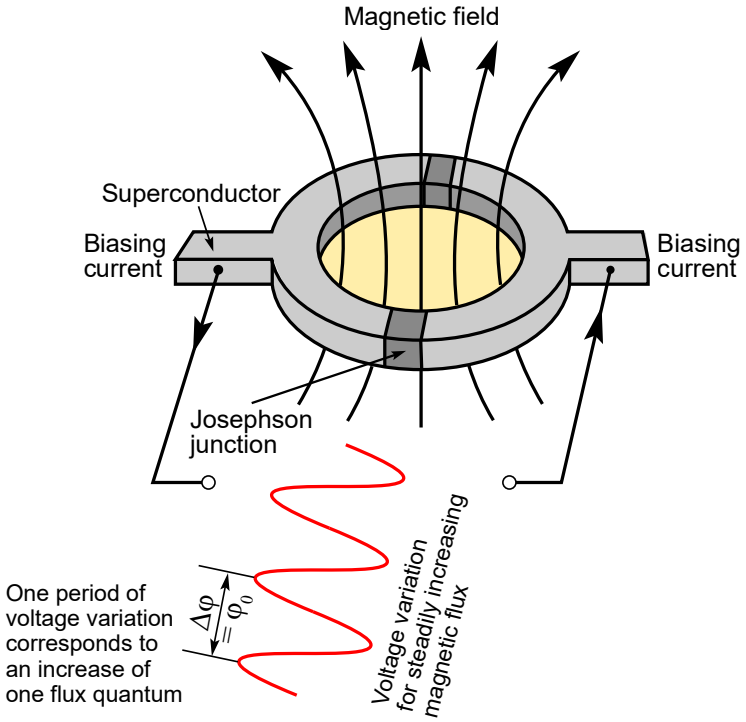

Figure 3.18: Principle of SQUID magnetometer. Adopted from Ref. [259].

SQUID is a ring of superconductor interrupted by one or more Josephson junctions, as schematically shown in Fig. 3.18. A Josephson junction is a thin insulating layer which interrupts a superconductor. Since the junction is non-superconducting only a tunnel current is able to flow through it. The electrical current density through a weak electric contact between two superconductors depends on the phase difference δ of the two superconducting wave functions. Moreover, the time derivative of δ is correlated with the voltage across this weak contact:

$$U = \frac{\hbar}{2e}\left(\frac{d\delta}{dt}\right). \tag{3.56}$$

A superconducting loop will contain flux only in multiples of the flux quantum $n\Phi_0$, where n is an integer, see Fig. 3.18. A change in flux applied to the loop will cause currents to oppose that change, leading to a change in the relative phase δ, which according to the Eq. 3.56 gives rise to a voltage. Therefore, such a structure can be used to convert magnetic flux into an electrical voltage, which is the basic working principle of a SQUID magnetometer.

SQUID can be operated as either rf or dc SQUID. The prefix rf or dc refers to whether the Josephson junction is biased with an alternating current rf or a dc current. Nearly all commercial SQUIDs are dc due to their lower noise. The most widely used SQUID magnetometer is offered by Quantum Design. SQUID magnetometry measurements presented in Chapters 6 and 7 were carried out using a 7-T Quantum Design MPMS 3 SQUID

vibrating sample magnetometer, capable of applying a 7 T field to the sample and operating from room temperature down to 1.5 K.

While the commercial SQUID is fully automated and often user-friendly, there are several possible pitfalls and artifacts of SQUID. Here we summarizes some of the most important ones, in particular, if low magnetic fields or small magnetic signals are to be detected, like in the case of diluted magnetic compounds, exhibiting soft ferromagnetic properties.

As we have already mentioned before, SQUID magnetometers are typically equipped with a superconducting magnet, whereas the strength of magnetic fields generated by the magnet is simply calculated from the current in the coils [256, 257]. A known issue of all types of superconducting magnets is the remanent field originating from trapped magnetic flux pinned at defects in the material of the superconducting coil [260]. It is directed antiparallel to the last experienced strong field by the magnet. Recording a magnetization curve up to high magnetic fields, this residual field can not be avoided or corrected since the commercial SQUID magnetometers do not measure the magnetic field at the location of the sample. Therefore, it leads to residual hysteresis for diamagnetic samples and an inverted hysteresis loop for paramagnetic samples.

In many cases, samples measured in SQUID come with a substrate, which can be diamagnetic or paramagnetic. Due to the larger volume of the substrate compared to a thin magnetic film, already at moderate external magnetic fields the diamagnetic moment of the substrate exceeds the ferromagnetic moment of the film because the diamagnetic moment increases linearly with field while the ferromagnetic moment quickly saturates with fields and stays constant. Therefore, in order to derive the magnetic properties of the sample, it is necessary to subtract a large diamagnetic background from a large measured signal to extract the small magnetic moment of interest. This entails that the accuracy and reproducibility of a single measurement has to be sufficient for a reliable extraction of the small ferromagnetic component.

In addition, there is another possible pitfall in SQUID: As already mentioned, the field is never directly measured so that the nominal and the actual field experienced by the sample are different. Consequently, if one calculates the diamagnetic contribution of the substrate from the nominal field, this results in small discrepancies to the actual diamagnetism due to the actual magnetic field experienced by the sample.

And finally, to derive the magnetization $M = m/V$, which is the more relevant quantity, one has to divide the magnetic moment m by the sample volume V. However, the sample volume has to be measured independently, which in general is not trivial, especially for a thin film on a diamagnetic substrate. Moreover, in many publications the result of mangetometry are often provided in μ_B/atom, which means that the number of atoms in the actual sample has to be determined independently as atoms/cm^3. The uncertainties of determining volume, density, or number of atoms in the sample may easily

become larger than the actual uncertainty in the measured total moment of the sample [256, 258].

Despite the aforementioned pitfalls, SQUID magnetometry is very useful and convenient technique for a rather quick lab-based (compared to XMCD requiring synchrotron radiation facility) magnetic characterizations of samples. Magnetic hysteresis loops $M(H)$ measured with SQUID are useful for extracting critical parameters such as saturation magnetization and coercive field. By measuring hysteresis both in-plane and out-of-plane, one can also determine the magnetic anisotropy of the sample. Temperature dependent measurements $M(T)$ are used to determine critical temperatures such as the Curie temperature T_C and the Néel temperature T_N by fitting the measured data to the Curie–Weiss law, as will be shown in Chapter 6.

Chapter 4

Comparing magnetic ground state properties of the V- and Cr-doped topological insulator $(Bi,Sb)_2Te_3$

As we have discussed in Chapter 2, an insulating ferromagnetic (FM) ground state is a fundamental prerequisite for the quantum anomalous Hall (QAH) effect observed in magnetic topological insulators (MTIs). Ferromagnetism can be achieved by doping topological insulators (TIs) with various transition metal atoms (TM), such as V, Cr, Mn or Fe [75–77, 81, 82, 85]. However, the QAH effect has been only observed in the V- and Cr-doped $(Bi,Sb)_2Te_3$ systems [8, 9, 24, 137, 261], with V-doping providing a more robust FM order and higher T_C, which is in turn favorable for realizing the QAH effect at higher temperatures [262]. Since the nature of FM coupling is not yet well understood [137], establishing microscopic differences between the strongly correlated V and Cr impurities would help with evaluating the relevance of the various proposed models of FM coupling [27, 28, 71, 73, 74] and eventually provide a better control of the QAH effect [8, 262].

Despite the fact that vanadium, rather than chromium, doping is the more promising avenue to optimized QAH properties [8], only qualitative XAS and XMCD studies of $V_z(Bi,Sb)_{2-z}Te_3$ have been published so far [30, 78, 263–265]. To better understand the difference between the two dopants, in the present chapter we provide a comprehensive XAS and XMCD comparison of V- and Cr-doped $(Bi,Sb)_2Te_3$ thin films, grown on Si(111) using molecular beam epitaxy (MBE). We model the detailed line shapes of the V and Cr spectra collected from freshly prepared surfaces with multiplet ligand-field theory (MLFT) calculations and determine their correlated many-particle ground states. Our analysis by MLFT goes beyond existing studies by allowing several charge-transfer states. It allows us to bypass XMCD sum rules and directly determine the values of both the orbital and spin moments, which are in good agreement with published magnetometry results [8, 263]. We find a strongly covalent ground state of the magnetic impurities dominated by the coherent superposition of one and two Te-ligand-hole configurations, with negligible contributions from a purely ionic 3+ configuration. The strong charge

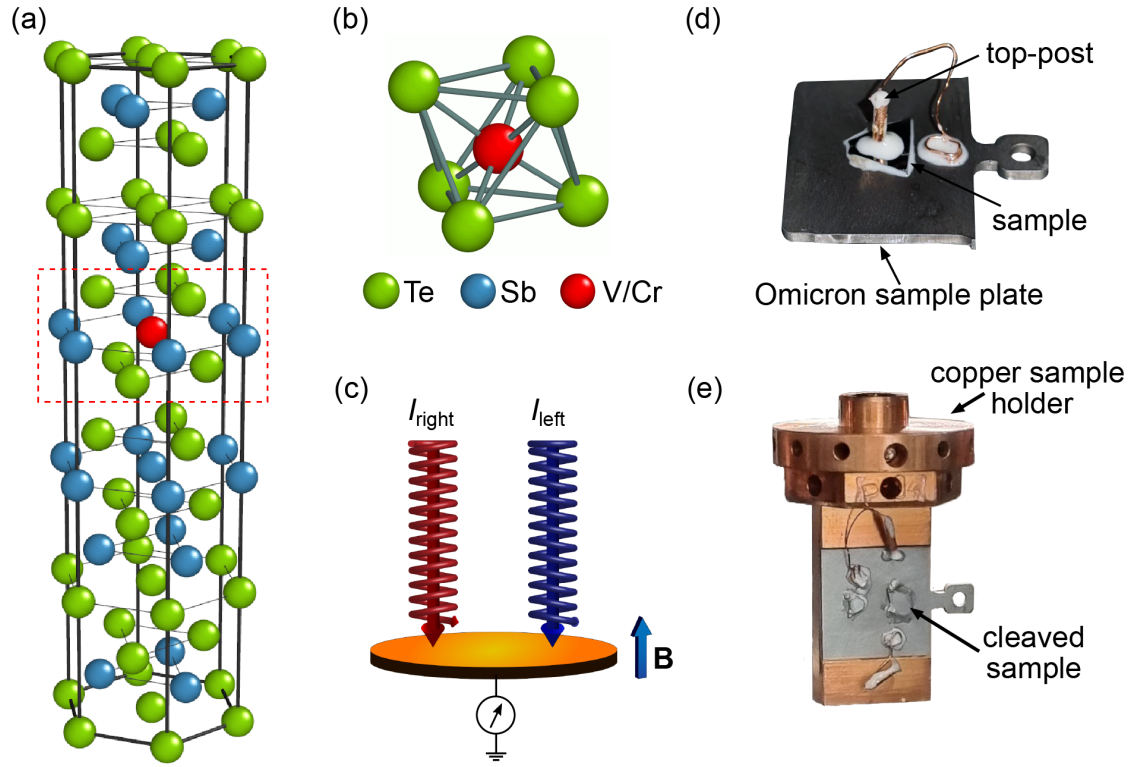

Figure 4.1: (a) Crystal structure of V/Cr-doped Sb_2Te_3 consisting of stacked quintuple layers along the c-axis (Te-Sb-Te-Sb-Te), separated by van der Waals gaps. (b) The V/Cr impurity substitutes Sb, which is surrounded by six Te atoms. The impurity atom has a slightly trigonally distorted O_h symmetry. The grey sticks are shown to highlight the octahedron and are not generally representative of chemical bonds. (c) Schematics of the experimental geometry for the XMCD measurements. The polarized and monochromatized photons are absorbed by the sample in a magnetic field applied parallel to the direction of the incoming beam. The X-ray absorption spectra are obtained by measuring the drain current (TEY). (d) Typical sample and the copper top-post glued on a sample plate. (e) Sample plate mounted in the copper sample holder inside of the UHV chamber and the samples cleaved by knocking off the post. An electrical contact can be achieved by placing a droplet of conducting glue between the sample and the plate (d) or by gluing the whole assembly with a conducting silver epoxy (e). Adapted from Ref. [79].

transfer from the ligands found in this work indicates the importance of Te $5p$ states for the magnetic coupling and, thus, the QAH effect in magnetically doped TIs. Parts of the data presented in this chapter were published in Ref. [79] and Ref. [108].

4.1 Samples and experimental details

The samples investigated consist of about 9 nm thick $Cr_z(Bi_{1-x}Sb_x)_{2-z}Te_3$ and $V_zSb_{2-z}Te_3$ films with $x = 0.9$ and $z = 0.1$, grown by MBE on H passivated Si(111) substrates. The samples were grown by Dr. Martin Winnerlein and Dr. Steffen Schreyeck from the department of Prof. Laurens W. Molenkamp, Universität Würzburg. The detailed growth conditions can be found elsewhere [68, 266]. After the growth of the films, a 100 nm Te

cap layer was deposited *in situ*, in order to protect the surface from contamination during sample transport. The morphology, thickness, and crystallinity of the layers were characterized by atomic force microscopy (AFM) at ambient conditions, X-ray reflectivity (XRR) measurements and X-ray diffraction (XRD).

The XAS and XMCD measurements at the V and Cr $L_{2,3}$ absorption edges were performed using the high field cryomagnet end station HECTOR of the BOREAS beamline at the ALBA synchrotron radiation facility (Barcelona, Spain) [204]. The detailed description of the end station in given in Chapter 3. The samples were glued with conducting silver epoxy onto Cu sample holders and mounted on the cold finger of a helium flow cryostat (see Fig. 4.1 (d, e)). Prior to the measurements, the Te capping layer was mechanically removed in the fast-entry chamber at a pressure of $\sim 10^{-9}$ mbar. The sample was then transferred into the spectroscopy chamber operated under UHV conditions, with a base pressure in the 10^{-11} mbar range. The effectiveness of this method to expose a clean sample surface was demonstrated using Bi_2Te_3 before [267]. We collected spectra encompassing the oxygen edge at the beginning and at the end of the measurements for each sample, which demonstrate that the surfaces have not changed throughout the experiment.

XAS measurements were carried out at 2 K by measuring the total electron yield (TEY) via the sample drain current normalized by the incoming photon intensity, giving a probing depth of 3–5 nm [174]. Circularly polarized X-rays with close to 100% polarization were used in normal incidence with respect to the sample surface and parallel to the applied magnetic field, as schematically illustrated in Fig. 4.1 (c). The area probed by the beam (about $100 \times 80 \mu m^2$) is much smaller than the sample size. The raw XAS spectra I_{left} and I_{right} measured with the helicity vector antiparallel (left) and parallel (right) to the fixed magnetic field of 3 T were scaled with respect to each other to have the same intensity at energies far from the resonances. We define the average XAS as $I_{\text{avg}} = (I_{\text{left}} + I_{\text{right}})/2$. Since only the resonant part of the spectra enters the sum rules, we subtract the background including the continuum edge jumps from the raw spectra: $I^{\text{res}}_{\text{left/right}} = I_{\text{left/right}} - I_{\text{bg}}$. The normalized XMCD signal then becomes $I_{\text{XMCD}} = (I^{\text{res}}_{\text{left}} - I^{\text{res}}_{\text{right}})/(I^{\text{res}}_{\text{left}} + I^{\text{res}}_{\text{right}})$. To cancel out any experimental drifts, for each XMCD we actually measured eight spectra in a row by altering the polarization according to the pattern LRRL LRRL.

4.2 Multiplet ligand-field theory calculations

In this work XAS and XMCD spectra for the V and Cr $L_{2,3}$ ($2p \rightarrow 3d$) absorption edges were calculated within the configuration-interaction scheme (see Section 3.5 in Chapter 3), considering a cluster consisting of the central transition metal cation surrounded by six tellurium ligands, as depicted in Fig. 4.1 (a, b). We consider the nominal $2p^6 3d^2$ (V^{3+}) and

$2p^6 3d^3$ (Cr^{3+}) configuration and further employ three additional charge-transfer states $d^{n+1}\underline{L}$, $d^{n+2}\underline{L}^2$ and $d^{n+3}\underline{L}^3$ to account for covalency effects (see Fig. 3.16). Here $\underline{L}^p$ denotes p holes in the Te $5p$ orbitals. In this manner, we go beyond existing atomic multiplet theory calculations performed for Cr in Bi_2Se_3 [112, 268] and in Sb_2Te_3 [113], where only states with one ligand hole $d^{n+1}\underline{L}$ were considered, as well as beyond crystal field multiplet calculations for Cr in Bi_2Te_3 [269]. It has been demonstrated that for highly covalent compounds (as those investigated in this work) the reduced basis calculations, in which at most one hole is allowed at the ligand site, overestimate the ionic character [270]. This is further confirmed by the results of this work. To fit the experimental XAS and XMCD spectra, we introduce the following fit parameters in the MLFT calculation: the scaling parameter β for the Hartree–Fock values of the Slater integrals; the charge-transfer (CT) energy Δ it costs to bring one electron from the ligand p to the TM d shell; the Coulomb interaction energies U_{dd} between the valence $3d$ electrons and U_{pd} between the $2p$ core electron and $3d$ electron; covalent hopping integrals $V_{t_{2g}}$ and V_{e_g} between the p orbitals at the ligand sites and the TM $3d$ orbitals of t_{2g} and e_g symmetry, respectively. Apart from the above terms, we also consider the crystal-field splitting parameter $10Dq$. We assume V or Cr to substitute Sb or Bi on the cation sites and describe the crystal field in octahedral (O_h) symmetry, with the C_4 axes of the octahedron along the TM–Te bonds (see Fig. 4.1 (b)). There is a slight distortion from a perfect octahedral (O_h) to trigonal (C_{3v}) symmetry. Within a point charge model, the distortion would result in an energy splitting of the t_{2g} orbitals (see Fig. 3.14) of less than 2 % as compared to $10Dq$. This is much smaller than the energy resolution of the XAS experiment and justifies our approximation.

As discussed in Chapter 3, we fix U_{dd}/U_{pd} to 0.83 and $pd\sigma/pd\pi$ to -2.0, which also allows us to reduce the parameter space and speed up fitting. Spin–orbit coupling was kept at its Hartree–Fock value. The simulations were performed using the Quanty software package for quantum many-body calculations, developed by Prof. M. W. Haverkort [245]. The spectral contributions from each of the split ground state terms to the absorption spectra were weighted by a Boltzmann factor corresponding to the experimental temperature of $T \approx 2$ K. The mean field effective potential was accounted for by introducing an exchange field term acting on the spin. We estimated the exchange field from the Curie temperature ($T_C = 45$ K for the V-doped sample and $T_C = 20$ K for the Cr-doped one, as shown in Fig. 4.3). Since the experiments were performed in an external magnetic field of 3 T, this was also included in the Hamiltonian. To account for the instrumental and intrinsic lifetime broadening, the calculated spectra were convoluted with a Gaussian function of 0.3 eV FWHM and with an energy-dependent Lorentzian profile of 0.2–0.3 eV FWHM.

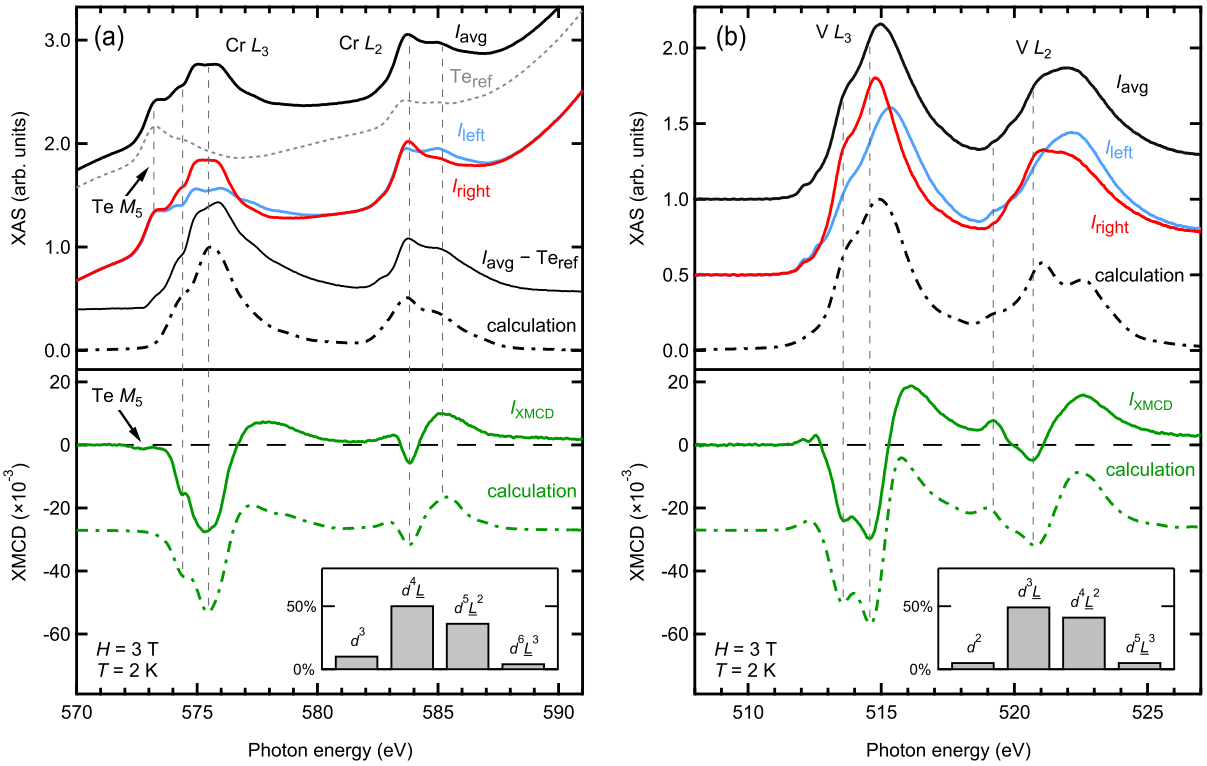

Figure 4.2: Experimental and calculated $L_{2,3}$ XAS and XMCD spectra. (a) $Cr_{0.1}(Bi_{0.1}Sb_{0.9})_{1.9}Te_3$ film. (b) $V_{0.1}Sb_{1.9}Te_3$ film. The top panels show experimental X-ray absorption data, obtained as described in section 4.1 (left circular polarization, I_{left}, light blue line; right circular polarization, I_{right}, dark red line; averaged over both polarizations, I_{avg}, bold black line). Polarization-averaged spectra calculated by the MLFT cluster model described in the text are shown as a dash-dotted line; to facilitate the comparison with experiment, in panel (a) we show Cr data (thin black line) corrected for the Te contribution using a Cr-free reference sample (Te_{ref}, dotted grey line). The bottom panels show the corresponding normalized experimental (I_{XMCD}, solid green line) and calculated XMCD spectra (dash-dotted green line). The insets show the contributions of different configurations to the ground state. The dashed vertical lines are drawn as a guide to the eye, highlighting the position of particular features in the spectra. The peak intensity of the calculated XAS spectrum was normalized to one. Taken from Ref. [79].

4.3 V and Cr $L_{2,3}$ XAS and XMCD

In Fig. 4.2 we compare the measured and calculated $L_{2,3}$ edge XAS and XMCD spectra for both the Cr- and V-doped samples. The Cr $L_{2,3}$ edges largely overlap with Te $M_{4,5}$ spectral features, which complicates the detailed comparison of experimental X-ray absorption spectra with calculations. To demonstrate this, we have highlighted the Te M_5 peak in Fig. 4.2 (a). The overlap with Te $M_{4,5}$ features, which extend to higher energies beyond the shown energy range, is the main reason for the strongly sloping background in the measured XAS. To simplify the visual comparison we have subtracted the Te $M_{4,5}$ spectrum measured in a Cr-free reference sample (Fig. 4.2 (a), grey dotted line). With the Te contribution eliminated, it is now obvious that at the main Cr L_3 peak the spectrum shows a double peak structure. It should be noted that this double peak feature is not

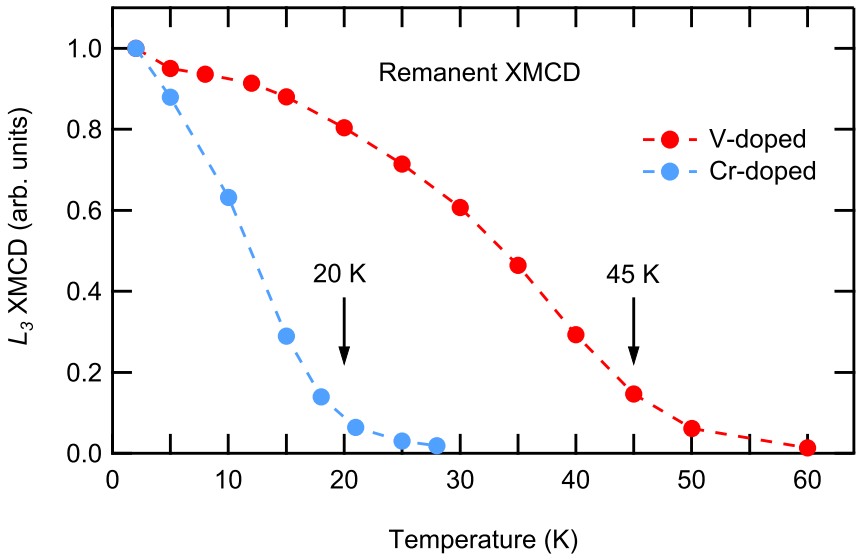

Figure 4.3: Temperature dependence of the remanent (10 mT) XMCD signal at the V (red circles) and Cr (blue circles) L_3 edges, from which the corresponding Curie temperatures can be estimates as $T_C^V \sim 45$ K and $T_C^{Cr} \sim 20$ K. The XMCD signal at $T = 2$ K has been normalized to 1.0. Taken from Ref. [79].

due to oxidation of Cr ions on the surface: Such oxidized surface Cr was reported for the Cr:Bi_2Se_3 system, its main contribution to both XAS and XMCD being ∼1.5 eV higher in energy [268]. Here we see no sign of oxidized surface Cr, which testifies to the purity of the sample surface. There is no indication of oxidized vanadium in the XAS data of the V-doped sample, either. It is noteworthy that the vanadium spectrum reveals a significant shoulder structure at the low-energy flank of the L_3 main peak. Overall, despite the high experimental resolution, both the Cr and V spectral line shapes are rather broad, showing no sharp multiplet structure, which is an indication of the strong covalency of the systems [174].

The corresponding normalized XMCD spectra at the V/Cr $L_{2,3}$ edges, displayed in the bottom panels of Fig. 4.2, demonstrate a persistent ferromagnetic state at low temperatures and a sizable magnetic moment carried by the TM 3*d* states. In Fig. 4.3 we show the strength of the XMCD signal as a function of temperature measured in the remanent state (10 mT). The thermal demagnetization curves indicate that the V-doped sample exhibits more robust ferromagnetism, with the Curie temperature ($T_C \sim 45$ K) more than twice as high as that of the Cr-doped sample ($T_C \sim 20$ K), in good agreement with previous works [8, 80]. The higher T_C is favorable to achieve a stable QAH state at higher temperatures [8, 262].

Fig. 4.4 (a, b) shows low-field magnetic hysteresis curves at the V and Cr L_3 edges, taken at 2 K, with the magnetic field applied perpendicularly to the sample surface. For both systems we observe a "square-shaped" hysteresis loop, exhibiting a relatively high remanence, as expected for an out-of-plane anisotropy, and coercive fields of H_C(V) ∼ 200

mT and $H_C(\mathrm{Cr}) \sim 20$ mT. The low coercive fields observed reveal the typical soft ferromagnetic properties of dilute systems. Fig. 4.4 (c, d) shows a comparison of V and Cr $L_{2,3}$ XMCD spectra for the same samples, measured at saturation ($B = 3$ T) and in remanence ($B = 0.01$ T) at low temperature of 2 K. While in V-doped Sb_2Te_3 the remanent and saturated spectra almost coincide, demonstrating that V ions remain almost fully saturated when going from saturation to remanence, in the Cr-doped sample the remanent XMCD is considerably lower than in saturation, indicating $\sim$ 17% decline of the Cr ions net magnetization along the surface normal.

The most noteworthy feature in the XMCD line shape of both ions, shown in Fig. 4.2 and Fig. 4.4, is the peak on the low-energy side of the L_3 edge, which resembles the one observed in Cr_2Te_3 [271], a compound characterized by strong hybridization of the TM $3d$ band with the ligand $5p$ band. Moreover, it is notable that the dichroism at both the L_2 and the L_3 edge of V is more pronounced as compared to Cr. In general, the line shape of the XMCD spectrum depends on the spin-polarization of the d band, defined as an imbalance between number of spin-up and spin-down d holes. The XMCD signal shows a more asymmetric line shape of the $L_{2,3}$ edges for small spin-polarizations (and hence small spin magnetic moments), and a more symmetric line shape for high spin-polarizations [110]. Overall, our XAS and XMCD data is consistent with previous reports on (V,Cr):$(Bi,Sb)_2Te_3$ [8, 104] thin films, as well as bulk samples [30, 78, 80, 264].

4.4 L-edge sum rule analysis

In the following we report the results of a sum rule analysis we applied to our data. A detailed description of the sum rules is given in Section 3.4.

The applicability of the spin sum rule depends on the question of how well the contributions of the L_3 ($j = 3/2$) and L_2 ($j = 1/2$) edges are separated in energy. Due to the strong jj mixing arising from the relatively small spin–orbit coupling in the $2p$ shell, there is considerable overlap of these contributions for light TM elements such as V and Cr. Therefore, in our spectra the cutoff energy E_{cutoff} separating the $j = 3/2$ and $j = 1/2$ contributions is in principle ill-defined, see Fig. 4.5. The correction factor C is introduced to compensate the resulting deviation. However, the determination of C obviously depends on the choice of E_{cutoff} and requires further modeling of the data, thus strongly limiting the usability of the spin sum rule for light TM elements. More details on the determination of C are given in Chapter 3.

Since the extracted magnetic moments depend in a nontrivial way on the input parameters controlling the normalization and background subtraction procedures described in section 4.1, as well as on the integration energy and the number of $3d$ holes n_h, we vary the input parameters in a random and uncorrelated way within the assumed confidence intervals and see how the final results get distributed, see Fig. 4.5 (b, c) and Fig. 4.6 (b, c).

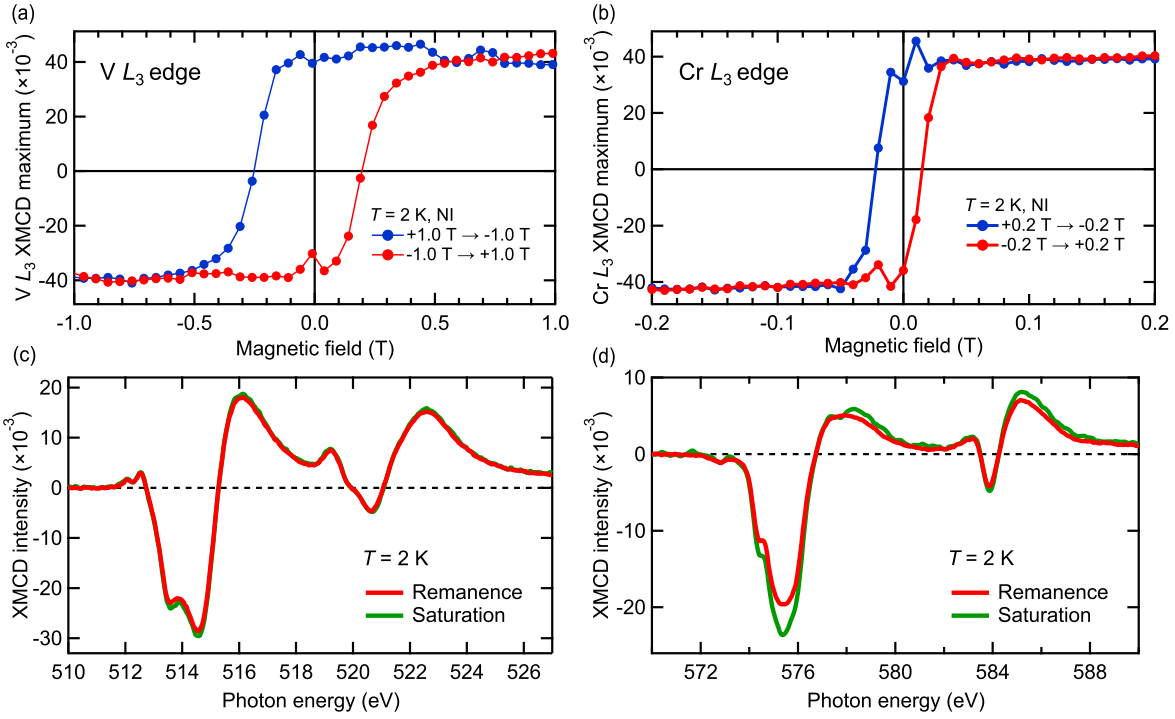

Figure 4.4: Magnetization curves ($I_{\text{right}} - I_{\text{left}}$) taken at the (a) V and (b) Cr L_3 edge, at a low temperature of 2 K, with the magnetic field applied in the out-of-plane direction. (c) V and (d) Cr $L_{2,3}$ absorption edges XMCD spectra taken at remanence ($B = 0.01$ T, red line) and saturation ($B = 3$ T, green line), at 2 K.

In this way one is able to account for possible conjoined effects of the input parameters and produce fair estimates for the uncertainties in m_{spin} and m_{orb}.

From the sum rule analysis, we obtain $m_{\text{spin}} = (2.0 \pm 0.3)\mu_B$/atom for V and $m_{\text{spin}} = (2.3 \pm 0.5)\mu_B$/atom for Cr. The orbital sum rule reveals an almost negligible value of $m_{\text{orb}} = (-0.01 \pm 0.02)\mu_B$/atom for Cr, while that of V is $m_{\text{orb}} = (-0.38 \pm 0.05)\mu_B$/atom. Thus, the small m_{orb} of the Cr ion does not significantly contribute to the total magnetic moment, suggesting a quenched Cr $3d$ orbital magnetic moment. The V ion carries moderate orbital magnetic moment, indicating the partial quenching of m_{orb}. The antiparallel alignment of m_{spin} and m_{orb} agrees with Hund's last rule for less than half-filled shells. It is worth mentioning that due to the $2p$–$3d$ core hole correlation effects in $L_{2,3}$ absorption spectra and various approximations made deriving the sum rules, as well as the ambiguity in the choice of the integration range and the definition of the number of $3d$ holes, the moments calculated using sum rules can strongly deviate from their true values [272]. For this reason, we obtain more reliable spin and orbital magnetic moments by fitting theoretical spectra to the experimental ones, as will be discussed below.

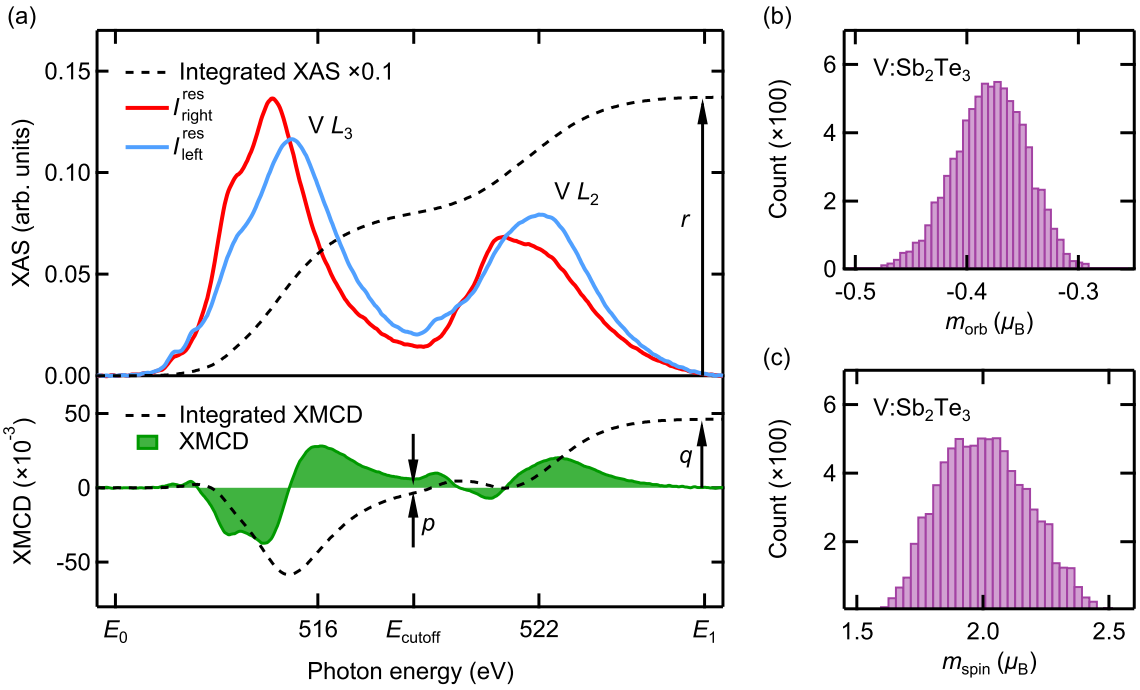

Figure 4.5: Sum rule analysis for the V-doped Sb_2Te_3 thin film. (a) Left- and right-circularly polarized XAS spectra of the V $L_{2,3}$ edges, obtained after the background correction described in section 4.1 (I^{res}_{left}, solid light blue line, and I^{res}_{right}, solid dark red line), along with the corresponding XMCD data (solid green line, lower panel). The dashed lines show the total integrated XAS and XMCD spectral weight, respectively. The arrows mark the values of r, p and q used in Eq. 3.27. E_0 and E_1 denote the onset and the end energy of the entire $L_{2,3}$ edges, and E_{cutoff} denotes the energy separating the L_3 and L_2 contributions. (b) and (c) Distribution of m_{orb} and m_{spin}, respectively, obtained by applying the sum rule analysis 8000 times, as described in the main text. Taken from Ref. [79].

4.5 MLFT analysis of the V and Cr $L_{2,3}$ XAS and XMCD spectra

In order to interpret our XAS and XMCD results and evaluate several physical parameters that control the electronic and magnetic properties of our V- and Cr-doped 3D TI's, we have analyzed the experimental spectra using MLFT calculations. The calculated XAS/XMCD spectra, plotted as dash-dotted lines in Fig. 4.2 (a) and (b), fit well with the experimental data, reproducing all essential multiplet features of the measured spectra. A good agreement is most notable for the XMCD spectra (green dash-dotted lines). Special attention was paid to reproduce all spectral features and their relative energy positions denoted by vertical dashed lines, especially the double-peak feature in the L_3 edge. In Fig. 4.7 (a) and (b) we show a separate comparison of the calculated right- and left-circularly polarized XAS spectra with the experimental $L_{2,3}$ edges of V and Cr. The multiplet structure is also displayed. The fact that a single realization of a local cluster is sufficient to reproduce the form of the experimental spectra rules out the coexistence

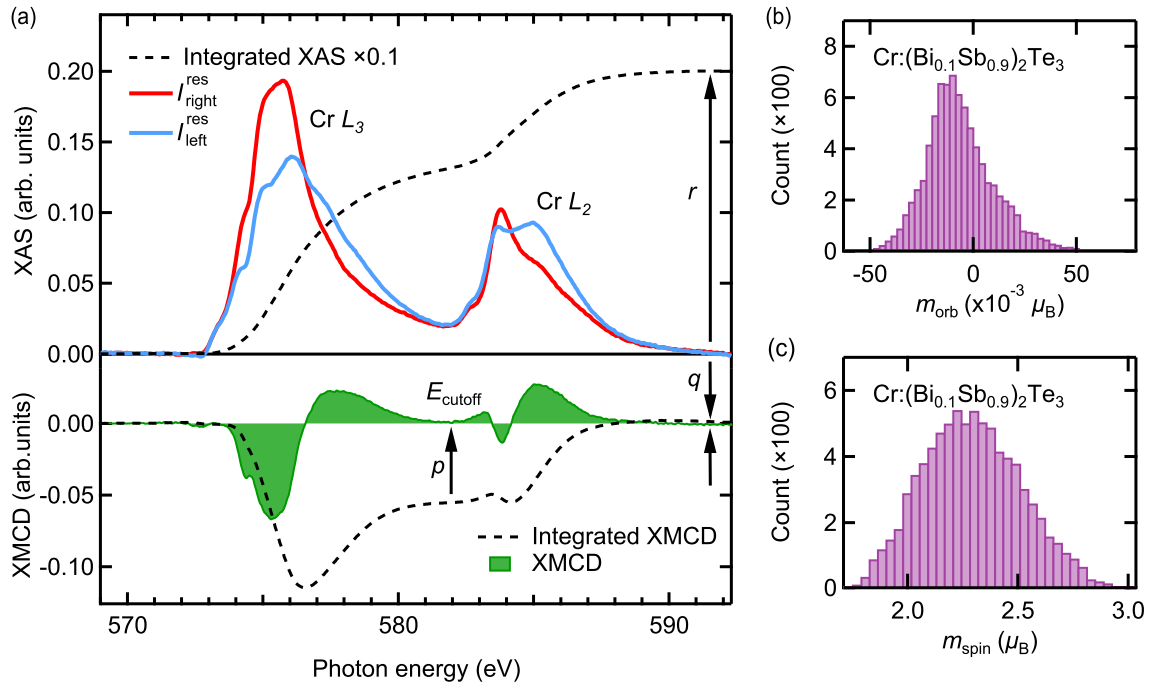

Figure 4.6: Sum rule analysis for Cr-doped $(Bi_{0.1}Sb_{0.9})_2Te_3$ thin film. (a) Left- and right-circularly polarized XAS spectra of Cr $L_{2,3}$ edges and corresponding XMCD spectrum. The dashed lines indicate the integrated total XAS and XMCD spectra. The arrows indicate r, p and q values defined in the manuscript. As one can notice integration of XMCD over both edges gives almost zero value of q. (b) and (c) Distribution of m_{orb} and m_{spin}, respectively, obtained my applying sum rule analysis 8000 times.

of distinct impurity valencies on different sites, as well as the simultaneous incorporation in the van der Waals gap or metallic impurity segregation. Optimized values of the Slater integrals and spin–orbit coupling constants used in the calculations for V $2p^63d^2$ and Cr $2p^63d^3$ initial state and for V $2p^53d^3$ and Cr $2p^53d^4$ final state are shown in Table 4.1. The listed Slater integrals indicate reduction to 65% (V) and 70% (Cr) of their original Hartree–Fock values. Due to the relaxation of atomic orbitals upon the $2p \rightarrow 3d$ excitation, we used separate sets of Slater integrals and the spin–orbit coupling constants ζ_{3d} for initial and final states, which improves the agreement between the calculated and experimental spectra.

The parameters used for the calculations best reproducing our data are listed in Table 4.2. It is well known that complex nonlinear fits [273] may be weakly sensitive to some of the fit parameters [274]. In our particular case we were fitting simultaneously XAS and XMCD spectra, which greatly mitigates these kind of problems. For example, XAS is weakly sensitive to the CT energy Δ and the on-site Coulomb repulsion U_{dd}, but inclusion of the XMCD into the merit function restores the sensitivity to these parameters. Having pinned down the optimal fit parameters by minimizing the merit function, we then checked the robustness by varying the parameters around their optimal values

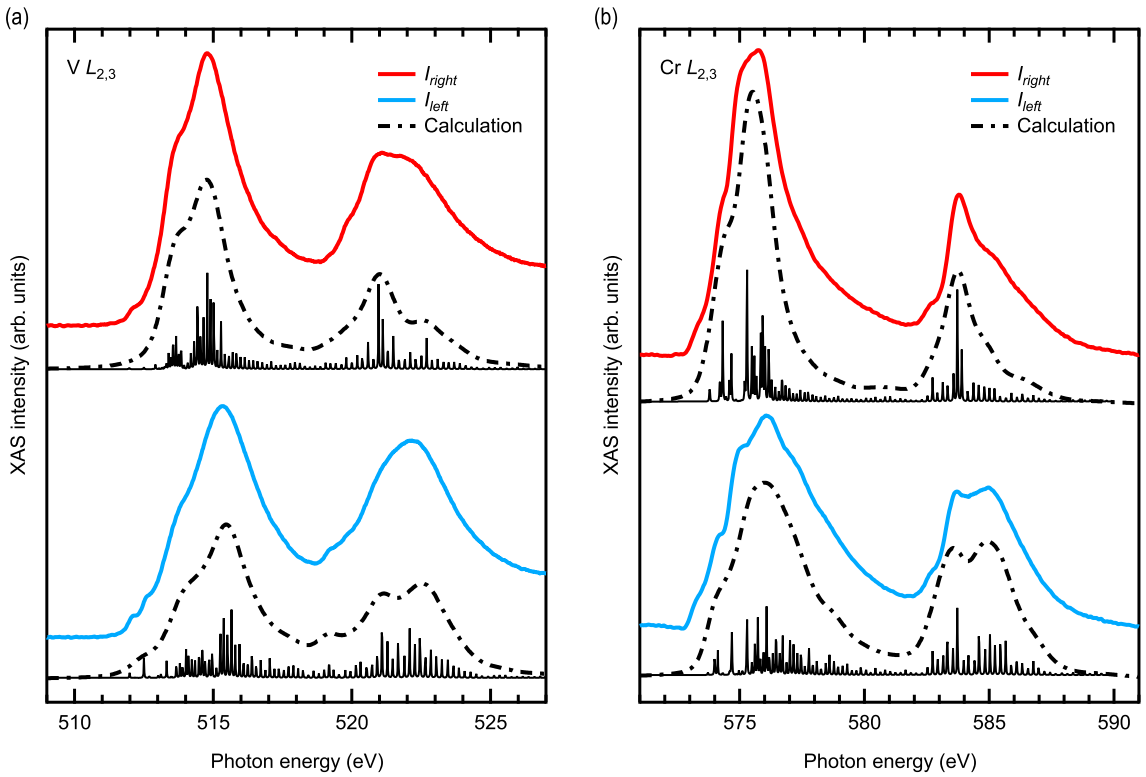

Figure 4.7: Experimental right- (solid red line) and left-circularly (solid blue line) polarized XAS spectra of (a) V $L_{2,3}$ edges and (b) Cr $L_{2,3}$ edges with corresponding calculated spectra (black dash-dotted lines). Delta peaks indicate the multiplet structure. A good agreement is observed between theory and experiment, validating the fitted parameters listed in Table 4.1 and Table 4.2.

in an uncorrelated manner, until a significant deviation between the modeled and measured data was obtained. In this way we were able to determine the uncertainties of the optimized fit values and the resulting d-shell occupation n_d, orbital and spin moments (see Table 4.3).

The experimental and theoretical values of the input parameters listed in Table 4.2 are well known for oxides [250, 275, 276]. For our compounds, in contrast to the oxides with more electronegative O ligands, one would expect a lower CT energy Δ, down to negative values as in the case of Cr_2Te_3 [271]. Prior to discussing our MLFT calculations, for simplicity, we can assume zero hoppings to the Te ligands. In this case, for the negative energy difference, $\Delta = E(d^{n+1}\underline{L}) - E(d^n)$, not the nominal configuration d^n, but the one with a ligand hole ($d^{n+1}\underline{L}$) becomes the actual ground state (see Fig. 3.16).

Indeed, the optimal fit yields $\Delta = -2.5$ eV for V and $\Delta = -2.0$ eV for Cr. As expected from the simplified considerations, these negative CT energies lead to a strong deviation from the nominal 3+ ionic ground state (see Table 4.3). The effect of the negative CT energy is so profound that the contribution of the nominal configuration is less than $\sim$10%.

Furthermore, the nonvanishing hoppings used in the calculation result in considerable contribution to the ground state from several different configurations, as illustrated in the

Table 4.1: Optimized Hartree-Fock values of the Slater integrals and spin–orbit coupling constants for V^{3+} and Cr^{3+} ions (in units of eV).

ion	state	configuration	$F_{dd}^{(2)}$	$F_{dd}^{(4)}$	ζ_{3d}	$F_{pd}^{(2)}$	$G_{pd}^{(1)}$	$G_{pd}^{(3)}$	ζ_{2p}
V^{3+}	initial	$2p^6 3d^2$	6.583	4.130	0.027				
	final	$2p^5 3d^3$	7.133	4.477	0.036	3.937	2.853	1.622	4.650
Cr^{3+}	initial	$2p^6 3d^3$	7.544	4.728	0.035				
	final	$2p^5 3d^4$	8.117	5.089	0.047	4.568	3.350	1.905	5.668

inset to Fig. 4.2. The small weight of the last configuration indicates that three charge-transfer states along with the nominal configuration are already sufficient for a correct microscopic physical model.

The observed considerable contributions of different configurations might in part be due to the local contraction of the ligand atoms towards the TM ion, compared to the undisturbed Te–Sb distance. This contraction was demonstrated by *ab initio* calculations [26, 277] and observed in extended X-ray absorption fine structure (EXAFS) experiments [278], which show direct evidence of structural relaxations around TM ions.

The calculated total spin and orbital angular momenta, as well as d-shell electron occupations are listed in Table 4.3. The resulting number of $3d$ electrons is $n_d = 3.47$ for V and $n_d = 4.33$ for Cr, which is much larger than the nominal $n_d = 2$ for V^{3+} and $n_d = 3$ for Cr^{3+} ions. In this context, it is worth noting that our analysis is consistent with a picture, in which the electronic charge is redistributed within the (V/Cr)-Te covalent bonds and does not contribute to the free carrier concentration.

For an isolated d-shell with d^3, d^4 or d^5 filling, placed in a crystal field of octahedral symmetry, one would expect a *complete* quenching of the orbital angular momentum and corresponding magnetic moment [279]. In reality, the orbital angular momentum is always partially unquenched. Among the reasons for the unquenching one would name spin–orbit coupling and hybridization with ligands. Indeed, for Cr we find an almost completely quenched orbital magnetic moment $m_{\mathrm{orb}} = -0.03\mu_{\mathrm{B}}$, mainly determined by the contribution of the $d^4\underline{L}$ configuration to the ground state, as can be seen in Table 4.3. In contrast, we see that both in experiment and theory vanadium consistently exhibits a

Table 4.2: Input parameters for the MLFT calculations obtained from the fit of XAS/XMCD spectra for $V_{0.1}Sb_{1.9}Te_3$ and $Cr_{0.1}(Bi_{0.1}Sb_{0.9})_{1.9}Te_3$ (in units of eV).

	$10Dq$	Δ	U_{dd}	U_{pd}	V_{e_g}	$V_{t_{2g}}$
$V_{0.1}Sb_{1.9}Te_3$	1.1	−2.5	3.8	4.6	1.1	0.65
$Cr_{0.1}(Bi_{0.1}Sb_{0.9})_{1.9}Te_3$	1.2	−2.0	3.5	4.2	1.4	0.82

Table 4.3: Configuration contribution to the ground state (see Eq. (3.45)), electron occupation n_d, z-component of orbital and spin angular momenta in units of $\hbar$, for V- and Cr-doped samples. The relative errors do not exceed about 10% and were estimated by varying the fit parameters to obtain statistically significant deviation between the modeled and measured XAS/XMCD spectra.

ion	expectation value	d^2	d^3	d^4	d^5	d^6	total
V^{3+}	$\langle\Psi_n\|\Psi_n\rangle$	0.049	0.484	0.413	0.054	–	1.000
	$\langle\Psi_n\|\hat{n}_d\|\Psi_n\rangle$	0.098	1.452	1.652	0.270	–	3.472
	$\langle\Psi_n\|\hat{L}_z\|\Psi_n\rangle$	0.062	0.306	0.169	0.015	–	0.552
	$\langle\Psi_n\|\hat{S}_z\|\Psi_n\rangle$	−0.049	−0.565	−0.514	−0.065	–	−1.193
Cr^{3+}	$\langle\Psi_n\|\Psi_n\rangle$	–	0.104	0.500	0.354	0.042	1.000
	$\langle\Psi_n\|\hat{n}_d\|\Psi_n\rangle$	–	0.312	2.000	1.770	0.246	4.328
	$\langle\Psi_n\|\hat{L}_z\|\Psi_n\rangle$	–	0.007	0.019	0.004	0.000	0.030
	$\langle\Psi_n\|\hat{S}_z\|\Psi_n\rangle$	–	−0.156	−0.808	−0.586	−0.059	−1.609

much larger $m_{\mathrm{orb}} = -0.55\mu_{\mathrm{B}}$, determined by the contribution of the $d^3\underline{L}$ and $d^4\underline{L}^2$ configurations. In view of comparable spin–orbit couplings and hybridization with the ligands, this may first seem unexpected. However, even in the aforementioned simple model of quenching [279], the d-shell filling plays a decisive role. In our realistic case, due to the complex interplay between spin–orbit coupling, Coulomb repulsion and hybridization to ligands, the resulting effect can only be understood quantitatively. To illustrate this in more detail, we vary the charge-transfer energy Δ, which affects the d-shell electron occupation, and plot in Fig. 4.8 the resulting expectation value of the orbital angular momentum. We clearly see how the increase of Δ leads to the expected decrease of d-shell occupation n_d and consequently to unquenching of the orbital moment. Hence, the difference between V and Cr becomes more evident, as the Cr has larger d-shell filling.

Now, we can compare the magnetic moments obtained using the sum rule analysis with those resulting from MLFT calculations. For V, the sum rule derived moments $m_{\mathrm{spin}} = (2.0 \pm 0.3)\mu_{\mathrm{B}}$/atom and $m_{\mathrm{orb}} = (-0.38 \pm 0.05)\mu_{\mathrm{B}}$/atom are reasonably close to the calculated $m_{\mathrm{spin}} = 2.39\mu_{\mathrm{B}}$/atom and $m_{\mathrm{orb}} = -0.55\mu_{\mathrm{B}}$/atom. This considerable m_{orb} could be related to the substantial magnetocrystalline anisotropy experimentally observed in V-doped Sb_2Te_3 [8, 76]. As for Cr, the sum rules provide consistent value for the orbital magnetic moment $m_{\mathrm{orb}} = (-0.01 \pm 0.02)\mu_{\mathrm{B}}$/atom, but not for the spin magnetic moment. The sum-rule derived spin moment for Cr $m_{\mathrm{spin}} = (2.3 \pm 0.5)\mu_{\mathrm{B}}$/atom is much smaller than the calculated one, $m_{\mathrm{spin}} = 3.22\mu_{\mathrm{B}}$, which could be attributed to the ambiguity in disentangling the overlapping Cr and Te edges. After all, the calculated total magnetic moments, $m_{\mathrm{tot}} = -2\langle S_z\rangle - \langle L_z\rangle = 1.84\mu_{\mathrm{B}}$/atom for V and $m_{\mathrm{tot}} = 3.19\mu_{\mathrm{B}}$/atom for Cr, are consistent with SQUID measurements [8] and recent DFT calculations [26, 30]

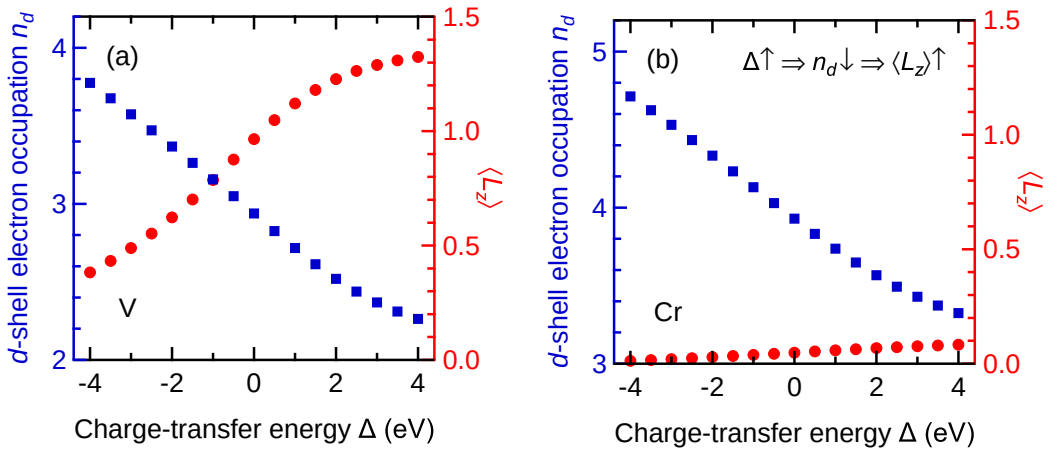

Figure 4.8: *d*-shell electron occupation n_d (blue squares) and expectation value of the orbital angular momentum $\langle L_z \rangle$ (red circles) of (a) V and (b) Cr as function of the charge-transfer energy Δ. Taken from Ref. [79].

for these systems.

4.6 *pd* hybridization – inducing magnetic moment at Te and Sb site

Our results confirm a strong charge-transfer effect from the host into the TM 3*d* states, with an enhanced covalency and a considerable *pd* hybridization taking place between TM dopants and host material. The strong *pd* hybridization is an important indicator for determining the type of exchange coupling mechanism and understanding ferromagnetism in these systems. It could induce magnetic moments at the otherwise non-magnetic Te and Sb atoms in the host lattice. To confirm this, we have measured XMCD spectra at Sb and Te $M_{4,5}$ absorption edges. Fig. 4.9 (a, b) shows XAS spectra (top panels) and XMCD spectra (bottom panels) measured at Sb $M_{4,5}$ edges of Cr- and V-doped samples, respectively. A clear reversal of left- and right-circularly polarized XAS intensities (blue and red curves, respectively) between Sb M_5 and M_4 edges indicates a substantial dichroism at the Sb site. The atomic concentration of Cr and V is identical in the respective samples, hence we can directly compare the strength of Sb XMCD between Cr- and V-doped samples. To do so, we have normalized the signal to the area under Sb M_4 edge after accurate background correction. The M_4 edge was chosen due to the overlap of the Sb M_5 edge with the O K-edge at 532 eV (the oxygen contamination comes from the beamline and shows no dichroism), which could lead to less reliable results. Moreover, for the V-doped sample the Sb M_5 absorption edge is close to V L_2 edge, which leads to an overlap of XMCD signals as seen in the low energy tail of the XMCD spectrum in the bottom panel of Fig. 4.9 (b). Using mean square deviation from zero as a measure for the

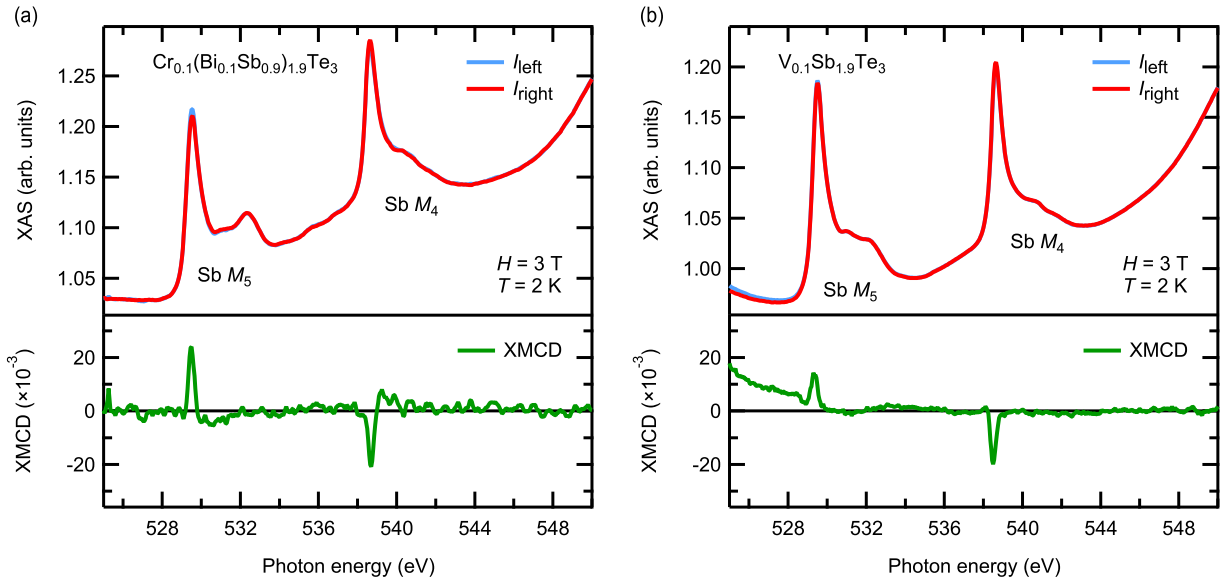

Figure 4.9: XAS and XMCD spectra measured around the Sb $M_{4,5}$ edges ($3d \rightarrow 5p$) of (a) $Cr_{0.1}(Bi_{0.1}Sb_{0.9})_{1.9}Te_3$ and (b) $V_{0.1}Sb_{1.9}Te_3$. Top panel: XAS spectra for left- (light blue curve) and right- (dark red curve) circularly polarized X-rays. Bottom panel: normalized XMCD spectra (green curve). Taken from Ref. [79].

dichroic strength, we found Sb XMCD to be 20% stronger in the Cr-doped sample than in the V-doped one.

Fig. 4.10 shows the circularly polarized XAS spectra of the V-doped sample measured at Te $M_{4,5}$ edges in an external magnetic field of 3 T. The corresponding XMCD spectrum plotted in green reveals a small magnetic moment induced at the Te site. Due to the very small size of the Te XMCD signal, this becomes a very challenging measurement, especially for thin films, requiring high signal quality and considerable statistics. Remarkably, here we were able to measure XMCD at $M_{4,5}$ edges with a robust XMCD line shape showing reversal of XMCD sign between M_4 and M_5 edges. As illustrated in Fig. 4.2 (a), the spectra of the Cr-doped sample exhibit XMCD at the Te $M_{4,5}$ edges as well. However, the strong energy overlap of the Te $M_{4,5}$ and the Cr $L_{2,3}$ edges in this sample hinders the direct comparison of Te XMCD strength with the V-doped system.

To investigate the presence of magnetic moments at the Sb and Te sites even with remnant magnetization, we measured Sb and Te $M_{4,5}$ XMCD at saturation and remanence, as shown in Fig. 4.11, confirming the ferromagnetic character of the ordering. As for the magnetic-field dependence, measuring the XMCD hysteresis curves in general is very time-consuming and specially the Te and Sb edges show very weak signal (an order of magnitude smaller than the V/Cr edges), in addition to large fluctuations and uncertainties at low-fields. We found these measurements for the Te and Sb edges not feasible. Instead, it is sufficient to measure XMCD at just two fields (saturation 3 T and remanent 0.01 T) to show nonzero intensity at zero magnetic field, indicating spontaneous magnetization in both the dopant and the host lattice.

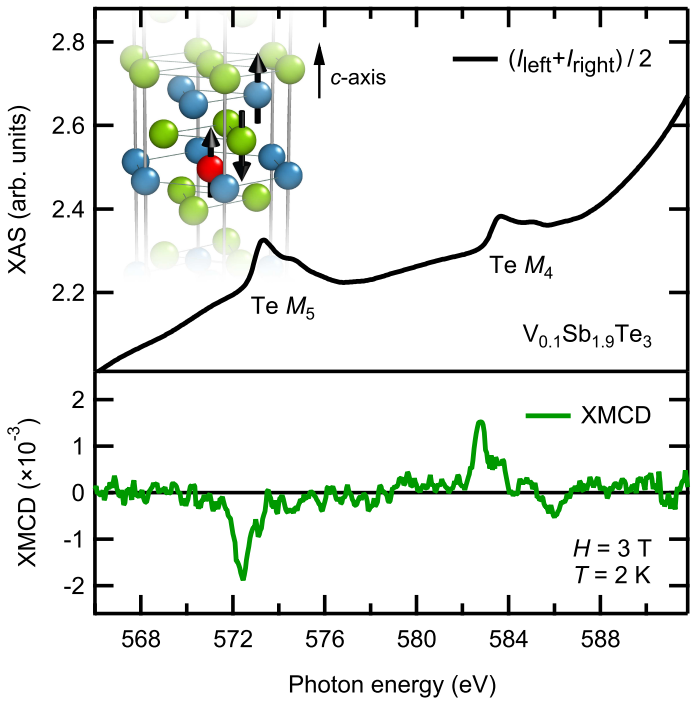

Figure 4.10: Averaged XAS (black curve) measured at the Te $M_{4,5}$ edges ($3d \rightarrow 5p$) of a $V_{0.1}Sb_{1.9}Te_3$ film. The green curve shows the corresponding XMCD spectrum $(I_{\text{left}} - I_{\text{right}})$ measured at $T = 2$ K and $H = 3$ T. The inset illustrates the relative magnetic moment orientations of TM ion and neighboring Te and Sb atoms within the one quintuple layer. Taken from Ref. [79].

In general, the strength of XMCD at Sb and Te sites is expected to depend on the TM doping concentration and the degree of pd hybridization [29, 30, 80]. One might assume that Sb has a pure ionic configuration [Kr] $4d^{10}\,5s^2\,5p^0$ with complete shells, and hence should exhibit no induced moment. However, this is not fully correct. In the Sb_2Te_3 systems, similar to the diluted semiconductors [105, 107], the p states are the main charge carriers. Thus the Sb $5p$ shell is not empty and exhibits a magnetic moment induced by the exchange interaction between the V/Cr and the Sb, even though it is of longer range than that between V/Cr and Te. So the same effect which results in a measurable XMCD at the Te $M_{4,5}$ edge also yields a non-vanishing XMCD at the Sb $M_{4,5}$ edge. This is further supported by the DFT analysis, showing that the main contribution to magnetic moments of Sb and Te results from the p states [30, 78, 80].

Further, we notice that the similar intensity of the XMCD signal with opposite signs at M_5 and M_4 edges suggests, according to the sum rules, that the total magnetic moments at Sb/Te sites are dominated by the contribution of the spin magnetic moment. However, uncertainties in the background determination and in the separation of the spectral weight of the Sb M_5 edge from the weight of the V edges, which lie a few eV below, prohibit a quantitative statement. The sign of the XMCD signal allows us to derive the mutual orientation of the moments at the TM substituent and the neighboring Te and Sb atoms. Keeping in mind that V/Cr $L_{2,3}$ edges correspond to $2p \rightarrow 3d$ transition, whereas

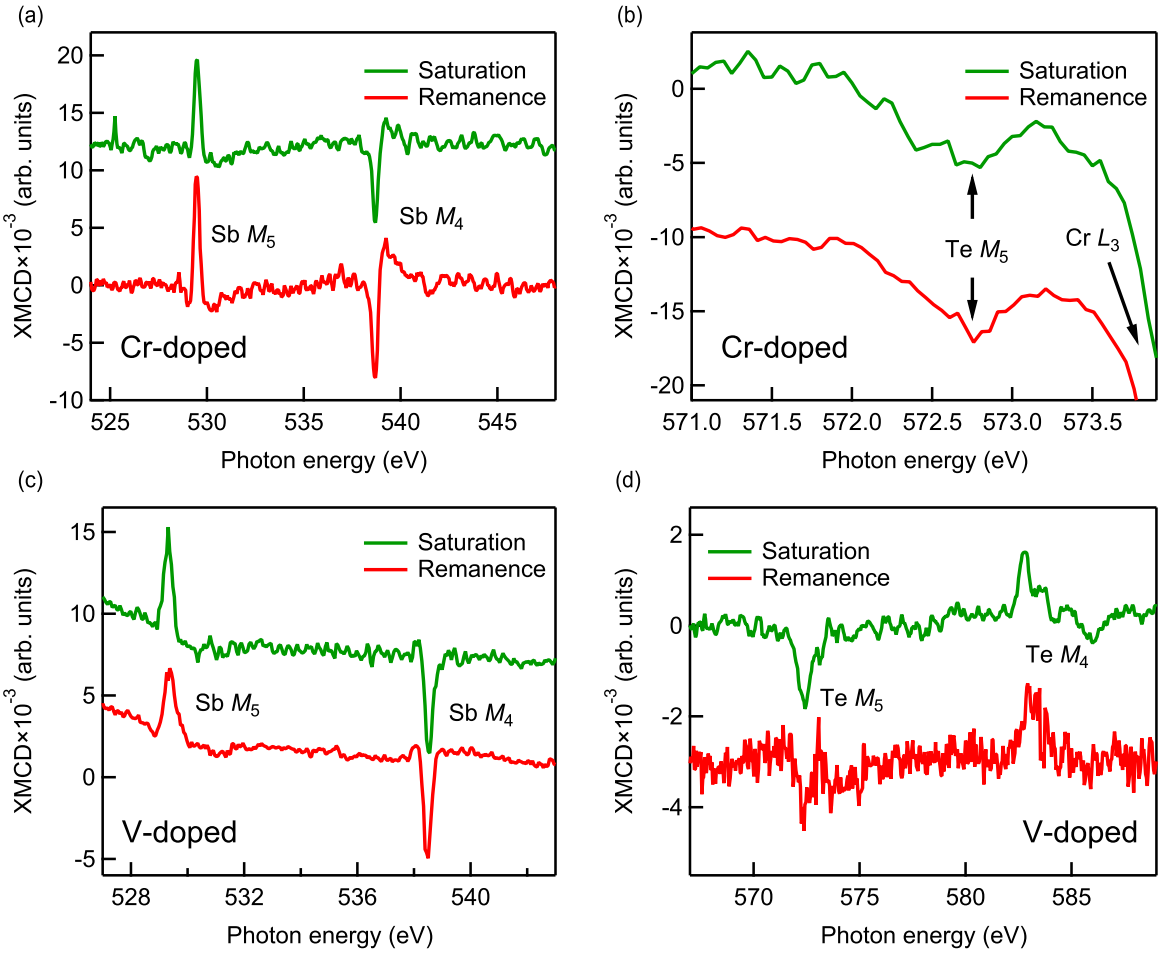

Figure 4.11: Sb $M_{4,5}$ XMCD in (a) a Cr-doped and (c) a V-doped sample, measured in remanence (red line) and saturation (green line) at 2 K. (b) and (d) Remanent and saturation XMCD signal at the Te $M_{4,5}$ absorption edges. The Cr $L_{2,3}$ edges overlay with Te $M_{4,5}$, hindering the direct comparison with the Te XMCD in the V-doped sample. Note that XMCD signals are not normalized, therefore one should not directly compare the intensities.

Sb/Te $M_{4,5}$ edges correspond to a $3d \rightarrow 5p$ transition, the opposite sign of XMCD for V/Cr and Sb edges indicates a parallel coupling between V/Cr $3d$ and Sb $5p$ moments, and the same sign of V/Cr and Te XMCD indicates an antiparallel alignment of their moments [280]. Hence, the relative magnetic moment orientations can be summarized as (TM,Sb)↑-(Te)↓ (see also the inset of Fig. 4.10), in good agreement with theoretical predictions [30].

4.7 Summary

In this chapter, we have studied the electronic and magnetic properties of V- and Cr-doped thin films of the TI $(Bi,Sb)_2Te_3$. Similar to our earlier works [281, 282], we have

constructed a MLFT model for the TM dopants in $(Bi,Sb)_2Te_3$. By analyzing the experimental XAS and XMCD, we obtained the values for the charge-transfer, Coulomb repulsion and hybridization energies, as well as for the crystal-field and Slater integrals, which will serve as an important input to future atomic multiplet calculations on similar systems.

The model clearly shows a strong charge-transfer from the Te ligands to the V/Cr $3d$ states, such that the nominally ionic $3+$ configuration contributes less than 10% to the ground state, while the major contribution is due to configurations with one and two ligand holes. This observation can be understood as a combined effect of a strongly negative charge-transfer energy and a considerable hybridization between TM $3d$ and ligand $5p$ states. The *pd* hybridization and, hence, the admixture of different configurations might in part be due to the local relaxation of the ligands toward the TM, as evidenced by *ab initio* calculations [277] and EXAFS experiments [278].

The MLFT fits allowed us to circumvent the inadequacy of the XMCD spin sum rule for the early transition metals and determine the orbital and spin moments directly from the many-particle ground state. In good agreement with published magnetometry data [8, 263], we have obtained total magnetic moments of $3.19\mu_B$ for Cr and $1.84\mu_B$ for V. In formal agreement with the expected quenching of the orbital moment for the d^3 configuration, the orbital magnetic moment on Cr is negligibly small, whereas for V we obtain $-0.55\mu_B$. The seeming violation of this expectation is a natural outcome of the d-shell filling, non-negligible hoppings to the ligands and effects of the spin–orbit interaction. The unquenched orbital moment could explain the substantial magnetocrystalline anisotropy observed in V-doped samples [8, 76].

Our measurements further show that not only the magnetic dopants V and Cr carry a magnetic moment, but also the nominally non-magnetic host atoms Sb and Te possess spin-derived moments. The magnetism of the Sb and Te atoms suggests that the observed local magnetic coupling mechanism might be in part mediated by Sb/Te $5p$ states through *pd* hybridization, following the Zener-type *pd*-exchange interaction scenario [27–30, 78]. Indeed, our work shows that *pd* hybridization yields a strong entanglement between charge transfer and magnetic ground state.

We provide a detailed microscopic insight into the electronic and magnetic properties of the magnetically doped 3D TI. Our results show that V with a d-shell electron occupation of $n_d = 3.47$ exhibits a more robust FM order as compared to Cr with $n_d = 4.33$, confirming the spin-polarized first-principle calculations by Vergniory *et al.* [29], which showed that the effective exchange interaction is reduced with the number of d electrons per TM atom. The differences in the magnetic ground state between V and Cr imply differences in the $3d$ local density of states, as recently observed in scanning tunneling spectroscopy [283] and resPES [104]. This could point to the origin of the more robust realization of the ideal QAH state in V-doped systems as compared to Cr-doped systems.

A deeper insight would require a systematic element-specific study of ground state electronic and magnetic properties of V and Cr impurities at the thresholds of the QAH effect and the recently reported metal-insulator transition at mK temperatures [284].

Chapter 5

The nature of ferromagnetism in the V- and Cr-doped topological insulator $(Bi,Sb)_2Te_3$

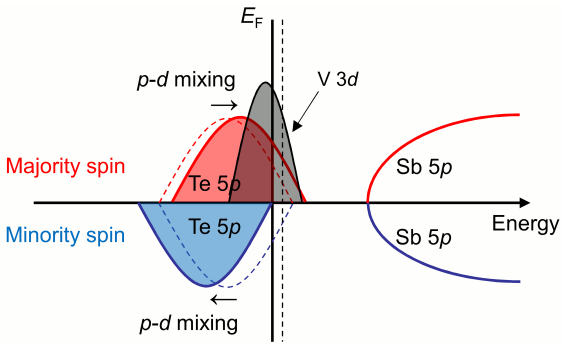

The discovery of the quantum anomalous Hall (QAH) effect in the magnetic topological insulators (MTIs) Cr:$(Bi,Sb)_2Te_3$ and V:$(Bi,Sb)_2Te_3$ raised a long-standing debate about their unexpectedly discrepant magnetic properties. Particularly, the magnetic coupling mechanisms underlying the onset of ferromagnetism in this MTIs have been intensively disputed and a variety of different scenarios have been put forward, as discussed in Chapter 2. It has been suggested that the variations in magnetic properties arise from differences in the electronic structure of the two systems [8]. However, there is still no comprehensive understanding of how these variations are related to the local electronic structure of the V and Cr impurities.

In this chapter, the open questions of the electronic states inducing the ferromagnetic (FM) coupling in MTIs are addressed. By combining key experiments, such as resonant photoemission spectroscopy (resPES) and x-ray magnetic circular dichroism (XMCD), with theoretical approaches, such as density functional theory (DFT) and multiplet ligand field theory (MLFT), the fundamental link between local impurity electronic structure and magnetic coupling in V- and Cr-doped $(Bi,Sb)_2Te_3$ thin films is established. Section 5.2 summarizes the results of Dr. Thiago Peixoto *et al.* [108], which explain the important role of impurity-state-mediated exchange interactions underlying the magnetic properties of MTIs. There I have contributed with measurements and MLFT analysis of the XAS/XMCD data. Next, in Section 5.3 I extend the ideas presented in Ref. [108] with the systematic analysis of the local electronic and magnetic properties of V-doped $(Bi,Sb)_2Te_3$ thin films as a function of impurity concentration.

5.1 Methods

5.1.1 Sample preparation and characterization

Thin films (about 9–10 nm thick) of $Cr_z(Bi_{1-x}Sb_x)_{2-z}Te_3$ and $V_z(Bi_{1-x}Sb_x)_{2-z}Te_3$ were grown by molecular beam epitaxy (MBE) on hydrogen-passivated Si(111) substrates and structurally characterized by Dr. Martin Winnerlein and Dr. Steffen Schreyeck from the department of Prof. Laurens W. Molenkamp, Universität Würzburg. The growth details and characterization, e.g. by x-ray diffraction, atomic force microscopy and Hall magnetotransport, confirming the realization of the QAH effect in the V-doped samples (for $x = 0.76 - 0.79$ and $z = 0.1 - 0.2$), are published elsewhere [20, 68, 137, 266]. After the growth, the films were capped by a protective Te layer (about 100 nm), which was mechanically removed in UHV conditions, prior to the spectroscopic measurements, revealing a chemically clean surface, see Fig. 5.1. Recent results have demonstrated the effectiveness of this decapping method on Bi_2Te_3 layers with high pristine quality [267]. The stoichiometries applied in this work are comparable to those that exhibited a stable and reproducible QAH effect.

5.1.2 XAS, XMCD and resPES

The XAS and XMCD data was acquired at the HECTOR end station, located at the BOREAS beamline of the ALBA storage ring (Barcelona, Spain) [204]. The detailed description of the end station in given in Section 3.2.3. The measurements were performed in total electron yield mode (TEY), under magnetic fields of up to 6 T and at temperatures down to 5 K.

The resPES experiments were conducted at the ASPHERE III end station located at beamline P04 of the PETRA III storage ring of DESY (Hamburg, Germany) by Philipp Kagerer and Dr. Thiago R. F. Peixoto from the group of Prof. Friedrich Reinert, Universität Würzburg. The on-resonant and off-resonant valence band photoemission spectra were taken at $h\nu_{on} = 514.8$ eV and $h\nu_{off} = 508$ eV for V-doped samples, and at $h\nu_{on} = 575.6$ eV and $h\nu_{off} = 560$ eV for Cr-doped ones, according to the respective XAS spectra in Fig. 5.2. The energy resolution of the resPES measurements was typically better than 67 meV. All experiments were performed in ultrahigh vacuum (UHV) at pressures below 3×10^{-10} mbar.

5.1.3 DFT calculations

The DFT calculations necessary for the understanding of electronic and magnetic properties of V and Cr impurities were performed by Dr. Philipp Rüßmann from the group of Prof. Stefan Blügel in Forschungszentrum Jülich. The Sb_2Te_3 and Bi_2Te_3 bulk crystals

were simulated using the experimental bulk lattice structure (see ref. [285] for Sb_2Te_3 and ref. [286] for Bi_2Te_3). The electronic structure was calculated within the local density approximation (LDA) [287] to DFT by employing the full-potential relativistic Korringa-Kohn-Rostoker Green's function method (KKR) [288, 289] with exact description of the atomic cells [290, 291]. The truncation error arising from an $l_{\max} = 3$ cutoff in the angular momentum expansion was corrected for using Lloyd's formula [292]. The V and Cr defects, together with a charge-screening cluster comprising the first two shells of neighboring atoms (consisting of about 20 surrounding scattering sites), were embedded self-consistently using the Dyson equation in the KKR method [289] and have been chosen to occupy the substitutional Sb/Bi position in the quintuple layers and structural relaxations were neglected, while keeping the direction of the impurity's magnetic moment fixed along the out-of-plane direction. The shift in the Fermi level occurring in $(Bi,Sb)_2Te_3$ was accounted for by adjusting the self-consistently computed Fermi level (E_F) of the host systems in the impurity embedding step. The exchange interactions among two impurities were computed using the method of infinitesimal rotations [293], which map the exchange interaction to the Heisenberg Hamiltonian $\mathcal{H} = \frac{1}{2}\sum_{\langle ij \rangle} J_{ij} \overrightarrow{s}_i \cdot \overrightarrow{s}_j$.

5.1.4 MLFT calculations

Theoretical XAS and XMCD spectra for the $L_{2,3}$ ($2p \rightarrow 3d$) absorption edges of V and Cr ions were calculated by means of a configuration interaction (CI) cluster model, considering the central TM ion surrounded by six ligands (Te anions). We take into account all the $2p-3d$ and $3d-3d$ electronic Coulomb interactions, as well as the SOC on every open shell of the absorbing atom. We consider nominal $2p^6 3d^n$ ($n = 2$ for V^{3+} and $n = 3$ for Cr^{3+}) configurations and further include three more charge-transfer (CT) states $d^{n+1}\underline{L}$, $d^{n+2}\underline{L}^2$ and $d^{n+3}\underline{L}^3$ ($\underline{L}^1$ denotes a hole in the Te $5p$ orbitals) to account for hybridization effects. To perform the CI calculation, the following fit parameters were introduced: scaling parameter β for the Hartree–Fock values of the Slater integrals, the CT energy Δ, the Coulomb interaction energy U_{dd} between the $3d$ electrons, the hybridization energy V_{e_g} and the octahedral crystal field parameter $10Dq$. The simulations were performed using the Quanty software for quantum many-body calculations, developed by Prof. M. W. Haverkort *et al.* [245]. We assume V/Cr ions embedded in the cation sites and describe the crystal field in O_h symmetry, with the C_4 axes of the octahedron along the V–Te bonds. The spectral contributions from each of the split ground state terms to the absorption spectra were weighted by a Boltzmann factor. The calculated spectra were broadened by a Gaussian function to account for the instrumental broadening and by an energy-dependent Lorentzian profile for intrinsic lifetime broadening. More details are given in Chapter 3.

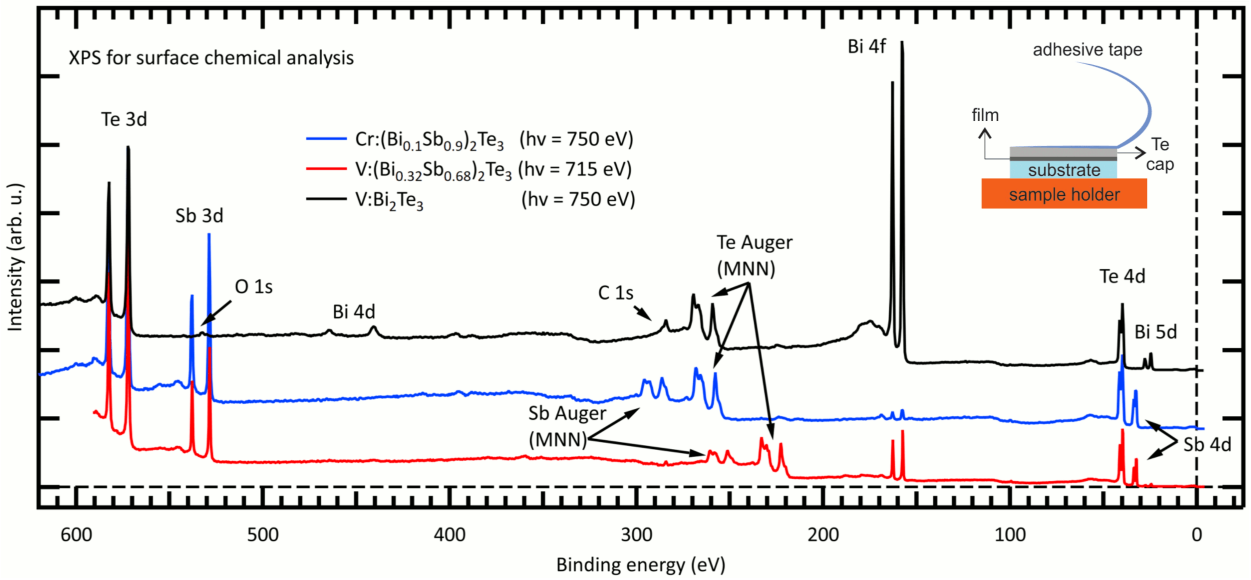

Figure 5.1: XPS spectra measured for the surface chemical analysis of the freshly cleaved samples used in this study, namely $V_{0.1}(Bi_{0.32}Sb_{0.68})_{1.9}Te_3$ (red curve, taken at $h\nu = 750$ eV), $Cr_{0.1}(Bi_{0.1}Sb_{0.9})_{1.9}Te_3$ (blue curve, taken at $h\nu = 750$ eV) and $V_{0.1}Bi_{1.9}Te_3$ (black curve, taken at $h\nu = 715$ eV), for the surface chemical analysis. All main host elemental core level peaks are identified, showing pristine intrinsic line shapes and respective plasmon features, and no traces of oxidation or any other contamination. Auger MNN complexes from Te and Sb are also identified. The comparatively low cross section and low concentration of the V and Cr impurities preclude the observation of their peaks. Minute traces of oxygen (O 1s) and carbon (C 1s) are detected, most likely from the residuous gas inside the UHV chamber. The inset shows the schematic diagram of the cap layer removal technique. Adapted from Ref. [108].

5.2 Effect of impurity states on the magnetism in MTIs

5.2.1 Surface chemical analysis of the samples

We start with the surface chemical analysis of the samples conducted by Peixoto *et al.* [108]. After decapping the samples under UHV conditions (typically $p < 1 \times 10^{-8}$ mbar), XPS survey scans were performed in order to confirm the complete mechanical removal of the protective Te capping layer, and guarantee the chemical cleanness and pristine quality of the surface. In Fig. 5.1 the XPS survey scans of freshly decapped samples used in this study, taken at various photon energies within the soft x-ray range, are shown. The sharpest peaks are the main core level lines of all the elements of the host compound, namely Te 3d, Sb 3d, Bi 4f, Te 4d, Sb 4d and Bi 5d, which exhibit typical line shapes for the pristine systems, with no sign of oxidation, demonstrating a successful exfoliation of the Te cap. The Auger MNN complexes of Te and Sb are also identified, showing the expected shift with photon energy (i.e. appearing at constant kinetic energy). Each spectrum is normalized to the Te 3d peaks. The V and Cr 2p peaks can not be distinguished due to their comparatively low excitation cross section in the soft X-ray range in comparison to the host elements, and due to their very low concentration. Weak oxygen (O 1s) and

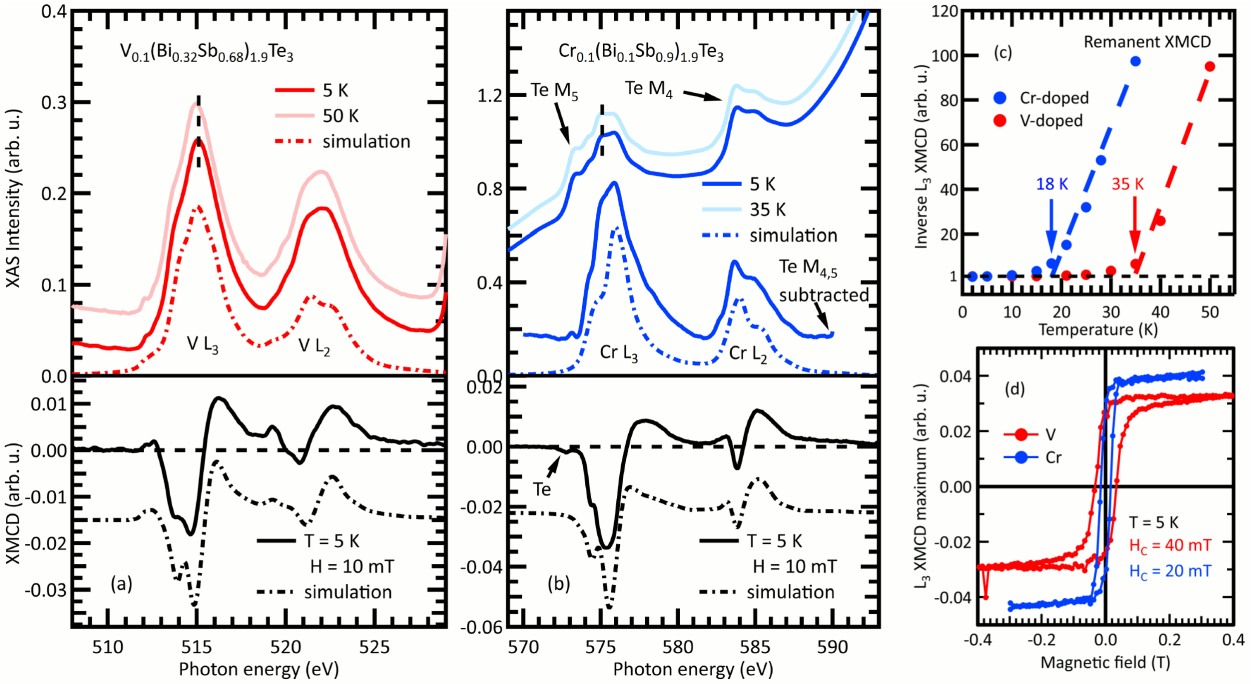

Figure 5.2: XAS (upper panels) and XMCD (lower panels) spectra of (a) $V_{0.1}(Bi_{0.32}Sb_{0.68})_{1.9}Te_3$ and (b) $Cr_{0.1}(Bi_{0.1}Sb_{0.9})_{1.9}Te_3$ thin films, respectively, at the V and Cr $L_{2,3}$ edges, taken at temperatures above (light colored curves) and below (dark colored curves) T_C. The contribution of the Te $M_{4,5}$ edges to the Cr $L_{2,3}$ spectrum in (b) was subtracted according to a reference spectrum measured on an undoped sample, and is also shown. The XMCD spectra (black circles) were measured in the remanent state, at 5 K, demonstrating a FM state for both systems. The small dip in the pre-edge of the Cr L_3 XMCD is attributed to the induced magnetic moment in the Te atoms. The corresponding dashed curves are spectra calculated by MLFT. (c) Temperature-dependence of the inverse remanent XMCD signal at the V (red circles) and Cr (blue circles) L_3 edges, from which $T_C(V) \sim 35$ K and $T_C(Cr) \sim 18$ K are estimated. (d) Hysteresis loops taken at the V and Cr L_3 edges, at 5 K, with the magnetic field applied in the out-of-plane direction, exhibiting coercive fields of $H_C(V) = 40$ mT and $H_C(Cr) = 20$ mT, respectively. Adapted from Ref. [108].

carbon (C 1*s*) peaks are detected, most likely coming from the residual gas inside the UHV chamber or outgassing from the sample surroundings, shortly after the mechanical exfoliation. These findings confirm the effectiveness of the *ex situ* mechanical removal method and guarantee a pristine surface quality of the van der Waals epitaxial thin films [267] studied here.

5.2.2 Electronic and magnetic ground state of V and Cr

The results presented here are from the study of Peixoto *et al.* [108]. Fig. 5.2 shows the XAS and XMCD spectra at the V and Cr $L_{2,3}$ edges, measured on $V_{0.1}(Bi_{0.32}Sb_{0.68})_{1.9}Te_3$ and $Cr_{0.1}(Bi_{0.1}Sb_{0.9})_{1.9}Te_3$ above and below the Curie temperature T_C. No energy shifts or changes in the branching ratio are observed at the $L_{2,3}$ edges with varying temperature across T_C, in contrast to the previous reports where an apparent energy shift was

interpreted as evidence of the van Vleck mechanism [101]. For the Cr case, we also show the intrinsic line shape, obtained by carefully subtracting a Te $M_{4,5}$ spectrum of an undoped reference sample. The XMCD spectra were measured at 5 K under a small applied magnetic field of 10 mT (remanent state), oriented perpendicular to the surface, i.e. along *c*-axis). They confirm a persistent FM state at this temperature, with a sizable magnetic moment carried by the TM 3*d* states in both V-doped and Cr-doped $(Bi,Sb)_2Te_3$ systems. The line shapes of our XAS and XMCD data demonstrate the pristine quality of the dilute MTI thin films, ruling out any possible clustering or oxidation, in good agreement with previous reports on V- and Cr-doped 3D topological insulators [78–80, 104]. Fig. 5.2 (c) shows the temperature dependence of the inverse L_3 XMCD signal for V- (red circles) and Cr-doped (blue circles) systems, in the remanent state. The extrapolation of the data near T_C, according to the Curie–Weiss law, allows us to estimate $T_C \approx 35$ K for the $V_{0.1}(Bi_{0.32}Sb_{0.68})_{1.9}Te_3$ and $T_C \approx 18$ K for the $Cr_{0.1}(Bi_{0.1}Sb_{0.9})_{1.9}Te_3$ films. Roughly a factor of 2 in T_C is found for the same V- and Cr-doping level, in good agreement with previous works [8, 29, 80]. Fig. 5.2 (d) shows low-field hysteresis loops at the V and Cr L_3 edges, taken at 5 K, with the magnetic field applied perpendicularly to the sample surface. The loops are square-shaped, exhibiting a relatively high remanence, as expected for an out-of-plane anisotropy, and coercive fields of $H_C(V) = 40$ mT and $H_C(Cr) = 20$ mT, respectively. The observed low coercivities reveal the typical soft ferromagnetic properties of dilute systems.

A state-of-the-art MLFT analysis (described in details in Section 3.5) has been performed to interpret the V and Cr $L_{2,3}$ line shapes and determine the magnetic ground state. As seen in Fig. 5.2 (a, b), the calculations reproduce all main features of the measured spectra, which is not possible if only combinations of integer ionic valencies are considered. We find a strong *pd* hybridization and a higher covalency in the ground state of the V and Cr impurities, i.e. a strong deviation from the 3+ ionic valence (V d^2, Cr d^3) [112, 113, 263]. The ground state is dominated by about 90% weight of charge-transfer states with one and two holes in the ligand orbitals. The resulting *d*-shell occupation is $d^{3.13}$ ($m_S = 2.33\mu_B$ per atom) for V and $d^{4.37}$ ($m_S = 3.32\mu_B$ per atom) for Cr, due to a substantial charge transfer (CT) from the ligand Te *p* states into the 3*d* impurity states, as a result of *pd* hybridization and the low electronegativity of the Te ligands [79]. Although the effective valence of the V and Cr impurities is strongly reduced (below 2+) from the nominal 3+ ionic valence, the assumption of nominally divalent ions in the MLFT model cannot reproduce the fine structure of the experimental line shapes [79] or the reported magnetic properties [8]. The observed spontaneous Te-(V, Cr) charge transfer is, therefore, attributed to the acceptor character of flat 3*d* impurity states at the top of the valence band in the presence of *pd* hybridization. Correspondingly, our first-principles calculations for single V and Cr impurities embedded in a quintuple layer of Sb_2Te_3 on an octahedral Sb

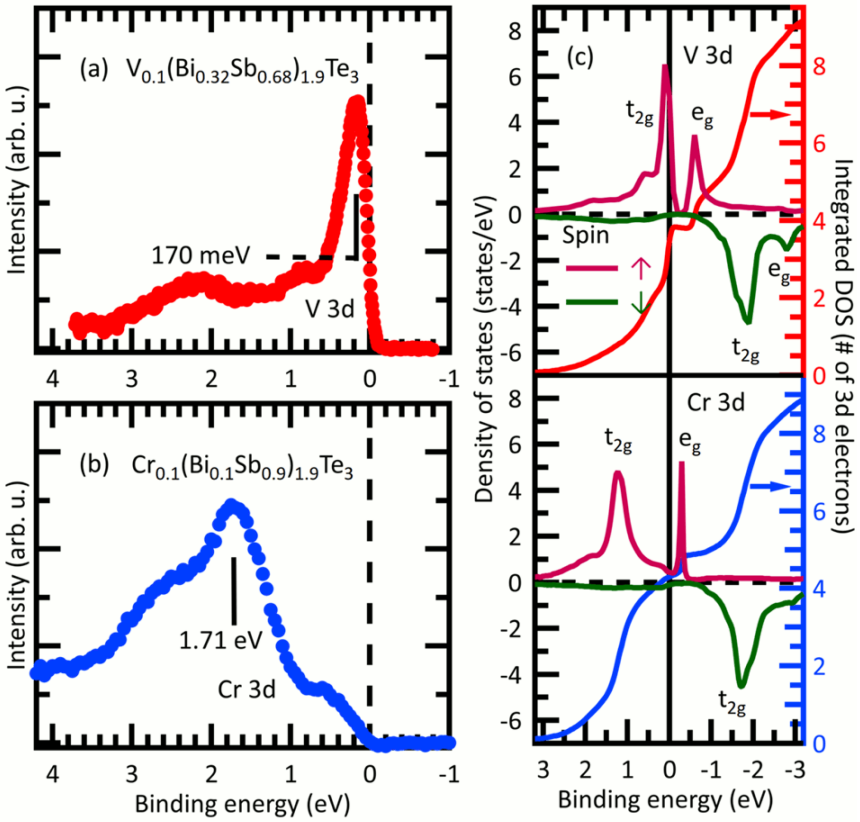

Figure 5.3: ResPES spectra at the L_3 edges of (a) V ($h\nu = 515$ eV) in $V_{0.1}(Bi_{0.32}Sb_{0.68})_{1.9}Te_3$ and (b) Cr ($h\nu = 575.6$ eV) in $Cr_{0.1}(Bi_{0.1}Sb_{0.9})_{1.9}Te_3$ thin films, at 30 K. (c) Calculated spin-up (magenta curves) and spin-down (green curves) 3*d* DOS and corresponding integrated DOS for substitutional V and Cr single impurities in Sb_2Te_3. The t_{2g} and e_g manifolds are identified. Taken from Ref. [108].

site, yield $d^{3.35}$ ($m_S = 2.51\mu_B$) and $d^{4.40}$ ($m_S = 3.72\mu_B$). This again confirms a substantial charge transfer from the ligand *p* states into the 3*d* impurity states as a result of *pd* hybridization.

5.2.3 Fingerprints of the impurity 3*d* states

To assess the contribution of the 3*d* states to the valence band (VB), resPES measurements at the V and Cr L_3 edges were conducted. The data shown in Fig. 5.3 (a, b) is obtained from the normalized difference between the on-resonant and off-resonant photoemission spectra, taken at 30 K, and represent the V and Cr 3*d* partial DOS. It illustrates a significant difference in the 3*d* DOS for V and Cr impurities. For V, the 3*d* states pile up predominantly in a narrow peak just below E_F with the center at $E_B = 170$ meV. On the other hand, the 3*d* states of Cr are broadly distributed over the VB of the host compound, with a maximum at $E_B = 1.71$ eV and low spectral weight near E_F. The first-principles calculations performed by Dr. Philipp Rüßmann nicely capture these main characteristics. Fig. 5.3 (c) shows the calculated spin-polarized 3*d* DOS and the corresponding integrated DOS for V (upper panel) and Cr (lower panel) impurities in Sb_2Te_3, which allow one to

assign the experimentally observed states to majority-spin (spin-up) t_{2g} states. The examination of the integrated 3*d* DOS at E_F allows one to extract the predicted *d*-shell filling of $d^{3.4}$ for V (red curve) and $d^{4.4}$ for Cr (blue curve) impurities, in good agreement with the MLFT analysis. Moreover, the calculations are able to reproduce the resPES data without self-interaction corrections, which suggests a minor role of the latter for the V and Cr occupied 3*d* states. While small self-interaction corrections tend to shift the 3*d* resonances deeper in the VB [27, 28, 30, 294], this is compensated by the natural charge doping of the host, as discussed below. These findings yet support previous resPES results [104, 265] and scanning tunnelling microscopy and spectroscopy studies of the electronic structure of V and Cr impurities in Sb_2Te_3 [30, 283, 295].

The presence of exchange-split 3*d* states at E_F leads to the emergence of localized magnetic moments and, possibly, long-range magnetic order. In order to study the effect of the impurity states on the magnetic coupling mechanism, we first consider the spin-up DOS of V and Cr impurities in Sb_2Te_3, calculated for different artificial shifts of the Fermi level (ΔE_F), i.e. different positions of E_F with respect to the bulk VB and conduction band (CB). This approach allows us to simulate the effect of *n*-type and *p*-type charge doping on the 3*d* states, i.e. the valence of the TM impurities [296]. The results for the spin-up V and Cr 3*d* DOS are shown in Fig. 5.4 (a, b). The grey-shaded areas correspond to the Sb_2Te_3 host total DOS, emphasizing the position of the impurity states with respect to the bulk band gap, where the topological surface states (TSS) typically lie. We find that the position of the impurity states depends sensitively on the charge doping, shifting towards higher binding energies when going from p-type (dark-colored curves) to n-type (light-colored curves) doping. In particular, the narrow V 3*d* peak gradually moves away from E_F. This trend is experimentally supported by our resPES data for $(Bi_{1-x}Sb_x)_2Te_3$ films with different Bi content, which will be discussed later in this chapter. For lower x, and thus higher *n*-doping [8, 25, 26], the V 3*d* peak shifts to significantly higher binding energies.

5.2.4 Magnetic exchange interactions

Next, the implications of the above findings for the magnetic exchange interactions are discussed based on the *ab initio* calculations performed by Dr. Philipp Rüßmann. Fig. 5.4 (c, d) shows the calculated exchange-coupling constants J_{ij} for different separation distances between two TM ions located in one atomic plane (intra-layer coupling, upper panels) and at neighboring atomic planes within the same quintuple layer (inter-layer coupling, lower panels), using the same ΔE_F values as in Fig. 5.4 (a, b)[1]. For both V and Cr, the inter-layer coupling is dominant, in good agreement with Ref. [29]. Overall, at nearest-neighbor (NN) distances the calculated J_{ij} contributions are larger for V,

[1] Note the corresponding color code.

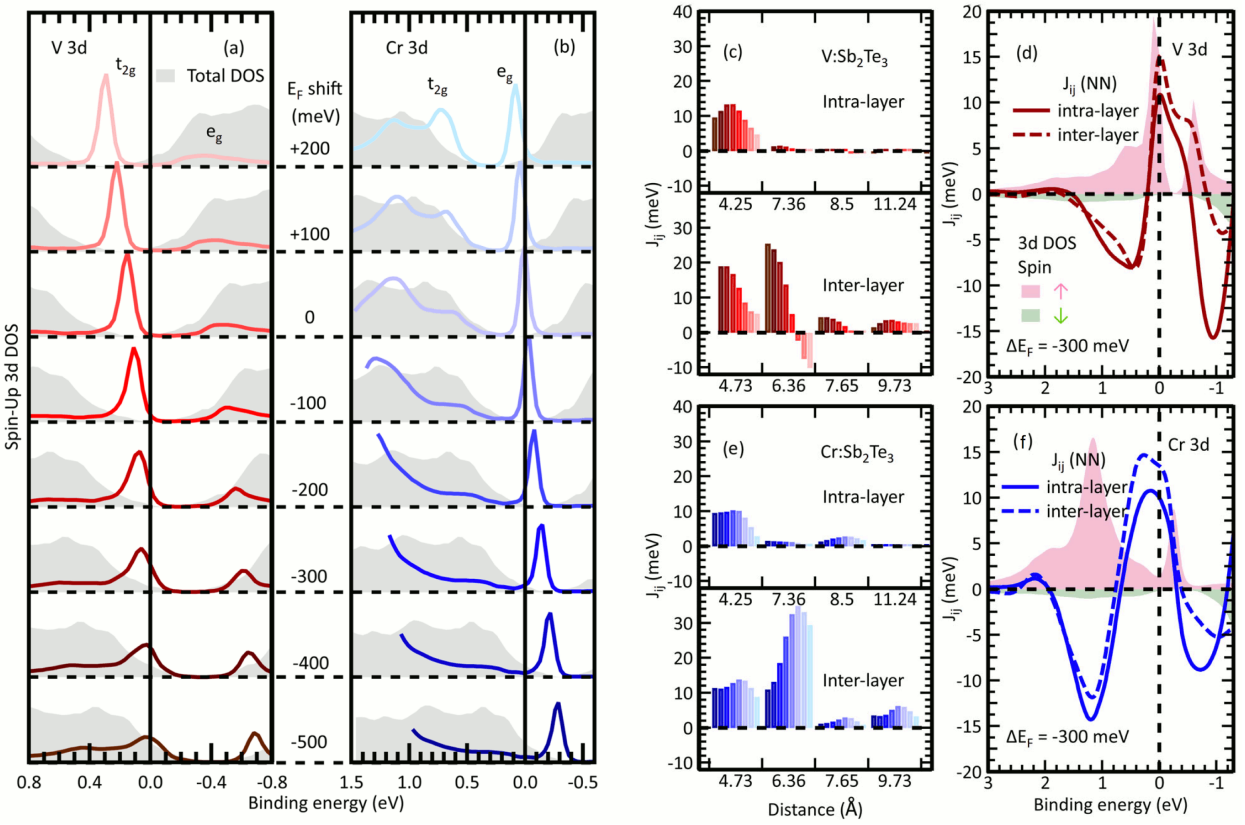

Figure 5.4: Spin-up partial 3*d* DOS of (a) V and (b) Cr impurities embedded in Sb_2Te_3, calculated for different positions of E_F in respect to the bulk VB and CB. The grey shaded areas correspond to the bulk total DOS of the Sb_2Te_3 host. (c) Intra-layer (upper panels) and inter-layer (lower panels) exchange coupling constants J_{ij} as a function of distance from the V and (d) Cr impurities, calculated for the same ΔE_F values as in (a) and (b) (note the corresponding color code). Energy dependence of the NN intra-layer (solid line) and inter-layer (dashed line) J_{ij}(E) in (e) V:Sb_2Te_3 and (f) Cr:Sb_2Te_3, for $\Delta E_F = -300$ meV. The corresponding spin-resolved 3*d* DOS are also plotted as shaded areas. Taken from Ref. [108].

while at the second and third neighbor positions the J_{ij} values for Cr are markedly larger. This behavior follows the spatial decay of the calculated impurity-induced features in the 3*d* DOS. Most importantly, the J_{ij} constant strongly varies with charge doping. Already small shifts of E_F give rise to considerable changes in J_{ij}, whose sign and strength are linked to characteristic features in the 3*d* DOS at E_F. For V, J_{ij} rapidly decreases in the *n*-doped regime, while for Cr the behavior is more complex and depends more strongly on the relative impurity positions. Fig. 5.4 (d, f) shows the energy dependence of J_{ij} for NN spins for $\Delta E_F = -300$ meV, which best corresponds to the experimental resPES data. The inter-layer and intra-layer components, shown as dashed and solid lines, exhibit qualitatively similar trends. In the same plots, the corresponding spin-up and spin-down 3*d* DOS are shown as shaded areas. For V, $J_{ij}(E)$ near E_F consists of a sharp peak overlapping with a broad flat ridge that spans between the onsets of the t_{2g} and e_g peaks. $J_{ij}(E)$ is maximum when E_F is positioned inside the V t_{2g} manifold, and

rapidly decreases otherwise. For Cr, the sharp peak in $J_{ij}(E)$ is absent, and only the broad ridge is seen. In sharp contrast to V, for Cr a maximal $J_{ij}(E)$ is found when E_F lies in the gap between the t_{2g} and e_g peaks. The calculated $J_{ij}(E)$ in Fig. 5.4 (f), thus, indicates a less pronounced dependence of the magnetic coupling on the E_F position for Cr. This may explain the stronger gate-voltage dependence of the magnetic properties observed in V-doped [8] as compared to Cr-doped films [9, 73, 113]. These distinct features in the V and Cr 3*d* DOS are fully in line with the resPES measurements in Fig. 5.3. Similar features in the exchange coupling constants have been extensively discussed in the context of dilute magnetic semiconductors [99, 100, 105, 277, 297–299]. By comparison, one may tentatively associate the sharp peak in $J_{ij}(E)$ for V with the double-exchange mechanism [28, 29, 78, 99, 297, 298, 300] and the broad ridge, found for both dopant types, with the FM superexchange mechanism [27, 105, 297, 299].

5.2.5 Influence of host stoichiometry on the impurity 3*d* states

To verify the predicted trends of the impurity-mediated magnetic exchange interactions with the charge doping of the host, the impact of the host stoichiometry on the local electronic and magnetic properties of V-doped $(Bi_{1-x}Sb_x)_2Te_3$ via Bi/Sb substitution is discussed. The resPES and XMCD data from $V_{0.1}(Bi_{0.32}Sb_{0.68})_{1.9}Te_3$ (green curve) and $V_{0.1}Bi_{1.9}Te_3$ (black curve) in Fig. 5.5 illustrate the strong variation of the magnetic properties with the position of the V impurity states. The maximum in the V 3*d* DOS in Fig. 5.5 (a) is found at $E_B = 170$ meV in the former, and at $E_B = 300$ meV in the latter, confirming the trend predicted by the above DFT calculations in Fig. 5.4. The observed trend may be attributed to the effect of CT from the host ions into the V impurities, resulting in fluctuations of the *d*–shell occupation [25, 26, 301].

The charge-transfer effect should also modify the unoccupied 3*d* states in the close vicinity of the E_F and, consequently, the mechanism of magnetic coupling, as well. Therefore, the effect of Bi/Sb substitution on the fine structure of the V $L_{2,3}$ edges is further investigated, in order to learn whether the modifications observed in the V 3*d* DOS in Fig. 5.5 (a) should also find correspondence in the XAS and XMCD spectra. Fig. 5.5 (b) shows XAS (upper panel) and XMCD spectra (lower panel) at the V $L_{2,3}$ edges of the same samples $V_z(Bi_{1-x}Sb_x)_{2-z}Te_3$ with $z = 0.1$, for different values of Sb content x. All spectra were measured at temperature of about 5 K, in an out-of-plane magnetic field of 3 T. The black, green and red curves represent samples with $x = 0.00, 0.68$ and 1.00, respectively. The spectra exhibit subtle changes in the low-energy part of the L_3 edge as a function of the Bi/Sb ratio. The insets show the L_3 edge in XAS (upper panel) and XMCD (lower panel) in detail. A gradual onset of the peak-like feature located at about $h\nu = 513.5$ eV with the increase of the Sb content x is apparent in the XAS spectra. Furthermore, this feature also contributes to the magnetic dichroism, affecting the detailed structure of the

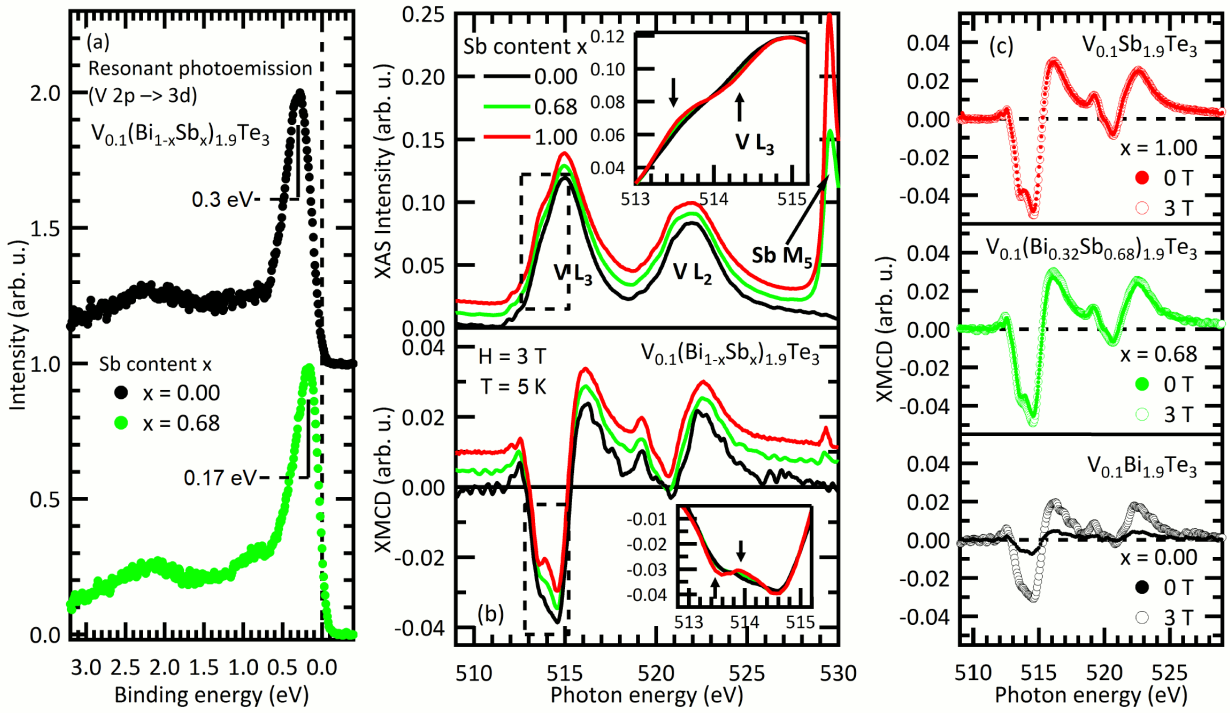

Figure 5.5: The influence of the host stoichiometry on the electronic and magnetic properties of V impurities. (a) resPES spectra of the V 3*d* states for $V_{0.1}Bi_{1.9}Te_3$ (black curve) and $V_{0.1}(Bi_{0.32}Sb_{0.68})_{1.9}Te_3$ (green curve) thin films. The V impurity band maximum is found at $E_B = 170$ meV for the latter and at $E_B = 300$ meV for the former. (b) XAS (upper panel) and XMCD (lower panel) at the V $L_{2,3}$ edges of $V_{0.1}Bi_{1.9}Te_3$ (black curves), $V_{0.1}(Bi_{0.32}Sb_{0.68})_{1.9}Te_3$ (green curves) and $V_{0.1}Sb_{1.9}Te_3$ (red curves), taken at 2 K, under an applied magnetic field of 3 T, perpendicular to the surface. The insets show a closer look of the L_3 edge (without offset between the spectra), where a secondary peak gradually appears at the low-energy side, and clearly affects the XMCD signal (pointed out by arrows) for Sb-rich V:$(Bi,Sb)_2Te_3$. (c) XMCD spectra at the V $L_{2,3}$ edges, taken at 2 K, in remanence (full circles) and saturation (hollow circles) for the same samples in (b). The remanent XMCD remains high in the Sb-rich phase and strongly recedes in the Bi-rich one. Adapted from Ref. [108].

double peak of the L_3 XMCD line shape and, consequently, the magnetic ground state. This is further confirmed in Fig. 5.5 (c) by comparison of the XMCD spectra from the same samples as in (a) and (b), now measured at 5 K in saturation (hollow circles) and remanence (full circles). While in V:Sb_2Te_3 and Sb-rich V:$(Bi,Sb)_2Te_3$ the remanent and saturated spectra almost coincide (remanent XMCD is about 97% and 89% of the saturation signal for the former and later), in $V_{0.1}Bi_{1.9}Te_3$ the remanent XMCD is critically lower than in saturation (about 26% of the saturation signal), demonstrating a suppression of FM interactions, coinciding with the shift of the V states away from E_F, as predicted in the theoretical calculations.

By changing the Bi concentration in $V_{0.1}(Bi_{1-x}Sb_x)_{1.9}Te_3$ from $x = 1.00$ to $x = 0.68$, T_C experiences an abrupt drop from 45 to 35 K, as shown in the Fig. 5.6 (f). From the normalized XMCD spectra measured at the Sb, Te, and V absorption edges for the samples

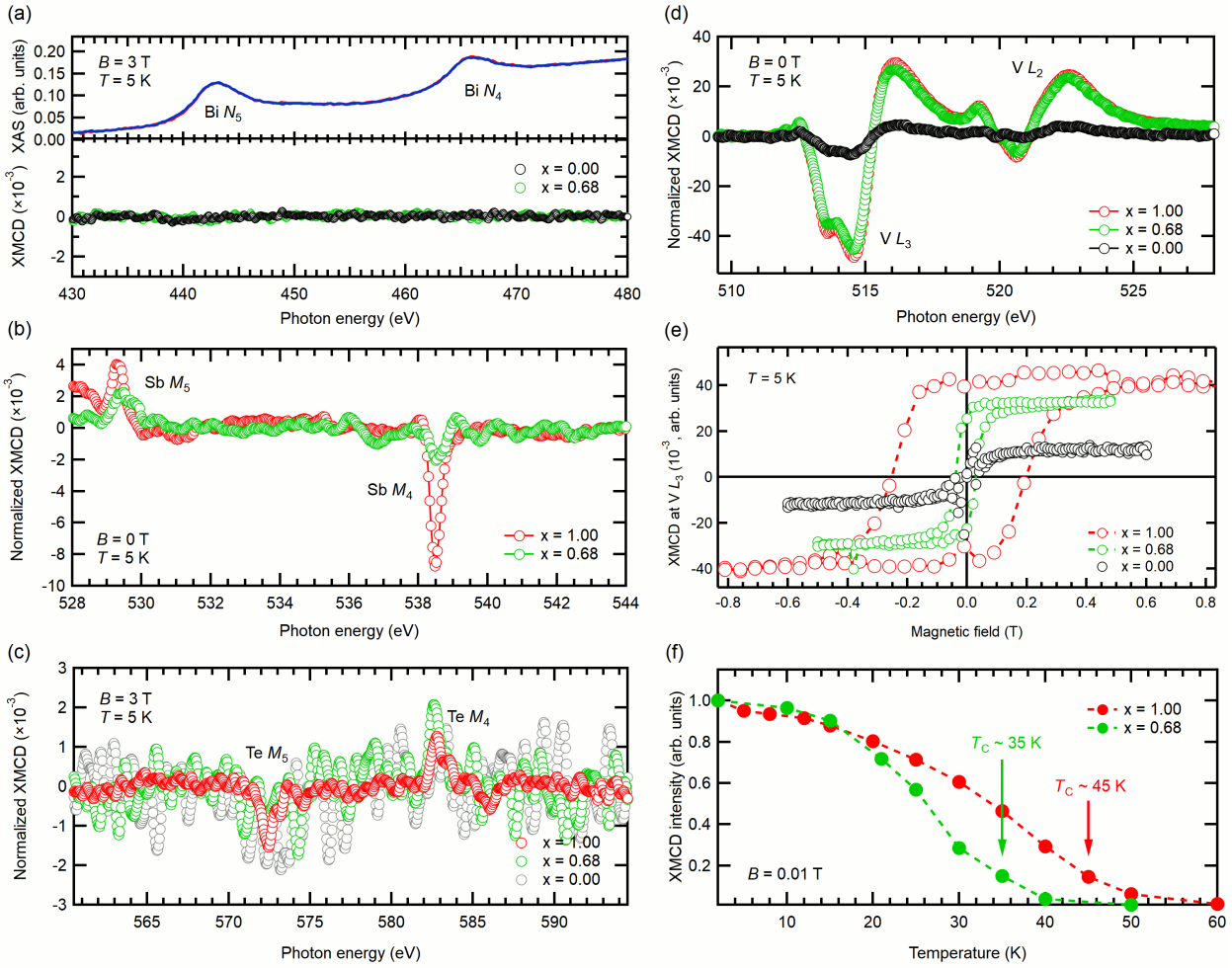

Figure 5.6: XMCD spectra of $V_{0.1}(Bi_{1-x}Sb_x)_{1.9}Te_3$ measured at (a) Bi $N_{4,5}$, (b) Sb $M_{4,5}$, (c) Te $M_{4,5}$ and (d) V $L_{2,3}$ edges, respectively, for the $x = 0$, 0.68, and 1 at 5 K. (e) XMCD intensity at the V L_3 edge as function of applied magnetic field for corresponding samples measured at 5 K. (f) Temperature-dependence of the remanent XMCD signal at the V L_3 edge, from which $T_C \sim 35$ K for $x = 0.68$ and $T_C \sim 45$ K for $x = 1$ are estimated.

with different Bi content, see Fig. 5.6 (b-d), one can see that their rapid decreases are in good agreement with the decreasing T_C stemming from the Bi doping effect. As for the Bi $N_{4,5}$ absorption edges, the XMCD measurements show no detectable XMCD even for the Bi-rich sample $V_{0.1}Bi_{1.9}Te_3$ at $B = 3$ T, as shown in Fig. 5.6 (a). The magnetization curves for different x at V L_3 shown in Fig. 5.6 (e) exhibit clear magnetic hysteresis. For $x = 1.00$ it shows $H_C \sim 200$ mT, while for $x = 0.68$ the coercive field is only $H_C \sim 40$ mT and for $x = 0.00$ it is even smaller, confirming that the substitutional Bi atoms significantly suppress the long-range magnetic order. To estimate quantitatively the change of the V ordered magnetic moment resulting from the suppression of FM interactions, we utilize $L_{2,3}$ edge sum rule analysis, in a similar way as discussed in Chapter 4. The results of the sum rule analysis are presented in Fig. 5.7. Fig. 5.7 (a) shows the estimated spin magnetic moment m_{spin} of V in $V_{0.1}(Bi_{1-x}Sb_x)_{1.9}Te_3$ as a function of Sb content x, both in saturation (3 T, empty circles) and remanence (0.01 T, full circles). As one can notice looking

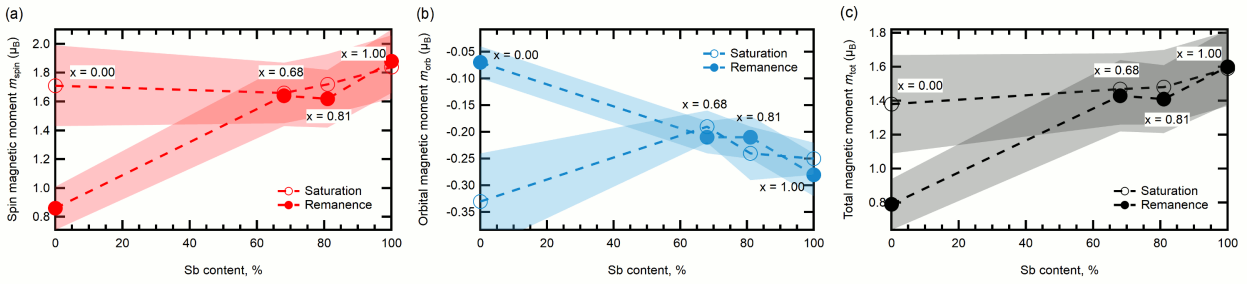

Figure 5.7: (a) Spin (m_{spin}), (b) orbital (m_{orb}) and (c) total (m_{tot}) magnetic moments of V in $V_{0.1}(Bi_{1-x}Sb_x)_{1.9}Te_3$ as function of Sb content x, estimated using V $L_{2,3}$ sum rule analysis for saturation (empty circles) and remanent (full circles) data acquired at $T \sim 5$ K. The shaded areas indicate the error bars.

at the remanent data, the spin magnetic moments within the error bars increase monotonically with the increase of Sb content, while for the saturation data it shows roughly a plateau. At the same time, the orbital magnetic moments in Fig. 5.7 (b) show the opposite behavior, suggesting unquenching of the orbital magnetic moment with the Sb content, which could be related to the change of the magnetocrystalline anisotropy (MCA) in the system. Overall, we observe the change of the ordered magnetic moment from $m_{tot} = (0.79 \pm 0.15)\mu_B$ for $V_{0.1}Bi_{1.9}Te_3$ sample to $m_{tot} = (1.60 \pm 0.22)\mu_B$ for $V_{0.1}Sb_{1.9}Te_3$, as shown in Fig. 5.7 (c).

The observed weakening of the ferromagnetism upon Bi doping in V:$(Bi,Sb)_2Te_3$ is in agreement with previous works [8, 78, 266], including the data reported for single-crystalline Cr:$(Bi,Sb)_2Te_3$ [80]. As illustrated in Fig. 5.6 (b), and also known from recent XMCD studies [30, 78–80, 263], the Sb ions become partially polarized in the presence of substitutional V or Cr, while Bi, on the other hand, remains unpolarized (see Fig. 5.6 (a)). Thus, these findings are consistent with a scenario where weakly localized, spin-polarized holes in Sb ions facilitate a longer ranged magnetic coupling in both systems [27, 294, 297, 298, 300]. The substitution of Sb by Bi, thus, gradually disrupts the network of spin-polarized p orbitals contributing to the stabilization of a robust FM state. Furthermore, the results show that the sharp V and Cr resonances are mostly localized inside the bulk band gap (see Fig. 5.4), indicating a considerable overlap with the TSS. Although the effect of the TSS on the magnetic interactions has not been explored here, the theory suggests that the presence of the Dirac electrons at the surface might as well have impact on the charge and magnetic ground states of 3d impurities in the vicinity of the surface and, consequently, on the pd magnetic interactions [296], potentially leading to modified magnetic properties as compared to the bulk. Conversely, the 3d impurity states may mediate spin scattering channels for the spin-momentum-locked Dirac electrons [295].

5.3 Influence of impurity concentration on the electronic and magnetic properties

The above discussion of the host stoichiometry and its influence on the electronic and magnetic properties of $V_{0.1}(Bi_{1-x}Sb_x)_{1.9}Te_3$ was manly based on our results presented in Ref. [108]. In this Section, I additionally discuss how the impurity concentration z affects the electronic and magnetic properties of $V_z(Bi_{0.23}Sb_{0.77})_{2-z}Te_3$ using about 10 nm thick films with $z = 0.09$, 0.24 and 0.34, grown by molecular beam epitaxy (MBE) on hydrogen-passivated Si(111) substrates by Dr. Steffen Schreyeck from the department of Prof. Laurens W. Molenkamp, Universität Würzburg. The XAS and XMCD data presented here were measured at the High-field Diffractometer end station of UE46 PGM-1 beam line at BESSY II [201] (see Section 3.2.2 for the end station description), in magnetic fields of up to 3 T and at nominal base temperature of about 5 K.

Fig. 5.8 (a-c) shows $L_{2,3}$ edge XAS (top panel) and XMCD (bottom panel) spectra for the *in situ* cleaved V-doped $(Bi_{0.23}Sb_{0.77})_2Te_3$ films with different V content varying from 1.8 at.% ($z = 0.09$) to 6.8 at.% ($z = 0.34$), measured in TEY mode with right- and left-circularly polarized x-rays (red and blue curves, respectively) at a low temperature of $T \sim 5$ K in a magnetic field of $B = 0.01$ T in case of remanent signal (dashed green curve) and $B = 3$ T applied along the surface normal (c-axis) in case of saturation signal (solid green curve). The XAS spectra averaged over the two polarizations are shown as black curves. No sign of oxidized V ions is observed in the samples, and the line shapes are consistent with data discussed in Chapter 4 and in Section 5.2. These XAS/XMCD results also rule out the possible clustering of V at increased doping concentrations in the samples, since otherwise, the XAS and XMCD line shapes would have been significantly modified.

The corresponding normalized XMCD spectra at the V $L_{2,3}$ edges, displayed in the bottom panels of Fig. 5.8 (a-c) in saturation (solid green curves) and remanence (dashed green curves) show a persistent ferromagnetic state at low temperatures and a sizable magnetic moment carried by V $3d$ states. The XMCD signal was normalized to the area under the total XAS spectrum after careful background corrections. Overall, the XAS/XMCD data demonstrate the pristine quality of the TM doped thin films, ruling out any possible secondary phase structure or oxidation, consistent with previous reports for V:$(Bi,Sb)_2Te_3$ [79, 80, 104, 108] thin films, as well as for bulk samples [30]. Fig. 5.8 (e) illustrates the change of XMCD signal amplitude as function of dopant concentration z for remanence (full circles) and saturation (empty circles). While the remanent XMCD signal decreases by a factor of about 8 with the concentration, the saturation data levels off to a plateau, indicating that the saturated magnetic moment is similar for all three samples, while the ordered moment is reduced. Intuitively, within the *pd* hybridization model one would expect the increase of magnetization with the concentration of the TM dopant [80, 105],

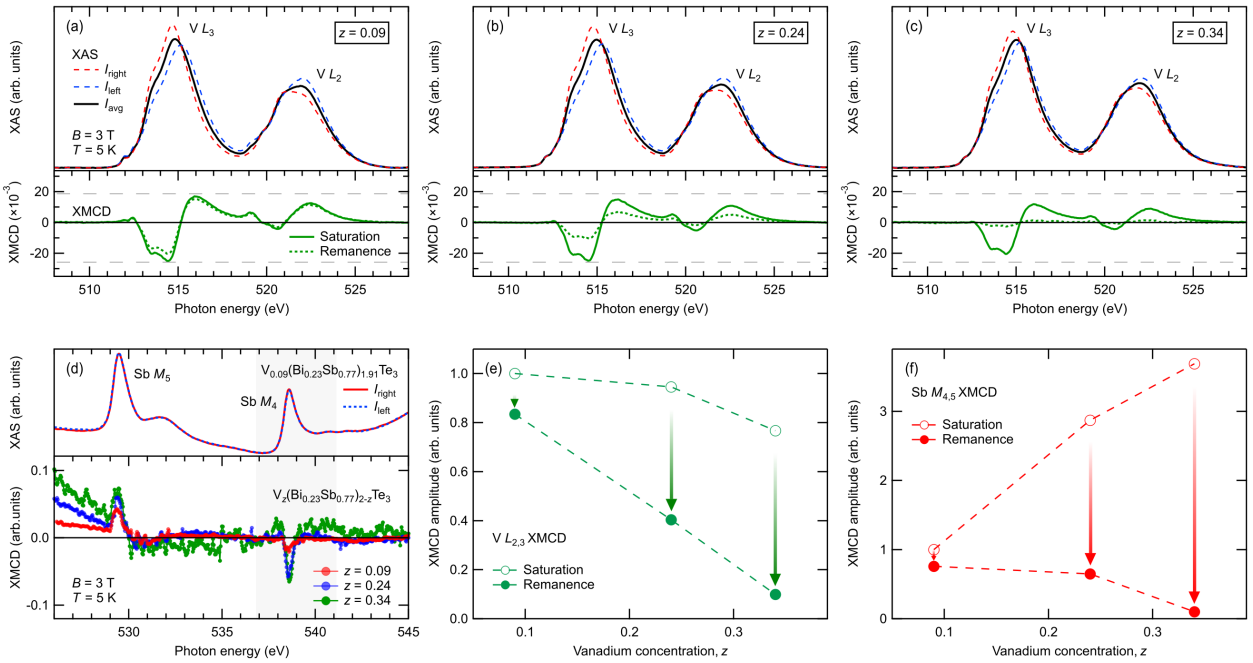

Figure 5.8: (a-c) Normalized XAS (upper panel) and XMCD (lower panel) spectra at V $L_{2,3}$ edges ($2p \rightarrow 3d$) of $V_z(Bi_{0.23}Sb_{0.77})_{2-z}Te_3$ for (a) $z = 0.09$, (b) $z = 0.24$ and (c) $z = 0.34$. (d) Normalized Sb $M_{4,5}$ ($3d \rightarrow 5p$) XAS and XMCD spectra for different dopant concentrations. The XMCD spectra were normalized to the intensity of the resonant part of the M_4 XAS (see the main text). (e) Amplitude of the XMCD signal at the V $L_{2,3}$ edges as function of the V concentration z, measured in an external magnetic field of 3 T (saturation, empty circles) and 0.01 T (remanence, full circles). (f) Amplitude of the XMCD signal at the Sb $M_{4,5}$ edges as function of the V concentration z. The arrows indicate a strong reduction of the induced magnetic moment at the Sb site with switched-off external magnetic field.

however here it does not seem to be the case. A deeper understanding of such behavior requires further theoretical support.

To examine the behavior of the induced magnetic moments at the non-magnetic elements in the host lattice, we measured the XMCD spectra at the Sb $M_{4,5}$, Te $M_{4,5}$ and Bi $N_{4,5}$ absorption edges. Fig. 5.8 (d) and Fig. 5.9 (a) show the circular-polarized XAS spectra (top panel) of $V_{0.09}(Bi_{0.23}Sb_{0.77})_{1.91}Te_3$ at the Sb $M_{4,5}$ and Te $M_{4,5}$ edges, respectively, measured in a magnetic field of 3 T and $T \sim 5$ K. Even though only a very slight difference can be seen in these normalized XAS spectra, they still show a clear reversal of the XAS intensities between the Sb/Te M_5 ($\sim$ 529.5 eV in case of Sb) and M_4 ($\sim$ 538.5 eV in case of Sb) edges. The bottom panels of Fig. 5.8 (d) and Fig. 5.9 (a) show the Sb and Te XMCD spectra for the three samples measured in saturation. The XMCD spectra were consistently normalized only to the intensity of the resonant part of the XAS M_4 edge (see gray area), since the Sb M_5 edge overlaps with the V L_2 edge, as seen in the low energy tails of the XMCD spectra in Fig. 5.8 (d) bottom panel. Fig. 5.8 (f) and Fig. 5.9 (b) show the strength of the XMCD at the Sb and Te $M_{4,5}$ edges, respectively, as function of the V concentration z. As seen in these figures, the XMCD saturation data (empty circles) exhibits an increase

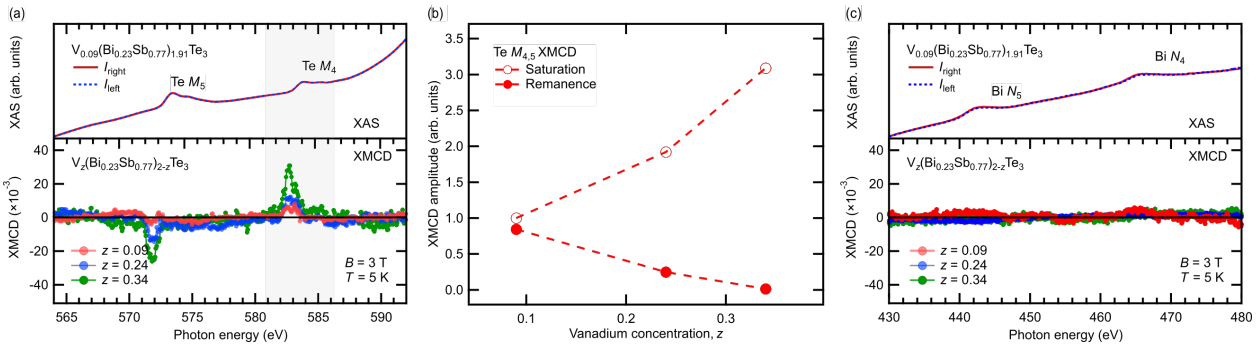

Figure 5.9: (a) Normalized Te $M_{4,5}$ ($3d \rightarrow 5p$) XAS and XMCD spectra for different dopant concentrations. The XMCD spectra were normalized to the intensity of the resonant part of the Te M_4 XAS (see the main text). (b) Amplitude of the XMCD signal at the Te $M_{4,5}$ edges as function of the V concentration z, at saturation (empty circles) and remanence (full circles). (c) XAS and XMCD signal at the Bi $N_{4,5}$ absorption edges. No detectable Bi spin polarization is observed.

of the intensity at the Sb and Te $M_{4,5}$ edges with the increase of V concentration, and this behavior is not following the changes at the V $L_{2,3}$ edges in Fig. 5.8 (e). However the remanent data (full circles) show similar behavior with V, i.e. the signal drops with the increase of V concentration. The XMCD measurements at the Bi $N_{4,5}$ absorption edges in 3 T magnetic field, shown in Fig. 5.9 (c), still indicate no detectable dichroic signal.

Intuitively, the increase of the saturation XMCD signal at the Sb and Te edges in Fig. 5.8 (f) and Fig. 5.9 (b) with V concentration can be understood as the increase in the total volume occupied by V polarized "blobs" relative to the total volume of the sample, whereas under a V "blobs" we understand the vicinity of a V ion containing spin-split Sb and Te local DOS. Thus, a higher proportion of Te/Sb atoms become magnetized due to the closer proximity to a V impurity.

To quantitatively illustrate the evolution of the XMCD signal with V concentration, in Fig. 5.10 we plot the results of the sum rule analysis at the V $L_{2,3}$ edges. Fig. 5.10 (d) and (e) shows the estimated spin m_{spin} and orbital m_{orb} magnetic moments in $V_z(Bi_{0.23}Sb_{0.77})_{2-z}Te_3$ as a function of the V content z, in saturation (3 T, empty circles) and remanence (0.01 T, full circles). It should be noted, that the XMCD amplitude, as plotted in Fig. 5.8 (e), scales with magnetic moment only as long as the value of $\langle T_z \rangle$ (see Eq. 3.27) remains negligible compared to the moments themselves. This, however, does not hold for V-doped samples (see Table. 3.1), where with the increase of V concentration the remanent spin magnetic moment drops only by a factor of 2.4, from $m_{spin} = (1.56 \pm 0.19)\mu_B$ to $m_{spin} = (0.65 \pm 0.14)\mu_B$. Meanwhile, the saturation data show a similar plateau as in Fig. 5.7. The "plateau" observed for the samples in Fig. 5.7 and Fig. 5.10 in saturation could be explained by the fact that V magnetic moment becomes "fully" saturated by the external magnetic field of 3 T (more collinear to the out-of-plane easy axis), reaching its maximum projection along c-axis. Fig. 5.10 (e) shows an increasing quenching of the orbital magnetic moment with V content, both in saturation and remanence. Based on

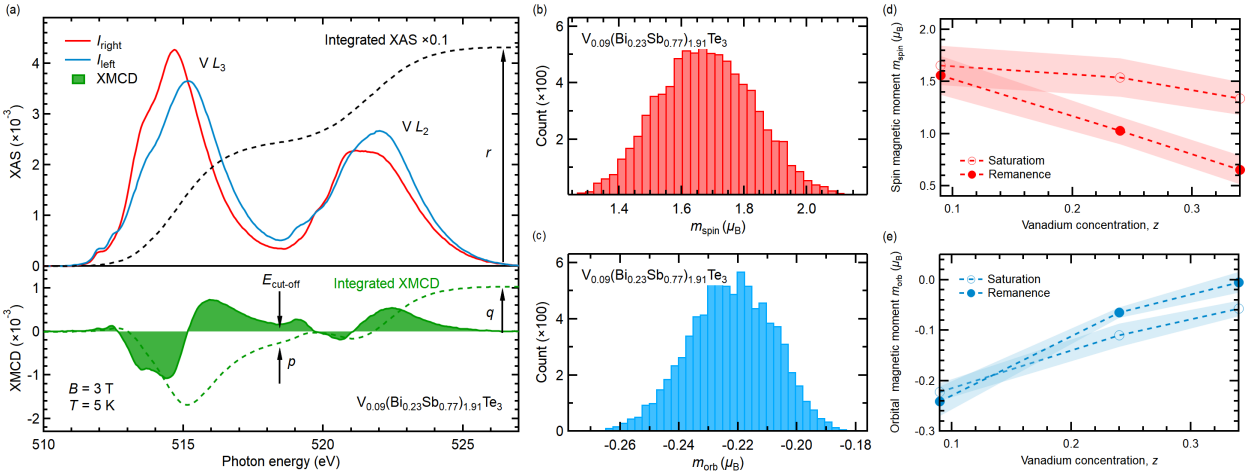

Figure 5.10: Sum rule analysis for the $V_z(Bi_{0.23}Sb_{0.77})_{2-z}Te_3$ thin films. (a) Left- and right-circularly polarized XAS spectra of the V $L_{2,3}$ edges of $V_{0.09}(Bi_{0.23}Sb_{0.77})_{1.91}Te_3$, obtained after the background correction described in Chapter 3 Section 3.3 (I_{left}, solid, light blue line, and I_{right}, solid dark red line), along with the corresponding XMCD data (solid green line, lower panel). The dashed lines show the total integrated XAS and XMCD spectral weight, respectively. The arrows mark the values of r, p and q used in Eq. 3.27. (b) and (c) Distribution of m_{spin} and m_{orb}, respectively, obtained by applying the sum rule analysis 8192 times, as described in the main text. (d) and (e) Spin (m_{spin}) and orbital (m_{orb}) magnetic moments as function of the V concentration z, estimated using sum rules for saturation (empty circles) and remanent (full circles) data. The shaded areas indicate the error bars, as described in the main text.

the Bruno model [302], which under certain conditions relates the MCA energy with the anisotropy of the orbital magnetic moment, one can argue that this increasing quenching of the orbital magnetic moment (along the easy c-axis) with increasing V content results in a reduction of MCA, which, in turn, can affect the hysteresis behavior.

Given the magnetic character of the TM 3d states, it is important to assess their contribution to the electronic band structure. The low concentration of the TM elements results in an extremely low relative intensity of the TM 3d states as compared to the host VB states. In order to circumvent this problem, resPES at the V L_3 edge ($2p \rightarrow 3d$ transition) was performed. This enhances the photoemission cross section of the TM 3d states by several orders of magnitude. By comparing VB photoemission spectra taken on- and off-resonant, one can quantitatively extract the contribution of the 3d states to the VB. Fig. 5.11 shows angle-integrated resPES measurements from pristine $V_{0.09}(Bi_{0.23}Sb_{77})_{1.91}Te_3$ and $V_{0.24}(Bi_{0.23}Sb_{77})_{1.76}Te_3$ thin films performed by Philipp Kagerer. The blue and the red curve in Fig. 5.11 represent the fingerprint of the V 3d states in the VB. These spectra are obtained from the normalized difference between the on- and off-resonant VB photoemission spectra shown in the inset, taken at 97 K. We observe no considerable difference between the V 3d states in low and highly doped samples: In both samples a strongly localised impurity band is found at $E_B \sim 180$ meV. The maximal difference between the peak positions for 1.8% (blue curve) and 4.8% (red curve) doped samples is 30 meV, while

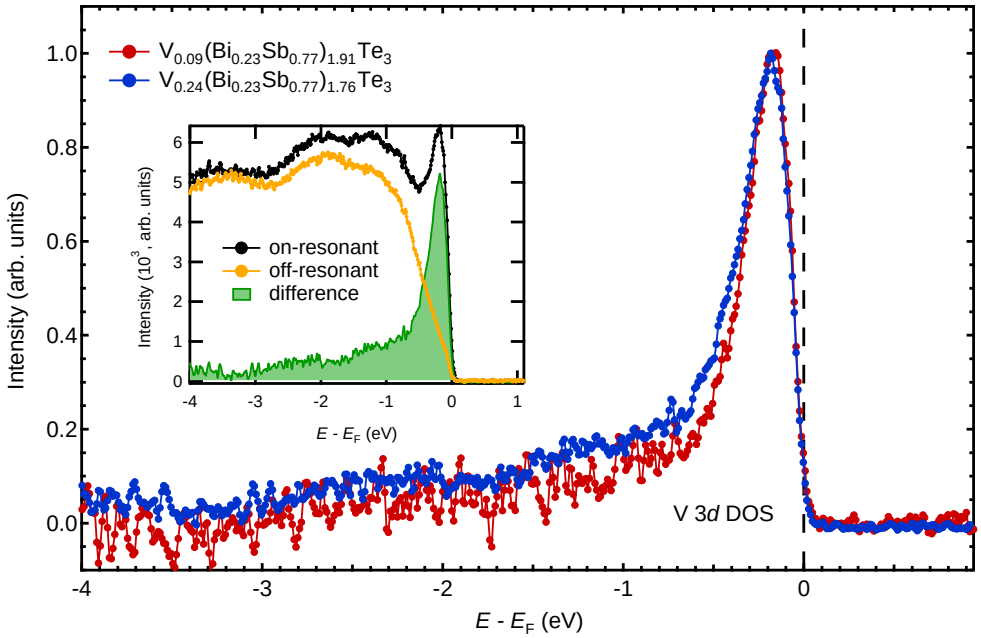

Figure 5.11: ResPES spectra at the L_3 edge of the V ($h\nu$ = 514.88 eV) in $V_{0.09}(Bi_{0.23}Sb_{0.77})_{1.91}Te_3$ (red curve) and $V_{0.24}(Bi_{0.23}Sb_{0.77})_{1.76}Te_3$ (blue curve) thin films, measured at 97 K. The inset shows the on- (orange curve) and off-resonant ($h\nu$ = 514.88 eV, black curve) VB photoemission spectra for $V_{0.24}(Bi_{0.23}Sb_{0.77})_{1.76}Te_3$.

the nominal experimental resolution is 53 meV.

The origin of induced magnetic moment at the Sb and Te sites can be understood by drawing an analogy to the well-known diluted magnetic semiconductor (Ga,Mn)As, where the magnetic moment induced at As (Ga) site is coupled anti-parallel (parallel) to the Mn 3*d* moment [105, 107]. The band diagram of V in $(Bi,Sb)_2Te_3$ is also quite similar to that for the Mn in Mn-doped GaAs, in which the impurity band formed by Mn 3*d* electrons is located at the top of the host GaAs VB, below the E_F [78, 303]. The schematic diagram in Fig. 5.12 allows for an intuitive understanding of the mechanism of inducing magnetic moment at the Sb and Te sites in V-doped $(Bi,Sb)_2Te_3$ based on Zener's *pd*-exchange mechanism [78, 299, 304]. Firstly, a strong *pd* hybridization (*p*-*d* mixing) between the V 3*d* and Te 5*p* states pushes the majority spin DOS of Te to higher energies above the E_F, as illustrated in Fig. 5.12 (b), while the minority spin DOS of Te is shifted to lower energies due to hybridization with the higher lying V minority 3*d* state (not shown). This hybridization reduces the occupancy of the Te 5*p* majority spin states, thus resulting in an antiparallel magnetic moment at the Te site, as probed by the XMCD. Hence, the hybridization with the occupied majority- and unoccupied minority-spin 3*d* states of V acts like a magnetic field on the valence band states, which induces a spin polarization in the host [105]. On the other hand, the Sb 5*p* states are dominant in the conduction band region, but they are also present around E_F. Therefore, a weak Sb 5*p* - V 3*d* mixing in the same atomic plane slightly enhances the majority spin DOS of Sb below E_F, resulting in

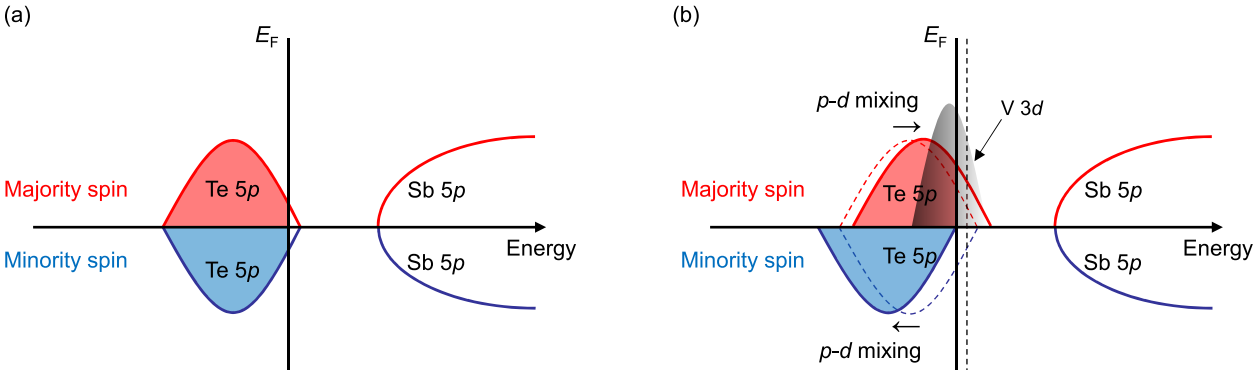

Figure 5.12: Schematic diagram of the $(Bi,Sb)_2Te_3$ spin-polarized DOS in the case of *pd* exchange (a) before and (b) after V doping. The dashed curves represent the valence band before interaction with the magnetic impurities. Adapted from Ref. [78].

a small magnetic moment parallel to the V moment. The absence of spin polarization at the Bi site in the XMCD measurements can be explained by the fact that Bi 6*p* unoccupied states are much higher in energy than Sb 5*p* states and the hybridization between the V 3*d* and Bi 6*p* states is negligible, which yields a negligible Bi moment, in contrast to the Sb and Te 5*p* states. Partial substitution of Sb by Bi induces extra bulk electron carriers that push the E_F into the bulk energy gap (see Fig. 5.4), which is one of the prerequisites for a realization of the QAH effect in this system. But it also results in weakening of the ferromagnetism, as was discussed in the previous Section. This phenomenon can be also qualitatively understood from the schematic diagram shown in Fig. 5.12 (b): Shifting the E_F towards the bulk energy gap increases the occupancy of the Te (and Sb) 5*p* majority spin states, while almost maintaining the occupancy of the minority spin states through spin splitting of the Te 5*p* states. Therefore the magnetic moments at the Te (and Sb) sites are reduced with the shifting of the E_F. Consequently, long-range magnetic order is suppressed due to the reduction of the magnetic moments in the host lattice, which mediated the local magnetic moment among V dopands [78].

5.4 Conclusion

The systematic experimental evidences and consistent theoretical results presented in this chapter highlight the central role of impurity-state-mediated exchange coupling for the magnetism in the doped MTI $Cr:(Bi,Sb)_2Te_3$ and $V:(Bi,Sb)_2Te_3$. The magnetism in these systems cannot be explained based solely on the van Vleck mechanism, originating from the topologically non-trivial band structure [71, 73, 101]. Instead, the theoretical calculations discussed in this chapter correctly elucidate the experimental observations on the basis of *pd* hybridization and *pd*-exchange coupling. They show that the kind and strength of the magnetic exchange coupling vary with the position of E_F in the 3*d* DOS, i.e. with the occupation of the impurity 3*d* states, thereby reconciling, in a unified theory,

the differences observed between V and Cr doping of $(Bi,Sb)_2Te_3$ films and the host stoichiometry dependence of their magnetic properties. Refinements of the theory, such as a consideration of local structural relaxations near the magnetic impurities, could yield further improvements towards a quantitative theoretical description.

Moreover, the impact of the impurity concentration on the electronic and magnetic properties of the doped MTIs has been systematically addressed. The origin of the induced magnetic moments at the otherwise non-magnetic Te and Sb atoms in the host lattice, as well as their role in mediating a robust ferromagnetism, is explained based on the Zener-type *pd*-exchange interaction scenario. This advance in the knowledge on the microscopic electronic and magnetic properties in V-doped and Cr-doped $(Bi,Sb)_2Te_3$ may eventually facilitate the better understanding of the microscopic origin of the QAH effect in these systems beneficial to potential spintronic applications [305].

Chapter 6

Incipient antiferromagnetism in the Eu-doped topological insulator Bi_2Te_3

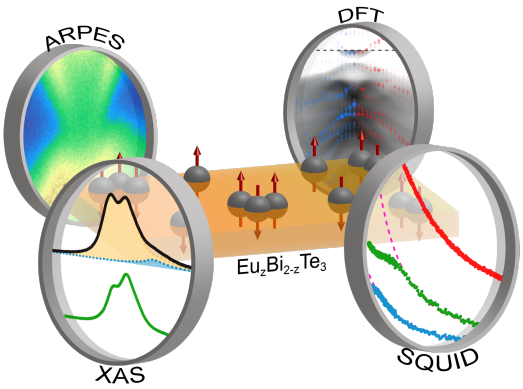

The enhancement of ferromagnetic (FM) properties achieved for V-doped $(Bi,Sb)_2Te_3$, with the Curie temperature (T_C) twice as high as that of the Cr-doped sample and about one order of magnitude larger coercivity at the same temperature compared to Cr doping [8, 9], unfortunately, has little influence on the onset temperature of the quantum anomalous Hall (QAH) effect. Therefore, as an alternative, it was suggested to use rare earth ions (RE) to magnetically dope the topological insulators (TIs), as RE ions typically exhibit larger magnetic moments than transition metal ions (TM) and thus promise the opening of a wider exchange gap in the Dirac surface states. Such doping would also allow for a decrease in the doping concentrations and thus the number of defects, leading to a more stable QAH effect at a higher temperature, as was discussed in Chapter 2.

In this chapter we scrutinize whether the conditions for a substantial gap formation in RE-doped TIs are present by combining spectroscopic and bulk characterization methods with theoretical calculations. We study $Eu_zBi_{2-z}Te_3$ thin films of high structural quality with Eu ions homogeneously incorporated up to a doping level of $z \sim 0.2$ [306]. We provide a comprehensive investigation of a series of samples with three different Eu concentrations. Combining XAS/XMCD obtained at $T \sim 10$ K and atomic multiplet calculations allows us to determine the valence state and magnetic moment of the dopants. Using superconducting quantum interference device (SQUID) magnetometry, we observe the onset of antiferromagnetism below about 10 K, which is somewhat unexpected given the prediction of ferromagnetism in the related chalcogenide $Eu_zBi_{2-z}Se_3$. Furthermore, we discuss the characterization of the electronic properties obtained by ARPES and resonant

photoemission spectroscopy (resPES) at 20 K. Since this is still above the antiferromagnetic (AFM) onset temperature, the topological surface state (TSS) remains intact and gapless for all Eu doping levels. Nevertheless, the photoemission measurements allows the establishment of a DFT model, which explains the onset of antiferromagnetism observed in SQUID data by the direct overlap of the wave functions of the Eu impurities. The results presented in this chapter support the notion that antiferromagnetism can coexist with TSS in rare-earth doped Bi_2Te_3 and call for spectroscopic studies in the kelvin range to look for novel quantum phenomena such as the QAH effect. The data presented here were published in Ref. [306] and Ref. [307].

6.1 Experimental

6.1.1 $Eu_zBi_{2-z}Te_3$ epitaxial films growth and characterization

The samples investigated in this work consist of 100 nm thick $Eu_zBi_{2-z}Te_3$ films, grown by molecular beam epitaxy on $BaF_2(111)$ substrates by Dr. Celso I. Fornari at the group of Prof. Friedrich Reinert, Universität Würzburg. The nominal Eu doping concentration is defined as $x_{Eu} = BEP_{Eu}/BEP_{Bi_2Te_3}$, where BEP is the beam equivalent pressure of the effusion cells. Four different samples were grown with x_{Eu} = 0%, 2%, 4% and 9%, which would correspond to $z = 0.00, 0.10, 0.20$ and 0.45 in the chemical formula $Eu_zBi_{2-z}Te_3$. Immediately after the growth, all samples were capped by a 100 nm layer of amorphous Te to protect the pristine surface from contamination for the x-ray absorption and photoemission measurements. The capping layer was later removed *in situ* right before the spectroscopic measurements [267]. The detailed growth conditions and a systematic characterization of the films quality can be found elsewhere [306]. X-ray diffraction (XRD) measurements and calculations together with scanning transmission electron microscopy (STEM) images indicate that Eu enters substitutionally on Bi sites up to 4% of doping, whereas for the 9% Eu-doped sample EuTe crystalline clusters of 5 to 10 nm are formed [306]. These clusters of EuTe grow epitaxially in the Bi_2Te_3 matrix with the (111) EuTe plane oriented parallel to the (0001) Bi_2Te_3 basal plane. Further studies using resPES, XAS, XMCD, SQUID and ARPES were carried out to better understand the mechanisms of the europium incorporation in Bi_2Te_3. The studies are presented in the following sections of this chapter.

6.1.2 X-ray absorption spectroscopy

X-ray absorption spectroscopy (XAS) and x-ray magnetic circular dichroism (XMCD) measurements were carried out using high-field diffractometers at UE46 PGM-1 beamline, BESSY II (see Section 3.2.2), and at beamline I10, Diamond Light Source (see Section 3.2.4). Both diffractometers operate under UHV conditions, with a base pressure in the 10^{-11} mbar range. The samples were glued with conducting silver epoxy adhesive onto Cu sample holder and mounted on the cold finger of a helium cryostat. The Te capping layer was mechanically removed *in situ* in the fast-entry chamber at a pressure of 10^{-9} mbar right before the actual measurements. The effectiveness of this method to expose a clean sample surface was demonstrated on Bi_2Te_3 before [79, 267].

XAS measurements at the Eu $M_{4,5}$ edges were performed at ∼10 K and in an external magnetic field of up to 9 T using circularly polarized light. The degree of circular polarization exceeds 95%. The absorption spectra were measured in the total-electron yield (TEY) mode via the sample drain current normalized to the incoming photon intensity (I_0). The TEY is known to be surface sensitive, with a probing depth of 3–6 nm [174, 208]. The XMCD signal was obtained as the difference between two XAS spectra measured in a fixed magnetic field with opposite circular polarizations in normal incidence geometry. The XAS spectra measured with the helicity vector antiparallel (left) and parallel (right) to the fixed magnetic field were scaled with respect to each other to have the same intensity at energies far from the resonances. Using these scaled intensities I_{left} and I_{right}, the average XAS is defined as $I_{\text{avg}} = (I_{\text{left}} + I_{\text{right}})/2$, while the *normalized* XMCD signal is defined as $I_{\text{XMCD}} = (I_{\text{left}} - I_{\text{right}})/(I_{\text{left}} + I_{\text{right}})$. Since only the resonant part of the spectra enters the sum rules, the linear background and the continuum edge jumps were subtracted from the raw spectra.

6.1.3 Angle-resolved photoemission spectroscopy

The photoemission spectra were measured both at laboratory- and synchrotron-based facilities by Dr. Celso I. Fornari and Dr. Thiago R. F. Peixoto at the group of Prof. Friedrich Reinert, Universität Würzburg. The laboratory-based angle-resolved photoemission spectroscopy (ARPES) measurements were performed in a UHV system equipped with a Scienta R4000 hemispherical analyzer using He I_α radiation ($h\nu = 21.2$ eV). The energy resolution was better than 18 meV and the angular resolution was 0.2°. The sample was cooled down to 20 K using a liquid He cryostat. The pressure during the measurement never exceeded 7×10^{-10} mbar.

The resonant ($h\nu \sim 1128$ eV) and off-resonant ($h\nu = 265$ eV) measurements in the soft x-ray regime were carried out at $T = 30$ K using the ASPHERE III end station of the P04 beamline at the PETRA III synchrotron facility (DESY, Hamburg, Germany), with a base pressure better than 2×10^{-10} mbar [308].

All studied samples were protected with a Te capping layer, which was removed *in situ* prior to the actual measurement.

6.1.4 Density functional theory calculations

The theoretical results necessary for the understanding of electronic and magnetic properties of Eu impurities were obtained in collaborations with the group of Prof. Stefan Blügel from Forschungszentrum Jülich. Dr. Philipp Rüßmann performed *ab initio* calculations which a presented and discussed in this chapter.

Density functional theory (DFT) calculations were performed for Bi_2Te_3 bulk crystals using the experimental bulk lattice structure [286] into which Eu defects were embedded. The electronic structure was calculated within the local spin density approximation [287] by employing the full-potential relativistic Korringa-Kohn-Rostoker Green's function method (KKR) [288, 309] with exact description of the atomic cells [290, 291]. The truncation error arising from an $\ell_{max} = 3$ cutoff in the angular momentum expansion was corrected for using Lloyd's formula [292]. The Eu defects were embedded self-consistently into the Bi_2Te_3 crystal using the Dyson equation in the KKR method [289] and have been chosen to occupy the substitutional Bi position (denoted by Eu_{Bi}) in the quintuple layers. A charge-screening cluster comprising the first three shells of neighboring atoms was included, and structural relaxations around the defect were neglected. All calculations include spin–orbit coupling self-consistently and were performed for an out-of-plane direction of the magnetic moments of the Eu atoms. Correlations within the localized $4f$ states of Eu were accounted for using an on-site Coulomb correction (LDA $+U$) [310] for varying values of the parametrization of $U \in \{0, 7, 8, 9\}$ eV and $J \in \{0, 0.75, 1.5\}$ eV. To calculate exchange interactions, pairs of Eu impurities were embedded into Bi_2Te_3 at different distances for substitutional Bi positions within the same quintuple layer. After the self-consistent impurity embedding calculation, the method of infinitesimal rotations [293] was used to compute exchange interaction parameters J_{ij} which correspond to the Heisenberg Hamiltonian $\mathcal{H} = \frac{1}{2}\sum_{i,j} \hat{e}_i J_{ij} \hat{e}_j$. Here $\hat{e}_i$ indicates the direction of the Eu magnetic moment and $i \neq j$ label the different magnetic Eu atoms. The J_{ij} parameters were calculated using a numerical smearing temperature of 100 K, which includes the effective contribution of electron scattering due to phonons or intrinsic defects in the Bi_2Te_3 host crystal that limit the coherence length of the electron's wave functions. Calculations at higher values of the smearing temperature showed a minor effect on the J_{ij}'s and are therefore not shown explicitly.

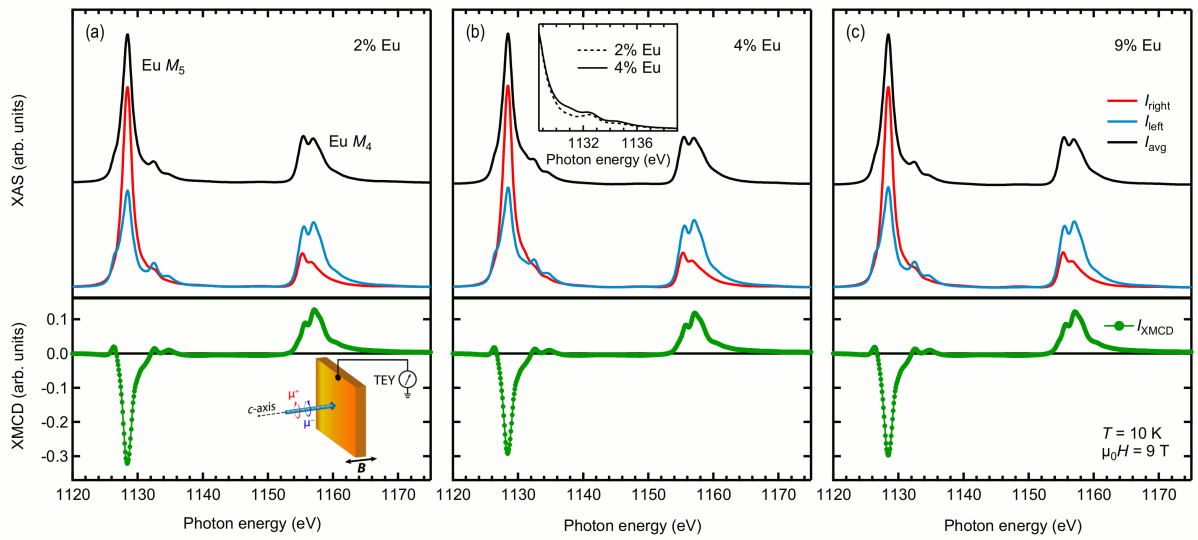

Figure 6.1: Experimental Eu $M_{4,5}$ edges XAS (top) and normalized XMCD (bottom) intensities of (a) 2%, (b) 4% and (c) 9% Eu-doped Bi_2Te_3 thin films, measured at $T = 10$ K in an external magnetic field of 9 T with left circular (I_{left}) and right circular (I_{right}) x-ray polarization. The inset in (a) schematically illustrates the experimental geometry. The inset in (b) highlights the additional small spectral weight at the M_5 edge of the 4% Eu-doped sample, which is absent for the other two samples. Taken from Ref. [307].

6.1.5 Bulk magnetometry

The overall magnetic properties of the $Eu_zBi_{2-z}Te_3$ films were measured using bulk-sensitive superconducting quantum interference device (SQUID) magnetometry at the group of Dr. Eberhard Goering, MPI IS Stuttgart. SQUID measurements were performed as a function of temperature and magnetic field using a 7 T Quantum Design MPMS 3 SQUID VSM. The diamagnetic contribution from the BaF_2 substrate was subtracted by high-field linear fitting of M(H) curves at elevated temperatures (not shown). The temperature dependence of the magnetization was measured in the field-cooled (FC) and zero-field-cooled (ZFC) regimes. In the ZFC measurement, the samples were cooled from room temperature to 2 K without any applied field. After cooling, a magnetic field of 0.1 T was applied perpendicular to the film c-axis, i.e., in-plane, and the magnetization was measured upon warming the samples. In the FC measurements the samples were cooled to 2 K in 0.1 T in-plane field and the data were acquired while heating, similar to ZFC.

6.2 Eu $M_{4,5}$ XAS and XMCD

Fig. 6.1 shows XAS and XMCD spectra at the Eu $M_{4,5}$ edges for the 2%, 4% and 9% Eu-doped Bi_2Te_3 samples. The measurements were conducted at a temperature of $T = 10$ K in an applied field of $B = 9$ T. The XAS line shapes of all three samples shown in the upper panels are nearly identical and indicate an overwhelming preponderance of Eu^{2+}

[240, 311]. The line shapes of the XMCD spectra shown in the lower panels confirm the Eu^{2+} character, corresponding to a $4f$ electron occupation of $n_f = 7$ ($S = 7/2$, $L = 0$ and $J = 7/2$). The small additional spectral weight observed in the 4% Eu-doped sample (see the inset of Fig. 6.1 (b)) probably stems from Eu^{3+}, most likely resulting from surface contamination with Eu_2O_3, as we show in Section 6.4 using atomic multiplet calculations. Eu^{3+} is nonmagnetic in the Hund's rule ground state ($S = 3$, $L = 3$ and $J = 0$) and therefore has no contribution to the XMCD spectrum [312, 313]. The electrons of the Eu $4f$ shell are not directly involved in the formation of chemical bonds, unlike the electrons of the $5d$ and $6s$ shells. For this reason, the Eu $M_{4,5}$ absorption spectrum is typically the same for metals, alloys and oxides, apart from small differences in the line shape due to the experimental and lifetime broadening [240].

It is worth mentioning that the strength of the normalized dichroism signal shown in the lower panel of Fig. 6.1, which is directly proportional to the $4f$ magnetic moment of the Eu ion, slightly decreases upon increasing Eu concentration. The same trend was reported for the concentration dependence of the Dy magnetization in Dy:Bi_2Te_3 films [120]. The XMCD spectra measured at low temperature in remanence (not shown) display no perceptible response for the entire range of studied concentrations of Eu, thus we observe no evidence for a long-range FM order, which is consistent with the SQUID results.

Previous XAS and XMCD studies of Bi_2Te_3 thin films doped with RE ions other than Eu revealed a 3+ valence of the dopants [114, 116, 118, 120–122, 314], in strong contrast with the 2+ valence of the Eu ions found here. This is likely due to the half-filled $4f$ shell of Eu^{2+}, [Xe] $4f^7$, having a very stable Hund's rule ground state ($^8S_{7/2}$) with no spin–orbit splitting and a large spin magnetic moment arising from 7 unpaired electrons. It is also in line with the observation that the trivalent state is the most stable in oxides, while the divalent state is more stable for the less electronegative chalcogens [306]. Overall, our XAS and XMCD spectra are in good agreement with those previously reported for Eu $M_{4,5}$ edges [315–317].

Fig. 6.2 (a) illustrates the strength of the XMCD signal as a function of external magnetic field measured at 10 K at normal incidence of the x-rays, revealing the field-dependent magnetization of Eu ions. The data was obtained by sweeping the out-of-plane applied magnetic field in a range of ± 12 T at the photon energy of the Eu M_5 edge XMCD peak maximum normalized to the off-resonant region. The shapes of the curves are fairly similar for all three Eu concentrations with the XMCD strength slightly decreasing by $\sim 6\%$ when going from 2% to 9% doping level. No evidence for opening of the hysteresis loop was observed for any of the three samples, which points towards the absence of long-range ordering of Eu moments. Indeed, the magnetization curves can be closely approximated by a Brillouin function (see Fig. 6.2 (a)), which is indicative of paramagnetic behavior. Besides, all magnetization curves are passing directly through

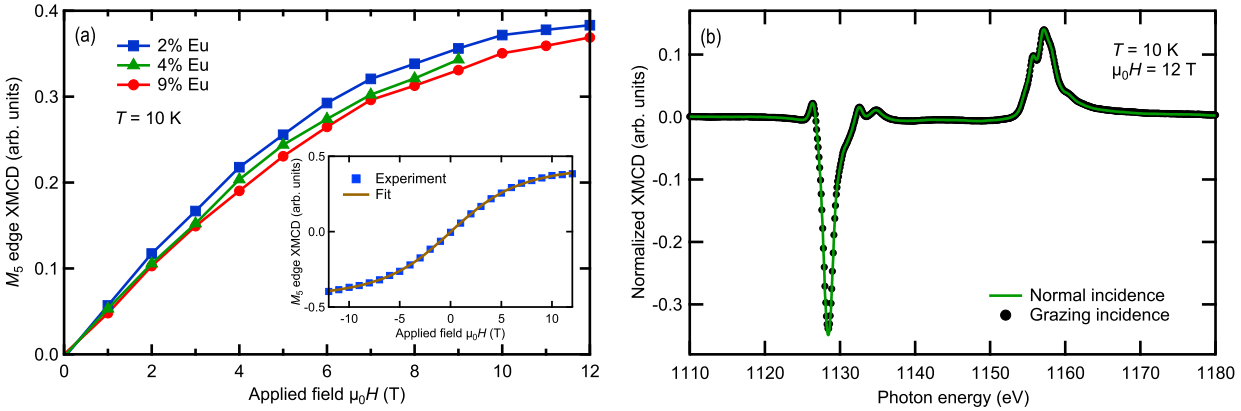

Figure 6.2: (a) Magnetic-field dependence of the M_5 edge XMCD TEY signal for 2% Eu-doped (squares), 4% Eu-doped (triangles) and 9% Eu-doped (circles) Bi_2Te_3 measured at $T = 10$ K, at normal incidence of the x-rays. The inset exemplarily illustrates the 2% Eu-doped sample fitted with a Brillouin function (brown line). (b) Normalized XMCD measured at 10 K in an external magnetic field of 12 T for normal incidence of the x-rays, as well as for 70° off-normal, i.e., nearly grazing incidence, showing no noticeable anisotropy. Taken from Ref. [307].

the origin, which once again indicates zero remanent magnetization and coercive field. Similar paramagnetic responses were also observed for Gd, Dy and Ho ions doped in thin films of Bi_2Te_3 [120–122, 314]. The comparison of XMCD spectra measured at 10 K and external magnetic field of 12 T with normal and grazing x-ray beam incidence is shown in Fig. 6.2 (b). No difference between the two spectra can be detected, suggesting no noticeable magnetic anisotropy.

6.3 *M*-edge sum-rule analysis

The spin and orbital magnetic moments, which determine the magnetic properties of our thin films, result from the interplay of the hybridization, spin–orbit coupling (SOC), crystal field (CF), Coulomb and exchange interactions. The highly localized and well screened $4f$ electrons of rare earth elements experience comparatively weak crystal fields ($\sim$ 100 meV) and small hybridizations, with the Coulomb and SOC interactions being the two dominating energies. Owing to this, RE ions can be considered as exhibiting isolated magnetic moments and, therefore, the materials often show a paramagnetic behavior.

The magnetic moment of the Eu ion can be relatively simply estimated using sum rule analysis. For $3d \rightarrow 4f$ transitions the sum rules are given by Eq. 3.31, as discussed in Chapter 3. To estimate the required value of $\langle T_z \rangle$ we performed atomic multiplet calculation for Eu^{2+} and found it to be negligibly small $\langle T_z \rangle = -0.004\hbar$, in good agreement with previously reported values [236]. The number of holes n_h was taken to be 7 for the Eu $4f^7$ valence shell. Similarly to our previous publication [79], we apply a correction factor to the spin sum rule in order to compensate for the jj mixing between the $3d_{5/2}$ and

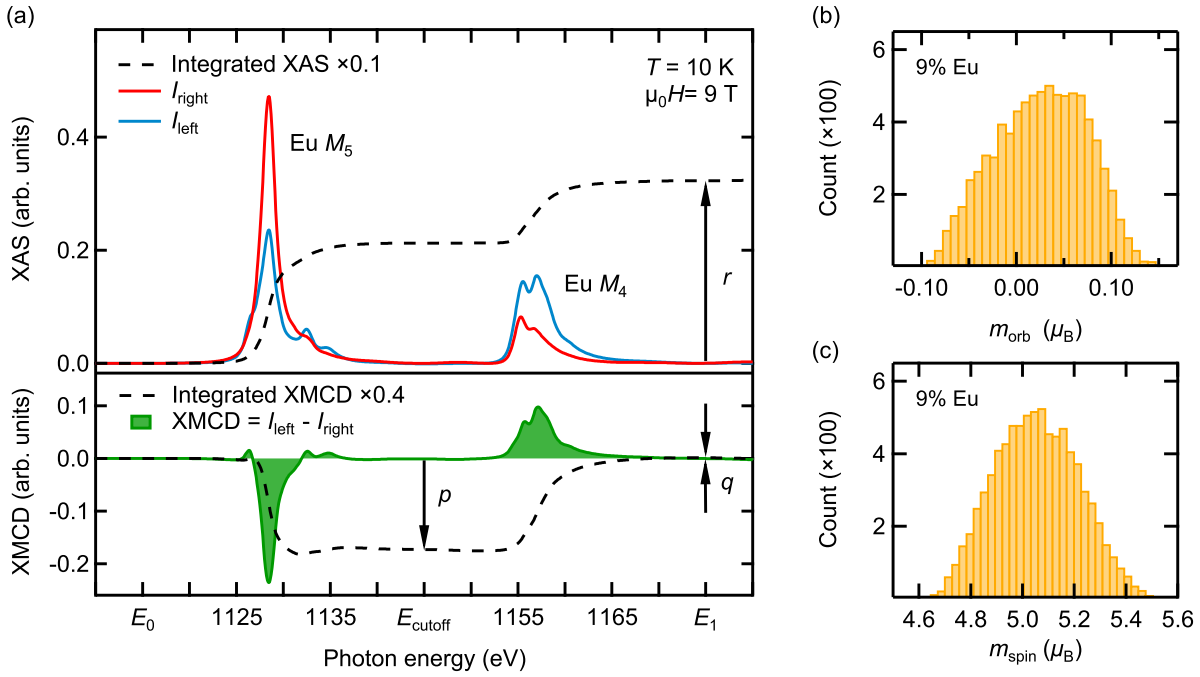

Figure 6.3: Sum rule analysis for the 9% Eu-doped sample. (a) Left- and right-circularly polarized XAS spectra of the Eu $M_{4,5}$ edges, obtained after the background corrections described in section 6.1 (I_{left}, solid, light blue line, and I_{right}, solid dark red line), along with the corresponding XMCD data (solid green line, lower panel). The dashed lines show the total integrated XAS and XMCD spectral weight, respectively. The arrows mark the values of r, p and q used in Eq. 3.31. E_0 and E_1 denote the onset and the end energy of the entire $M_{4,5}$ edges, and E_{cutoff} denotes the energy separating the M_4 and M_5 contributions. (b) and (c) Distribution of m_{orb} and m_{spin}, respectively, obtained after application of the sum rules 8192 times, for different sets of fitting parameters, as described in the main text. Taken from Ref. [307].

$3d_{3/2}$ core levels. However, for Eu^{2+} the correction factor has a rather small value of 1.06, indicating a low mixing of these two manifolds.

Since the extracted magnetic moments depend in a nontrivial way on the input parameters controlling the normalization and background subtraction procedures, as well as on the integration energy range (E_0, E_{cutoff} and E_1 shown in Fig. 6.3 (a)) and n_h, we vary the input parameters in a random and uncorrelated way within the assumed confidence intervals and examine how the final results get distributed, see Fig. 6.3 (b, c). In this way we are able to account for possible conjoined effects of the input parameters and produce fair estimates for the uncertainties in m_{spin} and m_{orb} [79].

Further, we notice that due to the paramagnetic behavior of the Eu magnetization, the external magnetic field of 9 T was not sufficient to saturate the magnetic moments at $T = 10$ K, the temperature at which the data for the sum rule analysis were collected. Therefore we fit the magnetic-field dependence of the M_5 edge XMCD signal with a Brillouin function, $B_J(x)$ with $x = \frac{g_J J \mu_B B}{k_B(T-\theta_p)}$ [318], as illustrated in the inset of Fig. 6.2 (a), which accounts for the finite temperature, and determine the scaling constant

Table 6.1: Spin, orbital and saturation magnetic moments estimated using XMCD sum rules for Eu $M_{4,5}$ absorption edges (in units of μ_B). The scaling factor $\mathcal{C}$ was obtained from the fit of the XMCD magnetic field dependence with a Brillouin function, as shown in Fig. 6.2.

Sample	m_{spin}	m_{orb}	m_{spin}^{sat}	$\mathcal{C}$
2% Eu	5.23 ± 0.21	-0.09 ± 0.06	6.64 ± 0.29	1.27 ± 0.02
4% Eu	4.85 ± 0.20	-0.06 ± 0.11	6.35 ± 0.47	1.31 ± 0.08
9% Eu	5.03 ± 0.22	0.02 ± 0.07	6.79 ± 0.39	1.35 ± 0.05

$\mathcal{C} = \mathrm{M}(T = 0, B = +\infty)/\mathrm{M}(T, B)$. This scaling constant is later used to obtain the magnetic moment at saturation by its value at finite T and B. The fit with a Brillouin function indicates that to reach 99% of the full saturation moment at $T = 10$ K, one would have to apply an external magnetic field of about 50 T.

The results of the sum rules application for the Eu ions are listed in Table 6.1. As expected for Eu^{2+} with its half-filled $4f$ shell, the orbital magnetic moment m_{orb} is almost completely quenched for all three concentrations. The values of the saturation spin magnetic moment m_{spin}^{sat}, within the error bars, are also consistent with the $^8S_{7/2}$ ground state for the 2% and 9% Eu-doped samples, while for the 4% doped sample there is some reduction, which could be explained by a non-dichroic contribution coming from the Eu^{3+} contamination.

In the following section, we will compare the moments obtained with the sum rule analysis with those obtained by atomic multiplet theory.

6.4 Atomic multiplet calculations

Theoretical XAS and XMCD spectra for the $M_{4,5}$ $(3d \rightarrow 4f)$ absorption of Eu^{2+} and Eu^{3+} ions were calculated using crystal field multiplet theory (CFT) in the framework developed by Thole *et al.* [240]. The calculation takes into account all the $3d - 4f$ and $4f - 4f$ electronic Coulomb interactions, as well as the spin–orbit coupling on every open shell of the absorbing atom. The initial values for the Slater integrals were approximated using Cowan's atomic Hartree–Fock (HF) code with relativistic corrections [173]. Their optimized values together with the spin–orbit coupling constants used in the calculations for the Eu^{2+} $3d^{10}4f^7$ and Eu^{3+} $3d^{10}4f^6$ initial state and for the Eu^{2+} $3d^9 4f^8$ and Eu^{3+} $3d^9 4f^7$ final state are shown in Table 6.2. The HF values of the direct Slater integrals F, determining the size of the electron-electron repulsion, were reduced to 84%, while those of the exchange Slater integrals G were reduced to 74% of their atomic values, to account for intra-atomic screening effects [240]. This downscaling of the Slater integrals was found to be optimal for the Eu $M_{4,5}$ XAS and XMCD spectra, accurately describing the total spread

Table 6.2: Optimized CFT parameters for Eu^{2+} and Eu^{3+} ions used in the atomic multiplet calculation (in units of eV). The best fit yields a reduction of the F and G Slater integrals to 84% and 74% of their Hartree–Fock values, respectively.

Ion	state	configuration	$F^{(2)}_{ff}$	$F^{(4)}_{ff}$	$F^{(6)}_{ff}$	ζ_{4f}	$F^{(2)}_{df}$	$F^{(4)}_{df}$	$G^{(1)}_{df}$	$G^{(3)}_{df}$	$G^{(5)}_{df}$	ζ_{3d}
Eu^{2+}	initial	$3d^{10}4f^7$	10.913	6.807	4.886	0.160	6.728	3.056	4.066	2.379	1.642	11.052
	final	$3d^{9}4f^8$	11.579	7.238	5.200	0.187	7.347	3.389	4.548	2.664	1.840	11.295
Eu^{3+}	initial	$3d^{10}4f^6$	11.826	7.422	5.340	0.175	7.270	3.330	4.446	2.603	1.797	11.048
	final	$3d^{9}4f^7$	12.428	7.812	5.624	0.202	7.866	3.656	4.922	2.885	1.993	11.291

of the lines in the $3d_{3/2}$ and $3d_{5/2}$ peaks. The strength of the spin–orbit coupling in the d-shell was scaled down to 99% for a better match to the experimental data. The relaxation of atomic orbitals upon the $3d \rightarrow 4f$ excitation leads to a slight change in the Slater integrals and the spin–orbit coupling constants ζ_{4f} and ζ_{3d}. To account for this effect, we used separate sets of these parameters for the initial and final states. As expected, this resulted in a better agreement between the calculated and experimental spectra. The hybridization effect between the localized f-electrons and conduction electrons is considered to be weak [319] and was therefore neglected in the calculations. In our calculation we consider only Eu atoms that substitute Bi in Bi_2Te_3, which entails C_{3v} symmetry of the CF. Since the nearest 6 Te atoms form almost a perfect octahedron, one could have used O_h symmetry, but we disregard the CF altogether. This simplification is justified by the effective shielding of the external electrostatic potential by the outer $5s$ and $5p$ shells, so the CF splitting in the f-shell turns out to be small ($\sim$100 meV) compared to the experimental resolution (120–250 meV) [320], and can be neglected in the current consideration. For comparison, in EuO with its divalent state of Eu, the CF value of 175 meV was obtained by means of multiplet calculations of anisotropic x-ray magnetic linear dichroism [321].

Calculations were performed using the Quanty software package for quantum many-body calculations, developed by Prof. M. W. Haverkort [245], which is based on second quantization and the Lanczos recursion method to calculate Green's functions, thus avoiding the explicit calculations of the final states. The spectral contributions of the splitted ground state terms to the absorption spectra were weighted using a Boltzmann factors corresponding to the experimental temperature of $T \approx 10$ K. Since the experiments were performed in an external magnetic field of 9 T, this was also included in the calculation. To account for the instrumental and lifetime broadening, the calculated spectra were convoluted with a Gaussian function with a standard deviation $\sigma = 0.2$ eV and with an energy-dependent Lorentzian profile with FWHM of 0.4–0.6 eV. The calculated spectra of Eu^{2+} and Eu^{3+} are linearly superposed with the relative energy position and the relative intensity as adjustable parameters.

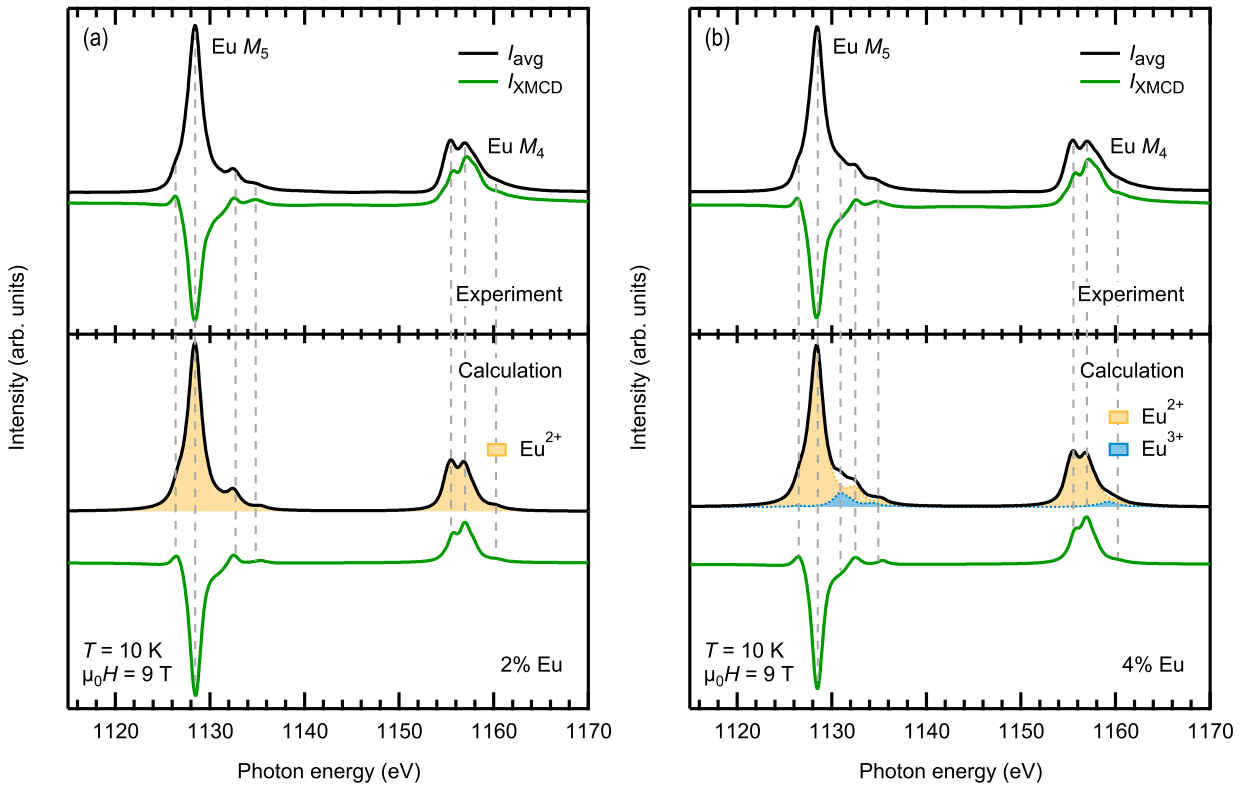

Figure 6.4: Top panel: Experimental Eu $M_{4,5}$ XAS averaged over the two polarizations and XMCD spectra of (a) 2% and (b) 4% Eu-doped Bi_2Te_3 measured at $T = 10$ K in an external magnetic field of 9 T. Bottom panel: Calculated average XAS and XMCD spectra for Eu^{2+} and Eu^{3+} obtained by atomic multiplet theory. The dashed vertical lines are drawn as a guide to the eye, highlighting the position of particular features in the spectra. Taken from Ref. [307].

Fig. 6.4 shows the comparison of calculated XAS and XMCD spectra for the 2% and 4% Eu-doped samples with experimental data measured at $T = 10$ K and $B = 9$ T. We obtain good agreement between experiment and theory, reproducing all essential spectral features and their relative energy positions denoted by vertical dashed lines. This good agreement for the RE $M_{4,5}$ edges is partly due to the CFT being ideally suited to describe transitions into well localized $4f$ states. The calculations for the 2% and 9% Eu-doped samples, see Fig. 6.4 (a), indicate that it is sufficient to consider only divalent Eu to reproduce the experimental spectra with no detectable presence of Eu^{3+}. On the other hand, the best fit to the experimental data for the 4% Eu-doped sample, shown in the lower panel of Fig. 6.4 (b), is obtained with spectral contributions of 93% from Eu^{2+} and 7% from Eu^{3+} ions. In the calculation, the Eu^{3+} spectrum was shifted by 2.5 eV towards higher energies compared to that for the Eu^{2+} state, which is consistent with previous works [311, 313, 322, 323]. According to the Hund's rules, one would expect a nonmagnetic ground state of Eu^{3+} $^7F_0$ ($S = 3$, $L = 3$, $J = 0$). Due to the nonvanishing interaction with the external magnetic field as compared to the spin–orbit interaction, there is a tiny magnetic moment in the $4f$ shell. However, Eu^{3+} XMCD is much smaller compared to

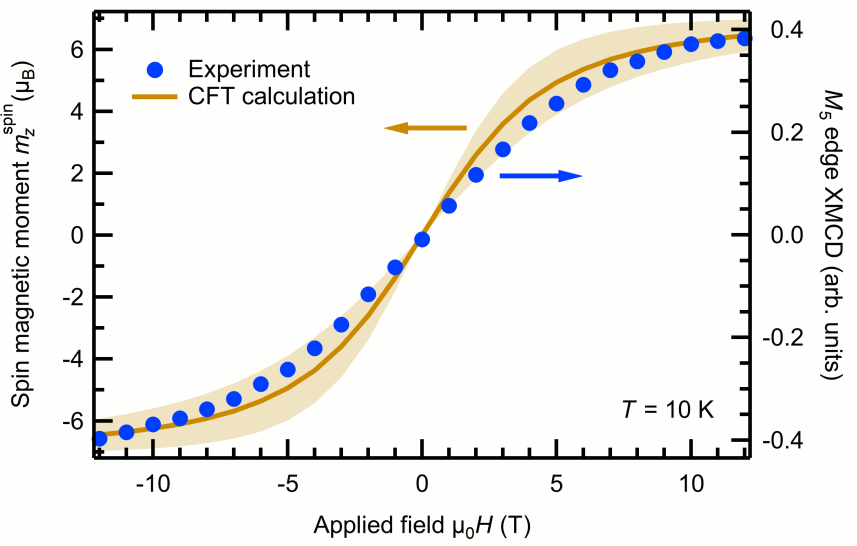

Figure 6.5: Magnetic-field dependence of the CFT calculated spin magnetic moment m_z^{spin} (solid line) and of the experimental M_5 edge XMCD TEY signal for the 2% Eu-doped Bi_2Te_3 thin film (full circles) measured at $T = 10$ K at normal incidence of the x-rays. The shaded area indicates the error, as estimated in the main text. Taken from Ref. [307].

Eu^{2+}. The magnetization arising from the Van Vleck paramagnetism of Eu^{3+} due to the admixture of low-lying excited states is also small, with a negligible contribution to the XMCD spectral shape.

The calculations, which were carried out for Eu^{2+} with the same temperature ($T = 10$ K) and external magnetic field ($B = 9$ T) as in the experiment, result in a finite orbital moment $m_z^{orb} = g_l \langle L_z \rangle = 0.02 \mu_B$, a spin magnetic moment $m_z^{spin} = g_s \langle S_z \rangle = 6.10 \mu_B$, and an effective magnetic moment $m^{eff} = \sqrt{\langle \mu^2 \rangle} = 7.91 \mu_B$. The nonvanishing orbital moment is due to the finite spin–orbit interaction in the $4f$ shell as compared to the Coulomb interaction. As for the Eu^{3+}, $m_z^{orb} = -0.07 \mu_B$ and $m_z^{spin} = 0.15 \mu_B$. Taking into account the experimental temperature uncertainty, we obtain $m_z^{spin} = (6.10 \pm 0.44) \mu_B$, which is reasonably close to the XMCD sum rules results listed in Table 6.1. Sum rules and atomic multiplet calculations also yield similar results for m_z^{orb}. Possible causes for the small deviation of the sum rules extracted spin magnetic moments from the multiplet calculations are non-magnetic contributions of the Eu sites or non-collinear alignment of the Eu moments in the paramagnetic phase, as well as partial AFM coupling between the Eu ions [126, 324].

Fig. 6.5 shows the magnetic field dependence of the CFT calculated m_z^{spin} for Eu^{2+}. Within the error bars resulting from experimental temperature uncertainty, it well reproduces the experimental field-dependent magnetization of Eu ions in Bi_2Te_3 at $T = 10$ K.

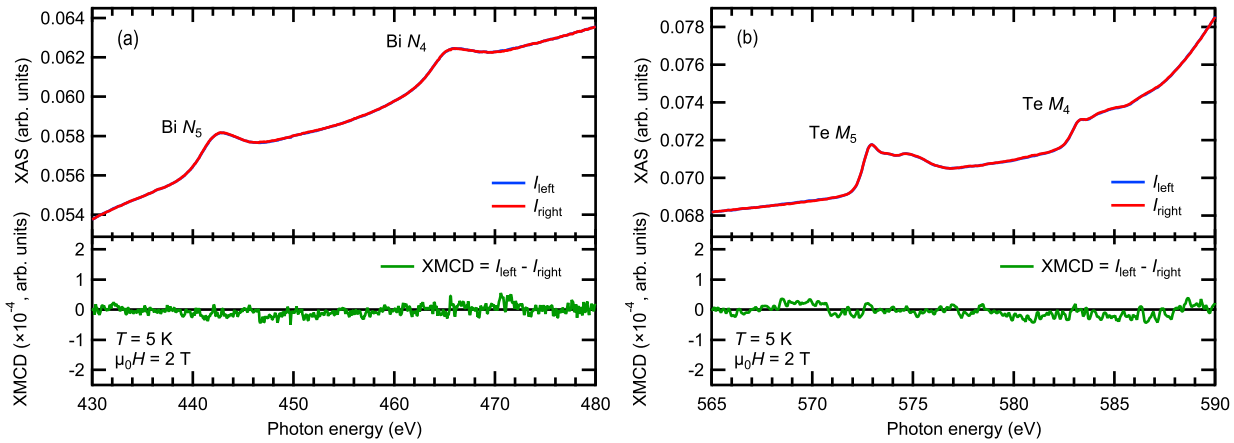

Figure 6.6: Normalized (a) Bi $N_{4,5}$ and (b) Te $M_{4,5}$ XAS (top panel) and XMCD (bottom panel) intensities of the 2% Eu-doped sample, measured at 5 K in an external magnetic field of 2 T. Taken from Ref. [307].

6.5 Te $M_{4,5}$ and Bi $N_{4,5}$ XAS and XMCD

In Chapter 4 and Chapter 5 we demonstrated a significant XMCD signal detected at the nominally non-magnetic Sb and Te host atoms of V- and Cr-doped $(Bi,Sb)_2Te_3$ due to the strong *pd*-hybridization between TM dopants and the host material. Here, in the case of Eu-doped Bi_2Te_3, we have also checked for dichroism at Bi and Te sites. Fig. 6.6 displays the XAS and XMCD measurements at the Bi $N_{4,5}$ and Te $M_{4,5}$ absorption edges at a temperature of 5 K in an applied magnetic field of 2 T. There is no spin polarization detectable on the Te and Bi sites for any dopant concentration. This indicates that a possible magnetic interaction between Eu atoms is not mediated through Te or Bi by means of some sort of indirect exchange.

6.6 Bulk magnetometry results

The bulk magnetic properties of our samples were investigated using a laboratory-based SQUID magnetometer at the group of Dr. Eberhard Goering, MPI IS Stuttgart. Fig. 6.7 shows the field-cooled magnetic susceptibility χ as a function of temperature for all three samples, measured in an in-plane applied magnetic field of 100 mT. The inset compares the inverse magnetic susceptibilities $1/\chi$ for all three samples as a function of temperature. The magnetic susceptibility data can be fitted using the Curie–Weiss law $\chi = \chi_0 + C/(T - \theta_p)$ (shown with solid black lines), where χ_0 represents the temperature-independent contribution, C is the Curie constant, and θ_p is the Weiss temperature. Fitting the data in the high temperature range ($T > 10$ K) reveals negative Weiss temperatures $\theta_p = -7.8$ K, -2.1 K and -5.6 K for the 2%, 4% and 9% Eu-doped samples, respectively. These negative values suggest the existence of AFM ordering at low temperatures, below

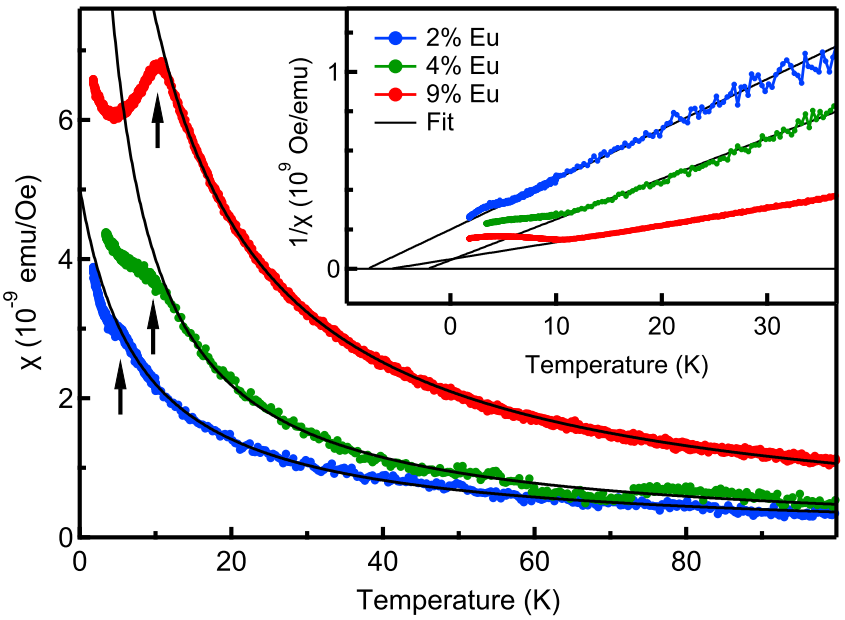

Figure 6.7: Field-cooled magnetic susceptibility χ for 2% Eu-doped (solid black), 4% Eu-doped (solid red) and 9% Eu-doped (solid blue) Bi_2Te_3 in a 2–100 K temperature range. The arrows indicate the Néel temperature estimated from the cusp in the $\chi(T)$ curves. In the inset, a comparison of the inverse magnetic susceptibility for the corresponding samples is shown at low temperatures from 2 K to 35 K. The black solid lines represent linear Curie–Weiss fits to the experimental data. Taken from Ref. [307].

the temperature of about 10 K at which the XMCD data was acquired. A similar behavior was also reported for Gd-, Dy- and Ho-doped Bi_2Te_3 thin films [114]. For the Gd-doped single crystals $Gd_xBi_{2-x}Te_3$ with $x = 0.20$, the magnetic phase transition from a PM phase to an AFM phase was reported to occur at the Néel temperature $T_N = 12$ K [130].

Whereas a negative Weiss temperature θ_p is a strong indication for the occurrence of AFM ordering, the value of $-\theta_p$ frequently deviates substantially from the Néel temperature T_N [325, 326]. However, antiferromagnets typically exhibit a cusp feature near the temperature at which $\chi(T)$ starts deviating from the Curie-Weiss law (see Fig. 6.7). T_N can be estimated from the position of this cusp [130, 325, 326]. For the 2% Eu-doped sample we find $T_N \approx 6.0$ K, while for the 4% and 9% samples the Néel temperature is about 9.0 K and 10.5 K, respectively. This seems to be the expected simple monotonic behavior as a function of Eu concentration. Increased concentration results in a higher interaction strength due to the shorter average distances between Eu ions, and hence in a higher Néel temperature.

At even lower temperatures, $\chi(T)$ increases again and tends to approach the Curie–Weiss curve to some extent, as was also observed for Ce and Gd doping [128, 130]. We attribute this to the paramagnetism usually present in strongly dilute systems in which

some magnetic ions are statistically too far away from others to couple antiferromagnetically. This interpretation is supported by the observation that the paramagnetic component is particularly strong for the 2% sample, which is the most dilute one. Finally, some paramagnetic impurities might potentially also be present in the substrate.

As we have previously discussed [306], the 9% sample, stretching the solubility limit of Eu in Bi_2Te_3, is prone to Eu inhomogeneities and clustering. Therefore it is possible that the much more pronounced cusp feature in the case of the 9% sample is related to AFM EuTe crystalline clusters. For example, for Eu-doped GeTe bulk crystals, AFM order was observed due to EuTe clusters at $T_N \approx 11$ K [327]. In fact, EuTe is a well known magnetic semiconductor and a prototypical Heisenberg antiferromagnet below $T_N = 9.8$ K [127].

6.7 Electronic properties

To study the effect of Eu dopants on the electronic structure of Bi_2Te_3 extensive laboratory- and synchrotron-based photoemission measurements were performed by Dr. Celso I. Fornari and Dr. Thiago R. F. Peixoto at the group of Prof. Friedrich Reinert, Universität Würzburg.

The laboratory-based angle-resolved spectra (ARPES) were taken at 20 K using He I_α radiation ($h\nu = 21.2$ eV) right after mechanical removal of the Te capping layer. In Fig. 6.8 (a-d) we show the data for all samples, including the undoped reference sample. While the M-shaped bulk valence band (VB) and the bulk conduction band (CB) can be seen for all samples, the topological surface state (TSS) is clearly observed only up to 2% doping. For the higher levels, the spectra are getting blurred because of the increased structural disorder [306]. To better highlight the bands, we supplement these data with the second derivative plots shown in Fig. 6.8 (e-h) [328, 329]. The gapless TSS can now be seen for all doping levels. The estimated Fermi velocity ranges from 2.55 eV·Å ($3.9 \cdot 10^5$ m/s) to 2.63 eV·Å ($4.0 \cdot 10^5$ m/s), which is in excellent agreement with the previous data for undoped bulk samples [330].

Fig. 6.8 (i) also shows a wide energy scan for the 2% sample. The red rectangle highlights the position of the TSS, the CB and the top of the VB. The VB observed at higher binding energies closely resembles that of the undoped Bi_2Te_3, with no signatures of Eu impurity bands. Here, though, one should keep in mind that the photoemission matrix elements may cause a drastic intensity variation between different bands. Under unfavorable conditions, this may result in swamping of a weak impurity signal by a more intense feature.

The photoemission intensity at the Dirac point (DP) in Fig. 6.8 is very low and one might think that there is a gap opening. However, this suppression of intensity, observed at a photon energy of $h\nu = 21.2$ eV, is due to the photoemission cross section of the surface state near the Dirac point. The effect is well known for undoped Bi_2Te_3 [331] and is not

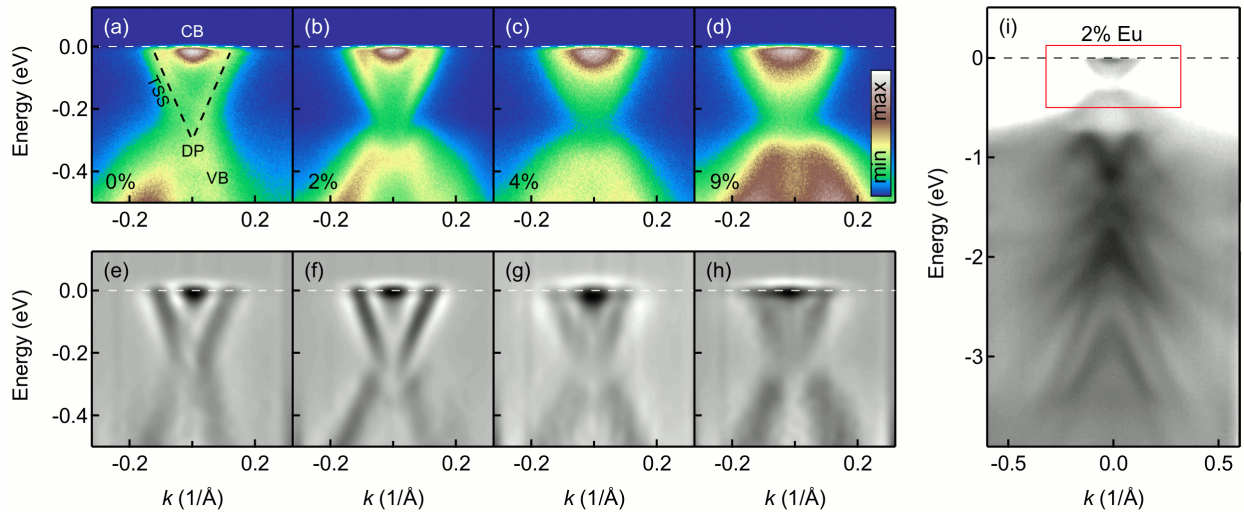

Figure 6.8: (a-d) ARPES spectra of Eu-doped Bi_2Te_3 thin films with doping ranging from 0% to 9%, measured near the $\bar{\Gamma}$ point at 20 K using a photon energy $h\nu = 21.2$ eV. (e-h) Corresponding second derivative plots. (i) Wide energy range spectrum near the $\bar{\Gamma}$ point for the 2% Eu-doped sample. Taken from Ref. [307].

related to the Eu-induced magnetism. In combination with the doping-induced disorder, the effect may give a false impression of a spectral gap. However, our energy distribution curve (EDC) and momentum distribution curve (MDC) analysis for doped samples (see Fig. 6.9) reveals practically an unmodified linear dispersion of the surface state down to the Dirac point and a finite spectral weight at the Dirac point itself, which speaks against any sizable exchange gap.

Clearly, performing ARPES experiments with variable photon energy one may systematically vary the cross section and provide more detailed insight. Such experiments would be especially beneficial at lower temperatures, helping to address the influence of the AFM order on the surface state in finer details. Fig. 6.9 (a) and (b) show EDCs and MDCs plots obtained from the spectrum in Fig. 6.8 (b), measured on 2% Eu-doped sample at 20 K with a photon energy $h\nu = 21.2$ eV. Despite the already mentioned low intensity close to the Dirac point due to photoemission cross section and some spectral blurring caused by increased structural disorder, no gap can be observed in the TSS.

To conclusively check for the presence of Eu impurity bands additional synchrotron-based measurements using different excitation energies were performed. Fig. 6.10 (a) shows a $\bar{\Gamma}\bar{M}$ spectrum taken from the 2% sample at 10 K using 265 eV photons. Along with the characteristic Dirac cones and the top of the VB, we now clearly see the impurity band located between 1.1 and 2.25 eV. To better illustrate the dispersion of different features, in Fig. 6.10 (b-f) several constant energy maps for binding energies ranging from 0 to 2.8 eV are shown. The hexagonal shapes denote the boundaries of the 2D Brillouin zones. Whereas the features seen at the Fermi level around the $\bar{\Gamma}$ points (Fig. 6.10 (a,b)) are due to the TSS and the CB, the band structure at higher binding energies outside the

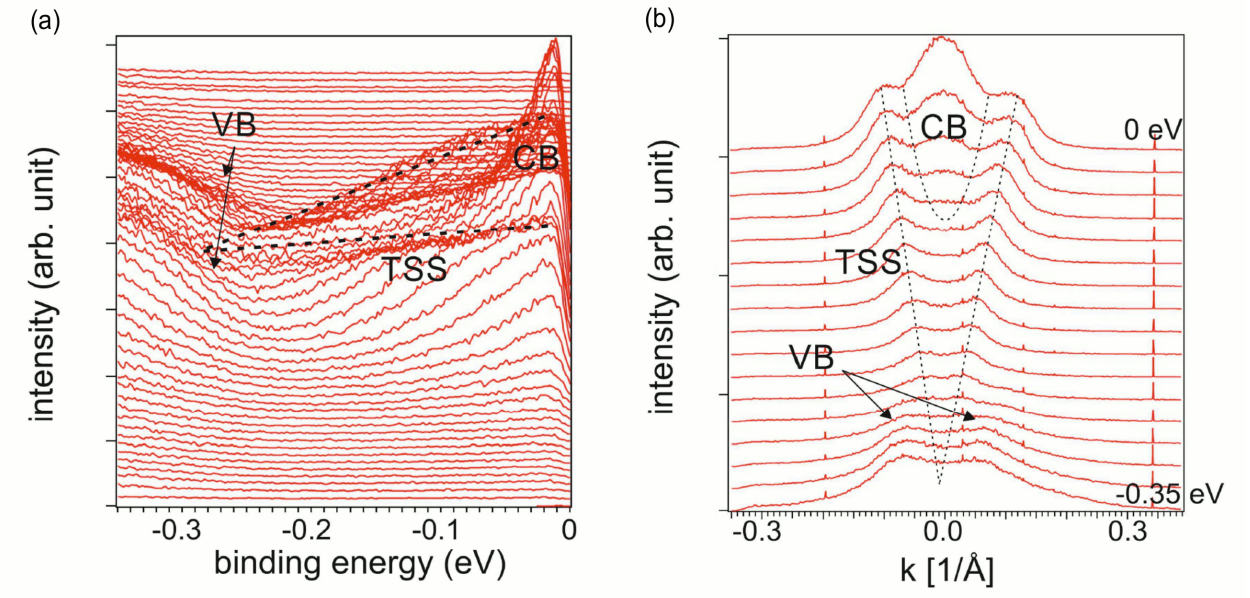

Figure 6.9: (a) EDC and (b) MDC plots obtained from spectrum in Fig. 6.8 (b) from 0 to -0.35 eV. The dashed-lines are guide to the eyes. CB stands for conduction band, VB for valence band and TSS for topological surface state.

region dominated by the impurity bands (Fig. 6.10 (a,c-f)) is very much like that of typical Bi_2Te_3.

As in the case of V-doped $(Bi,Sb)_2Te_3$ [104], to confirm that the observed flat feature is indeed the Eu $4f$ impurity band we have performed resPES measurements. Fig. 6.10 (g) shows the resPES spectra for the 4% doped sample taken with a photon energy ranging from 1120 eV to 1130 eV. For photon energies below the resonant one ($h\nu < 1120$ eV) only the Bi $5d$ core level and the valence band are visible. By gradually tuning the photon energy to the Eu $3d \rightarrow 4f$ resonance, we see a peak growing around 1.7 eV binding energy. The intensity increase is more than hundredfold, which eventually confirms that the observed feature is the Eu $4f$ impurity band.

6.8 Magnetic exchange coupling calculation

In order to understand the magnetic properties of Eu-doped Bi_2Te_3 and the magnetic exchange coupling mechanism between Eu ions, DFT calculations for bulk-doped Bi_2Te_3 including the effect of correlations within the LDA $+U$ method were performed by Dr. Philipp Rüßmann, as outlined in Section 6.1.4. The calculated electronic band structure of the host material overlaid with experimental ARPES data is shown in Fig. 6.10 (i). The band dispersion in the ΓM (red dots) and ΓK (blue dots) directions shows good agreement with the experimental data.

We find that the occupied $4f$ states of Eu_{Bi} exhibit a rigid shift down in energy with increasing $U^{\text{eff}} = U - J$, which changes the magnetic moment from $6.58\mu_B$ in the case

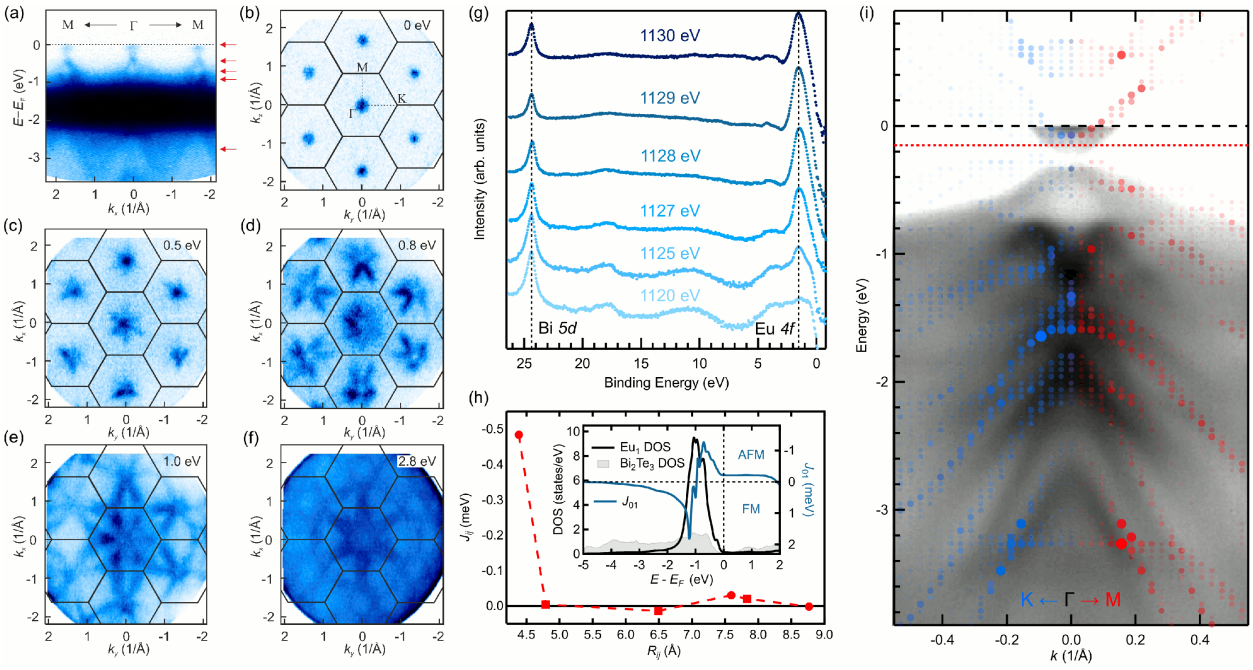

Figure 6.10: (a) Energy-momentum cut along the $\bar{\Gamma}\bar{M}$ direction for the 2% sample. (b-f) Constant energy maps for binding energies ranging from 0 to 2.8 eV. The hexagonal shapes are the boundaries of the 2D Brillouin zones. (g) ResPES data for the 4% sample, showing the Bi $5d$ and Eu $4f$ core levels. (h) Distance dependence of the exchange interaction J_{ij} between pairs of Eu impurities placed in the same (●) or neighboring (■) Bi layers within one quintuple layer. The inset shows $4f$ dominated total DOS of the Eu dimer (black) and total DOS of the host material (gray) together with the energy dependence of the exchange coupling strength J_{01} (blue). (i) LDA band structure and ARPES data for the 2% sample. The LDA bands are shown in ΓM and ΓK directions with symbols, whose size and opaqueness is proportional to the spectral weight. The red dotted line shows the position of the theoretical Fermi level, which differs from the experimental one by 150 meV due to the intrinsic n-doping in the measured sample. Taken from Ref. [307].

of pure LDA ($U = 0, J = 0$) to $6.94\mu_B$ in case of LDA $+U$ ($U^{\text{eff}} = 8.25\,\text{eV}$). The size of the magnetic moment and the bandwidth of the $4f$ states do not change much for U^{eff} values ranging from 4.25 to 9 eV, which indicates a stable half-filling of the Eu $4f$ orbitals and only a weak pf-hybridization with the Bi_2Te_3 host system. This is consistent with the very small and antiferromagnetically aligned induced magnetic moments in the first two Te and the first Bi neighbors around the Eu_{Bi} defect of $-8.0 \times 10^{-3}\,\mu_B$, $-4.3 \times 10^{-3}\,\mu_B$ and $-6.9 \times 10^{-5}\,\mu_B$, respectively. Additionally, band structure calculations in a $2 \times 2 \times 1$ supercell were performed, which show that the Eu_{Bi} impurity bands do not disperse due to the weak hybridization of the f states with its surrounding p states. This result agrees with the results of the ARPES measurements, see Fig. 6.10 (a).

In Fig. 6.10 (h) the distance dependent exchange coupling constants J_{ij} for $U^{\text{eff}} = 8.25\,\text{eV}$ are shown. The inset shows the impurity DOS and the energy-dependent exchange coupling J_{01} for nearest Eu_{Bi}-Eu_{Bi} neighbors ($R_{ij} = 4.38$ Å) which is in good agreement with the experimentally determined position of the Eu $4f$ states. We find weak AFM

interactions for the first-neighbor Eu_{Bi} impurities that are located on the same Bi layer. For larger distance between the Eu atoms the exchange interactions quickly decline. The energy-resolved J_{ij} reveals a flat plateau of AFM interactions above the Fermi level, which increases for smaller U^{eff} (not shown). This indicates AFM coupling arising from the direct overlap of the impurity wave functions [296, 299]. The strong spatial localization of the Eu $4f$ states explains the weakness of the interaction and the quick decrease with distance.

Additional calculations with a Fermi level shifted into the bulk conduction band show that the strength of the AFM exchange interactions can be increased by up to $\approx 50\%$ for Fermi level shifts of up to $\pm 0.4\,\text{eV}$. However, the weak pf-hybridization between Eu impurity and surrounding host atoms does not result in a significant increase of exchange interactions at larger distances.

6.9 Conclusions and Outlook

Realizing an AFM topological insulator by doping Bi_2Te_3 with Eu has turned out to be more challenging than realizing its FM counterpart, namely V or Cr doped Bi_2Te_3. One likely reason is the adverse effect of the random—and dilute—impurity distribution on establishing a staggered magnetization.

The disorder and charge doping induced by the non-isoelectronic substitution present another challenge as they can interfere with the integrity of the TSS. The presented comprehensive experimental and theoretical studies indicate that $Eu_zBi_{2-z}Te_3$ is not critically affected by these problems. First, the TSS remain detectable in the ARPES results at all Eu concentrations. This is noteworthy since Eu, unlike most other RE elements, enters Bi_2Te_3 as Eu^{2+} and thus leads to hole doping and disorder [306].

Second, for all Eu concentrations the SQUID data yield a negative Weiss temperature θ_p and a cusp-like feature in the $\chi(T)$ curve, which indicates the onset of AFM order for temperatures between 5 K and 10 K. Due to the thinness of the samples and the presence of Eu, it was not possible to measure the AFM correlation length experimentally using neutron diffraction. However, the AFM coupling between Eu atoms is corroborated by DFT calculations in the LDA $+U$ approximation, which well reproduce the photoemission data. The largest effective $J_{ij} = -0.5$ meV is found between Eu ions inside the same Bi layer with its energy comparable to the AFM onset temperature observed in the SQUID data. We point out that previous theoretical studies of $Eu_zBi_{2-z}Se_3$ predicted FM order [124], for which we found no evidence in our related telluride system.

Considering the hexagonal arrangement of the atoms in the Bi layer, one would expect the AFM order to get stronger with increasing Eu doping, but then at higher levels increasing frustration should suppress ordering. Counter to this intuition, our SQUID data seem to indicate an increasing AFM onset temperature of up to the 9% doping, for

which nearly one out of four Bi atoms is replaced by Eu. This is probably due to exceeded Eu solubility in the 9% sample and cluster formation of EuTe [306], which is a well known antiferromagnet with $T_N = 9.8$ K.

Whereas in $MnBi_2Te_4$ the interactions are FM within the Bi planes and AFM between the neighboring planes [31, 148], the theoretical calculations for $Eu_zBi_{2-z}Te_3$ presented here suggest antiferromagnetism of a different nature: It closely resembles that found in $Gd_zBi_{2-z}Te_3$, for which DFT calculations yield AFM coupling between Gd atoms inside a Bi plane [130], just like for the Eu atoms in our case. In addition, a gap formation was experimentally observed for Gd doping [131], but its connection to the in-plane AFM interactions still needs to be clarified.

In conclusion, our results warrant further investigations at temperatures below 10 K down to the kelvin range to better understand the character of the antiferromagnetism we observe and to experimentally establish its impact on the TSS. Kelvin-range photoemission and XAS experiments are challenging and were not performed for the present study. Yet, in the light of our results, XAS and dichroism measurements, including linear dichroism to characterize the AFM state, appear promising. Low-temperature ARPES needs to be performed to search for a gap opening in the TSS. The onset of antiferromagnetism over a substantial doping range corroborates the potential of RE doping to result in an AFM topological insulator with exotic quantum properties.

Chapter 7

Intermixing-driven surface and bulk ferromagnetism in the QAH candidate $MnBi_6Te_{10}$

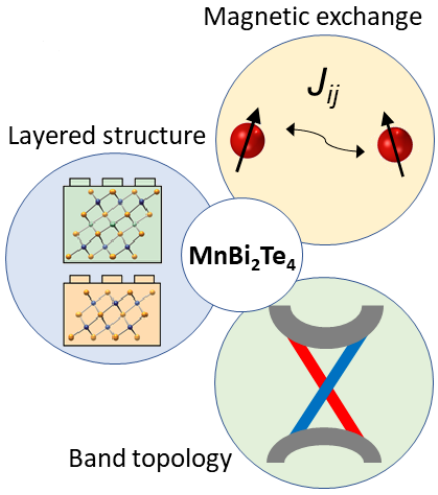

As discussed in Chapter 2, the first material shown to be an intrinsic magnetic topological insulator (IMTI) was $MnBi_2Te_4$ [31, 32], a member of the family of layered van der Waals topological materials $(MnBi_2Te_4)(Bi_2Te_3)_n$ (MBT_n, $n = 0-4$) [148]. This family of materials is among the most promising quantum anomalous Hall (QAH) effect systems thanks to its band-structure characteristics enabling the Dirac point well within the bulk band gap [332], as well as due to a robust magnetic subsystem, which is required to break time-reversal symmetry. The progenitor $MnBi_2Te_4$ consists of septuple layers (SL) centered by ferromagnetically (FM) ordered Mn. The SLs couple antiferromagnetically (AFM), leading to a complex layer-number dependence of the quantization effects hampering the QAH effect [42]. Interlacing the SL with an increasing number n of Bi_2Te_3 layers (QLs) reduces the AFM coupling and stabilizes an FM state for $n \geq n_{FM}$ [150, 151]. However, the exact n_{FM} is disputed, the mechanisms driving the FM state and n_{FM} are not understood, and the surface magnetism remains obscure.

Certainly, the main interest in IMTIs lies in the relation between the bulk and surface long-range magnetic ordering and the surface topological electronic properties. Thus, it is highly important to combine the study of bulk properties with techniques tailored to provide insight into the surface local magnetic and electronic properties. This is the goal of this chapter, in which we uncover robust FM properties of $MnBi_6Te_{10}$ ($n_{FM} = 2$) with $T_C \approx 12\,K$ both in the bulk and on the surface by using bulk-sensitive superconducting

quantum interference device (SQUID) magnetometry and surface-sensitive x-ray magnetic circular dichroism (XMCD). The clear FM characteristics seemingly contradict the weak AFM coupling anticipated by our density functional theory (DFT) calculations for the atomically ordered compound. This disagreement is resolved by including the x-ray diffraction (XRD) derived Mn substoichiometry and Mn/Bi site intermixing into the DFT calculations, as they enable FM configurations already for $MnBi_2Te_4$. By analyzing the intermixing ratios in our samples and comparing them to those reported showing no ferromagnetism, a connect to the growth conditions can be established. The spectroscopy results together with DFT and *ab initio* MLFT calculations allow us to determine in full detail the local magnetic and electronic properties of the Mn ions in the bulk and near the surface as a function of the temperature and the applied magnetic field, and deliver important microscopic physical parameters, including Mn 3*d*-shell occupation, the spin and orbital magnetic moments. These results suggest that carefully engineered intermixing plays a crucial role in accomplishing robust FM order and therefore could be the key towards enhanced QAH effect properties at elevated temperatures.

7.1 Materials and Methods

7.1.1 Crystal growth and characterization

The samples discussed in this chapter were grown and characterized by Dr. Laura Folkers and Prof. Anna Isaeva, Leibniz IFW Dresden. Platelet-like $MnBi_6Te_{10}$ crystals (diameter up to 1 mm, see Fig. 7.3) were mechanically separated from an ingot that had been obtained by slow cooling of a pelletized sample ($\varnothing$6 mm, max. pressure: 2 tons). The sample was mixed from the pre-synthesized phase pure MnTe and Bi_2Te_3 (0.85 : 2 at. %) powders. The pellet was evacuated and sealed off in a quartz tube under the dynamic vacuum ($p \leq 1 \times 10^{-3}$ mbar) and place at 923 K into a preheated two-zone tube furnace with the temperature control via external thermocouples. The ampule was cooled down to 858 K at the rate 1 K/hour, tempered for 14 days and then quenched in water.

Powder x-ray diffraction (PXRD) data were collected on an X'Pert Pro diffractometer (PANalytical) with Bragg-Brentano geometry operating with a curved Ge(111) monochromator and Cu-Kα_1 radiation ($\lambda = 154.06$ pm). Variable divergence slits were used on the X'Pert Pro equipment to keep the illuminated sample area constant. The phase composition of the polycrystalline ingot and individual crystals was estimated by Le Bail or Rietveld refinements in JANA2006 [333]. The preferred orientation of the crystallites was described by March-Dollase corrections, the roughness for Bragg-Brentano geometry was accounted for by the Suorti method.

Scanning electron microscopy (SEM) has been performed using a SU8020 (Hitachi) equipped with a Silicon Drift Detector (SDD) X-MaxN (Oxford) at U_a =2–5 kV. The composition of selected single crystals was determined by semi-quantitative energy dispersive x-ray analysis at 20 kV acceleration voltage.

7.1.2 Bulk magnetometry measurements

The bulk magnetometry measurements were conducted and analyzed by Bastian Rubrecht and Dr. Laura Teresa Corredor in the group of Dr. Anja Wolter, Leibniz IFW Dresden. Field and temperature dependent magnetization studies were performed using a Quantum Design superconducting quantum interference device (SQUID) magnetometer equipped with a vibrating sample magnetometer (VSM) option (MPMS3). The magnetization data of samples #1 – #4 are normalized to the real compositions determined via EDX. To obtain the absolute magnetization M per Mn atom, a precise knowledge of the sample mass is important. Samples #1 and #4 have an approximately 10 times smaller mass than sample #2, increasing the error of M. Nevertheless, the data for all four samples agree well with each other, see Fig. 7.6.

A setup made of two half-cylindrical quartz rods fixed with a small quantity of GE varnish to the main quartz VSM sample holder was designed to ensure an alignment of the crystals such that the external magnetic field was applied perpendicular to the crystal surface. Note that this setup, however, results in a rather temperature-independent (at not too low temperature) but non-negligible background contribution to the magnetic susceptibility, hindering a reliable extraction of the Curie-Weiss constant θ_{CW} and the temperature independent susceptibility χ_0 for our low-mass samples $MnBi_6Te_{10}$.

7.1.3 X-ray absorption spectroscopy

The XAS and XMCD measurements at the Mn $L_{2,3}$ absorption edges were performed using the high field cryomagnet end station HECTOR of the BOREAS beamline at the ALBA synchrotron radiation facility [204] (see Section 3.2.3) and at the high-field diffractometer at UE46 PGM-1 beamline, BESSY II [201] (see Section 3.2.2). The single crystals of $MnBi_6Te_{10}$ were glued with conducting silver epoxy onto Cu sample plates and mounted on the cold finger of a helium flow cryostat. Prior to the measurements, the samples were mechanically cleaved in the fast-entry chamber at a pressure of $\sim 10^{-9}$ mbar. The sample was then transferred into the spectroscopy chamber operated under UHV conditions, with a base pressure in the 10^{-11} mbar range. The effectiveness of this method to expose a clean sample surface using V- and Cr-doped $(Bi,Sb)_2Te_3$ was demonstrated before [79, 267].

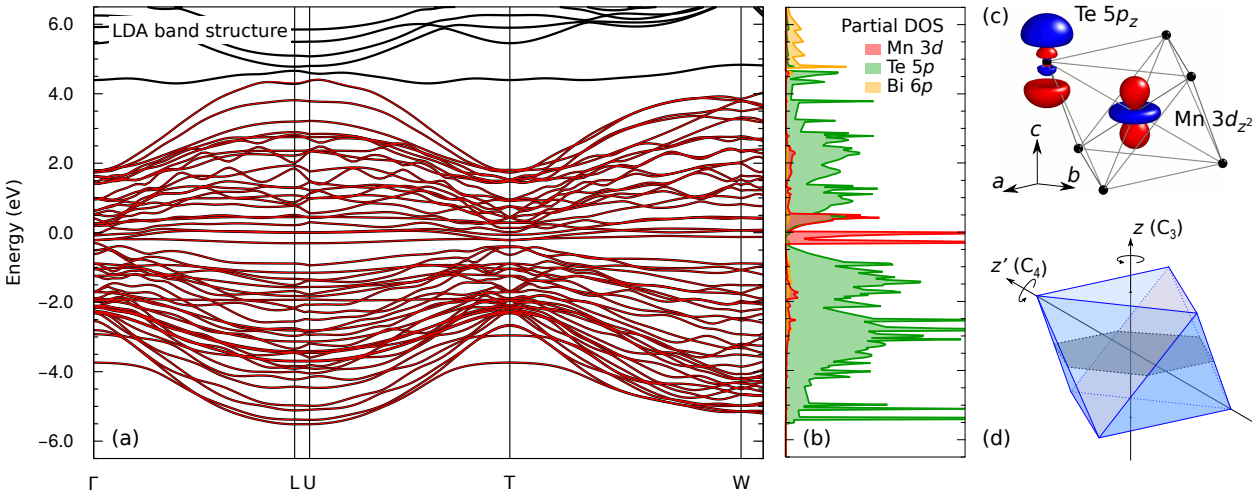

Figure 7.1: (a) LDA band structure of $MnBi_6Te_{10}$ (black curves) including the downfolded Wannier bands (red curves) with Mn $3d$, Te $5p$, and Bi $6p$ character. (b) Partial densities of states for Mn $3d$ (red), Te $5p$ (green), and Bi $6p$ (orange) states. (c) Geometry of the local $MnTe_6$ cluster used in the MLFT calculation, consisting of Mn cation surrounded by six Te ligands. Mn $3d_{z^2}$ and Te $5p_z$ Wannier orbitals (constant-amplitude surfaces) are shown with the $\pm$ signs labeled by red and blue. (d) $MnTe_6$ octahedron cage turned on its face, thus z-, x-, y-direction are no longer equivalent, which allows for non-vanishing liner dichroism. Also note C_3 rotational symmetry around z-axis, in contrast to C_4 symmetry observed for typical orientation of octahedron.

The measurements were carried out in the total electron yield (TEY) or fluorescence yield (FY) mode at magnetic fields of up to 6 T and at various temperatures in the 3.5–35 K range. The temperature was calibrated with a thermal sensor mounted at the sample position before the experiment. Especially below about 5 K, the actual sample temperature crucially depends on the thermal contact, increasing its error as compared to higher temperatures. The spectral intensity was normalized by the incoming photon intensity (I_0). We used circularly polarized light at both beamlines. The area probed by the beam at both facilities (about $120 \times 80 \mu m^2$) was much smaller than the sample size.

The raw XAS spectra measured with the helicity vector antiparallel (left) and parallel (right) to the fixed magnetic field were scaled with respect to each other to have the same intensity at energies far from the resonances to obtain I_{left} and I_{right}. We define the average XAS as $I_{\text{avg}} = (I_{\text{left}} + I_{\text{right}})/2$ and the XMCD signal as $I_{\text{XMCD}} = I_{\text{left}} - I_{\text{right}}$. The x-ray magnetic linear dichroism (XMLD) was measured in grazing light incidence and defined as the difference between the XAS spectra acquired with σ and π polarization (polarization vector perpendicular and parallel to the plane of incidence), $I_{\text{XMLD}} = I_\pi - I_\sigma$. To cancel out any experimental drifts, for each dichroism signal we measured eight spectra in a row by altering the x-ray polarization.

Table 7.1: Slater integrals obtained from DFT and spin–orbit coupling constants for Mn^{2+} ion (in units of eV).

ion	state	configuration	$F_{dd}^{(2)}$	$F_{dd}^{(4)}$	ζ_{3d}	$F_{pd}^{(2)}$	$G_{pd}^{(1)}$	$G_{pd}^{(3)}$	ζ_{2p}
Mn^{2+}	initial	$2p^6 3d^5$	9.432	5.813	0.040				
	final	$2p^5 3d^6$	10.196	6.290	0.053	5.335	3.838	2.177	6.846

7.1.4 Ab initio multiplet ligand-field theory

As a starting point to obtain input parameters for the MLFT modeling, self-consistent non-spin-polarized DFT calculations have been performed in FPLO [255] with the Brillouin zone sampled by the $2 \times 2 \times 2$ k-point mesh. The exchange-correlation potential was treated using the local density approximation with the scalar relativistic functional as proposed by Perdew and Wang [334]. We used the experimental crystal structure of $MnBi_6Te_{10}$ reported by Souchay *et al.* [157]. $MnBi_6Te_{10}$ crystallizes in the rhombohedral space group $R\bar{3}m$ (166) with the unit cell lattice parameters $a = 4.37$ Å and $c = 101.83$ Å. The compound exhibit alternation of quintuple Bi_2Te_3 (five layers, Te-Bi-Te-Bi-Te) and septuple $MnBi_2Te_4$ (seven layers, Te-Bi-Te-Mn-Te-Bi-Te) blocks along the c-axis with a van der Waals gap between the adjacent blocks. Mn has a slightly distorted octahedral coordination with six equidistant Mn-Te bonds of 3.00 Å, which entails C_{3v} symmetry of the crystal field.

The downfolding to a basis set of Mn $3d$, Te $5p$ and Bi 6 orbitals has been done using an energy window from -6 to 3 eV including an exponential decaying tail with a decay of 1 eV at the boundaries of the selected energy range. For the quality of the achieved downfolding, please see Fig. 7.1 (a). Among others, the obtained Wannier orbitals were used as an *ab initio* input for our MLFT calculations.

The MLFT calculations of the Mn $L_{2,3}$ edge XAS, XMCD and XMLD spectra were performed using the Quanty software package for quantum many-body calculations within the configuration-interaction scheme (see Chapter 3) considering the nominal $2p^6 3d^5$ (Mn^{2+}) configuration and further two additional charge-transfer states $d^6\underline{L}$ and $d^7\underline{L}^2$, where $\underline{L}^p$ denotes p holes in the Te $5p$ orbitals. The spectral contributions from each of the split ground-state terms to the absorption spectra were weighted by a Boltzmann factor corresponding to the nominal experimental temperature of $T \approx 2$ K. The mean-field effective potential was accounted for by introducing an exchange field term acting on the spin. We estimated the exchange field from the critical temperature $T_C \approx 12$ K for the $MnBi_6Te_{10}$. To account for the instrumental and intrinsic lifetime broadening, the calculated spectra were convoluted with a Gaussian function of 0.35 eV full width at half maximum (FWHM) and with an energy-dependent Lorentzian profile of $0.15 - 0.35$ eV FWHM.

All the input parameters for the MLFT were estimated from DFT, except for the charge-transfer energy Δ, the Coulomb interaction energies U_{dd} between the valence $3d$ electrons and U_{pd} between the $2p$ core electrons and $3d$ valence electrons, which are fitted to the experiment. Adopting published results, we fix U_{dd}/U_{pd} to 0.8, which also allows us to reduce the parameter space and speed up fitting [249, 250, 252, 275]. The Slater integrals obtained from DFT and spin–orbit coupling constants used in the calculations for the Mn $2p^63d^5$ initial state and $2p^53d^6$ final state are shown in Table 7.1. Due to the relaxation of atomic orbitals upon the $2p \rightarrow 3d$ excitation, we scaled up the DFT-derived $F_{dd}^{(2)}$ and $F_{dd}^{(4)}$ Slater integrals by 8% for final state, which improves the agreement between the calculated and experimental spectra. Spin–orbit coupling was kept at its Hartree–Fock value [177]. For the further enhancement of the agreement between the calculated and experimental spectra, we actually do not consider pure DFT estimates for crystal-field and hopping parameters, but rather fine-tune them around their DFT values to better reproduce the experimental XAS, XMCD and XMLD spectra. For this purpose we describe the crystal field in more simple octahedral (O_h) symmetry, with the C_4 axes of the octahedron along the Mn–Te bonds (see Fig. 7.1 (d)), instead of trigonal C_{3v} symmetry. This simplification is valid as a slightly distorted octahedral coordination would result in a small energy splitting of the t_{2g} orbitals as compared to already tiny $10Dq$ less than 100 meV, which has negligible impact on the calculated spectra. Moreover, the energy scale of the crystal-field splittings is smaller than the energy resolution of the XAS experiment and further justifies our approximation. The parameters used for the calculations best reproducing our data are listed in Table 7.2. It is well known that experiments involving charge-neutral excitations, such as XAS, are weakly sensitive to Δ, U_{dd} and U_{pd}. In our particular case we were fitting simultaneously XAS, XMCD and XMLD spectra, which greatly mitigates these kind of problems. The values of Δ of 1.1 eV, U_{dd} of 4 eV, and U_{pd} of 5 eV are in good agreement with what is reported in literature for (Ga,Mn)As [335–339] and Mn-doped Bi_2Se_3 [340] and Bi_2Te_3 [341]. As for the covalent hopping integrals $V_{t_{2g}}$ and V_{e_g} between the p orbitals at the ligand sites and the Mn $3d$ orbitals of t_{2g} and e_g symmetry, respectively, their values are well known for manganese oxides [245, 250, 276], but still lacking for other compounds with less electronegative ligands, such as Te. Therefore, these values we obtained for the hybridization energies, as well as for charge-transfer, Coulomb repulsion, crystal-field and Slater integrals might serve as an important input to future atomic multiplet calculations on similar compounds.

7.1.5 Bulk DFT (GGA+U) calculations

The simulations of structural models were performed by Dr. Jorge I. Facio in the group of Prof. Jeroen van den Brink, Leibniz IFW Dresden. Fully relativistic DFT calculations based on the Generalized Gradient Approximation (GGA) + U were performed with the

Table 7.2: Input parameters for the MLFT calculations obtained from DFT and further fit of XAS, XMCD and XMLD spectra for $MnBi_6Te_{10}$ (in units of eV).

	$10Dq$	T_{pp}	Δ	U_{dd}	U_{pd}	V_{e_g}	$V_{t_{2g}}$
$MnBi_6Te_{10}$	0.06	1.9	1.1	4.0	5.0	1.3	0.65

parametrization of Perdew, Burke, and Ernzerhof [342], using the Slater integrals presented in Table 7.1 and the full localized limit for the double-counting correction. The spin–orbit coupling was included in the four-component formalism as implemented in FPLO. The total energy difference between the FM and A-type AFM configurations was computed using for Brillouin zone integrations a linear tetrahedron method with a mesh having $14 \times 14 \times 14$ subdivisions. The magnetic anisotropy energy was calculated in the AFM state based on a mesh having $10 \times 10 \times 10$ subdivisions. The Mn $3d$ occupancy and the spin projection presented in the main text correspond to the gross projections. Details of the calculations of structural models with antisite defects are presented in the Section 7.2.2.

7.2 Results

7.2.1 Crystal growth and structure refinement

The results presented in this section were obtained by Dr. Laura Folkers and Prof. Anna Isaeva. $MnBi_6Te_{10}$ crystals were grown by slow crystallization from a melt. Besides $MnBi_6Te_{10}$, the obtained ingot contained admixtures of Bi_2Te_3 and $MnTe_2$, see Fig. 7.2. Observing side phases fully agrees with earlier studies of $MnBi_6Te_{10}$ melting and decomposition by differential scanning calorimetry [157]. Their occurrence can be related to crystal growth being a competitive process between $MnBi_6Te_{10}$, $MnBi_8Te_{13}$ and Bi_2Te_3, all having nearly the same crystallization temperatures.

A series of EDX (energy-dispersive x-ray spectroscopy) point measurements on individual crystals extracted from the ingot demonstrated a compositional range between Mn: 5.0, Bi: 36.6, Te: 58.4 and Mn: 4.2, Bi: 37.1, Te: 58.7 (in at. %). Our samples were thus consistently more Mn-deficient than expected from the nominal chemical formula $MnBi_6Te_{10}$ of the atomically ordered material (Mn: 5.9, Bi: 35.3; Te: 58.8). Again, this echoes earlier single-crystal structure refinement of $Mn_{0.73(4)}Bi_{6.18(2)}Te_{10}$ by x-ray diffraction published by Isaeva *et al.* [157], where it was systematically showed that Mn substoichiometry is determined by the Mn/Bi intermixing. Both features are also present in $Mn_{0.85}Bi_{2.10}Te_4$ [33] and $Mn_{0.75}Bi_{4.17}Te_7$ [149]. To facilitate perception, we denote our samples as $MnBi_6Te_{10}$ in the following text, keeping in mind that they are in fact substoichiometric.

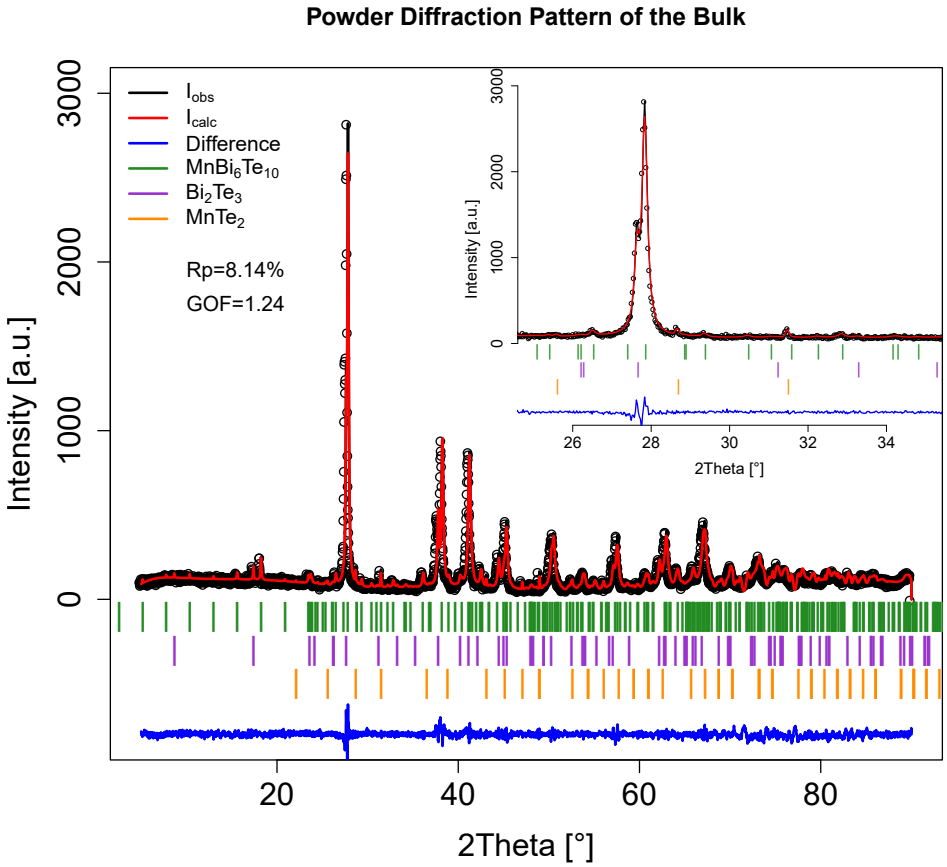

Figure 7.2: Experimental (black) and refined by the Le Bail method (red) PXRD patterns of the molten ingot, from which individual crystals were mechanically extracted. The difference curve is shown in blue ($R_p = 0.081$ %, $R_{wp} = 0.109$, GoF $= 1.24$); the vertical ticks mark the Bragg reflection positions for each identified phase. The sample is a three-phase mixture of $MnBi_6Te_{10}$ (sp. gr. $R\bar{3}m$, $a = 4.3667(2)$ Å, $c = 101.869(4)$ Å), Bi_2Te_3 (sp. gr. $R\bar{3}m$, $a = 4.3799(3)$ Å, $c = 30.491(2)$ Å) and $MnTe_2$ (sp. gr. $Pa\bar{3}$, $a = 6.9494(3)$ Å).

The present study was performed on four individual Mn-deficient $MnBi_6Te_{10}$ crystals (denoted as sample #1 − #4 henceforward; for their chemical compositions (EDX) see Fig. 7.3). Powder x-ray diffraction (PXRD) measurements, which required grinding the crystals to a homogeneous powder, were conducted after all other measurements had been finalized, in order to elucidate the underlying intermixing phenomenon. It was confirmed that all four samples exhibit the crystal lattice of $MnBi_6Te_{10}$ with a sequence of one SL and two QLs (Fig. 7.4 (a)) plus notable cation antisite disorder. $MnBi_6Te_{10}$ constituted the main phase as per Rietveld method and a firm link between the Mn content as found by EDX and the underlying crystal lattice of $MnBi_6Te_{10}$ could be established in our samples.

This approach is exemplified on sample #2, see Fig. 7.4 (b). It was confirmed that sample #2 was $Mn_{1-x}Bi_{6+x}Te_{10}$ ($x \approx 0.20 - 0.25$) which crystallized in the rhombohedral space group $R\bar{3}m$ (No. 166) with the unit cell lattice parameters $a = 4.36778(8)$ Å and $c = 101.8326(6)$ Å. To stabilize a further Rietveld refinement, the EDX compositions (*e.g.*

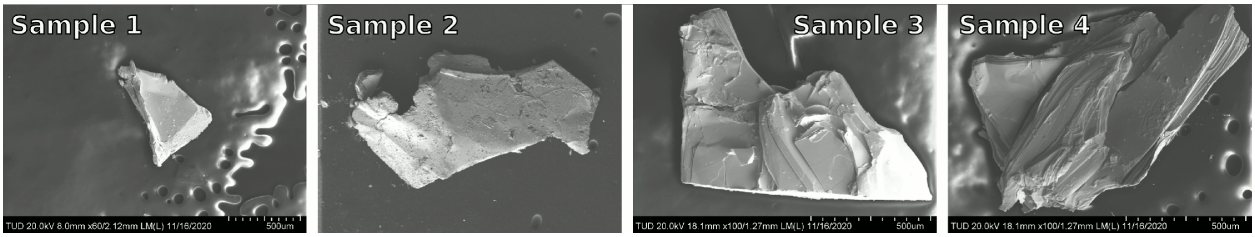

Figure 7.3: SEM images of selected $MnBi_6Te_{10}$ crystals (denoted left to right as sample #1–4) that were used for the presented SQUID magnetization and XMCD experiments. The found chemical compositions (EDX) are as follows (in at. %): Sample #1: Mn 4.1(4), Bi 37.5(4), Te 58.40(4); Sample #2: Mn 4.6(2), Bi 37.8(8), Te 57.6(7); Sample #3: Mn 4.5(3), Bi 36.9(2), Te 58.6(1); Sample #4: Mn 4.4(6), Bi 36.6(7), Te 59.0(5).

$Mn_{0.76}Bi_{6.24}Te_{10}$ or $Mn_{0.8}Bi_{6.2}Te_{10}$) were introduced as constraints. When cation Mn/Bi intermixing was allowed in the refinement, the reliability factors R_{all} and R_{obs} dropped down significantly, confirming that this phenomenon was undoubtedly present in the structure. Due to very low sample mass (1–2 mg), the acquired powder diffraction data did not allow one to settle in for just one particular intermixing model with a statistically unequivocal quantification. The refined Mn content is also strongly dependent on whether cation vacancies are allowed in the refinement. A structural solution without voids in the 3*a* and 6*c* positions was chosen. Despite the outlined uncertainties, all tested models with various composition constraints have in common that: 1) the Mn:Bi ratio in the 3*a* position in the center of an SL is close to 56:44; 2) the outer cation site of an SL (6*c*) contains up to 2 % Mn); 3) the QL always accommodates some Mn (2–7 % Mn) in the 6*c* cation sites. The presence of Mn in all cation positions accords with our earlier reported refinement on $Mn_{0.81}Bi_{6.13}Te_{10}$ single crystals [157] and is in contrast to the findings of Klimovskikh *et al.* [153]. Such subtle variations in intermixing patterns can dramatically impact the magnetic properties, as witnessed in the next subsection.

7.2.2 Bulk magnetism

Fig. 7.5 (a) shows the field-cooled (FC) and zero-field cooled (ZFC) normalized magnetization of sample #2 in an out-of-plane magnetic field of 10 mT. A phase transition into a long-range magnetically ordered state is observed at $T_C = 12.0$ K, determined by the inflection point, together with a notable FC/ZFC splitting around 10 K. These observations point towards a ferromagnetic alignment of the Mn spins in our $MnBi_6Te_{10}$ samples and contrast with the antiferromagnetic transition at $T_N \sim 11$ K so far reported for the nominal $MnBi_6Te_{10}$ composition [153, 155, 161, 162]. Our Curie-Weiss analysis in the temperature regime 100–400 K, shown in the inset of Fig. 7.5 (a), yields an effective moment of $m_{eff} = 5.8 \pm 0.1\ \mu_B$/Mn in close agreement with the value $m_{eff} = 5.67\mu_B$ calculated by MLFT (see below). The uniformity of all four $MnBi_6Te_{10}$ crystals is strongly supported by

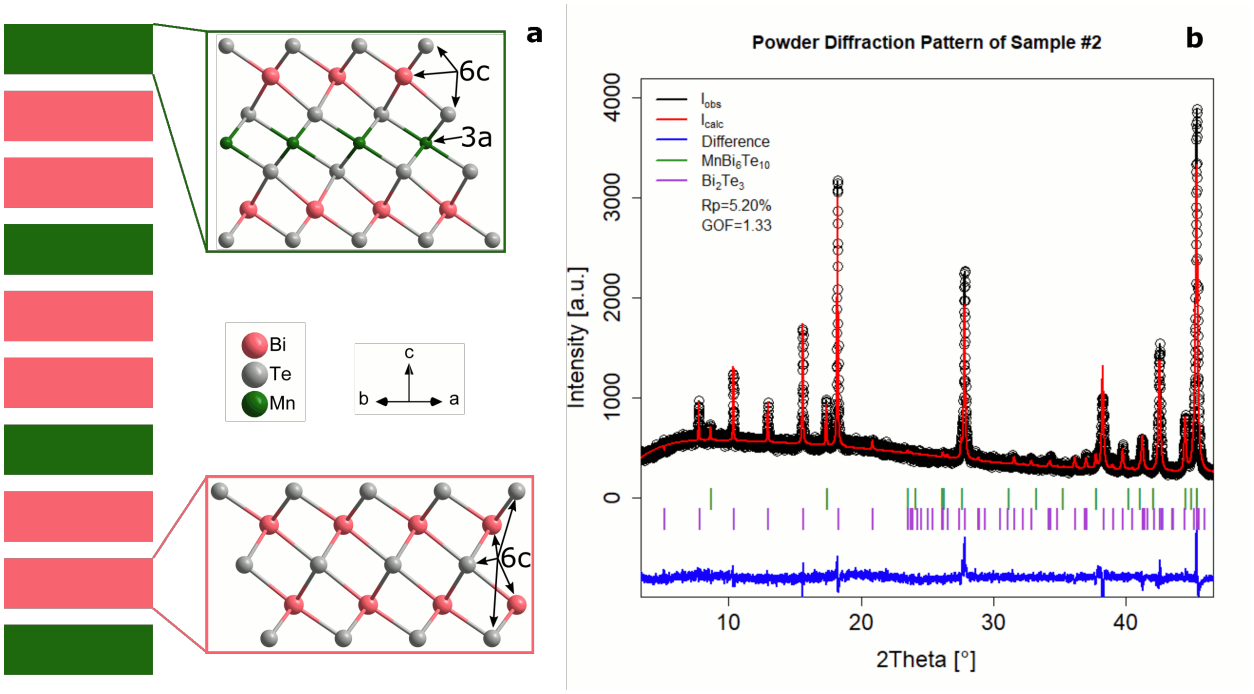

Figure 7.4: (a) The unit cell of $MnBi_6Te_{10}$ is sketched by slabs of red and green boxes, where green indicates a septuple layer and red indicates a quintuple layer. In the expanded views we show the atomic structure. The QL and SL are interleaved by van der Waals gaps. (b) Experimental (black) and refined by Rietveld method (red) powder X-ray diffraction pattern of the sample #2 in the 2θ range $5-45°$. The difference curve is shown in blue ($R_p = 0.055$, $wR_p = 0.071$, GoF = 1.48). A small fraction of Bi_2Te_3 comprises 7 wt. % ($R\bar{3}m$, $a = 4.3797(4)$ Å, $c = 30.4965(7)$ Å, $R_{obs} = 0.094$, $wR_{obs} = 0.096$, $R_{all} = 0.109$). The main phase is refined with the overall $Mn_{0.8}Bi_{6.2}Te_{10}$ composition ($R_{obs} = 0.079$, $wR_{obs} = 0.074$, $R_{all} = 0.104$).

the nearly identical SQUID magnetometry curves (see Fig. 7.6), with transition temperatures that vary by only 0.1 K.

The magnetization curves $M(H)$ in Fig. 7.5 (b) show clear FM loop openings, with a coercive field of $\mu_0 H_c \sim 32\,\mathrm{mT}$ at $T = 2\,\mathrm{K}$, and a finite remanent moment of $m_{\mathrm{total}} = (3.9 \pm 0.2)\mu_B/\mathrm{Mn}$ at zero magnetic field, categorizing $MnBi_6Te_{10}$ as a particularly interesting material for the realization of a high-temperature QAH effect [42, 155, 343]. The moment at 0.15 T is $m_{\mathrm{total}} = (4.2 \pm 0.2)\mu_B/\mathrm{Mn}$.

It is furthermore interesting to compare our results to analogously synthesized samples of the MBT_n family (Fig. 7.5 (c)). We observe a noteworthy trend as the number of quintuple Bi_2Te_3 layers n increases: $MnBi_2Te_4$ ($n = 0$) has a clear A-type AFM structure, whereas $MnBi_4Te_7$ ($n = 1$) exhibits a more complex behavior, in which robust low-temperature metamagnetic properties are established, which were shown to result from the competition between the uniaxial anisotropy K and the still sizable interlayer AFM interaction J [152]. Finally, in $MnBi_6Te_{10}$ ($n = 2$), as well as in $MnBi_8Te_{13}$ ($n = 3$), the FM properties clearly dominate, with FM order at the significant temperatures of $T_c = 12\,\mathrm{K}$ and 10 K, respectively. Consistent with this observation, the spin-flop transition found for

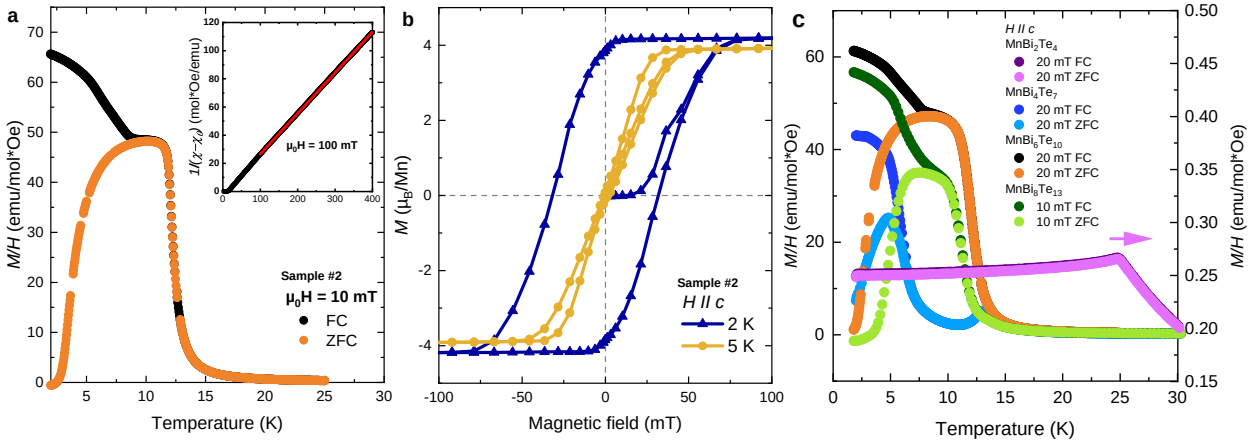

Figure 7.5: (a) Temperature-dependent normalized magnetization M/H of sample #2 with ZFC (orange symbols) and (FC (black symbols) protocols in an out-of-plane applied magnetic field of 10 mT. The inset shows the inverse magnetic susceptibility in a magnetic field of 100 mT together with a modified Curie-Weiss fit $\chi(T) = \chi_0 + C/(T - \Theta_{CW})$ of the data above 100 K (red solid line); for details see the Methods section. (b) Field-dependent magnetization of sample #2 measured in an out-of-plane applied magnetic field at $T = 2$ K and 5 K. No demagnetization correction was applied, and the magnetization was normalized to the Mn content obtained by EDX. (c) Temperature dependence of the normalized magnetization of analogously synthesized samples of the MBT_n family for ($n = 0, 1, 2, 3$).

$MnBi_2Te_4$ and $MnBi_4Te_7$ at fields of 3.5 T [31, 33, 148] and 0.1–0.3 T [149, 153, 162, 343], respectively, is absent in $MnBi_6Te_{10}$, and a magnetic moment of more than $4\mu_B$ is observed already above 80 mT in the latter after a ZFC procedure.

In order to confirm the reproducibility of the magnetometry data, field- and temperature-dependent measurements on several samples of $MnBi_6Te_{10}$ taken from the same batch were performed, see Fig. 7.6. Prior to that, all crystals were characterized by EDX as sub-stoichiometric $MnBi_6Te_{10}$, see Fig. 7.3. All four crystals exhibit very similar magnetic properties, showing a loop opening consistent with a FM state with coercive fields at $T = 2$ K in the $\sim$ 32–42 mT range and a finite remanence at zero magnetic field. The bottom panel of Fig. 7.6 shows the field- and zero-field-cooled normalized magnetization M/H for a temperature range of 1.8 K to 30 K in an out-of-plane external magnetic field of 10 mT. A phase transition with a strong increase of the absolute value M/H is observed at around $T_C = (12.0 \pm 0.1)$ K, determined by the inflection point, as well as a notable FC/ZFC splitting around 10 K. These observations are in contrast with an antiferromagnetic transition at $T_N \sim 11$ K of $MnBi_6Te_{10}$ reported by other authors [153, 155, 161, 162], which point towards possible differences in the Mn concentration and the Mn distribution between samples, such as the concentration of Mn/Bi intermixing due to the different growth conditions, as discussed in Subsection 7.2.1.

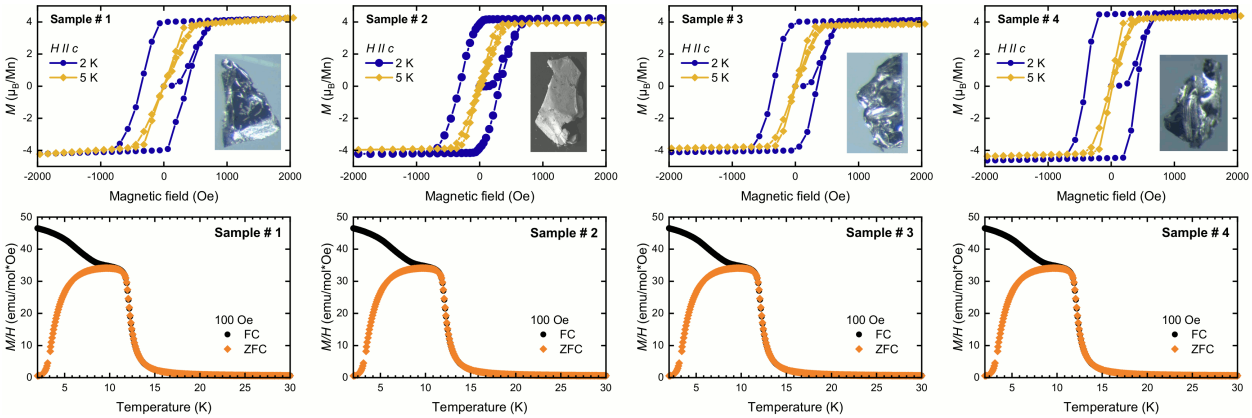

Figure 7.6: (Upper panel) Field-dependent magnetization curves taken on several crystals of $MnBi_6Te_{10}$ shown in the insets at 2 K and 5 K in an out-of-plane external magnetic field. No demagnetization correction has been applied. The absolute values of magnetization depend on the sample mass, which was about 10 times smaller for samples #1 and #4, thereby increasing the error, as well as on the real composition of each crystal. The Mn content in this series was evaluated by EDX yielding: 4.1(4) at. % Mn in Sample #1, 4.6(2) at. % Mn in Sample #2, 4.5(3) at. % Mn in Sample #3, and 4.4(6) at. % in Sample #4. (Bottom panel) Temperature-dependent normalized magnetization, measured with the zero-field cooled (ZFC) and field-cooled (FC) protocols (orange and black symbols respectively). The measurements were taken in an out-of-plane external magnetic field of 10 mT.

Bulk DFT (GGA+U) calculations

To better understand the magnetic properties of $MnBi_6Te_{10}$, fully relativistic DFT calculations based on the Generalized Gradient Approximation (GGA) $+U$ [342] neglecting intermixing were first performed by Dr. Jorge I. Facio. For the interaction parameters, the Slater integrals in Table 7.1 were used for the initial state. The results of total energy calculations for the A-type AFM configuration favor the out-of-plane over the in-plane magnetization by $\sim$ 0.4 meV per Mn. Additional calculations indicate that the A-type AFM configuration has a lower energy than the FM configuration. However, the small magnitude of the difference, $\sim$ 0.04 meV per Mn, naturally suggests that other mechanisms such as Bi/Mn intermixing might well be relevant for the magnetic ground state.

In particular, the effects of Mn/Bi intermixing defects on the magnetic structure were explored. Taking into account the Bi/Mn intermixing for $MnBi_6Te_{10}$, with its unit cell parameter $c > 100$ Å, requires a prohibitively long computational time. Instead, we focus on $MnBi_2Te_4$: In doing so, the reasonable assumption is made that if for $MnBi_2Te_4$ – the compound with the strongest out-of-plane AFM coupling – intermixing can tip the AFM/FM interplay towards ferromagnetism, it is a likely scenario that intermixing can also be responsible for the FM behavior in $MnBi_6Te_{10}$. Therefore, scalar relativistic calculations for various structural and magnetic models for $MnBi_2Te_4$ shown in Fig. 7.7 were performed considering a 2×2 supercell along the in-plane lattice vectors. In addition to the defect-free case (S_0), a single Mn vacancy (S_1), two Bi/Mn antisite defects (S_2 and S_3)

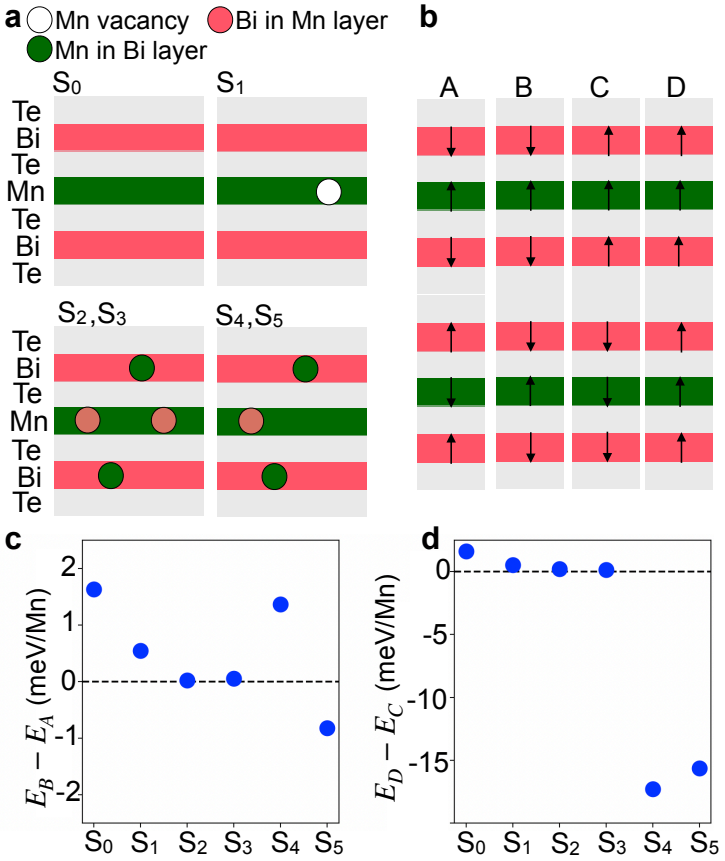

Figure 7.7: Intermixing models and their energies. (a,b) Schematic representation of the structural and magnetic models considered. In all magnetic models, ferromagnetic order is assumed within each atomic layer. (c) Difference between the total energies obtained from scalar relativistic calculations for the magnetic models B and A. (d) Same as (c) for the magnetic models D and C.

and one antisite defect plus an additional Mn in the outer layer (6*c* site of the SL block, S_4 and S_5) are considered. Models S_2 and S_3, as well as models S_4 and S_5, differ in the relative positions of the Bi atom in the central layer and the Mn atom in the Bi layer. For each structural model, four possible magnetic arrangements are considered. All models have in common that Mn moments order FM within any given atomic layer, but differ in the magnetic arrangement between the atomic layers within a SL, and between the atomic layers in the adjacent SLs (Fig. 7.7 (b)): In the model A(D), Mn are coupled AFM(FM) within each SL and also between the SLs. In the model B(C) the intralayer coupling is AFM (FM), while the interlayer coupling is FM(AFM).

Fig. 7.7 (c) shows the energy difference Δ_{BA} between the structural models that assume the intralayer AFM order and the interlayer FM (model B) or AFM (model A). It can be seen that in general Δ_{BA} is reduced (the tendency towards antiferromagnetism is weakened), when structural defects are considered. For example, a Mn-deficient model ($Mn_{0.75}Bi_{2.25}Te_4$) yields an energy difference between FM and A-type AFM three times smaller than in pristine $MnBi_2Te_4$. Furthermore, Δ_{BA} varies significantly between the

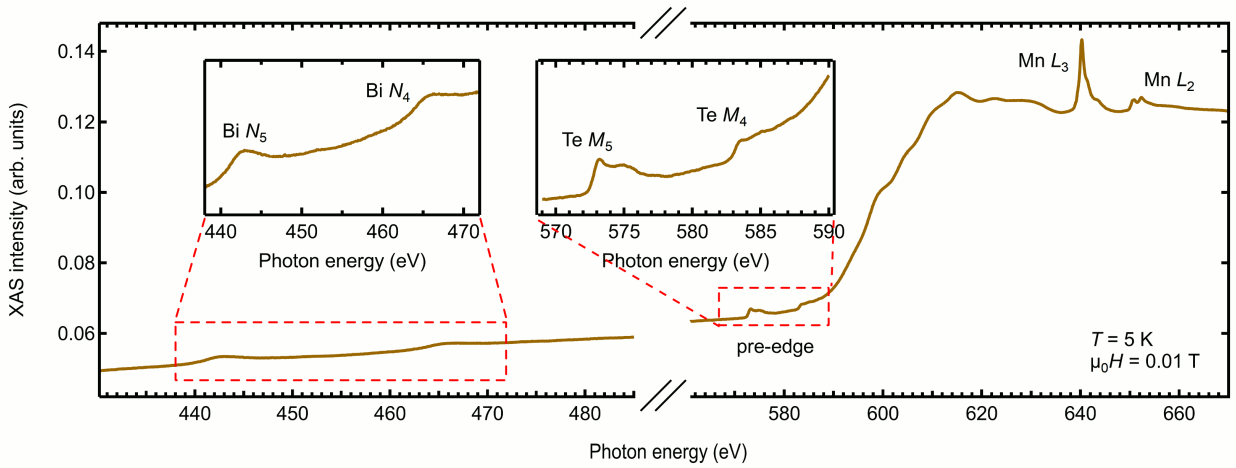

Figure 7.8: Overview wide-range XAS scan showing the Bi $N_{4,5}$, Te $M_{4,5}$ and Mn $L_{2,3}$ absorption edges of $MnBi_6Te_{10}$ measured with σ polarization of light at $T \sim 5$ K.

structural models, and in particular a FM order between the SLs is preferred for a configuration with additional Mn in the 6*c* site of the SL block. A similar conclusion can be reached for the models that assume the FM ordering between the atomic layers of a SL (models C and D, Fig. 7.7 (d)). These calculations do support the idea of differences in the spatial distribution of Mn as responsible for the overall FM or AFM order between SLs, which could thus explain the differences in the magnetic behavior of our $MnBi_6Te_{10}$ samples compared to other works in literature [153–155, 161, 162].

7.2.3 X-ray spectroscopy

We begin with the XAS characterization of our sample. Fig. 7.8 shows an overview spectrum measured with horizontal linear polarization σ at $T = 5$ K. It encompasses the relevant resonant absorption edges of all three elements comprising the sample, namely Bi $N_{4,5}$ ($4d \rightarrow 4f$), Te $M_{4,5}$ ($3d \rightarrow 5p$) and Mn $L_{2,3}$ ($2p \rightarrow 3d$).

For Te, there are distinct pre-edge features between about 570 and 585 eV, followed by a more intense main edge upturn between about 600 and 640 eV. This lineshape is very similar to that reported for V- and Cr-doped $(Bi,Sb)_2Te_3$ topological insulators (TIs) [78, 79, 101], as well as for $IrTe_2$, $AuTe_2$ and FeTe [344]. We adopt the interpretation put forward for $IrTe_2$ in Ref. [344], where the final state for pre-edge features was assigned to the Te $5p$ manifold, whereas the final state of the intense main edge features was ascribed to the *s-d-f* hybrid band of $6s$, $5d$, and $4f$ character.

Clearly, the Mn $L_{2,3}$ edges overlap with the intense Te edge, which is the main reason for the strongly sloped background of the measured Mn spectra, which are discussed below. This overlap distorts the Mn spectra of our $MnBi_6Te_{10}$ sample more severely as compared to measurements of $MnBi_2Te_4$, due to the proportionally larger Te content.

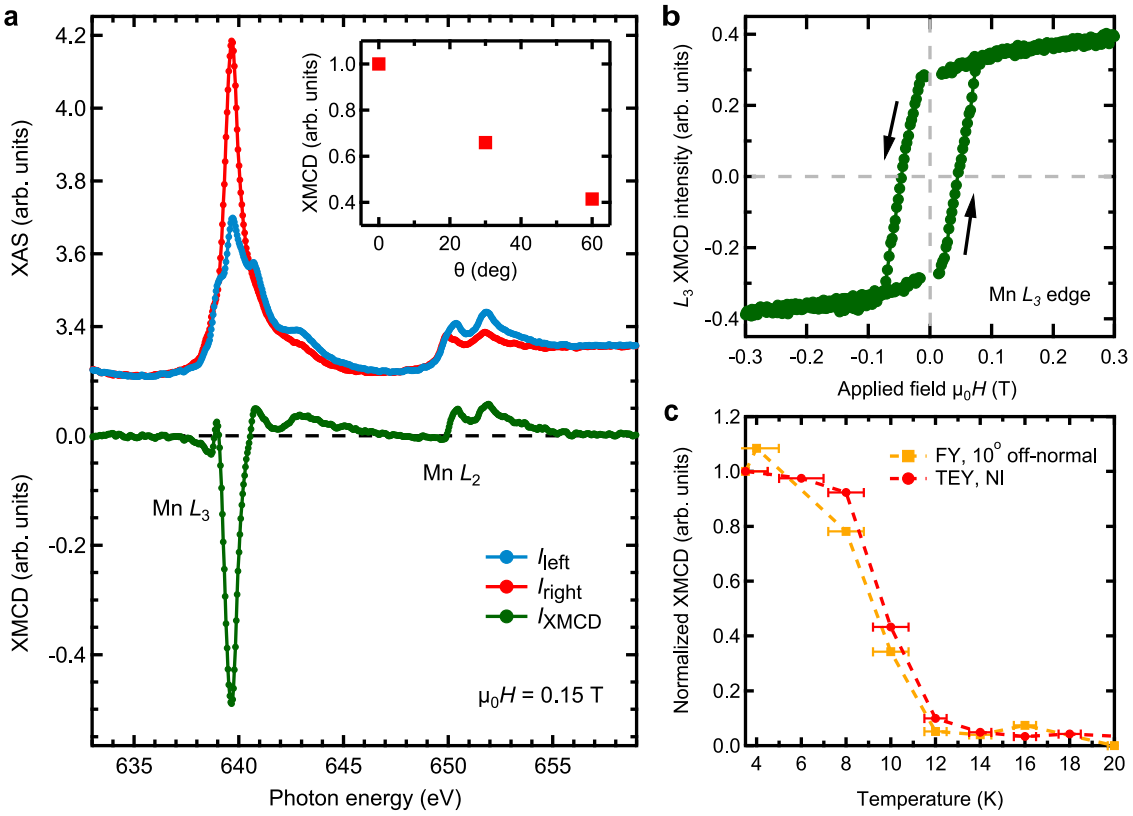

Figure 7.9: (a) Mn $L_{2,3}$ edge XAS data for sample #4 obtained with left (I_{left}, blue) and right (I_{right}, red) circularly polarized light in normal incidence at $T \approx 3.5$ K in a magnetic field of 0.15 T. The corresponding XMCD signal $I_{\text{XMCD}} = I_{\text{left}} - I_{\text{right}}$ is plotted below in green. The inset shows the angular dependence of the normalized remanent XMCD signal. (b) Magnetization curve of sample #4 ($I_{\text{right}} - I_{\text{left}}$) at $T \approx 3.5$ K, obtained as the Mn L_3 edge XMCD signal normalized by the XAS signal. (c) Temperature dependence of the remanent XMCD signal for sample #2 at the Mn L_3 edge measured at normal incidence in TEY mode (red) and 10° off normal incidence in FY mode (orange).

Next we focus on the Mn $L_{2,3}$ edge. To study the surface magnetic properties, we have performed XAS measurements in the TEY mode, which is element specific and has a probing depth on the nanometer scale. Due to the shallow escape depth, the topmost SL contributes the most to the signal. However, even for SL termination, the FM Mn sheet is buried about 0.55 nm below the surface, and significantly more for QL termination. Therefore, probing depth effects have to be considered, when interpreting the ordered magnetic moments obtained with XMCD. Fig. 7.9 (a) compares XAS spectra measured with x-rays of opposite circular polarization at $T \approx 3.5$ K and a magnetic field of $\mu_0 H = 0.15$ T along the surface normal; the bottom green line showcases the substantial XMCD signal. In the inset we show that the peak remanent XMCD signal scales inversely with θ, where θ is the angle between the magnetization direction and the x-ray beam. This decline of XMCD is a strong indication of an out-of-plane easy axis for the Mn moments. In general, the XAS and XMCD spectral line shapes closely resemble those of $MnBi_2Te_4$ [31] and $MnBi_4Te_7$ [149], Mn-doped Bi_2Te_3 [341], Bi_2Se_3 [340] and Sb_2Te_3 TIs [30], as well

as those measured in dilute magnetic semiconductors (DMS) such as (Ga,Mn)As [233, 338, 345, 346] and (Ga,Mn)P [347], which hints that the oxidation states and crystal fields are close in all these systems.

An important advantage of XMCD over bulk magnetometry is the possibility to measure element-specific magnetic hysteresis curves. It allows one to evaluate the contribution of each atomic species to the magnetic properties of the material [206]. In Fig. 7.9 (b) we show the magnetization obtained by measuring the peak L_3 XMCD signal at $T \approx 3.5\,\mathrm{K}$ within a field range of $\pm 0.3\,\mathrm{T}$. It exhibits a substantial remanence at $\mu_0 H = 0\,\mathrm{T}$, in sharp contrast to $MnBi_2Te_4$, which exhibits no remanent magnetization, and $MnBi_4Te_7$, which has a smaller remanence-to-saturation ratio [149]. Furthermore, we observe a coercive field of $\mu_0 H_c = 45\,\mathrm{mT}$. We caution against overinterpreting the similarity of this H_c with the bulk one: First, the data were measured at somewhat different temperatures, which has an effect on H_c (Fig. 7.5). Second, different ramping speeds were used, which, too, has an effect on H_c for magnetic TIs [348]. In addition, the hysteresis behavior of surface and bulk might be intrinsically different.

The hallmark of IMTIs is the interplay between the topological surface states (TSS) and the magnetization properties. One exciting possibility is that TSS may help to enhance the ordering temperature at the surface [90], which also was recently predicted for $MnBi_2Te_4$ [349]. Since such enhancement can expose the coupling between the surface Dirac fermions and the surface magnetization, it is of strong interest to analyze whether our experiments reveal a different surface critical temperature. In Fig. 7.9 (c) we compare the T-dependent remanent peak L_3 XMCD signal measured with surface sensitive TEY with the one measured with bulk sensitive total FY. Within the precision allowed by the T increments of 2 K, the transition temperatures at surface and bulk are consistent. We remark that the transition behavior as observed with SQUID and XMCD could differ somewhat due to the different measurement protocols: For XMCD, each point in Fig. 7.9 (c) was obtained after driving to $\mu_0 H = 3\,\mathrm{T}$ and back to remanence. In contrast, in SQUID measurements a conventional FC protocol at 10 mT was used.

To complement our XMCD data we have measured x-ray magnetic linear dichroism (XMLD) at the Mn $L_{2,3}$ edges and its temperature dependence, as shown in Fig. 7.10. While XMCD is proportional to the average magnetic moment $\langle \mathbf{M} \rangle$ along the light propagation direction, XMLD is proportional to the square of magnetic moment $\langle \mathbf{M}^2 \rangle$, therefore it allows to study spin orientations in ordered antiferromagnets with no net total magnetic moment. XMLD experiments detect the difference between the absorption of linearly polarized x-rays, parallel and perpendicular to the local magnetization axis in ferro- and antiferromagnetic materials. Fig. 7.10 (a) illustrates XAS spectra measured at $T \approx 3.5$ K in remanence with linearly polarized x-rays and corresponding grazing ($\theta = 60°$) and normal incidence ($\theta = 0°$) XMLD spectra. The vanishing XMLD signal at normal incidence (NI) indicates that the system is isotropic in plane. At the same time,

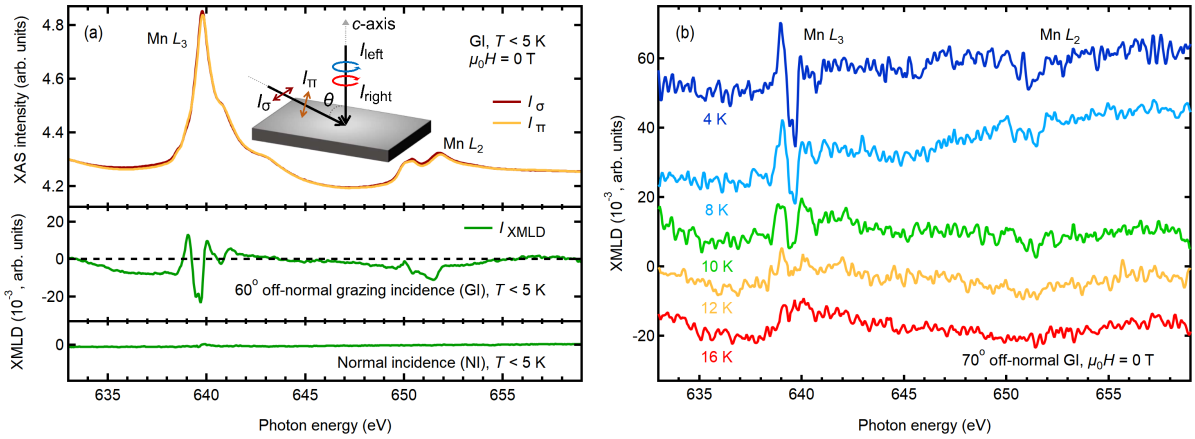

Figure 7.10: (a) Upper panel: Mn $L_{2,3}$ edge data obtained with σ (I_σ, red line) and π (I_π, orange line) linear x-ray polarization at $T \approx 3.5$ K and without external magnetic field applied. Measurements were performed at $\theta = 60°$ grazing incidence (GI), as depicted in the inset. Lower panel: Corresponding linear dichroism ($I_{XMLD} = I_\pi - I_\sigma$) measured at GI and normal incidence (NI). (b) Mn $L_{2,3}$ linear dichroism measured at different temperatures between $T \approx 4$ K and 16 K at $\theta = 70°$ GI.

non-vanishing XMLD in grazing incidence (GI) reveals strong out-of-plane anisotropy, which can be attributed to the presence of out-of-plane Mn 3*d* magnetic moments. As previously discussed, the strong overlap of spectral features related to Te with the Mn $L_{2,3}$ edges complicates the background corrections of XAS spectra. However, even with this complication, it is still clearly noticeable that the line shape of XAS and especially of XMLD is similar to those previously reported for $MnBi_2Te_4$ [33] and $MnBi_4Te_7$ [149], although the strength of the signal is considerably weaker. The temperature dependence of the grazing incidence XMLD signal is shown in Fig. 7.10 (b). The signal gradually vanishes between $T = 10$ K and $T = 12$ K, i.e., at the same critical temperature estimated from temperature-dependent XMCD. This points towards a magnetic rather than a crystal-field related origin of the linear dichroism signal, as will be also further discussed in the upcoming section with theoretical results.

Fig. 7.11 shows XAS and XMCD spectra measured on a representative sample of similar stoichiometry around the Te $M_{4,5}$ and Bi $N_{4,5}$ absorption edges at $T = 5$ K in an applied magnetic field of 6 T. Measurements at the Bi $N_{4,5}$ edges exhibit no XMCD, as can be seen in Fig. 7.11 (b). More interestingly, there is no XMCD at the Te $M_{4,5}$ edges either, see Fig. 7.11 (a), which is in contrast to results in the closely related V- and Cr-doped $(Bi,Sb)_2Te_3$ [78–80, 350], and which might indicate differences in the magnetic interactions of both compounds.

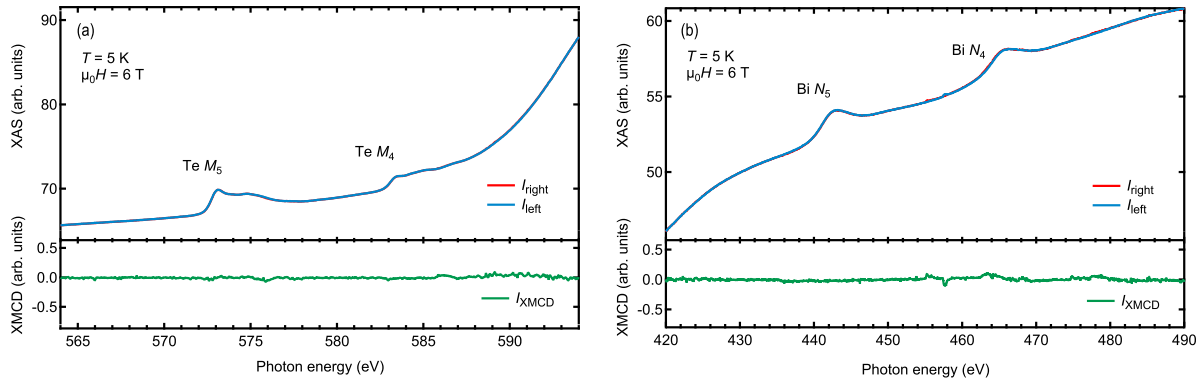

Figure 7.11: (a) Te $M_{4,5}$ edge XAS (TEY) spectra measured for left- (I_{left}, blue curve) and right- (I_{right}, red curve) circularly polarized x-rays (upper panel), together with the corresponding XMCD spectrum ($I_{\text{XMCD}} = I_{\text{left}} - I_{\text{right}}$, bottom panel). (b) Bi $N_{4,5}$ edge XAS (TEY) spectra measured for left- (blue curve) and right- (red curve) circularly polarized x-rays (upper panel), together with the corresponding XMCD spectrum (bottom panel). All measurements were performed at $T \approx 5$ K and $B = 6$ T.

7.2.4 *Ab initio* MLFT

In order to interpret our XAS and XMCD results, as well as to understand the origin of the XMLD signal, and in order to evaluate several physical parameters that control the electronic and magnetic properties of $MnBi_6Te_{10}$, we have performed *ab initio* MLFT calculations, which take into account both multiplet and band-structure effects [245], see Subsection 7.1.4. This approach allows to notably reduce the input parameters, such as direct F and exchange G Slater integrals, often estimated by scaling atomic Hartree–Fock values, crystal-field and covalent hopping parameters, by obtaining them *ab initio*. The theoretical aspects of the approach are comprehensively explained elsewhere [245, 254]. We start our *ab initio* MLFT calculations with conventional density function theory (DFT) calculations in local-density approximation (LDA) for the proper experimental crystal structure using the FPLO package [255]. Therefrom we compute a set of Wannier functions which we use to obtain the one body terms (such as CF and hybridization parameters) needed to set up the local MLFT cluster calculation. Many-body effects beyond LDA are subsequently treated on the MLFT level using the Quanty code [245, 351, 352]. The local cluster model considered consists of central Mn $3d$ Wannier orbitals surrounded by 6 Te ligand $5p$ Wannier orbitals in octahedral coordination, as shown in Fig. 7.1 (c). In contrast to conventional DFT, which describes only the ground state, our approach allows for various core level spectroscopy calculations including XAS/XMCD/XMLD, $2p$ core-level x-ray photoemission (XPS), and even resonant inelastic x-ray scattering (RIXS) [79, 244, 245, 353–355].

The calculated XAS and XMCD spectra for $MnBi_6Te_{10}$ displayed in Fig. 7.12 (a) show a very good agreement with the experimental data, reproducing all the multiplet features and their relative energy positions. This is most notable for the XMCD spectra.

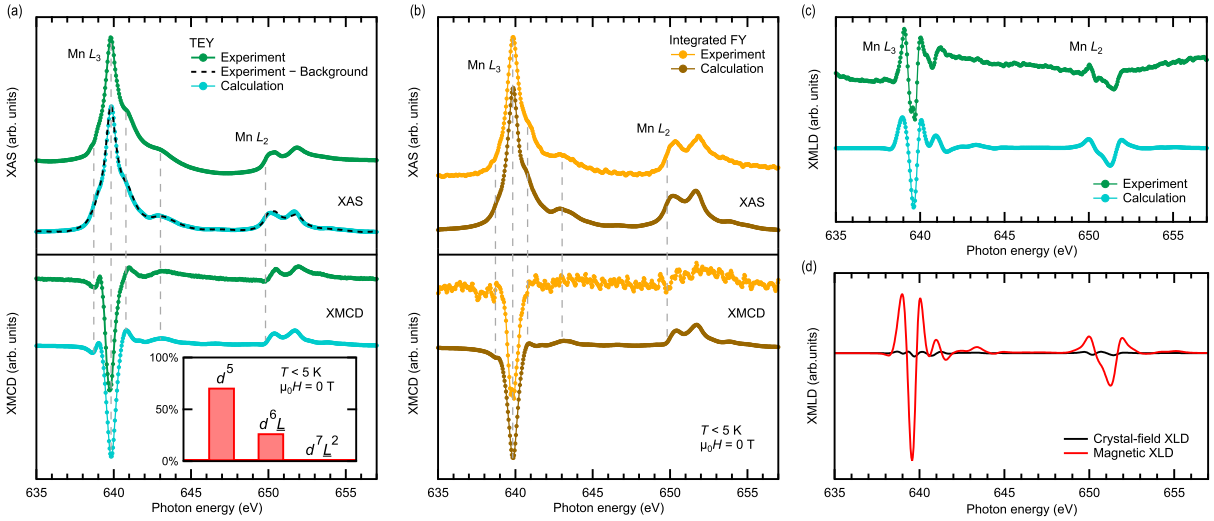

Figure 7.12: (a) Upper panel: Polarization-averaged, i.e. $(I_{\text{left}} + I_{\text{right}})/2$, experimental Mn $L_{2,3}$ XAS (TEY) spectrum (green, measured at $T \approx 3.5$ K in remanence) together with a calculated spectrum (blue), obtained using the *ab initio* MLFT cluster model described in the text. The black dashed line shows background-corrected XAS spectra for better comparison with the calculation. Bottom panel: Corresponding experimental and calculated XMCD spectra. The inset shows the contributions of different configurations to the ground state. The dashed vertical lines are guides to the eye, highlighting the position of particular features of the spectra. (b) Polarization-averaged experimental FY XAS and XMCD spectra (orange, measured at $T \approx 3.5$ K in remanence) of Mn $L_{2,3}$ edge together with calculated angle-integrated $3d \rightarrow 2p$ decay FY spectra (brown). (c) Experimental linear dichroism spectrum (green, measured at $T \approx 3.5$ K and at remanence) and a corresponding calculated spectrum, including both low symmetry crystal-field and magnetic contributions. (d) Separate contributions to the linear dichroism signal from low symmetry crystal-field (black curve) effects and magnetic interactions (red curve).

It is reasonable to expect no significant differences in the XAS and XMCD line shapes among the different members of the $(MnBi_2Te_4)(Bi_2Te_3)_n$ family, since locally, Mn is in the same $MnTe_6$ arrangement within the septuple layers. Whereas the nominal Mn^{2+} d^5 configuration ($^6S_{5/2}$) dominates with 71%, there is significant charge transfer from the Te ligands, resulting in a 27% contribution of $d^6\underline{L}$ and 2% contribution of $d^7\underline{L}^2$ to the ground state. This hints towards a considerable hybridization between Mn d and ligand p orbitals. The resulting $3d$ electron filling is $n_d = 5.31$, corresponding to an effective 1.69+ valence. We obtain $m_{\text{eff}} = \sqrt{\langle \mu^2 \rangle} = 5.67\mu_B$ for the local effective moment, as well as $m_{\text{spin}} = g_s\langle S_z \rangle = 4.68\mu_B$ and $m_{\text{orb}} = g_l\langle L_z \rangle = 0.008\mu_B$ for the maximal z-projections of the spin and orbital moments, respectively.

Finally, we observe that the electron filling and the magnetic moments resulting from our MLFT analysis are in excellent agreement with those calculated based on the DFT-GGA+U calculations (see above): We obtain $n_d = 5.3$ and $m^{\text{spin}} = 4.7\mu_B$ using the same interaction parameters as in MLFT. These results are also in good agreement with the bulk magnetometry data (see Subsection 7.2.2), as well as with published neutron diffraction data [159, 161, 356].

Having determined the ground state of the system, one can calculate different types of spectra, such as FY XAS. As was discussed in Chapter 3, FY XAS spectral line shape is subject to self-absorption and saturation effects in non-diluted samples, frequently resulting in strongly distorted spectral intensities. Moreover, FY XAS spectra are not proportional to the x-ray absorption cross section due to the intrinsic processes of the FY decay [213, 214]. To check if it is critical in our case, we have calculated the excitation of a Mn $2p$ electron into the $3d$ shell followed by a decay into the $2p$ shell, which is the dominant radiative channel [357]. Fig. 7.12 (b) shows the calculated angle-integrated FY XAS and XMCD spectra (brown curves) for Mn compared with the experiment (orange curves). The calculated XAS and XMCD spectra well reproduce the experiment, which again validates the determined ground state of Mn. Comparing the spectra in Fig. 7.12 (b), one can see that self-absorption and saturation effects are not detrimental. However the FY XAS spectra have an increased intensity of the L_2 absorption edge, meaning that the branching ratio in FY XAS is considerably different than that of TEY XAS, which is also nicely reproduced in our MLFT calculation. A further important observation is that the surface-sensitive TEY data in Fig. 7.12 (a), compared to FY spectra, does not show additional features indicative of higher oxidation states. Such features would be expected at a few eV above the main resonance, and their absence testifies to the pristine surface quality of our sample—a finding corroborated by our detailed MLFT fit. Thus, we can conclude that the Mn atoms close to the surface and in the bulk have similar local electronic properties.

Fig. 7.12 (c) shows a comparison between the experimental and calculated XMLD spectra, demonstrating a good agreement, especially for the Mn L_2 edge. There are two main sources that could cause linear dichroism, namely the magnetic interaction and crystal-field effects [358]. One may apprehend that distortion from the O_h high symmetry CF is negligible for $MnBi_6Te_{10}$, therefore such a crystal field does not split the orbitally highly symmetric high spin $3d^5$ ground state. However, even for a perfect octahedron, oriented as shown in Fig. 7.1 (d), non-vanishing CF linear dichroism might be observed, since x/y- and z-direction are no longer equivalent. In order to determine the actual source of the observed dichroism, we have calculated two sets of XMLD spectra. For the first, we assume finite CF splitting, but no magnetization. For the second, we set the crystal field to zero, but assume a collective magnetization, which is accounted for by a Weiss field, whose strength is set according to the experimentally observed ordering temperature of about 12 K. The two calculated XMLD spectra are shown in Fig. 7.12 (d). Indeed, we see that the CF effects are negligible and the observed dichroism is primarily caused by magnetic effects, which is in agreement with the vanishing of the linear dichroism above 10-12 K shown in Fig. 7.10 (b).

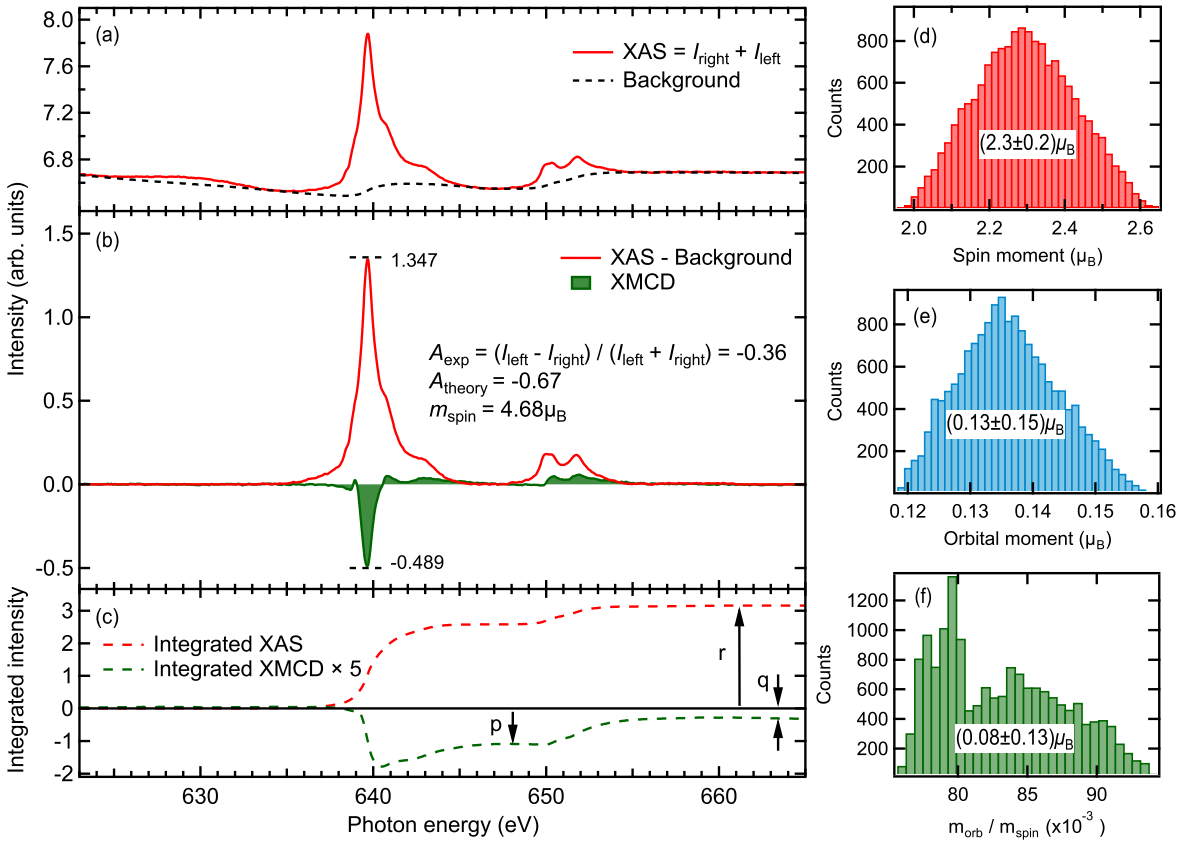

Figure 7.13: The sum rule analysis for $MnBi_6Te_{10}$ bulk crystal (sample #4). (a) Sum of the left- and right-circularly polarized XAS spectra of the Mn $L_{2,3}$ edges (red curve) and background (black curve). (b) XAS spectrum ($I_{left} + I_{right}$, red curve) after background correction together with XMCD ($I_{left} - I_{right}$, green filled curve). (c) Integrated intensities of XAS (red dashed curve) and XMCD (green dashed curve), where the latter is multiplied by 5 for clarity. The integrals p, q and r for the sum rules in Eq. 3.27 are indicated with arrows. (d-f) Distribution of m_{spin}, m_{orb} and m_{orb}/m_{spin}, respectively, obtained my applying sum rule analysis 16384 times as described in the main text.

7.2.5 XMCD Sum Rule Analysis

The MLFT analysis yields the *local* magnetic moments based on the spectral *shape*. The sum rules, in turn, relate the integrated Mn $L_{2,3}$ XMCD and XAS *intensity* to the *long-range ordered* orbital and spin magnetic moments near the surface [219–221], as discussed in Chapter 3). Alternatively, the Mn 3*d* spin magnetic moment can be obtained by determining the peak asymmetry of the experimental XMCD curve, $A = (I_{left} - I_{right})/(I_{left} + I_{right})$, i.e., the maximum of the L_3 XMCD divided by the maximum of the XAS summed over both polarizations, after suitable background correction of the XAS and correlating this result with the calculated spectra of comparable line width. In the following Subsections we start with the sum rules results for the surface-sensitive TEY spectra measured on sample #1 and sample #4 (see Fig. 7.3), and then compare the obtained magnetic moment with asymmetry analysis and SQUID measurements probing the bulk of the sample.

For $L_{2,3}$ edges the sum rules are given by Eq. 3.27. For Mn ion we use a value of

$n_h = 4.7$, i.e., assuming a $3d$ electron count of 5.3, inferred from the MLFT calculations, as well as from the DFT results. The estimation of $\langle T_z \rangle = -0.0002\hbar$ done for Mn by means of MLFT shows that in the particular case of Mn with predominant d^5 configuration, its contribution to the m_{spin} is negligible. Further, the correction factor $C = 1.40$ is used to compensate the deviation in spin sum rule due to the jj mixing (see Chapter 3 Section 3.4). The derived value of C is close to 1.47, estimated for (Ga,Mn)As having similar Mn $L_{2,3}$ XAS and XMCD line shapes [233].

The most significant source of error in our estimation of the magnetic moments from sum rules is the subtraction of the background and edge steps, which is an issue for $MnBi_6Te_{10}$, where Mn $L_{2,3}$ edges strongly overlap with Te $M_{4,5}$ edges due to the proportionally larger Te content, as can be seen in Fig. 7.8. Fig. 7.13 (a) shows the Mn $L_{2,3}$ XAS $= I_{\text{left}} + I_{\text{right}}$ measured at $T \approx 3.5$ K in 0.15 T field, together with the background used to separate the resonant part of the spectrum.

Prior to the sum rule analysis we normalize the left- and right-circularly polarized spectra at energies far from the resonances. After that we subtract the background indicated in Fig. 7.13 (a) from the XAS in order to exclude the non-magnetic contribution to the XAS spectra. The background-corrected XAS together with the XMCD is shown in Fig. 7.13 (b). The spectral part far from the resonance (between 620–634 eV and 660–670 eV) is manually set to zero. Further, we apply the sum rules 16384 times by randomly varying all parameters entering the analysis (such as n_d, C, $\langle T_z \rangle$, integration energy ranges, normalization energy range) around their optimal values. Thus we get statistical distributions of m_{spin}, m_{orb} and $m_{\text{orb}}/m_{\text{spin}}$ for Mn as illustrated in Fig. 7.13 (d-f). This estimate of the error bars also includes various background correction approaches using a simple linear background under L_3 and L_2, low-frequency Fourier harmonics as described in section E of the methods, as well as a Shirley background.

Our sum rule analysis of the spectra measured on sample #4 at $T \approx 3.5$ K and $B = 0$ T reveals a non-zero $m_{\text{spin}} = (2.1 \pm 0.3)\mu_B$/Mn, small $m_{\text{orb}} = (0.06 \pm 0.14)\mu_B$/Mn and $m_{\text{orb}}/m_{\text{spin}} = (0.04 \pm 0.10)\mu_B$/Mn. For $B = 0.15$ T the analysis yields $m_{\text{spin}} = (2.3 \pm 0.2)\mu_B$/Mn, $m_{\text{orb}} = (0.13 \pm 0.15)\mu_B$/Mn and $m_{\text{orb}}/m_{\text{spin}} = (0.08 \pm 0.13)\mu_B$/Mn, confirming an expected large spin- and small orbital-magnetic moment for the predominant d^5 configuration. The same analysis for sample #1 yields $m_{\text{spin}} = (2.0 \pm 0.35)\mu_B$/Mn and $m_{\text{orb}} = (0.20 \pm 0.07)\mu_B$/Mn, with the total moment $m_{\text{total}} = (2.2 \pm 0.4)\mu_B$/Mn compatible with sample #4 $m_{\text{spin}} = (2.4 \pm 0.30)\mu_B$/Mn within the error (see Table 7.3). The derived m_{spin} and m_{orb} have the same sign, corresponding to a parallel alignment of the spin and orbital moment in this ion, which agrees with the Hund's rule for a more than half filled d shell. The ratio of the orbital to spin magnetic moments we obtained is close to the value calculated for Mn-doped Bi_2Te_3 single crystals [341], as well as for (Ga,Mn)As thin films [233]. It is worth mentioning that the strong overlap of Mn $L_{2,3}$ and Te $M_{4,5}$ edges and an ambiguity in subtracting a Te contribution could lead to a significant error in the

derivation of spin and especially orbital magnetic moments of Mn.

7.2.6 XMCD peak asymmetry analysis

Since XMCD intensity scales with the magnetization M, whereas the isotropic XAS intensity remains constant, an alternative method to obtain the spin magnetic moment of the Mn is to determine the asymmetry of the experimental XMCD $A_{\text{exp}} = (I_{\text{left}} - I_{\text{right}})/(I_{\text{left}} + I_{\text{right}})$ after suitable background correction of the XAS and compare this result with the theoretical value A_{theory} obtained for MLFT calculated spectra of comparable line width . This circumvents complications and ambiguities in the sum rule analysis, especially when there is a large jj mixing, as in the case of Mn. However, if there is an unaccounted fraction of non-magnetic or antiferromagnetic Mn, the magnetic moment will be accordingly reduced.

Fig. 7.14 (c) shows that at the L_3 maximum the calculated Mn has an asymmetry $A_{\text{theory}} = -0.67$, which can be related to a ground-state spin moment of $4.68\mu_{\text{B}}$/Mn. For the experimental spectra measured on sample #4 in remanence (0 T) we obtain an asymmetry at the Mn L_3 peak maximum equal to $A_{\text{exp}} = -0.27$, while for spectra measured in 0.15 T $A_{\text{exp}} = -0.36$, see Fig. 7.13 (b). Comparing these values to the theoretical value, we obtain the ordered moment, i.e., the projection of the Mn spin magnetic moment on the magnetization direction (along the c-axis), $m_{\text{spin}} = \frac{-0.27}{-0.67} * 4.68\mu_{\text{B}} \approx 1.9\mu_{\text{B}}$/Mn in remanence and $m_{\text{spin}} \approx 2.54\mu_{\text{B}}$/Mn in external magnetic field of 0.15 T, which is about 10% larger than the sum rule result. The $\sim$ 25% decrease of the moment when going from 0.15 T to the remanence nicely agrees with the hysteresis behavior shown in Fig. 7.9 (b).

The above described simple asymmetry approach is based solely on two data points, which makes it prone to considerable errors in the estimated magnetic moment. The discussed background problem for Mn $L_{2,3}$ edges overlapping with Te $M_{4,5}$, further exacerbates the errors. Since XMCD intensity scales as a whole with magnetization M, here we suggest a more thorough method for estimating the spin magnetic moment. As in Chapter 3 Section 3.5, where we approximated the experimental spectrum $S(\omega)$ by a linear combination of resonant $R(\omega)$ and background $Bg(\omega)$ components, here one can try representing the experimental spectrum $S(\omega, T, B)$ measured in some arbitrary magnetic field and temperature by a linear combination of "basis" XAS $T(\omega)$ and XMCD $D(\omega)$ components:

$$S(\omega, T, B) \rightarrow \beta[T(\omega) + \alpha D(\omega)], \tag{7.1}$$

where β accounts for an overall unknown scaling of the experimental spectra, which we are not interested in, while the scaling factor α is proportional to the magnetic moment $\mu = k\alpha$ that we want to extract. Similar to the asymmetry approach, using in Eq. 7.1 a spectrum $S_0(\omega, T, B)$ with a known magnetic moment μ_0, one can fix the proportionality

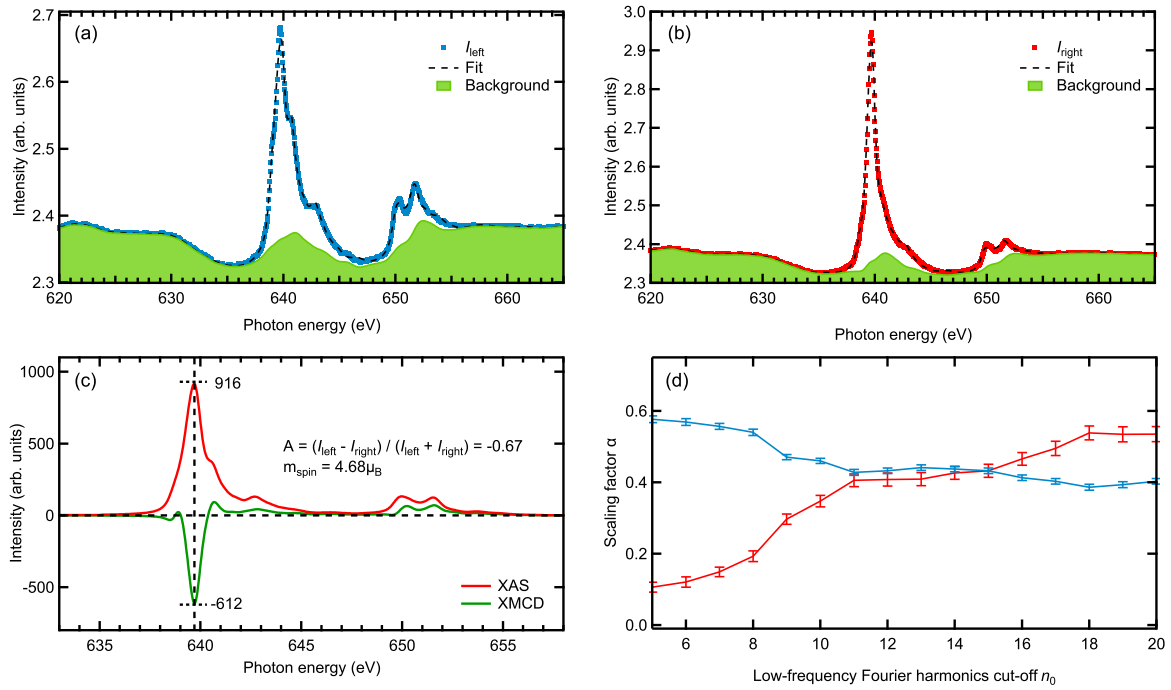

Figure 7.14: The asymmetry analysis of $MnBi_6Te_{10}$ (sample #4) XAS/XMCD spectra measured at $T \approx 3.5$ K in remnant field of 0 T. (a-b) Fitting results for left- (blue curve) and right-circularly polarized XAS spectra (red curve) of Mn $L_{2,3}$ edges using Eq. 7.1. The dashed lines indicate the fit result, while filled green curves show backgrounds obtained from low-frequency Fourier components. (c) Peak asymmetry A_{theory} for calculated XAS and XMCD spectra with 100% circularly polarized x-rays at the Mn L_3 absorption edge. The values of $(I_{\text{left}} - I_{\text{right}})$ and $(I_{\text{left}} + I_{\text{right}})$ are indicated by dashed horizontal lines. (d) The scaling factor α obtained from fitting the experimental spectra in panels (a-b) as function of low-frequency Fourier harmonics cut-off n_0 used in the model.

coefficient k to $k = \mu_0/\alpha_0$, so the magnetic moment for the unknown spectrum becomes $\mu = k\alpha = \mu_0\alpha/\alpha_0$.

The strong background in the experimental spectrum $S(\omega, T, B)$ does not allow for a perfect approximation and may falsify the value of α. However, if we expand Eq. 7.1 in a Fourier series, then owning to the smoothness of the background, it has much weaker negative impact on the high-frequency components, as compared to low-frequency components. Therefore, in order to improve the accuracy of the extracted α we rely only on high-frequency components. It is convenient to use theoretically calculated $T(\omega)$, $D(\omega)$ and μ_0, as shown in Fig. 7.14 (c). The results of such fitting for I_{left} and I_{right} spectra of sample #4 measured at $T \approx 3.5$ K in 0 T field can be seen in Fig. 7.14 (a,b). Fig. 7.14 (d) shows the scaling factor α obtained for left- (blue curve) and right-circularly polarized XAS spectra (red curve) as a function of the low-frequency cut-off n_0, i.e., in Eq. 7.1 we consider all Fourier harmonics n with $n \geqslant n_0$. The optimal fit for remanent data yields $\alpha = 0.43 \pm 0.02$ corresponding to $m_{\text{spin}} = (2.01 \pm 0.09)\mu_B$/Mn, while for 0.15 T data $\alpha = 0.54 \pm 0.05$ corresponding to $m_{\text{spin}} = (2.53 \pm 0.24)\mu_B$/Mn, which is consistent with

Table 7.3: Comparison of the magnetic moments obtained from analysis of XAS and XMCD data measured at $T \approx 3.5$ K and $B = 0.15$ T on $MnBi_6Te_{10}$ sample #1 and sample #4 with SQUID magnetometry results at $T = 2$ K (in units of μ_B/Mn).

Method	Sample #	m_{spin}	m_{orb}	m_{orb}/m_{spin}	m_{total}
Sum rules	1	1.99±0.35	0.20±0.07	0.14±0.08	2.19±0.4
	4	2.29±0.22	0.13±0.15	0.08±0.13	2.42±0.3
Asymmetry	1	2.18±0.30	–	–	–
	4	2.54±0.25	–	–	–
Asymmetry fit	1	2.15±0.33	–	–	–
	4	2.53±0.24	–	–	–
SQUID magnetometry	1	–	–	–	4.14±0.3
	4	–	–	–	4.52±0.3

the simple asymmetry approach results.

Table 7.3 summarizes the results of three different approaches for estimating the ordered moment of Mn in $MnBi_6Te_{10}$ compared to SQUID magnetometry results for sample #1 and sample #4. As one can clearly see all three approaches yield a similar ordered spin moment of $m_{spin} \approx 2.1\mu_B$/Mn for sample #1 and $m_{spin} \approx 2.45\mu_B$/Mn for sample #4. The total moment m_{total} estimated with sum rule analysis is reduced by about 40% in comparison to the one obtained with bulk sensitive SQUID magnetometry. Increasing the field to 6 T brings m_{total} of sample #4 to 3.9 μ_B, i. e. closer to SQUID magnetometry results and to the theoretical maximal moment (see Subsection 7.2.4).

The discrepancy can be understood by considering the differing regions probed by these techniques. SQUID averages over the full extent of the material, while TEY XMCD is a surface-sensitive probe. It is important to keep in mind that the indicated errors of the XMCD results only take into account statistical fitting and background estimate effects. However, the shallow probing depth of TEY can further bias the outcome: It is reasonable to expect that the QLs and the outer (6*c*) positions of the SLs contain a few percent of paramagnetic and possibly even AFM (with respect to the 3*a* positions) Mn, see section on growth and Fig. 7.4. Already for SL surface termination, the FM ordered Mn sheet (3*a* positions) is buried about 0.55 nm below the surface. At the same time, there is Mn in 6*c* positions closer to the surface, both in the very same SL and in QLs, which can terminate the surface in different parts of the sample. Therefore, already for a mean probing depth (MPD) of about 1 nm, the contribution of the FM Mn would be notably suppressed. MPD values between 1 and 2.5 nm have been reported for this photon energy range [210, 359]. Given the presence of the heavy elements Te and Bi, which might even further attenuate

the escaping electrons, an MPD close to 1 nm is not unrealistic and the involvement of probing depth effects is well conceivable.

7.3 Discussion

A major finding of our study is that the surface of $MnBi_6Te_{10}$ exhibits FM properties comparable to its bulk, with a robust FM subsystem in the topmost septuple layer, which can interact with the TSS. Indeed, recent ARPES reports suggest the opening of an exchange gap of about 15 meV [360].

As outlined in the Subsection 7.2.6 on sum rules, probing-depth effects can at least partially explain the 40% reduction of the XMCD-derived remanent moment as compared to the SQUID-derived bulk moment. Additional surface effects might influence magnetism and therefore warrant consideration. For one thing, an incomplete coordination by magnetic neighbors of the topmost SL might suppress the out-of-plane magnetic interactions. However, since these interlayer interactions are weak (see Subsection 7.2.2 on DFT), additional theoretical scrutiny would be required to elucidate, what role their further suppression might play. For another thing, a combined study involving DFT and XMCD suggests that TSS couple to magnetic atoms such as Co and Mn at the surface of Bi_2Te_3, contributing to their interaction by a RKKY-like mechanism [296]: Due to their highly localized nature, electrons in the TSS interact more strongly with magnetic moments than electrons in the bulk. This might contribute to the differences between the magnetic properties at the surface and in the bulk. Our results encourage similar calculations for $MnBi_6Te_{10}$.

We now discuss the mechanism inducing the crossover from a pronounced AFM towards an FM order as the number n of the QLs in the MBT_n stacking sequence increases (see Subsection 7.2.2 on bulk magnetism). The calculations for $MnBi_6Te_{10}$ in Subsection 7.2.2 yield an – albeit small – AFM coupling. Although the increasing $K/2J$ ratio with increasing n [152] certainly helps to stabilize the FM order for $n \geq n_{FM} = 2$ in our samples (see Subsection 7.2.2 and Fig. 7.5 (c)), the fact that previous studies reported $n_{FM} = 3$ [151, 153–155] hints at an additional phenomenon being involved. In the subsections on growth and DFT it was established that Mn/Bi antisite defects can drive enhanced FM properties. As we have shown for the family member with the strongest interlayer AFM coupling, the detailed intermixing pattern determines whether ferro- or antiferromagnetism is preferred. Hence, the here observed magnetic properties in $MnBi_6Te_{10}$ can well originate in a prevalence of intermixing patterns that favor FM order.

In this context, a comparison between the MBT_n series and the analogous Sb-based family $(MnSb_2Te_4)(Sb_2Te_3)_n$ (MST_n) becomes relevant. FM order in MST_n is observed to be more dominant even for $n = 0$. It is by now widely accepted that this FM behavior is driven by intermixing [160, 361, 362], which is facilitated in $MnSb_2Te_4$ as the sizes of Mn and Sb are more similar than those of Mn and Bi. Although the role of intermixing is more

disputed in MBT_n, a recent study reveals its crucial impact on the magnetic coupling in $MnBi_2Te_4$ [158].

We have established that the FM properties of our crystals are conditioned by the underlying cation intermixing. Whereas the Mn deficiency in $MnBi_6Te_{10}$ is often found by x-ray spectroscopy [151, 154, 155], the related intermixing is scarcely scrutinized. We compare our refinement with Ref. [153] to pinpoint what sets our samples apart. On the one hand, there are some commonalities, such as the presence of Mn/Bi intermixing, the absence of cation vacancies, and a strongly mixed occupancy on the 3*a* site. On the other hand, there are also substantial differences: The mixed 3*a* occupancy is more pronounced in our sample, in which we find 56% Mn (and 44% Bi), than in the sample studied in Ref. [153], which has 83% Mn (and 17 % Bi). Also, the Mn distribution over the 6*c* positions is distinctly different: We observe a higher Mn concentration in both 6*c* sites of the QLs, i.e. up to $Bi_{1.86}Mn_{0.14}Te_3$ vs. $Bi_{1.92}Mn_{0.08}Te_3$ in Ref. [153], and up to 2 % Mn in the outer positions of the SL that are reported defect-free in Ref. [153]. In general, the 3*a* site in our crystals is more Mn-depleted, so that these "stray" Mn atoms, which find no space on the 3*a* site, disperse over the entire layered stack by occupying 6*c* sites. Since this intermixing is less pronounced in the MBT_n studied in Ref. [153], it features increasingly competing FM and AFM interactions below 10 K.

Variations in the intermixing patterns may stem from subtle differences in synthetic procedures, whose strong correlations between the synthesis temperatures and the resultant cation disorder and magnetic order have been, by now, undoubtedly established for $MnSb_2Te_4$ [41, 160, 363]. Since the Bi-analogs have limited thermodynamic stability [33, 157] and, thus, offer very narrow growth temperature windows, their degrees of intermixing appear to be far less dramatic than in $MnSb_2Te_4$ and, therefore, more challenging to trace experimentally.

Finally, based on $2p \rightarrow 3d$ XAS, XMCD and XMLD we provide a detailed microscopic insight into the electronic and magnetic properties of the intrinsic magnetic topological insulator $MnBi_6Te_{10}$. Using *ab initio* MLFT we calculate the local ground-state properties and $L_{2,3}$ edge x-ray absorption spectra of Mn, which agree very well with our experimental data, in terms of both the line-shape profile and the relative energy positions of the multiplet features. Our results indicate a coherently mixed $d^5 - d^6 - d^7$ ground state with a predominant contribution of the d^5 configuration (71%), yielding a total d-shell electron occupation $n_d = 5.31$, corresponding to the $Mn^{1.69+}$ oxidation state. Nonetheless, the contribution of d^6 configuration is substantial (27%), i.e. the Mn is subject to significant covalency (not from large hopping integrals, but from a small charge-transfer energy), yet the high spin d^5 state survives this, allowing for robust magnetism. Our calculations also reproduce the experimentally obtained XMLD spectra and show that the observed linear dichroism is primarily due to the magnetic ordering, whereas the contribution of crystal-field effects can be neglected. The good agreement of the calculations with the

experimental spectra firmly indicates the validity of our theoretical approach and the reliability of the derived ground-state properties, as well as of the microscopic parameters, which will serve as an important input to future atomic multiplet calculations on the other members of the $(MnBi_2Te_4)(Bi_2Te_3)_n$ family or similar systems.

In summary, the prominent ferromagnetic characteristics of our sample, with a rather large T_C, and a substantial ordered, out-of-plane moment both in the bulk and at the surface, categorizes $MnBi_6Te_{10}$ as a particularly interesting candidate for the realization of a high-temperature QAH material [42, 155, 343].

Chapter 8

Summary and outlook

In this work we employed various soft x-ray spectroscopy techniques, such as XAS and XMCD, supported by resPES and ARPES results, to comprehensively and systematically study electronic and magnetic properties of a novel class of materials – magnetic topological insulators, which possess a variety of exotic quantum phenomena, including the QAH effect, with a great potential for future applications in low-dissipation electronics. The experimental techniques were combined with sample characterization, bulk magnetometry and theoretical methods, which all together allowed us to gain significant insights into the fundamental mechanism that underlie the collective magnetic ordering as well as local properties of several exemplary MTIs, and further to address the key open questions in these materials which are still highly debated. Below, we recapitulate the main findings and conclusions of this thesis and put them in a broader context to highlight possible new research directions for MTIs in anticipation of a great future for quantum materials.

We started in Chapter 4 by providing a detailed microscopic insight into the local electronic and magnetic properties of V-and Cr-doped $(Bi,Sb)_2Te_3$ to better understand the difference between these two prototypical QAH systems. We have determined the ground state of magnetic impurities and the microscopic parameters important for understanding the mechanics of magnetic coupling in these compounds by analyzing XAS and XMCD spectra with MLFT and magneto-optical sum rules. We have found a strongly covalent ground state of the magnetic impurities dominated by the coherent superposition of one and two Te-ligand-hole configurations, with negligible contributions from a purely ionic 3+ configuration. This strong charge transfer from the ligands to the V/Cr $3d$ states indicates the importance of Te $5p$ states for the magnetic coupling and, hence, for the QAH effect in magnetically doped TIs. In good agreement with published magnetometry data we have obtained total magnetic moments of $3.19\mu_B$ for Cr and $1.84\mu_B$ for V. In formal agreement with the expected quenching of the orbital moment for the d^3 configuration, the orbital magnetic moment on Cr is negligibly small, whereas for V we obtain $-0.55\mu_B$. The unquenched orbital moment could explain the substantial magnetocrystalline anisotropy observed in V-doped samples. Furthermore, the measurements presented in the chapter have shown that not only do the magnetic dopants V and Cr

carry a magnetic moment, but also the nominally nonmagnetic host atoms Sb and Te possess spin-derived moments, which suggests that the observed local magnetic coupling mechanism might be in part mediated by Sb/Te 5*p* states through *pd* hybridization, following the Zener-type *pd*-exchange interaction scenario.

Next, we continued in Chapter 5 by addressing the open questions on the microscopic origin of ferromagnetism in V- and Cr-doped $(Bi,Sb)_2Te_3$ MTIs. We have revealed an important role of the 3*d* impurities states in mediating magnetic exchange coupling underlying the magnetic interactions in V- and Cr-doped MTIs using state-of-the-art DFT and MLFT calculations in combination with XMCD and resPES. We have shown that the latter cannot be explained based solely on the recently reported van Vleck mechanism, bearing its origin on the topologically non-trivial band structure. In fact, the results presented in the chapter suggest a mechanism based on *pd* hybridization. Calculations have illustrated that the kind and strength of the magnetic exchange coupling varies with the position of E_F in the 3*d* DOS, i.e. with the impurity 3*d*-shell occupation. Further, we have systematically investigated the influence of the Bi/Sb substitution on the electronic and magnetic properties of the samples, as well as the dependence of their magnetic properties on the concentration of impurities. By increasing the Bi concentration, T_C experiences a significant drop from 45 to 35 K, the XMCD signal at the V, Sb and Te absorption edges rapidly decreases and the hysteresis loop closes, confirming that the substitutional Bi atoms significantly suppress the long-range magnetic order. To gain a quantitative information, using sum rules we have extracted the spin and orbital moments of V as a function of its concentration and the Bi/Sb ratio. Overall, we observe a change of the ordered total magnetic moment from $0.79\mu_B$ for the Bi-rich sample to $1.60\mu_B$ for the Sb-rich one. Furthermore, the remanent data illustrates a drop of the spin magnetic moment from $1.56\mu_B$ to $0.6\mu_B$ and a quenching of the orbital moment with the increase of V concentration from 1.8% to 6.8%. A deeper understanding of such behavior requires further theoretical investigations. Finally, we have qualitatively described the origin of the induced magnetic moments at the otherwise non-magnetic Te and Sb atoms in the host lattice by drawing an analogy to the well-known diluted magnetic semiconductor (Ga,Mn)As and explained their role in mediating a robust ferromagnetism based on the Zener-type *pd*-exchange interaction scenario.

Further, in Chapter 6 we have studied the effectiveness of introducing large local magnetic moments to enhance the exchange gap in TSS preferential for a high-temperature QAH effect, by doping prototypical TI Bi_2Te_3 with the rare earth element Eu. We have observed interesting and unexpected magnetic properties of this system for all investigated Eu concentrations using bulk magnetometry measurements, namely incipient antiferromagnetism below about 10 K. We have interpreted the $M_{4,5}$ edge XAS and XMCD spectra of Eu with atomic multiplet calculations and found that, unlike most other RE elements, Eu enters Bi_2Te_3 as Eu^{2+} and thus leads to hole doping and disorder. Furthermore, as

expected, doped Eu ions exhibit notably larger magnetic moment than in the case of transition metals, as consistently follows from our sum rule and atomic multiplet analysis. The onset of antiferromagnetism over a substantial doping range corroborates the potential of doping with rare earth elements to result in an AFM topological insulator with exotic quantum properties. Finally, the electronic properties of the system were characterized by ARPES and resPES at 20 K. Since this is still above the AFM onset temperature, the TSS remains intact and gapless for all Eu doping levels. Nevertheless, the photoemission measurements allowed for establishing a DFT model, which explains the onset of antiferromagnetism observed in SQUID, by the direct overlap of the wave functions of the Eu impurities.

In the next Chapter 7 we discussed robust FM order with $T_C \approx 12$ K we have uncovered both in the bulk and on the surface of $MnBi_6Te_{10}$ intrinsic MTI crystals by using bulk-sensitive SQUID magnetometry and surface-sensitive XMCD. The clear FM characteristics seemingly contradict the weak AFM coupling anticipated from DFT calculations for the atomically ordered compound. This disagreement can be resolved by including the XRD derived Mn substoichiometry and Mn/Bi site intermixing into the calculations, as they enable FM configurations already for $MnBi_2Te_4$. An analysis of the intermixing ratios in our samples and those reported showing no ferromagnetism allows for a connection to the growth conditions. The bulk magnetometry data indicate the opening of a considerable hysteresis loop for all samples consistent with an FM state with a coercive field of about 32 mT at $T = 2$ K and a finite remanence at zero magnetic field, in agreement with the XMCD field-dependent measurements, which categorizes $MnBi_6Te_{10}$ as a particularly interesting material for the realization of a high-temperature QAH effect. Furthermore, based on Mn $L_{2,3}$ XAS, XMCD and XMLD we have provided a detailed microscopic insight into the local electronic and magnetic properties of $MnBi_6Te_{10}$. Using *ab initio* MLFT we have calculated the x-ray absorption spectra of Mn, which agree very well with our experimental data, in terms of both the line shape and the relative energy positions of the multiplet peaks, and determined the local ground-state properties of Mn. Our results indicate a coherently mixed $d^5 - d^6 - d^7$ ground state with a predominant contribution of the d^5 configuration (71%), yielding a total d-shell electron occupation $n_d = 5.31$, corresponding to the $Mn^{1.69+}$ oxidation state. The fully-polarized spin magnetic moment per Mn below the critical temperature was found to be $4.69\mu_B$, while the orbital moment is almost completely quenched. Our calculations also reproduce the experimentally obtained XMLD spectra and show that the observed linear dichroism is primarily due to the magnetic ordering, whereas the contribution of crystal-field effects can be neglected. The results in this chapter suggest that carefully engineered intermixing plays a crucial role in achieving a robust FM order and therefore could be the key towards enhanced QAH effect properties.

Despite the great progress in understanding the QAH effect as well as other exotic

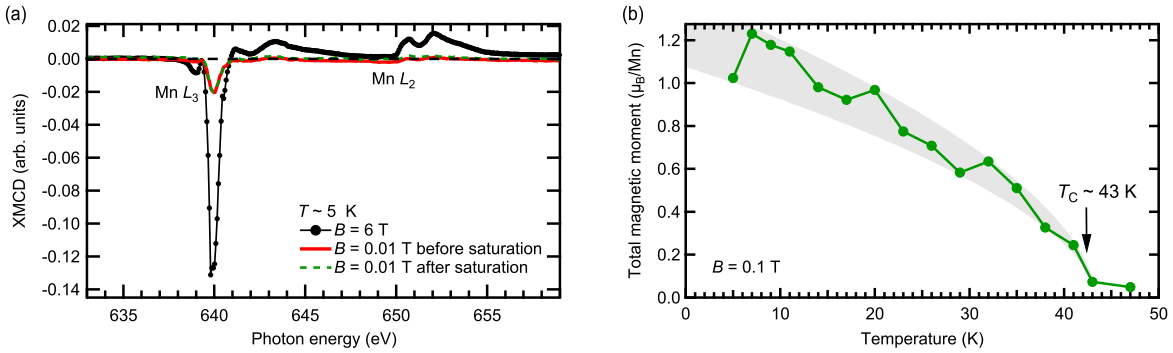

Figure 8.1: (a) Mn $L_{2,3}$ edge XMCD signal at 6 T (black curve), together with XMCD measured at $B = 0.01$ T before (red curve) and after (green dashed curve) saturation of the sample in 6 T field. (c) Total magnetic moment of the Mn ion extracted by means of sum rule analysis as a function of temperature at $B = 0.1$ T.

topological quantum effects, there is still a lot of work to be done and many open questions to be addressed in order to overcome the gap between fundamental researches and practical applications.

In the future, it will be intriguing to further explore different intrinsic MTIs to realize better structural and magnetic properties for the observation of the QAH effect at elevated temperatures. One particularly fascinating intrinsic MTI system is $MnSb_2Te_4$, which has recently attracted the attention of researchers because of its high transition temperature and possible ferromagnetic interaction between the septuple layers, in contrast to its isostructural sister compound $MnBi_2Te_4$. Interestingly, some reports suggest that depending on the composition and growth condition this material can be highly tunable between transition temperatures of about 20 K and 46 K, and from an antiferromagnetic to a ferro/ferrimagnetic ground state [160, 364–367]. DFT calculations found that the perfectly ordered $MnSb_2Te_4$ is antiferromagnetic [368] and topologically trivial [361, 367], while Mn/Sb site intermixing is decisive to render $MnSb_2Te_4$ both ferromagnetic and topologically nontrivial [160, 361]. In Fig. 8.1 we show our preliminary XAS and XMCD measurements on one of such off-stoichiometric $MnSb_2Te_4$ samples. Fig. 8.1 (a) displays a normalized saturation XMCD spectrum (black curve) together with spectra measured at a low field of $B = 0.01$ T, close to remanence, before and after going to 6 T saturation, indicating the existence of considerable remanent dichroic signal of the Mn. Further, the thermal demagnetization of the total magnetic moment of Mn in Fig. 8.1 (b), obtained using sum rules, suggests a ferromagnetic interaction between Mn atoms with a Curie temperature of $T_C \approx 43 \pm 2$ K. These preliminary observations indicate that $MnSb_2Te_4$ is a particularly interesting candidate for the realization of a high-temperature QAH material, and motivates further research in this direction.

Bibliography

[1] K. He, Y. Wang, and Q.-K. Xue, Annu. Rev. Condens. Matter Phys. **9**, 329 (2018).

[2] Y. Tokura, K. Yasuda, and A. Tsukazaki, Nat. Rev. Phys. **1**, 126 (2019).

[3] H. N. Khan, D. A. Hounshell, and E. R. H. Fuchs, Nat. Electron. **1**, 14 (2018).

[4] M. J. Gilbert, Commun. Phys. **4**, 70 (2021).

[5] N. Kim, T. Austin, D. Baauw, T. Mudge, K. Flautner, J. Hu, M. Irwin, M. Kandemir, and V. Narayanan, Computer **36**, 68 (2003).

[6] M. Z. Hasan and C. L. Kane, Rev. Mod. Phys. **82**, 3045 (2010).

[7] X.-L. Qi and S.-C. Zhang, Rev. Mod. Phys. **83**, 1057 (2011).

[8] C.-Z. Chang, W. Zhao, D. Y. Kim, H. Zhang, B. A. Assaf, D. Heiman, S.-C. Zhang, C. Liu, M. H. W. Chan, and J. S. Moodera, Nat. Mater. **14**, 473 EP (2015).

[9] C.-Z. Chang, J. Zhang, X. Feng, J. Shen, Z. Zhang, M. Guo, K. Li, Y. Ou, P. Wei, L.-L. Wang, Z.-Q. Ji, Y. Feng, S. Ji, X. Chen, J. Jia, X. Dai, Z. Fang, S.-C. Zhang, K. He, Y. Wang, L. Lu, X.-C. Ma, and Q.-K. Xue, Science **340**, 167 (2013).

[10] M. Götz, K. M. Fijalkowski, E. Pesel, M. Hartl, S. Schreyeck, M. Winnerlein, S. Grauer, H. Scherer, K. Brunner, C. Gould, F. J. Ahlers, and L. W. Molenkamp, Appl. Phys. Lett. **112**, 072102 (2018).

[11] B. Lian, X.-Q. Sun, A. Vaezi, X.-L. Qi, and S.-C. Zhang, Proc. Natl. Acad. Sci. U.S.A. **115**, 10938 (2018).

[12] C.-X. Liu, S.-C. Zhang, and X.-L. Qi, Annu. Rev. Condens. Matter Phys. **7**, 301 (2016).

[13] X. Zhang and S.-C. Zhang, in *Micro- and Nanotechnology Sensors, Systems, and Applications IV*, Vol. 8373 (International Society for Optics and Photonics, 2012) p. 837309.

[14] J. Wu, J. Liu, and X.-J. Liu, Phys. Rev. Lett. **113**, 136403 (2014).

[15] I. Žutić, J. Fabian, and S. Das Sarma, Rev. Mod. Phys. **76**, 323 (2004).

[16] F. Fei, S. Zhang, M. Zhang, S. A. Shah, F. Song, X. Wang, and B. Wang, Adv. Mater. **32**, 1904593 (2020).

[17] X.-L. Qi, T. L. Hughes, and S.-C. Zhang, Phys. Rev. B **82**, 184516 (2010).

[18] Q. L. He, L. Pan, A. L. Stern, E. C. Burks, X. Che, G. Yin, J. Wang, B. Lian, Q. Zhou, E. S. Choi, K. Murata, X. Kou, Z. Chen, T. Nie, Q. Shao, Y. Fan, S.-C. Zhang, K. Liu, J. Xia, and K. L. Wang, Science **357**, 294 (2017).

[19] R. Li, J. Wang, X.-L. Qi, and S.-C. Zhang, Nat. Phys. **6**, 284 (2010).

[20] S. Grauer, K. M. Fijalkowski, S. Schreyeck, M. Winnerlein, K. Brunner, R. Thomale, C. Gould, and L. W. Molenkamp, Phys. Rev. Lett. **118**, 246801 (2017).

[21] D. Xiao, J. Jiang, J.-H. Shin, W. Wang, F. Wang, Y.-F. Zhao, C. Liu, W. Wu, M. H. W. Chan, N. Samarth, and C.-Z. Chang, Phys. Rev. Lett. **120**, 056801 (2018).

[22] D. Zhang, M. Shi, T. Zhu, D. Xing, H. Zhang, and J. Wang, Phys. Rev. Lett. **122**, 206401 (2019).

[23] Y. Ou, C. Liu, G. Jiang, Y. Feng, D. Zhao, W. Wu, X.-X. Wang, W. Li, C. Song, L.-L. Wang, W. Wang, W. Wu, Y. Wang, K. He, X.-C. Ma, and Q.-K. Xue, Adv. Mater. **30**, 1703062 (2018).

[24] M. Mogi, R. Yoshimi, A. Tsukazaki, K. Yasuda, Y. Kozuka, K. S. Takahashi, M. Kawasaki, and Y. Tokura, Appl. Phys. Lett. **107**, 182401 (2015).

[25] J.-M. Zhang, W. Zhu, Y. Zhang, D. Xiao, and Y. Yao, Phys. Rev. Lett. **109**, 266405 (2012).

[26] J.-M. Zhang, W. Ming, Z. Huang, G.-B. Liu, X. Kou, Y. Fan, K. L. Wang, and Y. Yao, Phys. Rev. B **88**, 235131 (2013).

[27] J. Kim, S.-H. Jhi, A. H. MacDonald, and R. Wu, Phys. Rev. B **96**, 140410 (2017).

[28] J. Kim, H. Wang, and R. Wu, Phys. Rev. B **97**, 125118 (2018).

[29] M. G. Vergniory, M. M. Otrokov, D. Thonig, M. Hoffmann, I. V. Maznichenko, M. Geilhufe, X. Zubizarreta, S. Ostanin, A. Marmodoro, J. Henk, W. Hergert, I. Mertig, E. V. Chulkov, and A. Ernst, Phys. Rev. B **89**, 165202 (2014).

[30] M. F. Islam, C. M. Canali, A. Pertsova, A. Balatsky, S. K. Mahatha, C. Carbone, A. Barla, K. A. Kokh, O. E. Tereshchenko, E. Jiménez, N. B. Brookes, P. Gargiani, M. Valvidares, S. Schatz, T. R. F. Peixoto, H. Bentmann, F. Reinert, J. Jung, T. Bathon, K. Fauth, M. Bode, and P. Sessi, Phys. Rev. B **97**, 155429 (2018).

[31] M. M. Otrokov, I. I. Klimovskikh, H. Bentmann, D. Estyunin, A. Zeugner, Z. S. Aliev, S. Gaß, A. U. B. Wolter, A. V. Koroleva, A. M. Shikin, M. Blanco-Rey, M. Hoffmann, I. P. Rusinov, A. Y. Vyazovskaya, S. V. Eremeev, Y. M. Koroteev, V. M. Kuznetsov, F. Freyse, J. Sánchez-Barriga, I. R. Amiraslanov, M. B. Babanly, N. T. Mamedov, N. A. Abdullayev, V. N. Zverev, A. Alfonsov, V. Kataev, B. Büchner, E. F. Schwier, S. Kumar, A. Kimura, L. Petaccia, G. Di Santo, R. C. Vidal, S. Schatz, K. Kißner, M. Ünzelmann, C. H. Min, S. Moser, T. R. F. Peixoto, F. Reinert, A. Ernst, P. M. Echenique, A. Isaeva, and E. V. Chulkov, Nature **576**, 416 (2019).

[32] J. Li, Y. Li, S. Du, Z. Wang, B.-L. Gu, S.-C. Zhang, K. He, W. Duan, and Y. Xu, Sci. Adv. **5**, 10.1126/sciadv.aaw5685 (2019).

[33] A. Zeugner, F. Nietschke, A. U. B. Wolter, S. Gaß, R. C. Vidal, T. R. F. Peixoto, D. Pohl, C. Damm, A. Lubk, R. Hentrich, S. K. Moser, C. Fornari, C. H. Min, S. Schatz, K. Kißner, M. Ünzelmann, M. Kaiser, F. Scaravaggi, B. Rellinghaus, K. Nielsch, C. Hess, B. Büchner, F. Reinert, H. Bentmann, O. Oeckler, T. Doert, M. Ruck, and A. Isaeva, Chem. Mater. **31**, 2795 (2019).

[34] P. Rani, A. Saxena, R. Sultana, V. Nagpal, S. S. Islam, S. Patnaik, and V. P. S. Awana, J. Supercond. Nov. Magn. **32**, 3705 (2019).

[35] J.-Q. Yan, Q. Zhang, T. Heitmann, Z. Huang, K. Y. Chen, J.-G. Cheng, W. Wu, D. Vaknin, B. C. Sales, and R. J. McQueeney, Phys. Rev. Mater. **3**, 064202 (2019).

[36] D. S. Lee, T.-H. Kim, C.-H. Park, C.-Y. Chung, Y. S. Lim, W.-S. Seo, and H.-H. Park, CrystEngComm **15**, 5532 (2013).

[37] M. M. Otrokov, I. P. Rusinov, M. Blanco-Rey, M. Hoffmann, A. Y. Vyazovskaya, S. V. Eremeev, A. Ernst, P. M. Echenique, A. Arnau, and E. V. Chulkov, Phys. Rev. Lett. **122**, 107202 (2019).

[38] Y. Peng and Y. Xu, Phys. Rev. B **99**, 195431 (2019).

[39] Y. Gong, J. Guo, J. Li, K. Zhu, M. Liao, X. Liu, Q. Zhang, L. Gu, L. Tang, X. Feng, D. Zhang, W. Li, C. Song, L. Wang, P. Yu, X. Chen, Y. Wang, H. Yao, W. Duan, Y. Xu, S.-C. Zhang, X. Ma, Q.-K. Xue, and K. He, Chin. Phys. Lett. **36**, 076801 (2019).

[40] R. C. Vidal, H. Bentmann, T. R. F. Peixoto, A. Zeugner, S. Moser, C.-H. Min, S. Schatz, K. Kißner, M. Ünzelmann, C. I. Fornari, H. B. Vasili, M. Valvidares, K. Sakamoto, D. Mondal, J. Fujii, I. Vobornik, S. Jung, C. Cacho, T. K. Kim, R. J. Koch, C. Jozwiak, A. Bostwick, J. D. Denlinger, E. Rotenberg, J. Buck, M. Hoesch, F. Diekmann, S. Rohlf, M. Kalläne, K. Rossnagel, M. M. Otrokov, E. V. Chulkov, M. Ruck, A. Isaeva, and F. Reinert, Phys. Rev. B **100**, 121104(R) (2019).

[41] C. Liu, Y. Wang, H. Li, Y. Wu, Y. Li, J. Li, K. He, Y. Xu, J. Zhang, and Y. Wang, Nat. Mater. **19**, 522 (2020).

[42] Y. Deng, Y. Yu, M. Z. Shi, Z. Guo, Z. Xu, J. Wang, X. H. Chen, and Y. Zhang, Science **367**, 895 (2020).

[43] J. E. Moore, Nature **464**, 194 (2010).

[44] X. Kou, Y. Fan, M. Lang, P. Upadhyaya, and K. L. Wang, Solid State Commun. **215-216**, 34 (2015).

[45] E. M. Lifshitz and L. P. Pitaevskii, *Statistical physics: theory of the condensed state*, Vol. 9 (Elsevier, 2013).

[46] K. v. Klitzing, G. Dorda, and M. Pepper, Phys. Rev. Lett. **45**, 494 (1980).

[47] R. B. Laughlin, Phys. Rev. B **23**, 5632 (1981).

[48] D. J. Thouless, M. Kohmoto, M. P. Nightingale, and M. den Nijs, Phys. Rev. Lett. **49**, 405 (1982).

[49] B. A. Bernevig, in *Topological Insulators and Topological Superconductors* (Princeton university press, 2013).

[50] F. D. M. Haldane, Phys. Rev. Lett. **61**, 2015 (1988).

[51] C. L. Kane and E. J. Mele, Phys. Rev. Lett. **95**, 226801 (2005).

[52] C. L. Kane and E. J. Mele, Phys. Rev. Lett. **95**, 146802 (2005).

[53] P. Wang, J. Ge, J. Li, Y. Liu, Y. Xu, and J. Wang, The Innovation **2**, 100098 (2021).

[54] M. König, S. Wiedmann, C. Brüne, A. Roth, H. Buhmann, L. W. Molenkamp, X.-L. Qi, and S.-C. Zhang, Science **318**, 766 (2007).

[55] B. A. Bernevig, T. L. Hughes, and S.-C. Zhang, Science **314**, 1757 (2006).

[56] J. E. Moore and L. Balents, Phys. Rev. B **75**, 121306 (2007).

[57] L. Fu, C. L. Kane, and E. J. Mele, Phys. Rev. Lett. **98**, 106803 (2007).

[58] R. Roy, Phys. Rev. B **79**, 195322 (2009).

[59] L. Fu and C. L. Kane, Phys. Rev. B **76**, 045302 (2007).

[60] D. Hsieh, D. Qian, L. Wray, Y. Xia, Y. S. Hor, R. J. Cava, and M. Z. Hasan, Nature **452**, 970 (2008).

[61] H. Zhang, C.-X. Liu, X.-L. Qi, X. Dai, Z. Fang, and S.-C. Zhang, Nat. Phys **5**, 438 (2009).

[62] Y. Xia, D. Qian, D. Hsieh, L. Wray, A. Pal, H. Lin, A. Bansil, D. Grauer, Y. S. Hor, R. J. Cava, *et al.*, Nat. Phys **5**, 398 (2009).

[63] Y. Chen, J. G. Analytis, J.-H. Chu, Z. Liu, S.-K. Mo, X.-L. Qi, H. Zhang, D. Lu, X. Dai, Z. Fang, *et al.*, Science **325**, 178 (2009).

[64] C. B. Satterthwaite and R. W. Ure, Phys. Rev. **108**, 1164 (1957).

[65] T. Caillat, M. Carle, P. Pierrat, H. Scherrer, and S. Scherrer, J. Phys. Chem. Solids **53**, 1121 (1992).

[66] F. Rosi, B. Abeles, and R. Jensen, J. Phys. Chem. Solids **10**, 191 (1959).

[67] D. Kriegner, P. Harcuba, J. Veselý, A. Lesnik, G. Bauer, G. Springholz, and V. Holý, Journal of Applied Crystallography **50**, 369 (2017).

[68] N. V. Tarakina, S. Schreyeck, M. Duchamp, G. Karczewski, C. Gould, K. Brunner, R. E. Dunin-Borkowski, and L. W. Molenkamp, CrystEngComm **19**, 3633 (2017).

[69] C.-X. Liu, X.-L. Qi, X. Dai, Z. Fang, and S.-C. Zhang, Phys. Rev. Lett. **101**, 146802 (2008).

[70] C.-X. Liu, H. Zhang, B. Yan, X.-L. Qi, T. Frauenheim, X. Dai, Z. Fang, and S.-C. Zhang, Phys. Rev. B **81**, 041307 (2010).

[71] R. Yu, W. Zhang, H.-J. Zhang, S.-C. Zhang, X. Dai, and Z. Fang, Science **329**, 61 (2010).

[72] K. Nomura and N. Nagaosa, Phys. Rev. Lett. **106**, 166802 (2011).

[73] C.-Z. Chang, J. Zhang, M. Liu, Z. Zhang, X. Feng, K. Li, L.-L. Wang, X. Chen, X. Dai, Z. Fang, X.-L. Qi, S.-C. Zhang, Y. Wang, K. He, X.-C. Ma, and Q.-K. Xue, Adv. Mater. **25**, 1065 (2013).

[74] X. Kou, M. Lang, Y. Fan, Y. Jiang, T. Nie, J. Zhang, W. Jiang, Y. Wang, Y. Yao, L. He, and K. L. Wang, ACS Nano **7**, 9205 (2013).

[75] J. S. Dyck, W. Chen, P. Hájek, P. Lošťák, and C. Uher, Physica B **312-313**, 820 (2002).

[76] J. S. Dyck, v. Drašar, P. Lošťák, and C. Uher, Phys. Rev. B **71**, 115214 (2005).

[77] Z. Zhou, Y.-J. Chien, and C. Uher, Appl. Phys. Lett. **87**, 112503 (2005).

[78] M. Ye, T. Xu, G. Li, S. Qiao, Y. Takeda, Y. Saitoh, S.-Y. Zhu, M. Nurmamat, K. Sumida, Y. Ishida, S. Shin, and A. Kimura, Phys. Rev. B **99**, 144413 (2019).

[79] A. Tcakaev, V. B. Zabolotnyy, R. J. Green, T. R. F. Peixoto, F. Stier, M. Dettbarn, S. Schreyeck, M. Winnerlein, R. C. Vidal, S. Schatz, H. B. Vasili, M. Valvidares, K. Brunner, C. Gould, H. Bentmann, F. Reinert, L. W. Molenkamp, and V. Hinkov, Phys. Rev. B **101**, 045127 (2020).

[80] M. Ye, W. Li, S. Zhu, Y. Takeda, Y. Saitoh, J. Wang, H. Pan, M. Nurmamat, K. Sumida, F. Ji, Z. Liu, H. Yang, Z. Liu, D. Shen, A. Kimura, S. Qiao, and X. Xie, Nat. Comm. **6**, 10.1038/ncomms9913 (2015).

[81] J. Choi, S. Choi, J. Choi, Y. Park, H.-M. Park, H.-W. Lee, B.-C. Woo, and S. Cho, Phys. Status Solidi B **241**, 1541 (2004).

[82] Y. S. Hor, P. Roushan, H. Beidenkopf, J. Seo, D. Qu, J. G. Checkelsky, L. A. Wray, D. Hsieh, Y. Xia, S.-Y. Xu, D. Qian, M. Z. Hasan, N. P. Ong, A. Yazdani, and R. J. Cava, Phys. Rev. B **81**, 195203 (2010).

[83] H.-J. Kim, K.-S. Kim, J.-F. Wang, V. A. Kulbachinskii, K. Ogawa, M. Sasaki, A. Ohnishi, M. Kitaura, Y.-Y. Wu, L. Li, I. Yamamoto, J. Azuma, M. Kamada, and V. Dobrosavljević, Phys. Rev. Lett. **110**, 136601 (2013).

[84] Z. Zhou, M. Žabèík, P. Lošták, and C. Uher, J. Appl. Phys. **99**, 043901 (2006).

[85] V. Kulbachinskii, A. Kaminskii, K. Kindo, Y. Narumi, K. Suga, P. Lostak, and P. Svanda, Physica B Condens. Matter **311**, 292 (2002).

[86] Y. L. Chen, J.-H. Chu, J. G. Analytis, Z. K. Liu, K. Igarashi, H.-H. Kuo, X. L. Qi, S. K. Mo, R. G. Moore, D. H. Lu, M. Hashimoto, T. Sasagawa, S. C. Zhang, I. R. Fisher, Z. Hussain, and Z. X. Shen, Science **329**, 659 (2010).

[87] X.-L. Qi, T. L. Hughes, and S.-C. Zhang, Phys. Rev. B **78**, 195424 (2008).

[88] P. Wei, F. Katmis, B. A. Assaf, H. Steinberg, P. Jarillo-Herrero, D. Heiman, and J. S. Moodera, Phys. Rev. Lett. **110**, 186807 (2013).

[89] C. Lee, F. Katmis, P. Jarillo-Herrero, J. S. Moodera, and N. Gedik, Nat. Commun. **7**, 12014 (2016).

[90] F. Katmis, V. Lauter, F. S. Nogueira, B. A. Assaf, M. E. Jamer, P. Wei, B. Satpati, J. W. Freeland, I. Eremin, D. Heiman, *et al.*, Nature **533**, 513 (2016).

[91] L. D. Alegria, H. Ji, N. Yao, J. J. Clarke, R. J. Cava, and J. R. Petta, Appl. Phys. Lett. **105**, 053512 (2014).

[92] M. Lang, M. Montazeri, M. C. Onbasli, X. Kou, Y. Fan, P. Upadhyaya, K. Yao, F. Liu, Y. Jiang, W. Jiang, *et al.*, Nano Lett. **14**, 3459 (2014).

[93] Z. Jiang, C.-Z. Chang, C. Tang, P. Wei, J. S. Moodera, and J. Shi, Nano Lett. **15**, 5835 (2015).

[94] C. Tang, C.-Z. Chang, G. Zhao, Y. Liu, Z. Jiang, C.-X. Liu, M. R. McCartney, D. J. Smith, T. Chen, J. S. Moodera, and J. Shi, Sci. Adv. **3**, e1700307 (2017).

[95] S. V. Eremeev, V. N. Men'shov, V. V. Tugushev, P. M. Echenique, and E. V. Chulkov, Phys. Rev. B **88**, 144430 (2013).

[96] V. N. Men'shov, V. V. Tugushev, S. V. Eremeev, P. M. Echenique, and E. V. Chulkov, Phys. Rev. B **88**, 224401 (2013).

[97] L. J. Collins-McIntyre, L. B. Duffy, A. Singh, N.-J. Steinke, C. J. Kinane, T. R. Charlton, A. Pushp, A. J. Kellock, S. S. P. Parkin, S. N. Holmes, C. H. W. Barnes, G. van der Laan, S. Langridge, and T. Hesjedal, EPL (Europhysics Letters) **115**, 27006 (2016).

[98] P. P. J. Haazen, J.-B. Laloë, T. J. Nummy, H. J. M. Swagten, P. Jarillo-Herrero, D. Heiman, and J. S. Moodera, Appl. Phys. Lett. **100**, 082404 (2012).

[99] T. Dietl and H. Ohno, Rev. Mod. Phys. **86**, 187 (2014).

[100] T. Dietl, Nat. Mater. **9**, 965 (2010).

[101] M. Li, C.-Z. Chang, L. Wu, J. Tao, W. Zhao, M. H. W. Chan, J. S. Moodera, J. Li, and Y. Zhu, Phys. Rev. Lett. **114**, 146802 (2015).

[102] A. I. Figueroa, T. Hesjedal, and N.-J. Steinke, Appl. Phys. Lett. **117**, 150502 (2020).

[103] L. J. Collins-McIntyre, S. E. Harrison, P. Schönherr, N.-J. Steinke, C. J. Kinane, T. R. Charlton, D. Alba-Veneroa, A. Pushp, A. J. Kellock, S. S. P. Parkin, J. S. Harris, S. Langridge, G. van der Laan, and T. Hesjedal, EPL (Europhysics Letters) **107**, 57009 (2014).

[104] T. R. F. Peixoto, H. Bentmann, S. Schreyeck, M. Winnerlein, C. Seibel, H. Maaß, M. Al-Baidhani, K. Treiber, S. Schatz, S. Grauer, C. Gould, K. Brunner, A. Ernst, L. W. Molenkamp, and F. Reinert, Phys. Rev. B **94**, 195140 (2016).

[105] K. Sato, L. Bergqvist, J. Kudrnovský, P. H. Dederichs, O. Eriksson, I. Turek, B. Sanyal, G. Bouzerar, H. Katayama-Yoshida, V. A. Dinh, T. Fukushima, H. Kizaki, and R. Zeller, Rev. Mod. Phys. **82**, 1633 (2010).

[106] T. Dietl, H. Ohno, F. Matsukura, J. Cibert, and D. Ferrand, Science **287**, 1019 (2000).

[107] D. J. Keavney, D. Wu, J. W. Freeland, E. Johnston-Halperin, D. D. Awschalom, and J. Shi, Phys. Rev. Lett. **91**, 187203 (2003).

[108] T. R. F. Peixoto, H. Bentmann, P. Rüßmann, A.-V. Tcakaev, M. Winnerlein, S. Schreyeck, S. Schatz, R. C. Vidal, F. Stier, V. Zabolotnyy, R. J. Green, C. H. Min, C. I. Fornari, H. Maaß, H. B. Vasili, P. Gargiani, M. Valvidares, A. Barla, J. Buck, M. Hoesch, F. Diekmann, S. Rohlf, M. Kalläne, K. Rossnagel, C. Gould, K. Brunner, S. Blügel, V. Hinkov, L. W. Molenkamp, and F. Reinert, npj Quantum Mater. **5**, 87 (2020).

[109] X. F. Kou, W. J. Jiang, M. R. Lang, F. X. Xiu, L. He, Y. Wang, Y. Wang, X. X. Yu, A. V. Fedorov, P. Zhang, and K. L. Wang, J. Appl. Phys. **112**, 063912 (2012).

[110] J. Stöhr, J. Electron. Spectrosc. Relat. Phenom. **75**, 253 (1995).

[111] G. van der Laan and B. T. Thole, Phys. Rev. B **43**, 13401 (1991).

[112] A. I. Figueroa, G. van der Laan, L. J. Collins-McIntyre, S.-L. Zhang, A. A. Baker, S. E. Harrison, P. Schönherr, G. Cibin, and T. Hesjedal, Phys. Rev. B **90**, 134402 (2014).

[113] L. B. Duffy, A. I. Figueroa, L. Gładczuk, N.-J. Steinke, K. Kummer, G. van der Laan, and T. Hesjedal, Phys. Rev. B **95**, 224422 (2017).

[114] T. Hesjedal, Phys. Status Solidi A **216**, 1800726 (2019).

[115] S. E. Harrison, L. J. Collins-McIntyre, P. Schönherr, A. Vailionis, V. Srot, P. A. van Aken, A. J. Kellock, A. Pushp, S. S. P. Parkin, J. S. Harris, B. Zhou, Y. L. Chen, and T. Hesjedal, Sci. Rep. **5**, 15767 (2015).

[116] L. B. Duffy, N.-J. Steinke, J. A. Krieger, A. I. Figueroa, K. Kummer, T. Lancaster, S. R. Giblin, F. L. Pratt, S. J. Blundell, T. Prokscha, A. Suter, S. Langridge, V. N. Strocov, Z. Salman, G. van der Laan, and T. Hesjedal, Phys. Rev. B **97**, 174427 (2018).

[117] S. Li, S. E. Harrison, Y. Huo, A. Pushp, H. T. Yuan, B. Zhou, A. J. Kellock, S. S. P. Parkin, Y.-L. Chen, T. Hesjedal, and J. S. Harris, Appl. Phys. Lett. **102**, 242412 (2013).

[118] A. I. Figueroa, S. E. Harrison, L. J. Collins-McIntyre, G. van der Laan, and T. Hesjedal, Phys. Status Solidi RRL **10**, 467 (2016).

[119] J. Jensen and A. R. Mackintosh, *Rare Earth Magnetism: Structures and Excitations* (Clarendon Press, 1991).

[120] S. E. Harrison, L. J. Collins-McIntyre, S.-L. Zhang, A. A. Baker, A. I. Figueroa, A. J. Kellock, A. Pushp, S. S. P. Parkin, J. S. Harris, G. van der Laan, and T. Hesjedal, J. Phys. Condens. Matter **27**, 245602 (2015).

[121] S. E. Harrison, L. J. Collins-McIntyre, S. Li, A. A. Baker, L. R. Shelford, Y. Huo, A. Pushp, S. S. P. Parkin, J. S. Harris, E. Arenholz, G. van der Laan, and T. Hesjedal, J. Appl. Phys. **115**, 023904 (2014).

[122] S. E. Harrison, L. J. Collins-McIntyre, S. L. Zhang, A. A. Baker, A. I. Figueroa, A. J. Kellock, A. Pushp, Y. L. Chen, S. S. P. Parkin, J. S. Harris, G. van der Laan, and T. Hesjedal, Appl. Phys. Lett. **107**, 182406 (2015).

[123] C.-Z. Chang, P. Tang, Y.-L. Wang, X. Feng, K. Li, Z. Zhang, Y. Wang, L.-L. Wang, X. Chen, C. Liu, W. Duan, K. He, X.-C. Ma, and Q.-K. Xue, Phys. Rev. Lett. **112**, 056801 (2014).

[124] B. Deng, Y. Zhang, S. B. Zhang, Y. Wang, K. He, and J. Zhu, Phys. Rev. B **94**, 054113 (2016).

[125] T. Chen, W. Liu, F. Zheng, M. Gao, X. Pan, G. van der Laan, X. Wang, Q. Zhang, F. Song, B. Wang, B. Wang, Y. Xu, G. Wang, and R. Zhang, Adv. Mater. **27**, 4823 (2015).

[126] G. Will, S. Pickart, H. A. Alperein, and R. Nathans, J. Phys. Chem. Solids **24**, 1679 (1963).

[127] E. Schierle, E. Weschke, A. Gottberg, W. Söllinger, W. Heiss, G. Springholz, and G. Kaindl, Phys. Rev. Lett. **101**, 267202 (2008).

[128] H. S. Lee, J. Kim, K. Lee, A. Jelen, S. Vrtnik, Z. Jagličić, J. Dolinšek, and M. H. Jung, Appl. Phys. Lett. **107**, 182409 (2015).

[129] J.-H. Jun, J. Kim, S.-W. Kim, and M.-H. Jung, Sci. Rep. **10**, 9615 (2020).

[130] J. Kim, K. Lee, T. Takabatake, H. Kim, M. Kim, and M.-H. Jung, Sci. Rep. **5**, 10309 (2015).

[131] A. M. Shikin, D. A. Estyunin, Y. I. Surnin, A. V. Koroleva, E. V. Shevchenko, K. A. Kokh, O. E. Tereshchenko, S. Kumar, E. F. Schwier, K. Shimada, T. Yoshikawa, Y. Saitoh, Y. Takeda, and A. Kimura, Sci. Rep. **9**, 4813 (2019).

[132] A. J. Bestwick, E. J. Fox, X. Kou, L. Pan, K. L. Wang, and D. Goldhaber-Gordon, Phys. Rev. Lett. **114**, 187201 (2015).

[133] K. He, Y. Wang, and Q.-K. Xue, Annu. Rev. Cond. Matter Phys. **9**, 329 (2018).

[134] I. Lee, C. K. Kim, J. Lee, S. J. L. Billinge, R. Zhong, J. A. Schneeloch, T. Liu, T. Valla, J. M. Tranquada, G. Gu, and J. C. S. Davis, Proceedings of the National Academy of Sciences **112**, 1316 (2015).

[135] E. O. Lachman, A. F. Young, A. Richardella, J. Cuppens, H. R. Naren, Y. Anahory, A. Y. Meltzer, A. Kandala, S. Kempinger, Y. Myasoedov, M. E. Huber, N. Samarth, and E. Zeldov, Sci. Adv. **1**, 10.1126/sciadv.1500740 (2015).

[136] E. O. Lachman, M. Mogi, J. Sarkar, A. Uri, K. Bagani, Y. Anahory, Y. Myasoedov, M. E. Huber, A. Tsukazaki, M. Kawasaki, Y. Tokura, and E. Zeldov, npj Quantum Mater. **2**, 70 (2017).

[137] S. Grauer, S. Schreyeck, M. , K. Brunner, C. Gould, and L. W. Molenkamp, Phys. Rev. B **92**, 201304 (2015).

[138] E. D. L. Rienks, S. Wimmer, J. Sánchez-Barriga, O. Caha, P. S. Mandal, J. Růžička, A. Ney, H. Steiner, V. V. Volobuev, H. Groiss, M. Albu, G. Kothleitner, J. Michalička, S. A. Khan, J. Minár, H. Ebert, G. Bauer, F. Freyse, A. Varykhalov, O. Rader, and G. Springholz, Nature **576**, 423 (2019).

[139] M. M. Otrokov, T. V. Menshchikova, M. G. Vergniory, I. P. Rusinov, A. Y. Vyazovskaya, Y. M. Koroteev, G. Bihlmayer, A. Ernst, P. M. Echenique, A. Arnau, *et al.*, 2D Materials **4**, 025082 (2017).

[140] M. Otrokov, T. V. Menshchikova, I. Rusinov, M. Vergniory, V. M. Kuznetsov, and E. V. Chulkov, JETP Letters **105**, 297 (2017).

[141] R. S. K. Mong, A. M. Essin, and J. E. Moore, Phys. Rev. B **81**, 245209 (2010).

[142] Y. J. Chen, L. X. Xu, J. H. Li, Y. W. Li, H. Y. Wang, C. F. Zhang, H. Li, Y. Wu, A. J. Liang, C. Chen, S. W. Jung, C. Cacho, Y. H. Mao, S. Liu, M. X. Wang, Y. F. Guo, Y. Xu, Z. K. Liu, L. X. Yang, and Y. L. Chen, Phys. Rev. X **9**, 041040 (2019).

[143] P. Swatek, Y. Wu, L.-L. Wang, K. Lee, B. Schrunk, J. Yan, and A. Kaminski, Phys. Rev. B **101**, 161109 (2020).

[144] D. Nevola, H. X. Li, J.-Q. Yan, R. G. Moore, H.-N. Lee, H. Miao, and P. D. Johnson, Phys. Rev. Lett. **125**, 117205 (2020).

[145] Y.-J. Hao, P. Liu, Y. Feng, X.-M. Ma, E. F. Schwier, M. Arita, S. Kumar, C. Hu, R. Lu, M. Zeng, Y. Wang, Z. Hao, H.-Y. Sun, K. Zhang, J. Mei, N. Ni, L. Wu, K. Shimada, C. Chen, Q. Liu, and C. Liu, Phys. Rev. X **9**, 041038 (2019).

[146] H. Deng, Z. Chen, A. Wołoś, M. Konczykowski, K. Sobczak, J. Sitnicka, I. V. Fedorchenko, J. Borysiuk, T. Heider, Ł. Pluciński, *et al.*, Nat. Phys **17**, 36 (2021).

[147] J. Ge, Y. Liu, J. Li, H. Li, T. Luo, Y. Wu, Y. Xu, and J. Wang, Natl. Sci. Rev. **7**, 1280 (2020).

[148] J. Wu, F. Liu, M. Sasase, K. Ienaga, Y. Obata, R. Yukawa, K. Horiba, H. Kumigashira, S. Okuma, T. Inoshita, and H. Hosono, Sci. Adv. **5**, eaax9989 (2019).

[149] R. C. Vidal, A. Zeugner, J. I. Facio, R. Ray, M. H. Haghighi, A. U. B. Wolter, L. T. Corredor Bohorquez, F. Caglieris, S. Moser, T. Figgemeier, T. R. F. Peixoto, H. B. Vasili, M. Valvidares, S. Jung, C. Cacho, A. Alfonsov, K. Mehlawat, V. Kataev, C. Hess, M. Richter, B. Büchner, J. van den Brink, M. Ruck, F. Reinert, H. Bentmann, and A. Isaeva, Phys. Rev. X **9**, 041065 (2019).

[150] J. Wu, F. Liu, C. Liu, Y. Wang, C. Li, Y. Lu, S. Matsuishi, and H. Hosono, Adv. Mater. **32**, 2001815 (2020).

[151] C. Hu, L. Ding, K. N. Gordon, B. Ghosh, H.-J. Tien, H. Li, A. G. Linn, S.-W. Lien, C.-Y. Huang, S. Mackey, J. Liu, P. V. S. Reddy, B. Singh, A. Agarwal, A. Bansil, M. Song, D. Li, S.-Y. Xu, H. Lin, H. Cao, T.-R. Chang, D. Dessau, and N. Ni, Sci. Adv. **6**, 10.1126/sciadv.aba4275 (2020).

[152] A. Tan, V. Labracherie, N. Kunchur, A. U. B. Wolter, J. Cornejo, J. Dufouleur, B. Büchner, A. Isaeva, and R. Giraud, Phys. Rev. Lett. **124**, 197201 (2020).

[153] I. I. Klimovskikh, M. M. Otrokov, D. Estyunin, S. V. Eremeev, S. O. Filnov, A. Koroleva, E. Shevchenko, V. Voroshnin, A. G. Rybkin, I. P. Rusinov, M. Blanco-Rey, M. Hoffmann, Z. S. Aliev, M. B. Babanly, I. R. Amiraslanov, N. A. Abdullayev, V. N. Zverev, A. Kimura, O. E. Tereshchenko, K. A. Kokh, L. Petaccia, G. Di Santo, A. Ernst, P. M. Echenique, N. T. Mamedov, A. M. Shikin, and E. V. Chulkov, npj Quantum Mater. **5**, 54 (2020).

[154] H. Xie, D. Wang, Z. Cai, B. Chen, J. Guo, M. Naveed, S. Zhang, M. Zhang, X. Wang, F. Fei, H. Zhang, and F. Song, Appl. Phys. Lett. **116**, 221902 (2020).

[155] S. Tian, S. Gao, S. Nie, Y. Qian, C. Gong, Y. Fu, H. Li, W. Fan, P. Zhang, T. Kondo, S. Shin, J. Adell, H. Fedderwitz, H. Ding, Z. Wang, T. Qian, and H. Lei, Phys. Rev. B **102**, 035144 (2020).

[156] R. Lu, H. Sun, S. Kumar, Y. Wang, M. Gu, M. Zeng, Y.-J. Hao, J. Li, J. Shao, X.-M. Ma, Z. Hao, K. Zhang, W. Mansuer, J. Mei, Y. Zhao, C. Liu, K. Deng, W. Huang,

B. Shen, K. Shimada, E. F. Schwier, C. Liu, Q. Liu, and C. Chen, Phys. Rev. X **11**, 011039 (2021).

[157] D. Souchay, M. Nentwig, D. Günther, S. Keilholz, J. de Boor, A. Zeugner, A. Isaeva, M. Ruck, A. U. B. Wolter, B. Büchner, and O. Oeckler, J. Mater. Chem. C **7**, 9939 (2019).

[158] Y. Lai, L. Ke, J. Yan, R. D. McDonald, and R. J. McQueeney, Phys. Rev. B **103**, 184429 (2021).

[159] L. Ding, C. Hu, E. Feng, C. Jiang, I. A. Kibalin, A. Gukasov, M. Chi, N. Ni, and H. Cao, J. Phys. D: Appl. Phys. **54**, 174003 (2021).

[160] S. Wimmer, J. Sánchez-Barriga, P. Küppers, A. Ney, E. Schierle, F. Freyse, O. Caha, J. Michalička, M. Liebmann, D. Primetzhofer, M. Hoffman, A. Ernst, M. M. Otrokov, G. Bihlmayer, E. Weschke, B. Lake, E. V. Chulkov, M. Morgenstern, G. Bauer, G. Springholz, and O. Rader, Adv. Mater. **33**, 2102935.

[161] J.-Q. Yan, Y. H. Liu, D. S. Parker, Y. Wu, A. A. Aczel, M. Matsuda, M. A. McGuire, and B. C. Sales, Phys. Rev. Mater. **4**, 054202 (2020).

[162] M. Z. Shi, B. Lei, C. S. Zhu, D. H. Ma, J. H. Cui, Z. L. Sun, J. J. Ying, and X. H. Chen, Phys. Rev. B **100**, 155144 (2019).

[163] K. Urban, T. Brückel, W. Schweika, S. Blügel, L. Baumgarten, M. Lentzen, K. Tillmann, and C. M. Schneider, *Probing the Nanoworld: Microscopies, Scattering and Spectroscopies of the Solid State This spring school was organized by the Institute of Solid State Research of Research Centre Jülich on 12–23 March 2007.*, Tech. Rep. (Streumethoden, 2007).

[164] A. Mottana and A. Marcelli, in *A Bridge between Conceptual Frameworks* (Springer, 2015) pp. 275–301.

[165] Stumm von Bordwehr, R., Ann. Phys. Fr. **14**, 377 (1989).

[166] J. Stöhr, *NEXAFS spectroscopy*, Vol. 25 (Springer Science & Business Media, 1992).

[167] E. Beaurepaire, H. Bulou, F. Scheurer, and J. P. Kappler, *Magnetism: A synchrotron radiation approach*, Vol. 697 (Springer, 2006).

[168] B.-K. Teo, in *EXAFS Spectroscopy* (Springer, 1981) pp. 13–58.

[169] J. Stöhr and H. C. Siegmann, Solid-State Sciences. Springer, Berlin, Heidelberg **5**, 236 (2006).

[170] J. Als-Nielsen and D. McMorrow, *Elements of modern X-ray physics* (John Wiley & Sons, 2011).

[171] E. Fermi, *Nuclear physics: a course given by Enrico Fermi at the University of Chicago* (University of Chicago Press, 1950).

[172] P. A. M. Dirac, Proceedings of the Royal Society of London. Series A, Containing Papers of a Mathematical and Physical Character **114**, 243 (1927).

[173] R. D. Cowan, *The theory of atomic structure and spectra*, 3 (Univ. of California Press, 1981).

[174] F. De Groot and A. Kotani, Core Level Spectroscopy of Solids, Advances in Condensed Matter Science (2008).

[175] R. Laskowski and P. Blaha, Phys. Rev. B **82**, 205104 (2010).

[176] G. van der Laan, J. Zaanen, G. A. Sawatzky, R. Karnatak, and J.-M. Esteva, Phys. Rev. B **33**, 4253 (1986).

[177] M. W. Haverkort, *Spin and orbital degrees of freedom in transition metal oxides and oxide thin films studied by soft x-ray absorption spectroscopy*, Ph.D. thesis, Universität zu Köln (2005).

[178] J. Stöhr and Y. Wu, X-ray magnetic circular dichroism: Basic concepts and theory for 3d transition metal atoms, in *New Directions in Research with Third-Generation Soft X-Ray Synchrotron Radiation Sources*, edited by A. S. Schlachter and F. J. Wuilleumier (Springer Netherlands, Dordrecht, 1994) pp. 221–250.

[179] F. M. F. de Groot, Z. W. Hu, M. F. Lopez, G. Kaindl, F. Guillot, and M. Tronc, J. Chem. Phys. **101**, 6570 (1994).

[180] F. M. de Groot, H. Elnaggar, F. Frati, R. pan Wang, M. U. Delgado-Jaime, M. van Veenendaal, J. Fernandez-Rodriguez, M. W. Haverkort, R. J. Green, G. van der Laan, Y. Kvashnin, A. Hariki, H. Ikeno, H. Ramanantoanina, C. Daul, B. Delley, M. Odelius, M. Lundberg, O. Kuhn, S. I. Bokarev, E. Shirley, J. Vinson, K. Gilmore, M. Stener, G. Fronzoni, P. Decleva, P. Kruger, M. Retegan, Y. Joly, C. Vorwerk, C. Draxl, J. Rehr, and A. Tanaka, J. Electron Spectrosc. Relat. Phenom. **249**, 147061 (2021).

[181] B. T. Thole, R. D. Cowan, G. A. Sawatzky, J. Fink, and J. C. Fuggle, Phys. Rev. B **31**, 6856 (1985).

[182] G. van der Laan, B. T. Thole, G. A. Sawatzky, and M. Verdaguer, Phys. Rev. B **37**, 6587 (1988).

[183] J. L. Erskine and E. A. Stern, Phys. Rev. B **12**, 5016 (1975).

[184] G. Schütz, W. Wagner, W. Wilhelm, P. Kienle, R. Zeller, R. Frahm, and G. Materlik, Phys. Rev. Lett. **58**, 737 (1987).

[185] J. Stöhr, J. Magn. Magn. Mater. **200**, 470 (1999).

[186] S. W. Lovesey and S. P. Collins, *X-ray scattering and absorption by magnetic materials*, 1 (Oxford university press, 1996).

[187] U. Fano, Phys. Rev. **178**, 131 (1969).

[188] S. Hüfner, *Photoelectron spectroscopy: principles and applications* (Springer Science & Business Media, 2013).

[189] S. Suga and A. Sekiyama, *Photoelectron spectroscopy* (Springer, 2016).

[190] A. Damascelli, Phys. Scr. **T109**, 61 (2004).

[191] B. Lv, T. Qian, and H. Ding, Nat. Rev. Phys. **1**, 609 (2019).

[192] H. Hertz, Annalen der Physik **267**, 983 (1887).

[193] A. Einstein, Annalen der Physik **322**, 132 (1905).

[194] C. Nordling, E. Sokolowski, and K. Siegbahn, Phys. Rev. **105**, 1676 (1957).

[195] M. P. Seah and W. A. Dench, Surf. Interface Anal. **1**, 2 (1979).

[196] N. Mårtensson, M. Weinelt, O. Karis, M. Magnuson, N. Wassdahl, A. Nilsson, J. Stöhr, and M. Samant, Appl. Phys. A **65**, 159 (1997).

[197] C.-O. Almbladh and L. Hedin, 1b, Hrsg. E. Koch (North Holland, Amsterdam 1983) S **607904** (1983).

[198] P. Willmott, *An introduction to synchrotron radiation: techniques and applications* (John Wiley & Sons, 2019).

[199] C. J. Dietl, *Synthesis and electronic ordering phenomena of calcium ruthenate thin films*, Ph.D. thesis, Universität Stuttgart (2018).

[200] M.-E. Couprie and J.-M. Filhol, Comptes Rendus Physique **9**, 487 (2008), synchrotron x-rays and condensed matter.

[201] E. Weschke and E. Schierle, Journal of large-scale research facilities JLSRF **4**, 127 (2018).

[202] Bl29 - boreas webpage, `https://www.cells.es/en/beamlines/bl29-boreas`, accessed: 2022-02-10.

[203] A. Scherz, *Spin dependent x-ray absorption spectroscopy of 3d transition metals: systematics and applications* (dissertation. de, 2004).

[204] A. Barla, J. Nicolás, D. Cocco, S. M. Valvidares, J. Herrero-Martín, P. Gargiani, J. Moldes, C. Ruget, E. Pellegrin, and S. Ferrer, J. Sync. Rad. **23**, 1507 (2016).

[205] I10: Beamline for advanced dichroism experiments (blade), `https://www.diamond.ac.uk/Instruments/Magnetic-Materials/I10.html`, accessed: 2022-02-10.

[206] G. van der Laan and A. I. Figueroa, Coord. Chem. Rev. **277-278**, 95 (2014), following Chemical Structures using Synchrotron Radiation.

[207] R. Green, *Transition metal impurities in semiconductors: Induced magnetism and band gap engineering*, Ph.D. thesis, University of Saskatchewan Saskatoon (2013).

[208] F. de Groot, J. Electron Spectros. Relat. Phenomena **67**, 529 (1994).

[209] R. Nakajima, J. Stöhr, and Y. U. Idzerda, Phys. Rev. B **59**, 6421 (1999).

[210] M. Abbate, J. B. Goedkoop, F. M. F. de Groot, M. Grioni, J. C. Fuggle, S. Hofmann, H. Petersen, and M. Sacchi, Surf. Interface Anal. **18**, 65 (1992).

[211] J. Vogel and M. Sacchi, J. Electron Spectrosc. Relat. Phenom. **67**, 181 (1994).

[212] W. Gudat and C. Kunz, Phys. Rev. Lett. **29**, 169 (1972).

[213] F. de Groot, M. Arrio, P. Sainctavit, C. Cartier, and C. Chen, Solid State Commun. **92**, 991 (1994).

[214] R. Kurian, K. Kunnus, P. Wernet, S. M. Butorin, P. Glatzel, and F. M. F. de Groot, J. Phys. Condens. Matter **24**, 452201 (2012).

[215] A. J. Achkar, T. Z. Regier, H. Wadati, Y.-J. Kim, H. Zhang, and D. G. Hawthorn, Phys. Rev. B **83**, 081106 (2011).

[216] A. J. Achkar, T. Z. Regier, E. J. Monkman, K. M. Shen, and D. G. Hawthorn, Sci. Rep. **1**, 182 (2011).

[217] C. T. Chantler, J. Phys. Chem. Ref. Data **24**, 71 (1995).

[218] J. Végh, J. Electron Spectrosc. Relat. Phenom. **151**, 159 (2006).

[219] B. T. Thole, P. Carra, F. Sette, and G. van der Laan, Phys. Rev. Lett. **68**, 1943 (1992).

[220] P. Carra, B. T. Thole, M. Altarelli, and X. Wang, Phys. Rev. Lett. **70**, 694 (1993).

[221] C. T. Chen, Y. U. Idzerda, H.-J. Lin, N. V. Smith, G. Meigs, E. Chaban, G. H. Ho, E. Pellegrin, and F. Sette, Phys. Rev. Lett. **75**, 152 (1995).

[222] P. Carra, H. König, B. Thole, and M. Altarelli, Physica B Condens. Matter **192**, 182 (1993).

[223] A. Ankudinov and J. J. Rehr, Phys. Rev. B **51**, 1282 (1995).

[224] T. Jo, J. Phys. Soc. Jpn. **62**, 1814 (1993).

[225] R. Wu and A. J. Freeman, Phys. Rev. Lett. **73**, 1994 (1994).

[226] G. van der Laan, J. Synchrotron Radiat. **6**, 694 (1999).

[227] M. Altarelli, Il Nuovo Cimento D **20**, 1067 (1998).

[228] A. Scherz, *Spin-dependent x-ray absorption spectroscopy of 3d transition metals: systematics and applications*, Ph.D. thesis, Freien Universität Berlin (2003).

[229] B. T. Thole, P. Carra, F. Sette, and G. van der Laan, Phys. Rev. Lett. **68**, 1943 (1992).

[230] A. L. Ankudinov, J. J. Rehr, H. Wende, A. Scherz, and K. Baberschke, Europhys. Lett. **66**, 441 (2004).

[231] Y. Teramura, A. Tanaka, B. T. Thole, and T. Jo, J. Phys. Soc. Jpn. **65**, 3056 (1996).

[232] C. Piamonteze, P. Miedema, and F. M. F. de Groot, Phys. Rev. B **80**, 184410 (2009).

[233] K. W. Edmonds, N. R. S. Farley, T. K. Johal, G. van der Laan, R. P. Campion, B. L. Gallagher, and C. T. Foxon, Phys. Rev. B **71**, 064418 (2005).

[234] C. Piamonteze, P. Miedema, and F. M. F. de Groot, J. Phys. Conf. Ser. **190**, 012015 (2009).

[235] T. Oguchi and T. Shishidou, Phys. Rev. B **70**, 024412 (2004).

[236] G. van der Laan and B. T. Thole, Phys. Rev. B **53**, 14458 (1996).

[237] S. P. Collins, D. Laundy, C. C. Tang, and G. van der Laan, J. Phys. Condens. Matter **7**, 9325 (1995).

[238] J. Stöhr and H. König, Phys. Rev. Lett. **75**, 3748 (1995).

[239] C. J. Ballhausen, *Introduction to ligand field theory*, Tech. Rep. (McGraw-Hill,, 1962).

[240] B. T. Thole, G. van der Laan, J. C. Fuggle, G. A. Sawatzky, R. C. Karnatak, and J.-M. Esteva, Phys. Rev. B **32**, 5107 (1985).

[241] J. P. Crocombette and F. Jollet, J. Phys. Condens. Matter **8**, 5253 (1996).

[242] R. Zimmermann, P. Steiner, R. Claessen, F. Reinert, S. Hüfner, P. Blaha, and P. Dufek, J. Phys. Condens. Matter **11**, 1657 (1999).

[243] M. W. Haverkort, J. Phys. Conf. Ser. **712**, 012001 (2016).

[244] M. W. Haverkort, J. Phys. Conf. Ser. **712**, 012001 (2016).

[245] M. W. Haverkort, M. Zwierzycki, and O. K. Andersen, Phys. Rev. B **85**, 165113 (2012).

[246] V. I. Anisimov and O. Gunnarsson, Phys. Rev. B **43**, 7570 (1991).

[247] F. M. F. de Groot, J. C. Fuggle, B. T. Thole, and G. A. Sawatzky, Phys. Rev. B **42**, 5459 (1990).

[248] J. Zaanen, G. A. Sawatzky, and J. W. Allen, Phys. Rev. Lett. **55**, 418 (1985).

[249] A. E. Bocquet, A. Fujimori, T. Mizokawa, T. Saitoh, H. Namatame, S. Suga, N. Kimizuka, Y. Takeda, and M. Takano, Phys. Rev. B **45**, 1561 (1992).

[250] A. E. Bocquet, T. Mizokawa, T. Saitoh, H. Namatame, and A. Fujimori, Phys. Rev. B **46**, 3771 (1992).

[251] O. K. Andersen, W. Klose, and H. Nohl, Phys. Rev. B **17**, 1209 (1978).

[252] A. Fujimori and F. Minami, Phys. Rev. B **30**, 957 (1984).

[253] C. Lanczos, Journal of research of the National Bureau of Standards **45**, 255 (1950).

[254] J. Lüder, J. Schött, B. Brena, M. W. Haverkort, P. Thunström, O. Eriksson, B. Sanyal, I. Di Marco, and Y. O. Kvashnin, Phys. Rev. B **96**, 245131 (2017).

[255] K. Koepernik and H. Eschrig, Phys. Rev. B **59**, 1743 (1999).

[256] M. Buchner, K. Höfler, B. Henne, V. Ney, and A. Ney, J. Appl. Phys. **124**, 161101 (2018).

[257] R. L. Fagaly, Rev. Sci. Instrum. **77**, 101101 (2006).

[258] J. Clarke, J. Clarke, and A. I. Braginski, *The SQUID Handbook: Fundamentals and Technology of SQUIDs and SQUID Systems*, Vol. 1 (Wiley-Vch, 2003).

[259] P. Marcon and K. Ostanina, Progress in Electromagnetics Research Symposium (2012).

[260] M. A. Note, Quantum Design (2002).

[261] J. G. Checkelsky, R. Yoshimi, A. Tsukazaki, K. S. Takahashi, Y. Kozuka, J. Falson, M. Kawasaki, and Y. Tokura, Nat. Phys. **10**, 731 (2014).

[262] K. He, Y. Wang, and Q.-K. Xue, Natl. Sci. Rev. **1**, 38 (2013).

[263] L. B. Duffy, A. I. Figueroa, G. van der Laan, and T. Hesjedal, Phys. Rev. Mater. **1**, 064409 (2017).

[264] P. Sessi, R. R. Biswas, T. Bathon, O. Storz, S. Wilfert, A. Barla, K. A. Kokh, O. E. Tereshchenko, K. Fauth, M. Bode, and A. V. Balatsky, Nat. Comm. **7**, 12027 EP (2016), article.

[265] J. A. Krieger, C.-Z. Chang, M.-A. Husanu, D. Sostina, A. Ernst, M. M. Otrokov, T. Prokscha, T. Schmitt, A. Suter, M. G. Vergniory, E. V. Chulkov, J. S. Moodera, V. N. Strocov, and Z. Salman, Phys. Rev. B **96**, 184402 (2017).

[266] M. Winnerlein, S. Schreyeck, S. Grauer, S. Rosenberger, K. M. Fijalkowski, C. Gould, K. Brunner, and L. W. Molenkamp, Phys. Rev. Mater. **1**, 5332 (2017).

[267] C. I. Fornari, P. H. O. Rappl, S. L. Morelhão, T. R. F. Peixoto, H. Bentmann, F. Reinert, and E. Abramof, APL Mater. **4**, 106107 (2016).

[268] W. Liu, Y. Xu, L. He, G. van der Laan, R. Zhang, and K. Wang, Sci. Adv. **5**, 10.1126/sciadv.aav2088 (2019).

[269] B. Leedahl, D. W. Boukhvalov, E. Z. Kurmaev, A. Kukharenko, I. S. Zhidkov, N. V. Gavrilov, S. O. Cholakh, P. H. Le, C. W. Luo, and A. Moewes, Sci. Rep. **7**, 5758 (2017).

[270] P. Mahadevan and D. D. Sarma, Phys. Rev. B **61**, 7402 (2000).

[271] K. Yaji, A. Kimura, C. Hirai, M. Taniguchi, M. Koyama, H. Sato, K. Shimada, A. Tanaka, T. Muro, S. Imada, and S. Suga, Phys. Rev. B **70**, 064402 (2004).

[272] A. Scherz, H. Wende, C. Sorg, K. Baberschke, J. Minár, D. Benea, and H. Ebert, Phys. Scr. , 586 (2005).

[273] R. Storn and K. Price, J. Glob. Optim. **11**, 341 (1997).

[274] J. Tiilikainen, V. Bosund, M. Mattila, T. Hakkarainen, J. Sormunen, and H. Lipsanen, J. Phys. D: Appl. Phys. **40**, 4259 (2007).

[275] A. E. Bocquet, T. Mizokawa, K. Morikawa, A. Fujimori, S. R. Barman, K. Maiti, D. D. Sarma, Y. Tokura, and M. Onoda, Phys. Rev. B **53**, 1161 (1996).

[276] A. Tanaka and T. Jo, J. Phys. Soc. Jpn. **63**, 2788 (1994).

[277] P. Larson and W. R. L. Lambrecht, Phys. Rev. B **78**, 195207 (2008).

[278] Z. Liu, X. Wei, J. Wang, H. Pan, F. Ji, F. Xi, J. Zhang, T. Hu, S. Zhang, Z. Jiang, W. Wen, Y. Huang, M. Ye, Z. Yang, and S. Qiao, Phys. Rev. B **90**, 094107 (2014).

[279] P. Fazekas, Lecture Notes on Electron Correlation and Magnetism (1999).

[280] A. Kimura, S. Suga, T. Shishidou, S. Imada, T. Muro, S. Y. Park, T. Miyahara, T. Kaneko, and T. Kanomata, Phys. Rev. B **56**, 6021 (1997).

[281] V. B. Zabolotnyy, K. Fürsich, R. J. Green, P. Lutz, K. Treiber, C.-H. Min, A. V. Dukhnenko, N. Y. Shitsevalova, V. B. Filipov, B. Y. Kang, B. K. Cho, R. Sutarto, F. He, F. Reinert, D. S. Inosov, and V. Hinkov, Phys. Rev. B **97**, 205416 (2018).

[282] K. Fürsich, V. B. Zabolotnyy, E. Schierle, L. Dudy, O. Kirilmaz, M. Sing, R. Claessen, R. J. Green, M. W. Haverkort, and V. Hinkov, Phys. Rev. B **97**, 165126 (2018).

[283] W. Zhang, D. West, S. H. Lee, Y. Qiu, C.-Z. Chang, J. S. Moodera, Y. S. Hor, S. Zhang, and W. Wu, Phys. Rev. B **98**, 115165 (2018).

[284] X. Kou, L. Pan, J. Wang, Y. Fan, E. S. Choi, W.-L. Lee, T. Nie, K. Murata, Q. Shao, S.-C. Zhang, and K. L. Wang, Nat. Comm. **6**, 8474 (2015).

[285] H.-A. Ullner, Annalen der Physik **476**, 45 (1968).

[286] S. Nakajima, J. Phys. Chem. Solids **24**, 479 (1963).

[287] S. H. Vosko, L. Wilk, and M. Nusair, Can. J. Phys. **58**, 1200 (1980).

[288] H. Ebert, D. Ködderitzsch, and D. Minár, Rep. Prog. Phys. **74**, 096501 (2011).

[289] D. S. G. Bauer, *Development of a relativistic full-potential first-principles multiple scattering Green function method applied to complex magnetic textures of nano structures at surfaces*, Ph.D. thesis, RWTH Aachen University (2013).

[290] N. Stefanou, H. Akai, and Z. R., Comput. Phys. Commun. **60**, 231 (1990).

[291] N. Stefanou and R. Zeller, J. Phys. Condens. Matter **3**, 7599 (1991).

[292] R. Zeller, J. Phys. Cond. Matt. **16**, 6453 (2004).

[293] A. Liechtenstein, M. Katsnelson, V. Antropov, and V. Gubanov, J. Magn. Magn. Mater. **67**, 65 (1987).

[294] T. C. Schulthess, W. M. Temmerman, Z. Szotek, W. H. Butler, and G. Malcolm Stocks, Nat. Mater. **4**, 838 (2005).

[295] K. Sumida, M. Kakoki, J. Reimann, M. Nurmamat, S. Goto, Y. Takeda, Y. Saitoh, K. A. Kokh, O. E. Tereshchenko, J. Güdde, U. Höfer, and A. Kimura, New J. Phys. **21**, 093006 (2019).

[296] P. Rüßmann, S. K. Mahatha, P. Sessi, M. A. Valbuena, T. Bathon, K. A. Kokh, K. Fauth, S. Godey, A. Mugarza, O. E. Tereshchenko, P. Gargiani, M. Valvidares, E. Jiménez, N. B. Brookes, M. Bode, G. Bihlmayer, S. Blügel, P. Mavropoulos, C. Carbone, and A. Barla, J. Phys. Mater. **1**, 015002 (2018).

[297] P. Kacman, Semicond. Sci. Technol. **16**, R25 (2001).

[298] K. Sato, P. H. Dederichs, H. Katayama-Yoshida, and J. Kudrnovský, J. Phys. Condens. Matter **16**, S5491 (2004).

[299] B. Belhadji, L. Bergqvist, R. Zeller, D. P. H., K. Sato, and H. Katayama-Yoshida, J. Phys. Condens. Matter **19**, 436227 (2007).

[300] T. Jungwirth, J. Sinova, J. Mašek, J. Kučera, and A. H. MacDonald, Rev. Mod. Phys. **78**, 809 (2006).

[301] J. Zhang, C.-Z. Chang, Z. Zhang, J. Wen, X. Feng, K. Li, M. Liu, K. He, L. Wang, X. Chen, Q.-K. Xue, X. Ma, and Y. Wang, Nat. Commun. **2**, 574 (2011).

[302] P. Bruno, Phys. Rev. B **39**, 865 (1989).

[303] M. Kobayashi, I. Muneta, Y. Takeda, Y. Harada, A. Fujimori, J. Krempaský, T. Schmitt, S. Ohya, M. Tanaka, M. Oshima, and V. N. Strocov, Phys. Rev. B **89**,

205204 (2014).

[304] K. Sato, L. Bergqvist, J. Kudrnovský, P. H. Dederichs, O. Eriksson, I. Turek, B. Sanyal, G. Bouzerar, H. Katayama-Yoshida, V. A. Dinh, T. Fukushima, H. Kizaki, and R. Zeller, Rev. Mod. Phys. **82**, 1633 (2010).

[305] Q. L. He, T. L. Hughes, N. P. Armitage, Y. Tokura, and K. L. Wang, Nat. Mater. **21**, 15 (2022).

[306] C. I. Fornari, H. Bentmann, S. L. Morelhão, T. R. F. Peixoto, P. H. O. Rappl, A.-V. Tcakaev, V. Zabolotnyy, M. Kamp, T.-L. Lee, C.-H. Min, P. Kagerer, R. C. Vidal, A. Isaeva, M. Ruck, V. Hinkov, F. Reinert, and E. Abramof, J. Phys. Chem. C **124**, 16048 (2020).

[307] A. Tcakaev, V. B. Zabolotnyy, C. I. Fornari, P. Rüßmann, T. R. F. Peixoto, F. Stier, M. Dettbarn, P. Kagerer, E. Weschke, E. Schierle, P. Bencok, P. H. O. Rappl, E. Abramof, H. Bentmann, E. Goering, F. Reinert, and V. Hinkov, Phys. Rev. B **102**, 184401 (2020).

[308] J. Viefhaus, F. Scholz, S. Deinert, L. Glaser, M. Ilchen, J. Seltmann, P. Walter, and F. Siewert, Nuclear Instruments and Methods in Physics Research Section A: Accelerators, Spectrometers, Detectors and Associated Equipment **710**, 151 (2013), the 4th international workshop on Metrology for X-ray Optics, Mirror Design, and Fabrication.

[309] The jülich kkr codes, `https://jukkr.fz-juelich.de`, accessed: 2022-02-10.

[310] H. Ebert, A. Perlov, and S. Mankovsky, Solid State Commun. **127**, 443 (2003).

[311] T. Kinoshita, H. P. N. J. Gunasekara, Y. Takata, S.-i. Kimura, M. Okuno, Y. Haruyama, N. Kosugi, K. G. Nath, H. Wada, A. Mitsuda, M. Shiga, T. Okuda, A. Harasawa, H. Ogasawara, and A. Kotani, J. Phys. Soc. Jpn. **71**, 148 (2002).

[312] H. Wada, A. Nakamura, A. Mitsuda, M. Shiga, T. Tanaka, H. Mitamura, and T. Goto, J. Phys. Condens. Matter **9**, 7913 (1997).

[313] V. Kachkanov, M. J. Wallace, G. van der Laan, S. S. Dhesi, S. A. Cavill, Y. Fujiwara, and K. P. O'Donnell, Sci. Rep. **2**, 969 (2012).

[314] A. Figueroa, A. Baker, S. Harrison, K. Kummer, G. van der Laan, and T. Hesjedal, J. Magn. Magn. Mat **422**, 93 (2017).

[315] N. A. Anderson, M. Hupalo, D. Keavney, M. C. Tringides, and D. Vaknin, Phys. Rev. Mater. **1**, 054005 (2017).

[316] E. Negusse, J. Dvorak, J. S. Holroyd, M. Liberati, T. S. Santos, J. S. Moodera, E. Arenholz, and Y. U. Idzerda, J. Appl. Phys. **105**, 07C930 (2009).

[317] J. H. Richter, B. J. Ruck, M. Simpson, F. Natali, N. O. V. Plank, M. Azeem, H. J. Trodahl, A. R. H. Preston, B. Chen, J. McNulty, K. E. Smith, A. Tadich, B. Cowie, A. Svane, M. van Schilfgaarde, and W. R. L. Lambrecht, Phys. Rev. B **84**, 235120 (2011).

[318] C. Kittel and P. McEuen, *Introduction to solid state physics*, Vol. 8 (Wiley New York, 1996).

[319] S. J. Oh and S. Doniach, Phys. Rev. B **26**, 2085 (1982).

[320] A. B. Shick, L. Havela, A. I. Lichtenstein, and M. I. Katsnelson, Sci. Rep. **5**, 15429 (2015).

[321] G. van der Laan, E. Arenholz, A. Schmehl, and D. G. Schlom, Phys. Rev. Lett. **100**, 067403 (2008).

[322] R. S. Selinsky, D. J. Keavney, M. J. Bierman, and S. Jin, Appl. Phys. Lett. **95**, 202501 (2009).

[323] T. Kawamoto, K. Fujita, H. Akamatsu, T. Nakamura, T. Kinoshita, M. Mizumaki, N. Kawamura, M. Suzuki, Y. Kususe, S. Murai, and K. Tanaka, Phys. Rev. B **88**, 024405 (2013).

[324] B. Díaz, E. Granado, E. Abramof, P. H. O. Rappl, V. A. Chitta, and A. B. Henriques, Phys. Rev. B **78**, 134423 (2008).

[325] J. M. D. Coey, *Magnetism and Magnetic Materials* (Cambridge University Press, 2010).

[326] K. H. Hellwege, *Einführung in die Festkörperphysik*, Vol. 34 (Springer-Verlag, 2013).

[327] L. Kilanski, M. Górska, M. Arciszewska, A. Podgórni, R. Minikayev, B. Brodowska, A. Reszka, B. J. Kowalski, V. E. Slynko, and E. I. Slynko, Acta Phys. Pol. A **134**, 950 (2018).

[328] A. Damascelli, Z. Hussain, and Z.-X. Shen, Rev. Mod. Phys. **75**, 473 (2003).

[329] S. Thirupathaiah, T. Stürzer, V. B. Zabolotnyy, D. Johrendt, B. Büchner, and S. V. Borisenko, Phys. Rev. B **88**, 140505(R) (2013).

[330] Y. L. Chen, J. G. Analytis, J.-H. Chu, Z. K. Liu, S.-K. Mo, X. L. Qi, H. J. Zhang, D. H. Lu, X. Dai, Z. Fang, S. C. Zhang, I. R. Fisher, Z. Hussain, and Z.-X. Shen, Science **325**, 178 (2009).

[331] P.-Y. Chuang, S.-H. Su, C.-W. Chong, Y.-F. Chen, Y.-H. Chou, W.-C. Chen, C.-M. Cheng, K.-D. Tsuei, C.-H. Wang, Y.-W. Yang, *et al.*, RSC Adv. **8**, 423 (2018).

[332] R. C. Vidal, H. Bentmann, J. I. Facio, T. Heider, P. Kagerer, C. I. Fornari, T. R. F. Peixoto, T. Figgemeier, S. Jung, C. Cacho, B. Büchner, J. van den Brink, C. M. Schneider, L. Plucinski, E. F. Schwier, K. Shimada, M. Richter, A. Isaeva, and F. Reinert, Phys. Rev. Lett. **126**, 176403 (2021).

[333] V. Petříček, M. Dušek, and L. Palatinus, Z. Kristallogr. Cryst. Mater **229**, 345 (2014).

[334] J. P. Perdew and Y. Wang, Phys. Rev. B **45**, 13244 (1992).

[335] J. Fujii, M. Sperl, S. Ueda, K. Kobayashi, Y. Yamashita, M. Kobata, P. Torelli, F. Borgatti, M. Utz, C. S. Fadley, A. X. Gray, G. Monaco, C. H. Back, G. van der Laan, and G. Panaccione, Phys. Rev. Lett. **107**, 187203 (2011).

[336] K. W. Edmonds, G. van der Laan, N. R. S. Farley, R. P. Campion, B. L. Gallagher, C. T. Foxon, B. C. C. Cowie, S. Warren, and T. K. Johal, Phys. Rev. Lett. **107**, 197601

(2011).

[337] J. Okabayashi, A. Kimura, T. Mizokawa, A. Fujimori, T. Hayashi, and M. Tanaka, Phys. Rev. B **59**, R2486 (1999).

[338] K. W. Edmonds, N. R. S. Farley, R. P. Campion, C. T. Foxon, B. L. Gallagher, T. K. Johal, G. van der Laan, M. MacKenzie, J. N. Chapman, and E. Arenholz, Appl. Phys. Lett. **84**, 4065 (2004).

[339] T. Pincelli, V. Lollobrigida, F. Borgatti, A. Regoutz, B. Gobaut, C. Schlueter, T.-L. Lee, D. J. Payne, M. Oura, K. Tamasaku, A. Y. Petrov, P. Graziosi, F. M. Granozio, M. Cavallini, G. Vinai, R. Ciprian, C. H. Back, G. Rossi, M. Taguchi, H. Daimon, G. van der Laan, and G. Panaccione, Nat. Commun. **8**, 16051 (2017).

[340] L. J. Collins-McIntyre, M. D. Watson, A. A. Baker, S. L. Zhang, A. I. Coldea, S. E. Harrison, A. Pushp, A. J. Kellock, S. S. P. Parkin, G. van der Laan, and T. Hesjedal, AIP Adv. **4**, 127136 (2014).

[341] M. D. Watson, L. J. Collins-McIntyre, L. R. Shelford, A. I. Coldea, D. Prabhakaran, S. C. Speller, T. Mousavi, C. R. M. Grovenor, Z. Salman, S. R. Giblin, G. van der Laan, and T. Hesjedal, New J. Phys. **15**, 103016 (2013).

[342] J. P. Perdew, K. Burke, and M. Ernzerhof, Phys. Rev. Lett. **77**, 3865 (1996).

[343] C. Hu, K. N. Gordon, P. Liu, J. Liu, X. Zhou, P. Hao, D. Narayan, E. Emmanouilidou, H. Sun, Y. Liu, H. Brawer, A. P. Ramirez, L. Ding, H. Cao, Q. Liu, D. Dessau, and N. Ni, Nat. Commun. **11**, 97 (2020).

[344] K. Takubo, R. Comin, D. Ootsuki, T. Mizokawa, H. Wadati, Y. Takahashi, G. Shibata, A. Fujimori, R. Sutarto, F. He, S. Pyon, K. Kudo, M. Nohara, G. Levy, I. S. Elfimov, G. A. Sawatzky, and A. Damascelli, Phys. Rev. B **90**, 081104 (2014).

[345] K. W. Edmonds, G. van der Laan, A. A. Freeman, N. R. S. Farley, T. K. Johal, R. P. Campion, C. T. Foxon, B. L. Gallagher, and E. Arenholz, Phys. Rev. Lett. **96**, 117207 (2006).

[346] G. van der Laan, K. W. Edmonds, E. Arenholz, N. R. S. Farley, and B. L. Gallagher, Phys. Rev. B **81**, 214422 (2010).

[347] P. R. Stone, M. A. Scarpulla, R. Farshchi, I. D. Sharp, E. E. Haller, O. D. Dubon, K. M. Yu, J. W. Beeman, E. Arenholz, J. D. Denlinger, and H. Ohldag, Appl. Phys. Lett. **89**, 012504 (2006).

[348] E. Golias, E. Weschke, T. Flanagan, E. Schierle, A. Richardella, E. D. Rienks, P. S. Mandal, A. Varykhalov, J. Sánchez-Barriga, F. Radu, N. Samarth, and O. Rader, Appl. Phys. Lett. **119**, 132404 (2018).

[349] M. Scholten, J. I. Facio, R. Ray, I. M. Eremin, J. van den Brink, and F. S. Nogueira, Phys. Rev. Research **3**, L032014 (2021).

[350] M. F. Islam, C. M. Canali, A. Pertsova, A. Balatsky, S. K. Mahatha, C. Carbone, A. Barla, K. A. Kokh, O. E. Tereshchenko, E. Jiménez, N. B. Brookes, P. Gargiani, M. Valvidares, S. Schatz, T. R. F. Peixoto, H. Bentmann, F. Reinert, J. Jung, T. Bathon,

K. Fauth, M. Bode, and P. Sessi, Phys. Rev. B **97**, 155429 (2018).

[351] Y. Lu, M. Höppner, O. Gunnarsson, and M. W. Haverkort, Phys. Rev. B **90**, 085102 (2014).

[352] M. W. Haverkort, G. Sangiovanni, P. Hansmann, A. Toschi, Y. Lu, and S. Macke, EPL **108**, 57004 (2014).

[353] S. Agrestini, C.-Y. Kuo, M. Moretti Sala, Z. Hu, D. Kasinathan, K.-T. Ko, P. Glatzel, M. Rossi, J.-D. Cafun, K. O. Kvashnina, A. Matsumoto, T. Takayama, H. Takagi, L. H. Tjeng, and M. W. Haverkort, Phys. Rev. B **95**, 205123 (2017).

[354] S. Glawion, J. Heidler, M. W. Haverkort, L. C. Duda, T. Schmitt, V. N. Strocov, C. Monney, K. J. Zhou, A. Ruff, M. Sing, and R. Claessen, Phys. Rev. Lett. **107**, 107402 (2011).

[355] Y. Utsumi, D. Kasinathan, K.-T. Ko, S. Agrestini, M. W. Haverkort, S. Wirth, Y.-H. Wu, K.-D. Tsuei, D.-J. Kim, Z. Fisk, A. Tanaka, P. Thalmeier, and L. H. Tjeng, Phys. Rev. B **96**, 155130 (2017).

[356] L. Ding, C. Hu, F. Ye, E. Feng, N. Ni, and H. Cao, Phys. Rev. B **101**, 020412 (2020).

[357] B. Liu, C. Piamonteze, M. U. Delgado-Jaime, R.-P. Wang, J. Heidler, J. Dreiser, R. Chopdekar, F. Nolting, and F. M. F. de Groot, Phys. Rev. B **96**, 054446 (2017).

[358] M. W. Haverkort, S. I. Csiszar, Z. Hu, S. Altieri, A. Tanaka, H. H. Hsieh, H.-J. Lin, C. T. Chen, T. Hibma, and L. H. Tjeng, Phys. Rev. B **69**, 020408 (2004).

[359] B. H. Frazer, B. Gilbert, B. R. Sonderegger, and G. De Stasio, Surf. Sci. **537**, 161 (2003).

[360] C. Yan, Y. Zhu, S. Fernandez-Mulligan, E. Green, R. Mei, B. Yan, C. Liu, Z. Mao, and S. Yang, (2021), arXiv:2107.08137 [cond-mat.mtrl-sci] .

[361] Y. Liu, L.-L. Wang, Q. Zheng, Z. Huang, X. Wang, M. Chi, Y. Wu, B. C. Chakoumakos, M. A. McGuire, B. C. Sales, W. Wu, and J. Yan, Phys. Rev. X **11**, 021033 (2021).

[362] W. Ge, P. M. Sass, J. Yan, S. H. Lee, Z. Mao, and W. Wu, Phys. Rev. B **103**, 134403 (2021).

[363] L. C. Folkers, L. T. Corredor, F. Lukas, M. Sahoo, A. U. B. Wolter, and A. Isaeva, Zeitschrift für Kristallographie - Crystalline Materials **237**, 101 (2022).

[364] D. Y. Yan, M. Yang, P. B. Song, Y. T. Song, C. X. Wang, C. J. Yi, and Y. G. Shi, Phys. Rev. B **103**, 224412 (2021).

[365] X.-M. Ma, Y. Zhao, K. Zhang, S. Kumar, R. Lu, J. Li, Q. Yao, J. Shao, F. Hou, X. Wu, M. Zeng, Y.-J. Hao, Z. Hao, Y. Wang, X.-R. Liu, H. Shen, H. Sun, J. Mei, K. Miyamoto, T. Okuda, M. Arita, E. F. Schwier, K. Shimada, K. Deng, C. Liu, J. Lin, Y. Zhao, C. Chen, Q. Liu, and C. Liu, Phys. Rev. B **103**, L121112 (2021).

[366] P. Li, J. Yu, Y. Wang, and W. Luo, Phys. Rev. B **103**, 155118 (2021).

[367] L. Zhou, Z. Tan, D. Yan, Z. Fang, Y. Shi, and H. Weng, Phys. Rev. B **102**, 085114 (2020).

[368] S. Eremeev, M. Otrokov, and E. Chulkov, J. Alloys Compd. **709**, 172 (2017).

List of publications

- P. Kagerer, C. I. Fornari, S. Buchberger, T. Tschirner, L. Veyrat, M. Kamp, **A. Tcakaev**, V. Zabolotnyy, S. L. Morelhão, B. Geldiyev, S. Müller, A. Fedorov, E. Rienks, P. Gargiani, M. Valvidares, L. C. Folkers, A. Isaeva, B. Büchner, V. Hinkov, R. Claessen, H. Bentmann, and F. Reinert, *Two-dimensional ferromagnetic extension of a topological insulator*, 10.48550/ARXIV.2207.14421 (2022).

- R. Gaina, S. Sarkar, M. Soulier, J. Khmaladze, E. Perret, **A. Tcakaev**, V. Hinkov, M. Bonura, E. Weschke, and C. Bernhard, *Magnetic field dependence of the copper charge density wave order in a $YBa_2Cu_3O_7/Nd_{0.65}(Ca_{0.7}Sr_{0.3})_{0.35}MnO_3$ superlattice*, Phys. Rev. B 104, 174513 (2021).

- T. R. F. Peixoto, H. Bentmann, P. Rüßmann, **A. Tcakaev**, M.Winnerlein, S. Schreyeck, S. Schatz, R. C. Vidal, F. Stier, V. Zabolotnyy, R. J. Green, C. H. Min, C. I. Fornari, H. Maaß, H. B. Vasili, P. Gargiani, M. Valvidares, A. Barla, J. Buck, M. Hoesch, F. Diekmann, S. Rohlf, M. Kalläne, K. Rossnagel, C. Gould, K. Brunner, S. Blügel, V. Hinkov, L. W. Molenkamp, and F. Reinert, *Non-local effect of impurity states on the exchange coupling mechanism in magnetic topological insulators*, npj Quantum Materials 5, 87 (2020).

- M. Dettbarn, V. B. Zabolotnyy, **A. Tcakaev**, R. Sutarto, F. He, Y. Chen, R. J. Green, and V. Hinkov, *Strain induced stabilization of a static Jahn-Teller distortion in the O^*-phase of $La_{7/8}Sr_{1/8}MnO_3$*, 10.48550/ARXIV.2011.07108 (2020).

- **A. Tcakaev**, V. B. Zabolotnyy, C. I. Fornari, P. Rüßmann, T. R. F. Peixoto, F. Stier, M. Dettbarn, P. Kagerer, E. Weschke, E. Schierle, P. Bencok, P. H. O. Rappl, E. Abramof, H. Bentmann, E. Goering, F. Reinert, and V. Hinkov, *Incipient antiferromagnetism in the Eu-doped topological insulator Bi_2Te_3*, Phys. Rev. B 102,184401 (2020), *editors' Suggestion*.

- P. Kagerer, C. I. Fornari, S. Buchberger, S. L. Morelhão, R. C. Vidal, **A. Tcakaev**, V. Zabolotnyy, E. Weschke, V. Hinkov, M. Kamp, B. Büchner, A. Isaeva, H. Bentmann, and F. Reinert, *Molecular beam epitaxy of antiferromagnetic $(MnBi_2Te_4)(Bi_2Te_3)$ thin films on BaF_2 (111)*, Journal of Applied Physics 128, 135303 (2020).

- C. I. Fornari, H. Bentmann, S. L. Morelhão, T. R. F. Peixoto, P. H. O. Rappl, **A. Tcakaev**, V. Zabolotnyy, M. Kamp, T.-L. Lee, C.-H. Min, P. Kagerer, R. C. Vidal, A.

Isaeva, M. Ruck, V. Hinkov, F. Reinert, and E. Abramof, *Incorporation of Europium in Bi_2Te_3 Topological Insulator Epitaxial Films*, J. Phys. Chem. C 124, 16048 (2020).

- **A. Tcakaev**, V. B. Zabolotnyy, R. J. Green, T. R. F. Peixoto, F. Stier, M. Dettbarn, S. Schreyeck, M. Winnerlein, R. C. Vidal, S. Schatz, H. B. Vasili, M. Valvidares, K. Brunner, C. Gould, H. Bentmann, F. Reinert, L. W. Molenkamp, and V. Hinkov, *Comparing magnetic ground-state properties of the V- and Cr-doped topological insulator $(Bi, Sb)_2Te_3$*, Phys. Rev. B 101, 045127 (2020), *editors' Suggestion*.

Acknowledgments

During my postgraduate studies, I had the honor of working with many prominent scientists and participating in a number of interesting and challenging projects. The research work presented here would not have been possible without the help and support of many people, to whom I would like to express my gratitude.

First and foremost, I want to thank my supervisor, Prof. Vladimir Hinkov, for giving me the opportunity to conduct the research in his group at the University of Würzburg and for providing me with the guidance and counsel I needed to succeed in the PhD. I especially appreciate the freedom to work on different topics and develop my own interests. His trust and support have been one of the main factors that made my experience in his group invaluable. I would also like to thank for the many opportunities to do beamtimes at synchrotron facilities all around the world, attend conferences, workshops and summer schools. In addition to scientific support, I am very grateful to Prof. Vladimir Hinkov for his help with administrative issues related to the comfortable stay of me and my family in Germany.

Likewise, I would like to express my deep gratitude to my day-to-day supervisor Dr. Volodymyr Zabolotnyy for his immense guidance and enormous support. It was an invaluable experience for me to witness his dedication to science. I have learned a lot about physics in general and about x-ray spectroscopy in particular as a result of his patient teaching. He is not only an excellent supervisor, but also an attentive interlocutor, helpful partner during the experiments at synchrotron facilities, valuable supplier with dedicated computer codes and inexhaustible source of interesting ideas.

I am grateful to the head of the Experimental Physics IV chair, Prof. Ralph Claessen, for the friendly working atmosphere at the chair and the best conditions for research, as well as for the scientific discussions during our chair seminars. Special thanks to our office administrator Mrs. Monika Seifer, who can be rightly called the "Mother" of the Experimental Physics IV. I am very grateful to her for her invaluable help with all organizational problems that arose during my PhD, including business trips, orders, applications and events. I would like to specifically thank her for the support she gave me when I moved to Germany, for help in finding housing, for useful hints and, of course, for the practice and help in learning German.

The research projects discussed in this thesis have been published in several peer-reviewed publications. These publications were the result of the combined efforts of

many co-authors. Therefore, I would like to thank them all for their direct contributions to the projects, the fruitful discussions we shared, and their assistance in preparing the manuscripts. Especially, I would like to thank the group of Prof. Friedrich Reinert at Experimental Physics VII, namely Dr. Hendrik Bentmann, Dr. Celso Fornari, Dr. Thiago Peixoto and Philipp Kagerer for the very fruitful collaboration during my PhD, which led to several joint publications. I would also like to acknowledge Prof. Karl Brunner, Prof. Charles Gould, Dr. Eberhard Goering, Dr. Laura Corredor, and Dr. Anja Wolter for the scientific discussions on numerous subjects, including the magnetic properties of TIs, for their contribution with bulk magnetometry data and help with manuscripts preparations.

A substantial part of my experimental work was carried out at various synchrotron light facilities, including the UE46 PGM-1 beamline at BESSY II and the BOREAS beamline at ALBA. This experimental work would not have been successful without the support of the beamline scientists. I would like to thank Dr. Eugen Weschke and Dr. Enrico Schierle at the UE46 PGM-1 beamline at BESSY II, and Dr. Manuel Valvidares and Dr. Pierluigi Gargiani at the BOREAS beamline at ALBA, for their superb support at numerous beamtimes, during which I learned much about the operation and maintenance of beamlines and had great discussions about the data analysis and new experimental ideas. I am also grateful to Dr. Peter Bencok at the I10 beamline at Diamond and Dr. Fadi Choueikani at the DEIMOS beamline at SOLEIL for their great support during the XAS/XMCD measurements.

During my PhD I was fortunate to use excellent MTI samples. I am very grateful to Dr. Steffen Schreyeck and Dr. Martin Winnerlein from the department of Prof. Laurens W. Molenkamp (Experimental Physics III) for providing me with V- and Cr-doped $(Bi,Sb)_2Te_3$ thin films of excellent quality. Likewise, I want to thank Dr. Celso Fornari at Experimental Physics VII for providing Eu-doped Bi_2Te_3 films. Furthermore, I like to express my gratitude towards Prof. Anna Isaeva and Dr. Laura Folkers for providing intrinsic MTI crystals and their structure characterization. Special thanks to Prof. Anna Isaeva for fruitful discussions and help with manuscript preparations.

I am especially grateful to Dr. Philipp Rüßmann, Dr. Jorge Facio, Prof. Robert Green and Prof. Maurits Haverkort for their strong theoretical support and many scientific discussions, which led to the successful interpretation of the experimental data. Special thanks to Prof. Maurits Haverkort and to his student Simon Heinze for teaching and helping me with MLFT calculations in QUANTY. Also, I would like to thank Dr. Domenico Di Sante for teaching me the basics of DFT.

It was a pleasure to work with other members in the group of Prof. Vladimir Hinkov: Michael Dettbarn, Benjamin Katter and, of course, a former member Fabian Stier. I sincerely appreciated our discussions on different topics during the coffee breaks, the exchanges we had and the team work during the numerous beamtimes we shared. I also thank all other members of the Experimental Physics IV chair for providing a pleasant

working atmosphere and pleasant collaborations during the long or short overlaps we had in Würzburg.

Last but not least, I would like to express my deepest gratitude to my parents for their unconditional love, understanding, trust in me, and endless support. Especially, I want to thank my father Valid, who, despite the many difficulties and deprivations of being a refugee of two wars in Chechnya, despite his health problems due to these wars, was my first teacher, instilled in me a love of science in general and physics in particular, and has always supported me both morally and materially in my endeavors and on my further path in science.